# Concentric Tube Robots: Design, Deployment, and Stability

By

Hunter Bryant Gilbert

Dissertation

Submitted to the Faculty of the

Graduate School of Vanderbilt University

in partial fulfillment of the requirements

for the degree of

DOCTOR OF PHILOSOPHY

in

Mechanical Engineering

August, 2016

Nashville, Tennessee

Approved:

Robert J. Webster III, Ph.D.

Michael Goldfarb, Ph.D.

Nilanjan Sarkar, Ph.D.

Nabil Simaan, Ph.D.

Michael I. Miga, Ph.D.

# ACKNOWLEDGMENTS

I would like to acknowledge the many people who have contributed to this dissertation in various ways. It would not have been possible without their time, effort, and support, and I am forever grateful for their contributions.

My advisor Bob Webster has been instrumental in the creation of this work. His foresight and guidance have directed me to the right problems. As a true mentor, he has helped me to develop professionally as a researcher and has provided me with not only technical skills and knowledge but also much needed advice and encouragement. He truly desires to help others achieve their own goals, and he contributes greatly to the success of all those around him. I truly hope that I will be a mentor to others as effectively and meaningfully as he has been to me.

I would also like to thank my dissertation committee: Bob Webster, Nabil Simaan, Michael Miga, Michael Goldfarb, and Nilanjan Sarkar. They have given their valuable time in support of this dissertation, and have provided helpful feedback that has improved it substantially. Many anonymous reviewers have also contributed greatly to the improvement of the content of this dissertation.

I would like to thank the National Science Foundation, the National Institutes of Health, and Vanderbilt University, which have all provided essential funding to support this work. In particular, the graduate research fellowship from the NSF granted me the flexibility to explore many of the topics contained herein more thoroughly than I likely would have otherwise been able to.

The Mechanical Engineering department staff have been immensely helpful during my time at Vanderbilt. I am thankful to Suzanne Weiss, Jean Miller, and Myrtle Daniels for reminding me of forgotten deadlines and for their willingness to help me with the myriad logistical and organizational problems that came my way, sometimes of my own creation.

I am also grateful for the welcoming and collaborative atmosphere that has been sustained by all of the members, both former and present, of the MED Lab and the CAOS Lab. It would be difficult to overstate how important all of the members of these labs have been in supporting me

over the past six years. Some parts of this work were the direct result of collaboration with my fellow lab members, and others have been heavily influenced through many conversations over coffee. I can safely say that not a single part of this work is without their influence. The work in Chapter 2 would not have been possible without the hard work of Phil Swaney, Ray Lathrop, Arthur Mahoney, and Trevor Bruns. I would also like to thank Paul Russell and Kyle Weaver, who have guided the development of the robotic system for endonasal surgery by providing both their medical knowledge and the much-needed perspective from the clinical side. Jessica Burgner taught me much of what I know about software development for robotics, which has been essential to my work. Caleb Rucker patiently taught me the kinematics of concentric tube robots upon my arrival at Vanderbilt, and has also provided valuable insights over many years. This is especially true with regard to Chapter 4. This chapter is also the direct result of a collaboration with Richard Hendrick, and his insights have been essential in understanding stability in concentric tube robots. Clinical input from Joseph Neimat was critical to the development of the application to the treatment of epilepsy as described in Chapter 5, and I am grateful to Eric Barth and Dave Comber for their continuing of this project beyond what is shown in this dissertation.

Lastly, and certainly not least, I am thankful for my wonderful family whom I love dearly: my parents, Ann and Louis, and my sister, Amanda. Their unwavering support has enabled me to persevere in my efforts.

TABLE OF CONTENTS

LIST OF TABLES

LIST OF FIGURES

# Chapter 1

# Introduction & Review

## 1.1 Concentric Tube Robots

Concentric tube robots, also known as active cannulas, are one of the smallest members of the broader family of continuum (i.e. continuously flexible) robots [1, 2, 3]. They are made from several tubes that are nested within one another concentrically (Figure 1.1). These tubes are pre-curved and made of elastic material (usually superelastic nitinol). When the tubes are grasped at their respective bases, and linear insertion/retraction and axial rotation motions are applied, they interact elastically and make one another bend and twist. The net result is a needle-sized robot that can elongate and bend in a manner that has been likened to a miniature tentacle.

While it is possible that applications will be developed outside medicine in the future, to date the motivating applications for concentric tube robots have come exclusively from surgery and interventional medicine, and two distinct methods of use have been identified. The robot can act as a steerable needle or be used as a miniature teleoperated manipulator. In both contexts, the robot can be enter the body in a variety of ways, including through the skin, through the vascular system, through a natural orifice, or through the ports in a rigid or flexible endoscope that is itself inserted into the body. In the trans-endoscope embodiment, concentric tube robots have been proposed for use in neurosurgery [4], transoral throat surgery [5], transoral lung biopsy and therapy deliv-

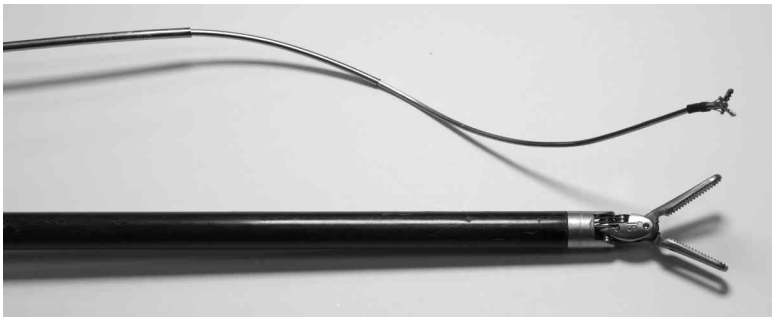

Figure 1.1: A concentric tube robot next to a standard da Vinci laparoscopic tool.

ery [6, 7], and transgastric surgery [8]. In the transvascular embodiment, concentric tube robots have been proposed for a variety of intracardiac procedures where they enter the heart through the vascular system [9, 10, 11, 12]. In the natural orifice embodiment, transurethral prostate [13], transnasal skull base[14], and transoral throat [5] applications have been proposed, and it is likely that surgeries through other natural orifices will be pursued in the future. In the percutaneous, needle-like embodiment, applications that have been suggested include fetal umbilical cord blood sampling [15], ultrasound guided liver targeting and vein cannulation [16], vascular graft placement for hemodialysis [17], thermal ablation of cancer [18, 19], prostate brachytherapy [20], retinal vein cannulation [21, 22, 23], epilepsy treatments [24], and general soft tissue targeting procedures [25, 26, 27].

Of all these applications, the two that have been studied most extensively are the cardiac applications of Dupont et al. and the endonasal applications of Webster et al. This includes the first ever use of a concentric tube robot in a live animal by Gosline et al. [28, 11]. It also includes the first insertion of a concentric tube robot into a human cadaver by Burgner et al. [29, 14]. Many researchers have also explored the use of concentric tube robots as steerable needles in a variety of phantom and ex vivo tissues, as discussed in the following subsection.

### 1.1.1 Use as Steerable Needles

When cast as steerable needles, there are several ways concentric precurved tubes can be used. The term "steerable needle" typically refers to devices that harness tip-tissue interaction forces to steer [30, 31, 32]. Consistent with this, Salcudean et al. demonstrated a concentric tube design in which a small section of a circularly curved wire extends from an outer tube [33]. In this steering paradigm, as the needle is inserted into tissue with the wire held at a fixed angle and distance of deployment, tip-tissue interaction forces will cause the shaft of the needle to bend. Changes in the distance of wire deployment and the axial wire angle control the curvature and direction of bending. Loser adopted a different approach where needle shaft curvature could be controlled independently of needle insertion via two fully overlapping precurved tubes which could rotate

with respect to one another [25]. With such a needle, a mid-insertion curvature change would cause forces to be applied to tissue along the entire needle shaft, deforming tissue in order to aim the needle towards the desired target.

In many steerable needle contexts, it is desirable to apply minimal deformation to tissue, and one wishes to maintain the needle's shaft exactly along the curved trajectory through which the tip has traveled. This is referred to as "follow-the-leader" insertion [34]. Early work, which neglected tube elastic interaction, implicitly assumed that concentric tube robots would automatically deploy in this manner [35]. However, the accumulation of experimental results and modeling advances soon showed that tube elastic interaction is typically significant. It also showed, perhaps counter intuitively, that concentric circularly precurved tubes do not achieve a circular conformation when axially rotated (see e.g. [36]). Both these factors make follow-the-leader deployment more challenging than it might at first seem.

However, a useful simple special case that can deploy in an exact follow-the-leader manner was identified early in the history of concentric tube robots. It consists of a circularly curved inner tube or wire that extends from a straight outer tube. The earliest recorded use of this concept in a needle was likely in 1985 when the Mammalok product came to market [37], and the same basic concept has been employed many times since (e.g. [38, 39, 26, 16, 18, 17, 27, 40], among others). Chapter 5 is dedicated to a model-based analysis of follow-the-leader behavior.

An advantage of using concentric tube robots as steerable needles is that concentric tube robots do not rely on tissue forces to steer, so their mechanical properties do not need to be perfectly matched to the properties of the tissue through which they pass. Moreover, they are one of only two steerable needle technologies that can follow the leader through both open and liquid filled cavities in addition to soft tissues (the other is tendon actuation [41]).

### 1.1.2 Use as Miniature Manipulators

The basic idea of using a curved nitinol tube to deflect the tip of a manual laparoscopic tool was described in several references from the early 1990s [42, 43, 44, 45]. These apparently led to the

commercial Roticulator (Medtronic, formerly Covidien, formerly United States Surgical Corporation), which originally used a precurved nitinol tube [42], and remains on the market today with a precurved plastic tube as the bending element. The idea of a teleoperated robotic manipulator with multiple precurved tubes was developed independently and first proposed simultaneously by Sears and Dupont and by Webster, Okamura, and Cowan in 2006 [8, 26]. In this context, the device acts as a teleoperated slave robot in a manner conceptually similar to the patient side manipulator of the da Vinci system by Intuitive Surgical, Inc. These initial papers in 2006 began a period of rapid advancement in concentric tube modeling. This laid the foundation for much additional research, which was aimed at making concentric tube robots useful in a master-slave context.

### 1.1.3 Development History

The commercial Mammalok product mentioned earlier appears to be the earliest device incorporating concentric tubes and/or wires made from precurved nitinol [46]. Introduced in 1985, it was the first commercial nitinol device used in an interventional procedure, if orthodontic arch wires are excluded. In 1992, Melzer described the use of a curved tube to deflect a manual laparoscopic tool [44], and Cuschieri and Buess described a similar idea involving a telescoping curved dissection blade [45]. In 1995, Melzer and Winkel at Daum GmbH (Schwerin, Germany) developed the SMARTGuide, which was patented in 1995 and CE marked in 1996 [39]. In 1997, Melzer described the use of the SMARTGuide in image-guided interventions [38]. In 2005, Loser used two counterrotated fully overlapping curved nitinol tubes to change the curvature of a needle he applied in an image-guided surgery setting [25]. Three groups (initially unaware of one another) then began simultaneous independent development of concentric tube robots, with first publications in 2005 and 2006 [8, 26, 35]. These publications and subsequent rapid modeling progress brought concentric tube robots to the general consciousness of the surgical robotics community.

## 1.2 Modeling

### 1.2.1 Model Formulation

Model development began with simple models, which were continually generalized via the incorporation of additional physical effects. The simplest possible model by Furusho et al. [35, 16] considered only geometry, assuming that every tube was infinitely stiff compared to all within it. Bending mechanics was included first by Loser for two fully overlapping tubes [25], and then by Webster et al. [8, 47] and Dupont et al. [26, 48] for general collections of tubes. Torsion was included first in straight sections of the device [8, 47], and then in curved sections with circular or general tube precurvatures [49, 50, 36, 51, 48]. External loading has been incorporated by considering the robot to be a single curved rod [52, 53], and more generally by describing the relative tube rotations induced by the external loads [54, 55, 53]. The above models have been used to enable teleoperation, and form the basis for mechanics-based control, design, and sensing.

While there remains some activity in modeling, researchers appear to have more or less converged on a model which leverages the theory of special Cosserat rods to describe each component tube as a continuum which undergoes bending and torsion [55, 48]. Though future developments could potentially prove otherwise, at present it appears that these models have reached a "sweet spot," striking a balance between model complexity and accuracy.

All models to date neglect the effects of shear and axial extension of the rods, which are good assumptions for thin beams like the tubes in a concentric tube robot. The basic modeling approach is to write down a Cosserat rod equation for each tube, and then enforce concentricity by requiring all tubes to conform to the same curvature as a function of arc-length, leaving them free to rotate axially with respect to each other. This results in a system of differential equations with mixed boundary conditions. The boundary conditions at the base of the robot are the axial angles of the tubes, and the boundary conditions at the tip are internal moments that vanish because there is no material beyond the tip to support them. After this mechanics problem is solved in order to determine the axial tube angles along the robot, one must still integrate along the robot to determine

the space curve of the robot itself (or this can be done simultaneously). This model has been derived from both Newtonian equilibrium of forces and moments [48, 55] and energy minimization [51, 36], and the two approaches have been shown to be equivalent [55, 51]. Experimental testing of the model has shown that, with calibration, mean error in the prediction of tip position can be as low as 1% to 3% of overall arc length [55, 36, 48, 53].

External loading has been included in this modeling framework in two ways. One method is to consider the effects of loads on the model equations directly [55, 53]. A more computationally efficient, approximate way of handling external loads is to first solve the unloaded model and then treat the robot as a single curved rod that deforms under external loads [53, 56]. This approach does not model relative tube axial rotations induced by external loads, and whether or not the loss in accuracy is significant depends on the robot design and external loading conditions.

The models have also been extended to provide the differential kinematic maps for actuation (Jacobian matrix) and external loading (compliance matrix) [57, 58]. These maps have enabled resolved-rates-style algorithms for real-time control of concentric tube robots, as discussed further in Section 1.3. Additional factors like tube tolerances and friction have been explored, though not yet integrated into the modeling framework described above. A complicating factor in the use of concentric tube robots, which is captured in the above modeling framework, is the presence of multiple solutions. Rapid "snapping" may occur when tube actuation causes the robot to transition from one solution to another [47, 36, 48]. This effect is the subject of Chapter 4.

### 1.2.2 Model Solution

In contrast to the model formulation, no consensus has yet emerged as to the best way to evaluate concentric tube robot models. The model equations for two tubes with circular precurvature have been solved analytically using elliptic integrals [36, 48]. However, no analytical solutions have yet been found for robots consisting of more than two tubes, or for precurvature that varies with arc length. Hence, model equations are typically solved numerically.

Numerical implementations have most often used a "shooting" method, which iteratively ad-

justs unknown state values at one end of the robot until the boundary conditions are satisfied at the other end. This procedure can be performed either base-to-tip, guessing the unknown values at the proximal end and integrating to the distal end [59], or tip-to-base [53]. It was originally assumed that group preserving integration methods were required for the geometric integration [48, 36]. However, in practice it has been shown that integration of the rotation matrix via standard explicit Runge-Kutta methods introduces numerical error that is negligible compared to kinematic error, as one would expect from the numerical examples in [60].

Simplifications to the model such as piecewise linearization enhance the speed of solution, and sensing the unknown proximal boundary conditions with torque sensors alleviates the need for root-finding techniques [61]. This choice does not necessarily find a solution that agrees with the distal boundary conditions, but the advantages may outweigh this drawback. There remain open questions in model evaluation. These relate to determination of which numerical methods are most efficient and numerically stable, the accuracy of various approximations, and the characterization of the "snapping" behavior (also known as "bifurcation") mentioned earlier. In Chapter 3, a real-time model solution method is provided that is fast and accurate, and which does not require either model linearization or functional approximation.

## 1.3 Control

### 1.3.1 Kinematic Control

The main goal of kinematic control to date has been teleoperation. Two general frameworks have been proposed for kinematic control of concentric tube robots. The first involves precomputation of the model solutions over the entire workspace via one of the methods described in the previous section. To these solutions, an approximate forward kinematics model can be fit, such as a multidimensional Fourier series which is computationally efficient to invert via numerical root finding and can be evaluated at 1000 Hz [48]. The main advantages to this method are the consistent speed, suitability for real-time inverse kinematics, and the ability to identify numerical

problems with solution of the model equations offline while the device is not performing a task. One disadvantage is that this method is unable to account for concentric tube robots which exhibit multiple solutions in the forward kinematics, which reduces the possible design space. Another is that the torsional effects of external loading cannot be considered.

A second general approach involves rapid solution of the model equations and computation of the manipulator Jacobian and compliance matrices [57]. Previous implementations in C++ were limited to about 200 to 400 Hz [14], but in Chapter 3 it is shown that with careful implementation, this rate can be substantially increased. The differential forward kinematic mapping is then used to update the actuator configuration iteratively to solve the inverse kinematics [29]. The advantages to this method are the ability to control robots which exhibit multiple solution behavior, the ability to immediately control new designs without precomputation or code changes, and the ability to control robots under known external loads. The main disadvantages are the increased programming effort required for fast model solution and Jacobian computation.

### 1.3.2 Motion Planning

Optimal motion planners can enable obstacle avoidance and generate actuation sequences needed to deploy along anatomical structures or to targets. Examples of prior work include planning paths around critical brain structures [62], through tubular anatomy such as the bronchi of the lung [7], and through the passages of the nasal sinuses [63]. Some of the first planners used simplified kinematic models employing circular arcs and were based on penalty methods that convert the constrained optimization problem of avoiding obstacles while maintaining a tip location into an unconstrained optimization problem [62, 7]. A different technique, termed Rapidly-Exploring Roadmaps, was first applied with the transmissional torsion model to find optimal plans [64], and later expanded to include the fully torsionally compliant kinematic model [63]. These planning algorithms typically require many thousands to millions of evaluations of the forward kinematic mapping, and this is one of the main motivations for the focus on computational efficiency in Chapter 3.

## 1.4 Sensing

Image guidance is a critical part of many surgical procedures. These include teleoperated procedures where virtual fixtures [65] are used, as well as procedures where the concentric tube robot is used as a needle. One can use the mechanics-based model described in Section 1.2.1 to predict where the robot will be, provided that the procedure can tolerate errors of approximately 3% of the arc length of the robot, and loads applied to the robot (if significant) are known. However, often this will not be the case, so real-time sensing and closed loop control will be required. An example of the use of visual feedback in tip position control was the use of a closed form Jacobian derived from the transmissional torsion model in [66]. In the remainder of this section we discuss the methods that are being investigated to sense the shape of the robot for such purposes, as well as methods to estimate applied loads. Force sensing based on deflection models are the subject of Chapter 6.

### 1.4.1 Magnetic and Fiber Optic Shape Sensing

Standard, off-the-shelf magnetic tracking systems can be used for tip pose sensing, and also in principle to provide the pose at discrete points along the robot. These have been used by Mahvash and Dupont for stiffness modulation [56, 67], by Burgner et al. for image guidance [14], and by Xu et al. for model validation and evaluation of tracking performance [58, 61]. In principle, such sensing could be used in conjunction with the robot model to estimate the entire curve of the robot. There has been recent interest in the surgical robotics community in fiber Bragg grating sensors in needles [68, 69, 70, 71] and other optical sensing techniques (see e.g. [72]), and these results have recently been extended to include strain-based sensing of shape and forces in concentric tube robots [73].

### 1.4.2 Force Sensing

Due to the inherent flexibility of the concentric tube robot, it will be useful to know the interaction forces between the robot and the environment for both accurate control and user feedback. A wide variety of force sensors have also been investigated in the context of minimally invasive surgical tools [72], but the only one that has been specifically designed for and applied to a concentric tube robot is a tip force sensor which measures force magnitude and contact angle based on electrical resistance of fluid-filled channels [74, 75].

## 1.5 Design

There are three distinct aspects of concentric tube robot design. Perhaps the one that has received the most attention to date is the selection of tube properties (curvatures, lengths, diameters, number of tubes) appropriately based on application requirements. However, beyond this, one must also construct a suitable actuation unit that grasps the tubes at their respective bases and applies telescopic and axial rotation motions to each. Lastly, one must design the surgical end effectors necessary to accomplish the surgical objective.

### 1.5.1 Tube Design

Optimal selection of tube properties has been the focus of substantial research, and was discussed in the earliest papers on use of concentric tube devices as robotic manipulators [8, 26], which provided ways to determine maximum curvatures and idealizations intended to facilitate design intuition. Since then, a number of authors have investigated algorithms for optimal tube design, using a variety of models and assumptions. Anor et al. planned piecewise constant curvature paths through the brain ventricles for choroid plexus cauterization [76]. Torres et al. used circular precurvatures with the torsionally compliant model to develop a rapidly-exploring random tree algorithm to create a design together with an actuator plan for collision-free insertion through a lung lumen [77]. Burgner et al. also used the torsionally compliant model and introduced volume-based

coverage objective functions to design robots that are able to optimally cover a desired workspace with their tips [78, 14].

These results have motivated the development of two results in this dissertation. First, the efficient and stable computational routine of Chapter 3 is useful for the algorithms that design optimal robot shapes. Second, the shape setting method described in Chapter 2 was developed in order to accurately and rapidly prototype the designs which are created by these computational routines.

### 1.5.2 Actuation Unit Design

Actuation units have only recently become a topic of interest in the concentric tube robot research community, with early papers simply showing photographs of actuation units with little discussion on their design [26, 66]. A differential drive is described in [5], although this has the drawback of requiring long holes to be drilled through screws. Modular bimanual (two arm) [14] and quadramanual (four arm) [79] robots designed for endonasal surgery have also been presented. Single-arm MRI-compatible designs using piezoelectric motors [80] and pneumatic cylinders [81] have been constructed and demonstrated in MRI environments. A highly compact actuation unit for controlling one curved tube deployed through an endoscope port was described in [4]. Another compact and inexpensive (potentially disposable) actuation unit using a spline screw for CT-guided procedures was described in [27]. Consideration has also been given to reusable actuation units. An autoclavable hand operated actuation unit design was presented in [19]. An autoclavable and biocompatible motorized actuation unit (with a bagging procedure for the motor pack) was described in [40], and applied to evacuation of intracerebral hemorrhages.

### 1.5.3 End Effector Design

A number of innovative end effectors have been developed for concentric tube robots. Dupont et al. developed remarkable metal microelectromechanical systems (MEMS) end effectors specifically for concentric tube robots for cardiac tissue approximation and tissue resection [82, 11, 12].

Burgner et al. mounted a gripper from a flexible endoscopic tool to the tip of a concentric tube robot and also developed a curette end effector for endonasal surgery [14].

## 1.6 Dissertation Contributions

The overarching goal of this thesis is to provide advancements which are necessary for making concentric tube robots clinically ready surgical devices. The subsections below are four areas in which this dissertation contributes to the state of the art in concentric tube robots.

### 1.6.1 Actuation Hardware and Tube Shaping

The actuation hardware presented in this dissertation builds upon previous work in [79] to satisfy the surgical workflow requirements for endonasal surgical procedures. The robot is specifically designed to deliver multiple concentric tube robots through a single nostril. There are three salient points which separate this design from prior actuation units. First, this platform is capable of delivering four tools through a single nostril via the use of a funnel-like tube collector, which provides surgeons with more dexterous tools at the operating site. Second, the tools are modular and can be easily attached or removed from the main body of the actuation unit. This feature facilitates simple pre- and post-surgical workflows and allows the tool to be sterilized separately from the robot. Third, a sterile barrier separates the tool modules from the bulk of the robot, which prevents the need for sterilizing the electronics and motors. This paradigm is similar to the commercially successful da Vinci robot from Intuitive Surgical.

In addition to the actuation unit, a method for shape setting superelastic Nitinol tubes to match specific design requirements is presented in this dissertation. The method uses pulsed DC current to heat the tubes under closed-loop control with resistive feedback, which has not been studied before in the context of shape setting Nitinol parts. Although, in principle, box furnaces can be used for shape setting Nitinol, previous experience indicated that repeatability and accuracy were both major problems for prototype quantities. The experiments we present for the electrical method indicate that it is preferable to the box furnace method in prototyping laboratories.

### 1.6.2 Software for Robot Control

The software design presented in this dissertation facilitates real-time control of concentric tube robots. Although the literature on concentric tube robots contains many suggestions for how to solve the torsionally compliant model equations, none of the existing literature adequately addresses real-time solution of the model for teleoperation. The concentric tube kinematic model possesses orders of magnitude more computational complexity than those of rigid serial or parallel manipulators, making model computation speed important for online operation in surgical robots and offline computation in automated designers and planners.

The solution presented in this dissertation avoids iterative methods wherever possible, and is shown to enable model solution for three tubes at rates greater than 5 kHz, whereas the fastest of prior implementations, which both used a simpler model and made more approximations, was reported at approximately 1 kHz [61]. We also study the numerical convergence of the method we propose, which is an important consideration for safety in a real-time medical robot.

### 1.6.3 Model Analysis: Elastic Stability

The study of elastic stability is one of the primary theoretical contributions of this dissertation. Although it has been known since early in the development of concentric tube robots that they may suddenly "snap" from one configuration to another under particular choices of design and actuation, this behavior had not previously been reconciled with the community-accepted torsionally compliant model. We provide in this dissertation a study of elastic stability from energetic principles, culminating in a relative measure of stability that can inform automated planners, designers, and real-time controllers about the stability of concentric tube robots of any design at arbitrary configurations. This contribution will be important for advancing the use of high curvature robots in practice.

### 1.6.4 Model Analysis: Follow-the-Leader

In the follow-the-leader deployment paradigm, the shaft of the robot follows the tip as it increases in length, as the body of a snake follows its head. Previously, it was known that concentric tube robots could accomplish this type of motion in only a few special cases, which included only a single circularly curved tube, two or more circularly curved tubes in plane with one another, or the case where outer tubes are so stiff as to render the elastic interaction between the tubes negligible.

In this dissertation the mechanics-based model is analyzed and the potential space of follow-the-leader designs is expanded to include helical tube designs, which greatly increases the design space available for either human or computational designers. In addition, approximate follow-the-leader deployment is studied to show that particular classes of designs can achieve behavior similar to perfect follow-the-leader behavior with errors that are clinically acceptable for many needle insertion tasks.

### 1.6.5 Intrinsic Force Sensing

Intrinsic force sensing has been proposed as an interesting way to leverage the inherent compliance of continuum robots [83] to obtain additional information about the interaction of the robot and the environment. Moreover, it has already been shown that the behavior of an impedance-type controller can be recreated for concentric tube robots by using a model of an elastic rod [67]. However, there has not yet been an analysis of predictive accuracy for the intrinsic force sensing capabilities of concentric tube robots using position feedback. Motivated by the near ubiquity of magnetic position tracking equipment in neurosurgical suites, Chapter 6 details the design and performance of an optimal state-estimation framework based on magnetic tracking feedback. A standard fixed interval smoothing algorithm is applied to predict external loads based on the observed deflection. Force sensing experiments indicate that the full mechanics-based model for concentric tube robots can provide force estimates that are reasonably accurate in terms of both magnitude and direction across widely varying system states, including high-torsion configurations.

## 1.7 Review of the Concentric Tube Robot Model

This chapter reviews the preliminary mathematical modeling techniques and the derivation of the state-of-the-art concentric tube robot model which was introduced by Rucker et al. and by Dupont et al. [55, 48]. Many of the following chapters rely on this modeling framework. This model has previously been shown to be accurate to approximately 3% of the total arc length of the robot [55]. By assuming that the deformation of the tubes when they are combined and/or placed under external loads is entirely in bending, and neglecting the effects of shear and elongation, a set of first order, nonstiff, nonlinear differential equations models the behavior of the robot under actuation and external loading. The model is derived in this chapter from first principles using an energy analysis, and the notation is introduced inline with the concepts.

### 1.7.1 Framing the Curves

The shape of each of the $N$ tubes is described by the curve in space which lies along the centerline of the tube. A stationary coordinate frame $I$ is introduced, as shown in Figure 1.2. Prior to combining the tubes concentrically, the shape is described by the vector-valued function $\boldsymbol{p}_i^*(s_i)$ for the $i^{\text{th}}$ tube. Derivatives of this function with respect to $s_i$ are assumed to exist as needed. The curve is parameterized so that $s_i$ represents the arc length along the curve, i.e. $ds_i$ is the differential arc element, $ds_i^2 = dx^2 + dy^2 + dz^2$. Parameterizing the curves by $s_i$ thus implies that

$$\left\| \frac{\partial \boldsymbol{p}_i^*}{\partial s_i} \right\| = 1$$

The domain of each function $\boldsymbol{p}_i^*$ is $[0, L_i]$, where $L_i$ is the length of the $i^{\text{th}}$ tube. Naturally, the curve describing each tube exists on a separate arc length coordinate $s_i$.

In order to represent the finite diameter of each of the component tubes, each of the space curves is then *framed*, providing a right-handed coordinate frame

$$F_i^* = \left\{ \boldsymbol{x}_i^*(s_i), \boldsymbol{y}_i^*(s_i), \boldsymbol{z}_i^*(s_i) \right\}$$

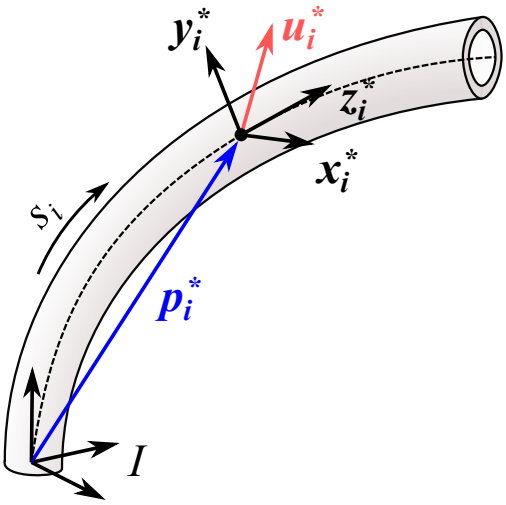


Figure 1.2: The $i^{\text{th}}$ tube's shape before deformation is described by the position $\boldsymbol{p}_i^*$ as a function of arc length $s_i$. At each point along the centerline curve a coordinate frame is attached.

at each point along each of the curves. Let the rotation matrix $\mathbf{R}_i^*$ be the transformation from the inertial frame to this frame, so that in coordinates of the frame $I$, the matrix $\mathbf{R}_i^* = \begin{bmatrix} \boldsymbol{x}_i^* & \boldsymbol{y}_i^* & \boldsymbol{z}_i^* \end{bmatrix}$. This matrix is an element of the special orthogonal group $SO(3)$ which consists of all possible rotation matrices.

Unless otherwise noted, vector quantities with subscript $\alpha$ will be represented by coordinate vectors in terms of the coordinate frame $F_\alpha$, for any subscript $\alpha$. The basis vectors of the moving frame (e.g. $\boldsymbol{x}$) can be interpreted either to represent the abstract physical vectors or to be coordinate vectors written in the inertial coordinate frame $I$. When the standard basis for $\mathbb{R}^3$ is indicated, the symbols $\boldsymbol{e}_1$, $\boldsymbol{e}_2$, and $\boldsymbol{e}_3$ will be used, defined by

$$\boldsymbol{e}_1 = \begin{bmatrix} 1 \\ 0 \\ 0 \end{bmatrix} \qquad \boldsymbol{e}_2 = \begin{bmatrix} 0 \\ 1 \\ 0 \end{bmatrix} \qquad \boldsymbol{e}_3 = \begin{bmatrix} 0 \\ 0 \\ 1 \end{bmatrix} \tag{1.1}$$

The unit vector $\boldsymbol{z}_i^*(s_i)$ of the frame $F_i^*$ is chosen first to be tangent to the curve, so that

$$(\boldsymbol{p}_i^*)' = \boldsymbol{z}_i^* = \mathbf{R}_i^* \boldsymbol{e}_3 \tag{1.2}$$

The other two vectors in $F_i^*$ are mutually perpendicular and span the cross section of the tube. The frame is chosen as a Bishop frame, which is locally roll-free about the tangent [84]. Because the frame remains orthonormal and right handed, there is an "angular velocity" vector $\boldsymbol{u}_i^*(s_i)$, termed the precurvature vector, which describes the rate of change of the frame vectors with respect to arc length, as

$$\frac{\partial}{\partial s_i}\mathbf{R}_i^* = \mathbf{R}_i^* \begin{bmatrix} 0 & -u_{iz}^* & u_{iy}^* \\ u_{iz}^* & 0 & -u_{ix}^* \\ -u_{iy}^* & u_{ix}^* & 0 \end{bmatrix} = \mathbf{R}_i^* \widehat{\boldsymbol{u}}_i^* \tag{1.3}$$

Here, $u_{ix}^*$, $u_{iy}^*$, and $u_{iz}^*$ are the coordinates of the curvature vector in the moving frame, and the "hat" function $\widehat{\boldsymbol{u}}$ takes a vector from $\mathbb{R}^3$ converts it to the skew-symmetric cross-product matrix, an element of the space $\mathfrak{so}(3)$, which consists of all matrices of the skew-symmetric form in (1.3). The inverse of the "hat" function, the "vee" function, performs the opposite conversion from $\mathfrak{so}(3)$ to $\mathbb{R}^3$. The space $\mathfrak{so}(3)$ is the Lie algebra associated with the group $SO(3)$, and represents the ways in which "small rotations" vary from the identity matrix. For rotations $R$ which are close to the identity, $R = I + \widehat{\boldsymbol{w}} + \mathcal{O}\left(\|\boldsymbol{w}\|^2\right)$ for some $\widehat{\boldsymbol{w}}$ which is an element of $\mathfrak{so}(3)$.

The Bishop framing convention sets $u_{iz}^* = 0$, which is permissible since the remaining two degrees of freedom are enough to completely describe $\boldsymbol{z}_i^*$ for an arbitrary curve (this is because the time rate of change of a unit vector is always orthogonal to the vector itself). Let the symbol $\boldsymbol{x}'(s_i)$ denote the partial derivative of $\boldsymbol{x}$ with respect to arc length $s_i$ (the derivative is taken with respect to the naturally defined arc length coordinate for each tube). Frequently the arguments to functions will be dropped for convenience of notation so that $\boldsymbol{x}' = \boldsymbol{x}'(s_i)$. From equation (1.3), together with the fact that

$$\left(\boldsymbol{p}_i^*\right)'' = \left(\boldsymbol{z}_i^*\right)'$$

the curvature components are found as

$$\begin{aligned} u_{ix}^* &= -\boldsymbol{y}_i^* \cdot \left(\boldsymbol{p}_i^*\right)'' \\ u_{iy}^* &= \boldsymbol{x}_i^* \cdot \left(\boldsymbol{p}_i^*\right)'' \end{aligned} \tag{1.4}$$

With a curve $\boldsymbol{p}_i^*(0)$ specified, and an initial condition for $\boldsymbol{x}_i^*(0)$ and $\boldsymbol{y}_i^*(0)$, equations (1.3) and (1.4) may be solved together as an initial value problem to yield the precurvature components and the frame simultaneously.

The combination of the position $\boldsymbol{p}_i^*$ and rotation matrix $\mathbf{R}_i^*$ forms an element of the special Euclidean group $SE(3)$, and will be denoted by $\boldsymbol{g}_i^* = (\boldsymbol{p}_i^*, \mathbf{R}_i^*)$. As a homogeneos transformation matrix,

$$\boldsymbol{g}_i^* = \begin{bmatrix} \mathbf{R}_i^* & \boldsymbol{p}_i^* \\ \mathbf{0}_{1\times 3} & 1 \end{bmatrix} \tag{1.5}$$

The rigid body velocity of the frame $\boldsymbol{g}_i^*$ is given by $\boldsymbol{\xi}_i^*$. This vector is composed of the twist coordinates

$$\boldsymbol{\xi}_i^* = \begin{bmatrix} \boldsymbol{v}_i^* \\ \boldsymbol{u}_i^* \end{bmatrix} \tag{1.6}$$

where $\boldsymbol{u}_i^*$ is the "angular velocity" with respect to the arc-length parameter $s$ and $\boldsymbol{v}_i^*$ is the "linear velocity" with respect to the arc-length parameter. These twist coordinates are in terms of the body-frame coordinate basis, so that the linear velocity coordinates $\boldsymbol{v}_i^*$ correspond to the vector velocity

$$\boldsymbol{p}' = v_{ix}^* \boldsymbol{x}_i^* + v_{iy}^* \boldsymbol{y}_i^* + v_{iz}^* \boldsymbol{z}_i^* \tag{1.7}$$

The modeling choice that $(\boldsymbol{p}_i^*)' = \boldsymbol{z}_i^*$ yields immediately that $\boldsymbol{v}_i^* = \boldsymbol{e}_3$. The twist coordinates $\boldsymbol{\xi}_i^*$ can be used in the compact formula

$$(\boldsymbol{g}_i^*)' = \boldsymbol{g}_i^* \widehat{\boldsymbol{\xi}}_i^* \tag{1.8}$$

to write all of the geometric differential equations describing the pre-curved shape of the $i^{\text{th}}$ tube.

The mapping $\widehat{(\cdot)} : \mathbb{R}^6 \to \mathfrak{se}(3)$ is given by

$$\widehat{\boldsymbol{\xi}}_i^* = \begin{bmatrix} 0 & -u_{iz}^* & u_{iy}^* & v_{ix}^* \\ u_{iz}^* & 0 & -u_{ix}^* & v_{iy}^* \\ -u_{iy}^* & u_{ix}^* & 0 & v_{iz}^* \\ 0 & 0 & 0 & 0 \end{bmatrix} \tag{1.9}$$

when $\boldsymbol{g}_i^*$ is interpreted as a homogeneous transformation matrix as in (1.5). The Lie algebra $\mathfrak{se}(3)$ corresponding to the Lie group SE(3) consists of matrices of the form in 1.9.

### 1.7.2 The Energy of Bending and Twisting

The stored elastic energy in each tube is given by the Kirchhoff kinetic analogy. Envision that the framing of each tube described in the previous section has become permanently attached to the material of each tube, so that infinitesimal units of material along the centerline of the tubes become uniquely associated with an element $\boldsymbol{g}_i^*(s_i)$. Denote the variables describing the deformed state with the same characters as the undeformed ones, but with the star removed. It is assumed that the tubes do not exhibit deformation in either shear or extension. A cross section at $s$ defined by the plane $\{\boldsymbol{x}_i^*(s_i), \boldsymbol{y}_i^*(s_i)\}$ remains a cross section after the deformation. This implies that the tangent vectors to the centerline, which are normal to perpendicular cross sections of the tubes, are transformed between the deformed and undeformed states by a pure rotation.

After deforming, each tube now has its shape described by a new curvature vector $\boldsymbol{u}_i$, which describes the evolution of the frame $F_i = \{\boldsymbol{x}_i, \boldsymbol{y}_i, \boldsymbol{z}_i\}$ after deformation. The frame $F_i$ is the frame $F_i^*$ after the deformation, and this allows one to naturally compare the curvature vectors before and after deformation. In general, the deformed curvature vector $\boldsymbol{u}_i$ can have a non-zero component along any direction. Let the change in curvature between the reference and deformed shapes be $\Delta\boldsymbol{u}_i = \boldsymbol{u}_i - \boldsymbol{u}_i^*$.

The stored elastic energy in the $i^{\text{th}}$ tube is

$$E_i[\boldsymbol{u}_i] = \int_0^{L_i} W_i(\Delta \boldsymbol{u}_i)\, ds_i \tag{1.10}$$

The function $W_i$ is the strain energy density function which depends only on the change in curvature. To second order and assuming small strains[1], $W_i(\Delta \boldsymbol{u}_i) = (1/2)\, \Delta \boldsymbol{u}_i \cdot \mathbf{K}_i \Delta \boldsymbol{u}_i$. In this expression $\mathbf{K}_i$ is a linear map and the term $\mathbf{K}_i \Delta \boldsymbol{u}_i$ is interpreted as the internal moment carried by the tube. This is in a similar form as the expression for the kinetic energy of a rotating rigid body, $E = (1/2)\, \boldsymbol{\omega} \cdot \mathbf{I}\boldsymbol{\omega}$, and is termed the Kirchhoff kinetic analogy [36].

Since the tubes have a ring-like cross section, the stiffness map $\mathbf{K}_i$ is diagonal when expressed in the local frame $F_i$, which is naturally aligned with the principal moments of inertia. The matrix of $\mathbf{K}_i$ is given by

$$\mathbf{K}_i = \begin{bmatrix} E_i I_{i,xx} & 0 & 0 \\ 0 & E_i I_{i,yy} & 0 \\ 0 & 0 & G_i J_{i,z} \end{bmatrix} \tag{1.11}$$

The constants $E_i$ and $G_i$ are the Young's modulus and shear modulus of the material of the $i^{\text{th}}$ tube (intrinsic material properties), and $I_{i,xx}$ and $I_{i,yy}$ are the second area moment taken about the principal axes passing through the centroid of the cross section. $J_{i,z}$ is the polar second area moment. For an annular shape, $I_{xx} = I_{yy} = I$, and $J_z = I_{xx} + I_{yy}$, and if the material is isotropic, $G = E/(2(1+\nu))$ where $\nu$ is Poisson's ratio. For convenience, define $k_{ib} = E_i I_{i,xx}$ as the bending stiffness and $k_{it} = G_i J_{i,z}$ as the torsional stiffness, so that $\mathbf{K}_i = \text{diag}(k_{ib}, k_{ib}, k_{it})$.

The total elastic energy stored in collection of $N$ tubes is the sum of the energy stored in each tube,

$$E[\boldsymbol{u}_1, ..., \boldsymbol{u}_n] = \sum_{i=1}^{N} \int_0^{L_i} \Delta \boldsymbol{u}_i^T \mathbf{K}_i \Delta \boldsymbol{u}_i\, ds_i \tag{1.12}$$

[1]Most concentric tube robots undergo strains of less than a few percent

### 1.7.3 Combining the Tubes Concentrically

Because the tubes are placed concentrically with one another, there is only one space curve $\boldsymbol{p}_B(s)$ after deformation, so that $\boldsymbol{p}_i(s) = \boldsymbol{p}_B(s)$ for all $i$, and all functions have been reparameterized in terms of a single "backbone" arc length coordinate. Figure 1.3 shows the frames of each tube after the tubes conform to a common centerline. This constraint is holonomic, as it is an algebraic function of the system states, and can be differentiated to be expressed on the tangent vectors, $\boldsymbol{z}_i(s) = \boldsymbol{z}_B(s)$ for all $i, j$.

The robot arc length $s$ is defined so that $s = 0$ occurs at the constrained point where the tubes exit the actuation unit. The tubes are actuated at robot arc lengths $\beta_i \leq 0$ so that we have $N$ functions

$$s_i(s) = s - \beta_i \tag{1.13}$$

which relate the robot arc length to the arc length along each tube. The robot arc length $s$ is then defined on the interval $\beta \leq s \leq L$ where

$$\beta = \min_i\{\beta_i\}$$

$$L = \max_i\{\beta_i + L_i\}$$

The parameters for each tube are then naturally defined on the tube's individual arc-length function $s_i(s)$, e.g. the torsional stiffness $k_{it}(s_i(s))$.

Define a new frame $\{\boldsymbol{x}_B, \boldsymbol{y}_B, \boldsymbol{z}_B\}$ that describes the final space curve of the combined tubes, with $\boldsymbol{z}_B$ tangent to the curve. This new frame is again chosen to be a Bishop frame, so that the associated curvature coordinate vector $\boldsymbol{u}_B$ satisfies the constraint $\boldsymbol{e}_3 \cdot \boldsymbol{u}_B = 0$. At each arc length, the frames attached to the material of each tube are related to this "backbone" frame by a rotation about $\boldsymbol{z}_B$, so that for the rotation matrices,

$$\mathbf{R}_i = \mathbf{R}_B \mathbf{R}_z(\psi_i) \tag{1.14}$$

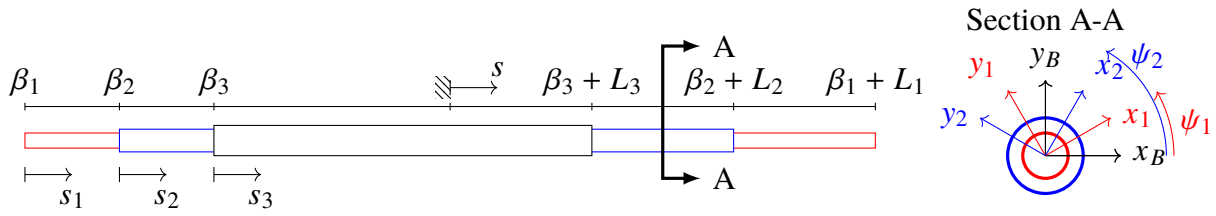


Figure 1.3: A depiction of a concentric tube robot which has been straightened for clarity, with arc lengths $\beta_i$ and $\beta_i + L_i$ located at the proximal and distal ends of the tubes, respectively. The section view A-A depicts the centerline Bishop frame and the material-attached frames of tubes 1 and 2, with angles $\psi_1$ and $\psi_2$ labeled.

where $\mathbf{R}_z$ is the standard $z$-axis rotation matrix,

$$\mathbf{R}_z(\psi) = \begin{bmatrix} \cos\psi & -\sin\psi & 0 \\ \sin\psi & \cos\psi & 0 \\ 0 & 0 & 1 \end{bmatrix} \tag{1.15}$$

Equation 1.14 should be understood as a definition of the variable $\psi_i$. For ease of notation, let $\mathbf{R}_{\psi_i} = \mathbf{R}_z(\psi_i)$.

From (1.14), a relation on the curvatures is derived by considering the arc length derivative of each side of the equation:

$$\boldsymbol{u}_i = \mathbf{R}_{\psi_i}^T \boldsymbol{u}_B + \psi_i' \boldsymbol{e}_3 \tag{1.16}$$

Because this constraint on the curvatures was derived from the holonomic position constraints, it can be substituted into the total energy functional, to yield $E[\boldsymbol{u}_B, \psi_1, ..., \psi_N]$, prior to the application of the Euler-Lagrange equations. This reduces the set of unknowns from $3N$ quantities to only $2+N$ quantities, and provides a set of generalized coordinates.

### 1.7.4 The Free-Space Model Equations

Because the curvature functions $\boldsymbol{u}_i$ are expressed in terms of $\boldsymbol{u}_B$ and $\psi_i'$, and the arc length variables $s_i$ are related to $s$ by 1.13, the total energy can be written as a single integral

$$E[\boldsymbol{u}_B, \psi_1, ..., \psi_N] = \int_\beta^L F(s, \boldsymbol{\psi}, \boldsymbol{\psi}', \boldsymbol{u}_B)\, ds \tag{1.17}$$

Deriving the model equations under free-space conditions (no externally applied forces or torques) requires only the application of the Euler-Lagrange equations to the energy functional $E$ for each of the unknown functions $\boldsymbol{u}_B(s)$ and $\psi_1(s)$ through $\psi_N(s)$. The details of this procedure are included in Appendix A.1. This results in the set of differential equations below which describe the kinematics of a concentric tube robot.

**Concentric Tube Robot Kinematics.** The spatial configuration of a concentric tube robot is determined by the solution to a boundary value problem with first order states $\psi_i$, $(k_{it}\psi_i')$, $\boldsymbol{p}_B$, and $\mathbf{R}_B$. The solution is governed by the differential equations

$$\psi_i' = \begin{cases} k_{it}^{-1}(k_{it}\psi_i') & 0 \le s_i(s) \le L_i \\ 0 & \text{otherwise} \end{cases} \tag{1.18a}$$

$$(k_{it}\psi_i')' = \begin{cases} -\boldsymbol{u}_B^T \mathbf{K}_i \dfrac{\partial \mathbf{R}_{\psi_i}}{\partial \psi_i} \boldsymbol{u}_i^* & 0 \le s_i(s) \le L_i \\ 0 & \text{otherwise} \end{cases} \tag{1.18b}$$

$$\boldsymbol{p}_B' = \mathbf{R}_B \boldsymbol{e}_3 \tag{1.18c}$$

$$\mathbf{R}_B' = \mathbf{R}_B \widehat{\boldsymbol{u}}_B \tag{1.18d}$$

with boundary conditions

$$\boldsymbol{p}_B(0) = \mathbf{0}, \quad \mathbf{R}_B(0) = \mathbf{I} \tag{1.19a}$$

$$\psi_i(\beta) = \alpha_i, \quad (k_{it}\psi_i')(L) = 0 \tag{1.19b}$$

It will sometimes be convenient to refer to the torsional moments as $m_{iz} = (k_{it}\psi_i')$.

The Euler-Lagrange equation for the unknown $\boldsymbol{u}_B$ results in an algebraic constraint

$$\frac{\partial L}{\partial \boldsymbol{u}_B} = 0 \tag{1.20}$$

This equation may be explicitly solved for $\boldsymbol{u}_B$ to provide the backbone curvature as a function of the states:

$$[\boldsymbol{u}_B(s)]_{xy} = \left[\mathbf{K}^{-1} \sum_{i \in P(s)} \mathbf{K}_i \mathbf{R}_{\psi_i} \boldsymbol{u}_i^*\right]_{xy} , \tag{1.21}$$

with

$$\mathbf{K}(s) = \sum_{i \in P(s)} \mathbf{K}_i(s) ,$$

and the set $P(s) = \{i \in \mathbb{N} : 1 \leq i \leq N \wedge 0 \leq s_i(s) \leq L_i\}$ is the set of indices of tubes which are present at the arc length $s$. Note that by definition, $\boldsymbol{u}_B \cdot \boldsymbol{e}_3 = 0$. The operator $[\cdot]_{xy}$ is defined as the orthogonal projection onto the first two coordinate axes, i.e. $[\boldsymbol{x}]_{xy} = \left(\mathbf{I} - \boldsymbol{e}_3 \boldsymbol{e}_3^T\right) \boldsymbol{x}$.

The physical interpretation of equation (1.21) is that the curvature of the collection of tubes is a weighted vector sum of the precurvatures, with the weight given by the tube's bending stiffness. The rotation matrix $\mathbf{R}_{\psi_i}$ is present to express the coordinates in a common frame. Because the precurvature vectors $\boldsymbol{u}_i^*$ and the final backbone curvature $\boldsymbol{u}_B$ are all chosen in the Bishop convention with the third coordinate equal to zero, the arc-length derivative of the angles $\psi_i$ is directly proportional to the torsional moment carried by that tube.

### 1.7.5 Incorporating External Loads

When an external force or torque is present on the robot, the model equations change only slightly. In this case, two extra states must be added and corresponding differential equations added which govern their behavior These two states represent the total internal moment and total internal force carried by the entire collection of tubes, as though they were represented by a single rod.

The internal force $\boldsymbol{n}$ and internal moment $\boldsymbol{m}$ are governed by the Cosserat equations

$$\begin{aligned} \boldsymbol{m}' &= -\boldsymbol{p}_B' \times \boldsymbol{n} \\ \boldsymbol{n}' &= -f \end{aligned} \tag{1.22}$$

Boundary conditions on $\boldsymbol{n}$ and $\boldsymbol{m}$ are determined by the external loading situation. In the case of a tip load $\boldsymbol{F}_{tip}$, the boundary condition is $\boldsymbol{n}(L) = \boldsymbol{F}_{tip}$. Typically, the free-moment condition $\boldsymbol{m}(L)$ holds as the natural boundary condition, unless an applied torque exists at the end-effector, in which case $\boldsymbol{m}(L) = \boldsymbol{M}_{tip}$.

The algebraic relationship on the the final curvature $\boldsymbol{u}_B$ and the precurvatures $\boldsymbol{u}_i^*$ becomes

$$\left[\left(\sum_{i=1}^{N} k_{ib}\right)\boldsymbol{u}_B - \sum_{i=1}^{N} k_{ib}\mathbf{R}_{\psi_i}\boldsymbol{u}_i^*\right]_{xy} = \left[\mathbf{R}_B^T\boldsymbol{m}\right]_{xy} \tag{1.23}$$

A variational derivation of this equation is included in Appendix A.2.

# Chapter 2

## Endonasal System Hardware

This chapter describes two major contributions to concentric tube robot design and fabrication. The first is the design of a new system for endonasal surgery, including mechanical design, electronics, and control software. The second is a new method for rapidly and accurately shape setting the tubes of the concentric tube manipulators themselves. The first contribution is currently in preparation for publication in an archival journal. The second has been published in IEEE Robotics and Automation Letters [85].

The robotic system described in this chapter is a second-generation system for endonasal surgery featuring concentric tube manipulators. It is an evolution of the system originally presented in [14], that includes many advancements made with the intent of satisfying real-world surgical workflow requirements. The system consists of two main parts: an actuation unit, which contains all motors and electronics, and the concentric tube manipulators delivered into the patient.

There are three salient points which separate this robot system from prior concentric tube robot systems in the literature (including [14]). First, this system is capable of delivering four concentric tube manipulators through a single nostril via the use of a funnel-like tube collector; prior robots have delivered fewer manipulators. Second, the manipulators are attached to the robot in a modular way using a cartridge interface, which has not previously been accomplished. This means that they can be removed and replaced with new manipulators (e.g. having a different end effector) during surgery, without removing the entire robot from the patient. This enables the tools to be sterilized separately from the actuation unit. Third, a sterile barrier separates the tool modules from the actuation unit, which makes it unnecessary to sterilize the electronics and motors. This overall paradigm is similar to, and inspired by, the commercially successful da Vinci robot from Intuitive Surgical.

The other major contribution of this chapter is a method to rapidly and reliably fabricate Niti-

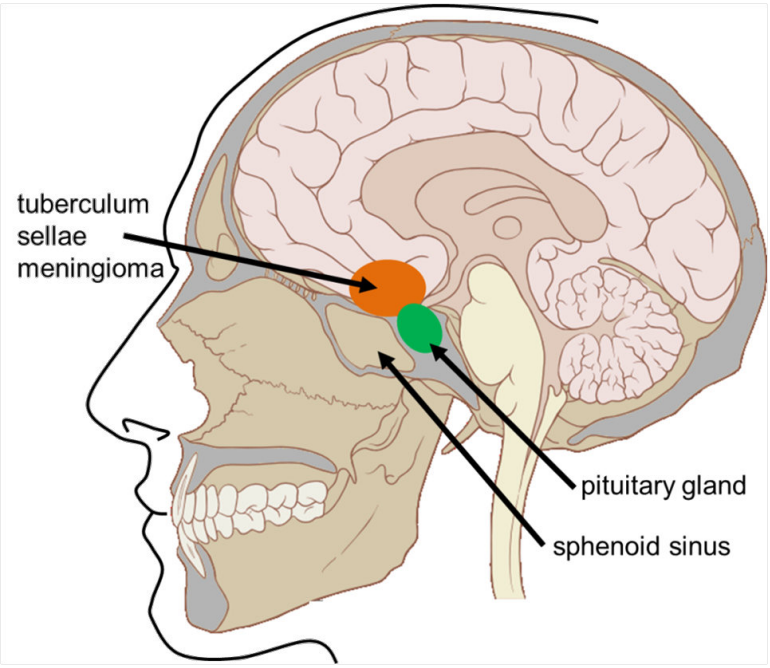


Figure 2.1: The motivation for the design of a new actuation unit is the unique set of challenges posed by endonasal surgical access to the pituitary gland and skull base.

nol tubes with desired curvatures. The method uses pulsed DC current to heat the tubes under closed-loop control with resistive feedback. This technique has not previously been explored for the purpose of shape setting Nitinol.

## 2.1 Medical Motivation

Pituitary tumor removal surgery is a significant public health challenge. One in six people will have a pituitary tumor at some point in their lives, and 1 in 100 of these will require surgery (>1 cm in diameter tumor) [86] Traditionally, surgery to remove pituitary tumors and other tumors at the skull base (Fig. 2.1) requires transcranial or transfacial access [87]. In these approaches, large, traumatic openings must be created in the patient's forehead (followed by brain retraction) or cheek (leading to disfigurement). Endonasal skull base surgery reduces invasiveness [88], resulting in less trauma, fewer complications, and shorter surgical durations [89, 90]. However, despite these compelling advantages for the patient, only a small percentage of skull base surgeries are done endonasally. One can infer from [91, 92, 93] that this number is certainly less than 50% and most

likely below 20%, though exact statistics are not available in the clinical literature.

This endonasal approach is not deployed more frequently despite its demonstrated benefits to the patient because existing surgical instruments have limited dexterity and approach angles [94, 89], and simultaneously manipulating several of them through a nostril while performing complex surgical procedures is so technically challenging that only a small number of expert surgeons can accomplish it [95]. Even for these experts, mortality rates remain non-negligible (0.9% [96]), and there remain many contraindications for the endonasal approach, including occlusion of the surgical site by delicate neurovascular structures (e.g. carotid arteries, optic nerves), inability to fully reconstruct the dura due to lack of tool dexterity, and long surgery duration [97, 89]. All these contraindications are directly related to limitations in instrument dexterity and visualization, which motivates the development of the robotic system we describe in this paper. Such a robot can potentially increase surgical dexterity and reduce the technical complexity of the procedure for surgeons, thereby increasing the percentage of patients who benefit from the endonasal approach.

### 2.2 Related Work, Workflow, and How Robots Can Assist the Surgeon

While many robotic systems have been developed for intravascular interventions (e.g. the robot discussed in [98]), as well as natural orifice surgery through other body orifices (e.g. [99, 100, 101]) or single abdominal ports (e.g. [102, 103, 104]), comparatively few systems have been targeted at endonasal surgery. This is likely due to the smaller size of the nostril compared to other natural orifices (e.g. the throat, single abdominal port, etc.). The few endonasal robotic systems that do exist are best considered in terms of their function within the entire surgical workflow.

The workflow of endonasal surgery is as follows: Surgery begins with widening of the nasal passage as necessary, to permit access to the anterior wall of the sphenoid sinus. Then, under endoscopic visualization, the sphenoid sinus is exposed by drilling through the anterior wall, followed by drilling of the posterior wall, providing access to the tumor. The surgeon then resects the tumor using hand-held tools with straight shafts. Though a variety of end-effector designs are possible on these hand-held tools, curettes (rings of metal for scraping away tumor material), are

used most often and most extensively. Since pituitary tumors are very soft (similar in consistency to brain tissue), and these rings are thin, yet not particularly sharp, they are useful for scraping away tumor tissue while sparing blood vessels or nerves they may inadvertently contact. Image guidance systems are also usually employed during the surgery. These systems (e.g. BrainLab AG, Medtronic Inc.) allow registration of intraoperative anatomy and tool positons with preoperative medical images. Prior robots developed for endonasal surgery have been used to ensure safety during the initial bone drilling operations needed to expose the surgical site [105, 106]. Robots have also been used to assist in endoscope manipulation [107, 108], and a 4 mm continuum robot has been developed to steer a camera in the sinus cavity for visual inspection [109].

For endonasal robots, the limited space available in the nostril opening, combined with the need to work dexterously within the cavities in the head, implies that instrument shafts must be small in diameter while enabling dexterous motions of the instrument tips. A recently invented robot design that matches these characteristics is the concentric tube robot concept, which is also known by the name active cannula [48, 55]. Mechanics-based models of these robots have been developed over the past several years (see [48] and [55], and references therein), and the latest models can describe the shape of the device for the general case of arbitrarily many tubes, with arbitrary precurvatures, in the presence of arbitrary external loading. These advanced models lay the foundation for adaptation of concentric tube robots to specific surgical procedures, and progress has been made in applications including cardiac surgery [9], neurosurgery [76], lung interventions [7], and endonasal surgery [29], which is the focus of this paper.

As an extension of our earlier systems for the same purpose in [79, 14], our research is unique among robotic systems previously proposed for endonasal surgery [105, 106, 107, 109] and complements them by providing a novel way to resect tumors and dexterously manipulate tissues after surgical site exposure. To elaborate upon this, a single endonasal surgery could potentially make use of our system while also using all previously suggested robotic approaches for other aspects of the overall surgical procedure. Such a hypothetical surgery would begin with virtual fixture-assisted drilling [105, 106] followed by use of robot-controlled cameras [107, 109] to provide

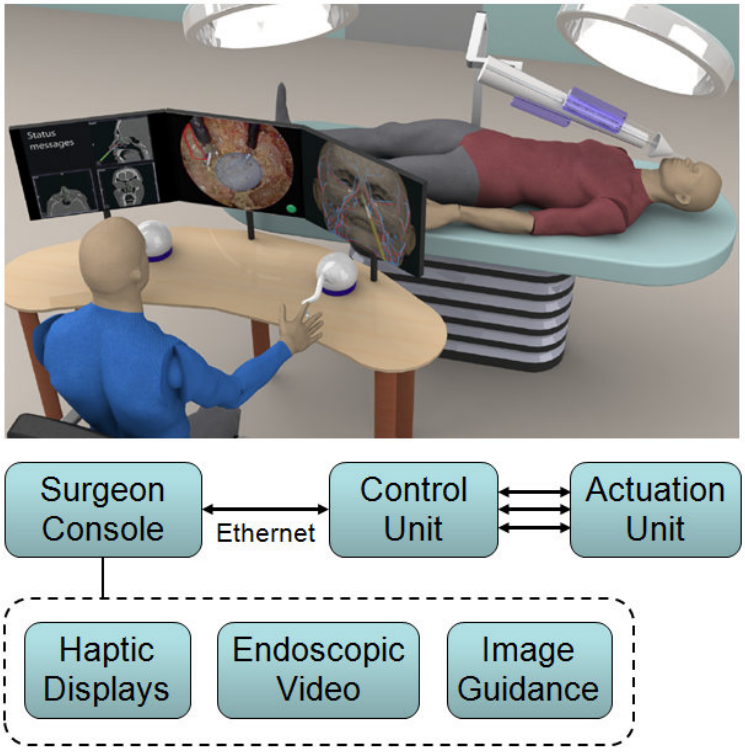


Figure 2.2: A system concept rendering which illustrates the architecture.

visualization of the end-effectors of the system described in this paper, as the surgeon uses them to resect a skull base tumor.

## 2.3 System Concept

Our system concept is illustrated in Fig. 2.2. In it, the surgeon sits at a console and remotely operate the robot. The robot is held on a support arm over the patient, delivering up to three concentric tube manipulators through the nostrils, which can be equipped with a variety of end-effectors. The surgeon console features two user input devices for teleoperation, an image guidance system, and monitors for displaying endoscopic views and additional information. Detailed information on the robotic actuation unit and surgeon console we have constructed are found in the following sections.

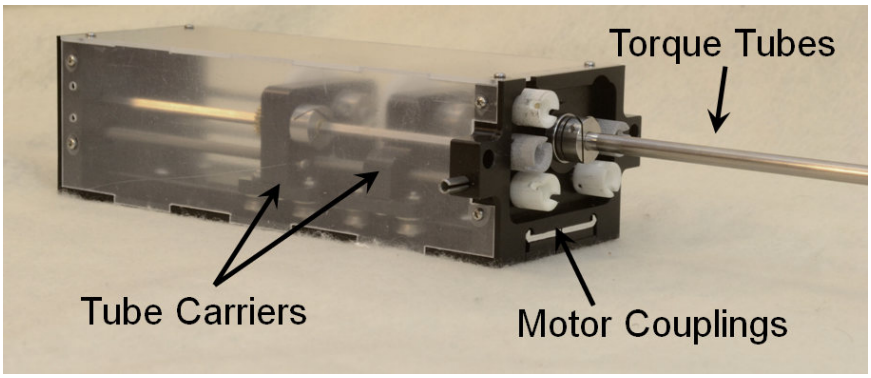


Figure 2.3: A single interchangeable tube cassette.

## 2.4 Actuation Unit Design

The major design objectives for the actuation unit were to achieve the force, velocity, and workspace specifications described in [14], and to introduce interchangable, sterilizable tool modules and a bagging system for motors and electronics. In addition, it was designed to be more compact and lightweight than previous versions, facilitating gross positioning of the device during a procedure.

One of the key features of this robotic system is modularity. Each concentric tube manipulator is attached to an individual 'module' (shown in Fig. 2.3) containing mechanical components which transmit power from the motors to the tubes. These modules are identical in their exterior dimensions and interface to the motors, but have different tubes and end effectors attached, and can be docked into any of the four available module carriers based on the desired position of the tool. Installation of the tool cartridge is quick and easy; a large handle is simply rotated to lock the module in place. A tapered fit between guide pins and mating holes ensures proper alignment. The central channel can accept any tube diameter up to a specified value, enabling a variety of tools to be used with a single standardized module design.

Operating room sterility requirements place stringent constraints on the mechanical design of a surgical device. To address this, the tool modules were designed to contain only autoclavable and biocompatible components, such that they can be sterilized and reused between procedures. The motors, which are not sterilizable, are located outside of the modules, behind a sterile barrier (the

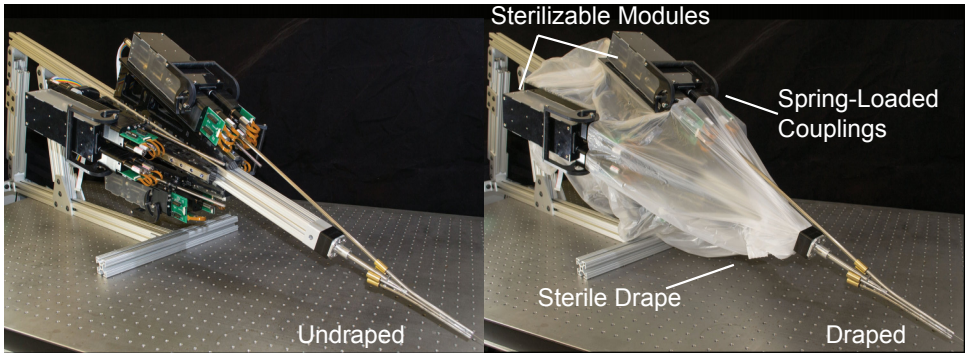


Figure 2.4: Draping of nonsterilizable components.

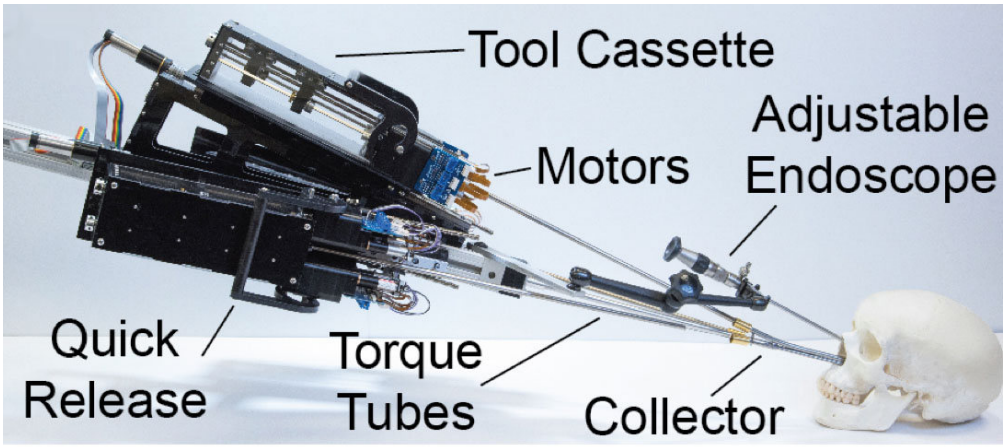


Figure 2.5: The prototype actuation unit.

drape shown in Fig. 2.4). They transmit power to the tubes on the sterile side via a spring-loaded coupling, shown in Fig. 2.3, which is integrated into the drape.

The prototype actuation unit is displayed in Figure 2.5. Each module carrier contains six motors. Brushless motors (Maxon USA) were selected for their power-to-weight ratio. Each contains a 2000 counts per rev encoder and a planetary gear head. Two motors are coupled to a leadscrew responsible for the relative translation of the innermost cannula tubes with respect to the outer tube. Each of three motors drives a pair of spur gears (3:1 reduction ratio) via a square shaft to individually rotate one of the three tubes. The sixth motor on the module carrier is available to provide an additional degree-of-freedom for end effectors. Four additional motors, one located behind each module carrier, control the translation of the modules relative to the robot base. This enables bulk insertion or retraction of a tool.

To reduce the length of Nitinol tubing under torsion, we have a designed a second system of tubes, which we call “transmission tubes," to transmit torque without torsional energy storage. This design element was added in response to the lessons learned from the stability analysis shown later in Chapter 4. The transmission tubes allow the design to maintain sufficient curvature in the concentric tubes to perform useful tasks, even with the actuated locations positioned many multiples of the curved tube lengths away from the end effector. This enables the tool modules to be slightly larger, as the taper angle back to the modules provides more space. As a result, the modules can be fabricated using conventional machining techniques and with off-the-shelf commercial parts.

The tool module are attached the base central backbone of the unit with angled brackets, pointing the tools towards their common insertion point at the nostril. Four stainless steel tubes positioned at this convergence gradually transition the tools into a compact and parallel configuration. The exit point of this tube collector fits within an ellipse with a major diameter of 14 mm, meeting the constraint that it should fit within a below-average size female nostril [110].

To provide high-definition endoscopic video to the surgeon, a Karl Storz EndoCAMeleon rod lens adjustable endoscope with adjustable lens direction is used as for viewing the surgical site, and a high definition digital endoscope camera is used to capture the video and relay it to the surgeon console. The scope is fastened to the robot with an adjustable arm for easy positioning to the desired viewing angles. For the pituitary tumor removal, this scope provides excellent image quality and the adjustable viewing angle allows it to be placed out of the workspace of the concentric tube robots anterior to the surgical site.

In order to ensure the robot is easy to maneuver while over the patient, custom embedded microcontroller boards and brushless motor amplifiers (Maxon USA) are located physically on the robot to drive the motors. This prevents having a large tether with hundreds of conductors, which would hinder gross positioning of the robot. Four ethernet cables, a video cable, and a power cable connect the robot to a nearby mobile patient-side cart. Video data passes directly through for minimal latency, and the ethernet is switched by a gigabit ethernet switch, so that a single video

cable and single data cable connect the patient-side cart to the surgeon console.

## 2.5 Surgeon Console

During the operation, the surgeon will be seated at a console containing a large-format display, two Phantom Omni haptic devices, and a networked system of computers which performs the data processing for the haptic devices and runs the high level controller for the robot. A photograph of the console is shown in Fig. 2.6. Each Phantom Omni is connected to a dedicated server, and a third rackmount server runs the user interface software which displays the video and provides the image guidance views.

Control data is handled over an IP network via either TCP or UDP depending on the type of data. Data which corresponds to single events, such as a request to change the state of a node in the system from stopped to running, are handled via TCP. Network traffic corresponding to rapidly updating quantities such as the current positions of the haptic devices or the current desired motor positions in the actuation unit are sent via UDP. UDP introduces less jitter and less latency into the communication in comparison to TCP. The gigabit ethernet network has more than adequate bandwidth to handle all control traffic. Although ethernet is not traditionally considered a real-time network, the types of signals carried over the ethernet network are low bandwidth (typically on the order of a few Hz) in comparison to the data rate for each signal (typically on the order of hundreds of Hz), and an occasional delayed packet has no ill effects.

## 2.6 Electrical Tube Shaping

In addition to the hardware that controls the concentric tube robots, we have also developed a method for prototyping concentric tube robots with desired precurvatured shapes. Nitinol has long been used in robotics for its shape memory properties [111]. Its superelastic properties are also valuable and have enabled steerable needles [31], multi-backbone continuum robots [112], tendon-actuated continuum robots [113], and concentric tube robots [114, 48, 55, 115], among others. It is sometimes useful in these robots (and more generally in medical devices [116]) to

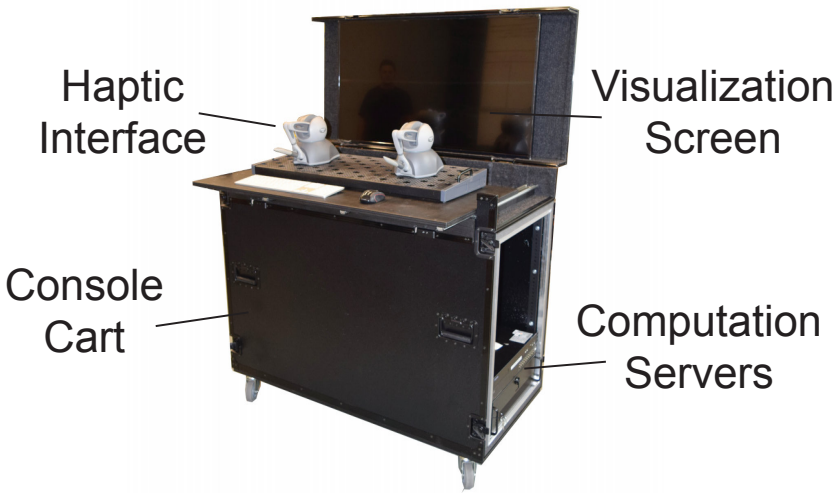


Figure 2.6: The mobile surgeon console includes two haptic interfaces, a large-format display, three rack-mount computers and a Gigabit ethernet switch for communication.

shape set a nonlinear space curve into the material in these robots. Indeed, for concentric tube robots in particular, this is what enables the robot to work at all.

For concentric tube robots, the latest numerical design algorithms can produce specific tube precurvatures needed to accomplish surgical tasks such as intracerebral hemorrhage evacuation [40], transoral lung biopsy [117], intracardiac surgery [9], intraventricular interventions [118], transurethral prostate removal [119], and transnasal pituitary surgery [14]. Optimal design for stable robot operation has also been considered [120, 121]. In all of these cases, a set of tubes must be produced that match the output of the design algorithm.

However, making curved devices out of Nitinol from the straight stock material one can typically purchase is not straightforward due to the difficulty of selecting the proper shape setting treatment that will both impart the desired shape accurately and retain the superelastic properties of the material. Optimization of the material properties of Nitinol is known to be a challenge [122], and creating optimized parts typically requires specialized equipment and considerable experience with specific techniques, which are often guarded as trade secrets by Nitinol manufacturers. Since custom fabrication of very low volume prototypes by Nitinol manufacturers introduces substantial costs and time delays into the research process, a quick, easy, and accurate shape setting technique

is highly desirable.

The creation of Nitinol samples with desired curvature and other properties (e.g. retaining superelasticity) typically requires many heat treatment attempts with different samples, varying treatment times and temperatures [123]. In general, many heating methods may be used, and the best have high heat transfer rates to the part and precise temperature control. Salt bath furnaces and fluidized beds are two of the best methods that have these properties, but the equipment required for these is expensive and potentially hazardous, making them poorly suited for quick prototyping in a typical laboratory setting. Hence, researchers are typically forced to resort to small box furnaces (ovens), despite the fact that shape setting is not highly repeatable or predictable using this method [124]. For concentric tube robots, shape setting in a box furnace has been described in the literature [115, 125].

The method described here is quick and easy to set up in a laboratory—particularly in academic laboratories focused on medical device or robotics prototyping rather than metallurgy. While this is not the first time electrical resistance heating of Nitinol has been proposed, it is the first time that a practical, step-by-step method for achieving it in such a setting has been described in the literature, and the first time it has been considered in the context of concentric tube robots. Smith and Hodgsen noted that electrical resistance annealing is one of many possible shape setting methods but did not provide details other than to note that care must be taken to avoid overheating [124]. Malard et al. presented results of high power electrical heat treatment of Nitinol wires but did not address re-shaping superelastic Nitinol into a new, superelastic shape, which is required in concentric tube robots and useful in prototyping other medical devices [126].

Our system uses real-time resistance measurements to regulate temperature, much like the resistance-based control techniques that have been explored in the area of shape-memory actuator control. Models for the solid state phase transition in electrically heated shape memory actuators have been developed to account for the interdependence of temperature, strain, and resistivity, and closed loop control of these actuators has been studied extensively using both resistance and direct temperature measurements [127, 128, 129, 130, 131]. However, none of these papers address

Nitinol that begins and ends in the superelastic condition at room temperature, and moreover none address closed loop resistance feedback at the high temperature range needed to shape set Nitinol tubes and wires.

The following sections provide an inexpensive and easy to build electrical shape setting system with resistive feedback, together with practical insights for shape setting Nitinol accurately in a typical robotics laboratory. Our approach is to heat superelastic Nitinol samples by pulsed direct current resistive heating. Through simultaneous power application and measurement, we show that it is possible to achieve rapid, reliable shape setting.

## 2.7 The Drawbacks of Box Furnace Shape Setting

Before describing the electrical shape setting approach, we first motivate it by illustrating the challenges inherent to traditional furnace-based approaches. Furnace-based approaches are typically recommended by Nitinol manufacturers for low-volume prototyping applications in laboratories focused on medical device prototyping or robotics where the focus is not on metallurgical research.

Shape setting recommendations from Nitinol manufacturers include temperature ranges of 400-550 °C, and time ranges from less than one minute to 20 minutes or more [132, 133]. The quality of results one obtains are highly sensitive to both the time and temperature used. Indeed, it is known that the specific time, temperature, fixture design and heating method will typically all need to be adjusted to obtain the desired results [123]. Thus, a large factorial study is typically required, which is feasible in commercial settings where high volumes are to be produced, but can be prohibitively time consuming and costly in low volume prototyping applications.

In a large factorial study of this type within the recommended temperature and time ranges, many samples would emerge no longer superelastic, their transition temperatures having been accidentally moved above room temperature by the shape setting process. And even "successful samples" that remain superelastic and take on some curvature will often end up with curvatures substantially different than the desired curvature (i.e. the curvature of the jig into which they were

placed).

To illustrate this by example, we followed exactly the time (10 minutes) and temperature (500 °C) recommended to us verbally by one manufacturer. The process recommended by the manufacturer was:

1. Constrain the Nitinol in a metal fixture in the desired final shape.

2. Heat the part and fixture for 10 minutes in an air furnace at a temperature of 500 °C, and

3. Quench the part and fixture in room temperature water to sharply define the heating time and avoid aging effects.

We shape set a Nitinol tube according to this process in a fixture made from two aluminum plates with brass pins between them, which initially constrained the Nitinol to the desired curvature (see Figure 1). The tube had an outer diameter of 1.16 mm and an inner diameter of 0.86 mm, and the fixture was designed with a radius of curvature of 33.3 mm.

As shown in Figure 1, significant springback occurred after the part was removed from the fixture after quenching. This effect makes the fabrication of a part with a desired shape difficult, since accounting for this much springback in the fixture would require additional experimentation, time and material.

Thus, shape setting Nitinol in a box furnace is challenging for low volume prototyping applications. To provide a better method of shape setting, we now turn our attention to the electrical heating method.

## 2.8 Electrical Shape Setting

We use direct Joule heating to shape set Nitinol prototype parts. This method was inspired by the work of Wang et al. who showed that short-duration DC electrical heating to a surface temperature of about 430 °C for approximately 10 s did not substantially change the mechanical properties of superelastic Nitinol as it was received from the manufacturer [134], although they did

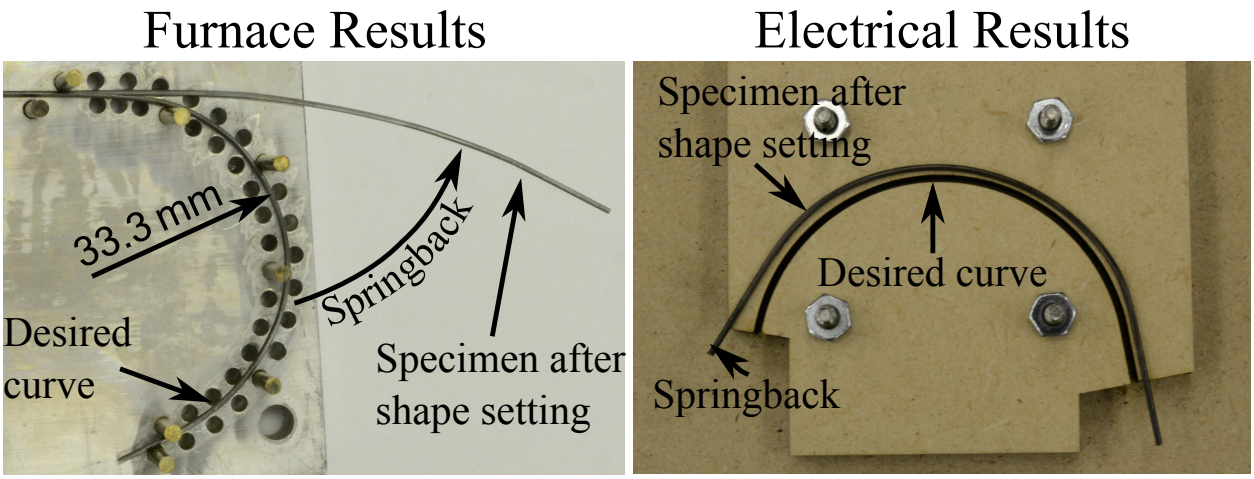


Figure 2.7: A comparison of traditional air furnace-based shape setting and the electrical technique. (Left) A fixture with metal pins was placed in the oven at manufacturer recommended temperature and duration. The sample does take on precurvature, but with a much lower curvature than the desired 33.3 mm radius (i.e. with substantial springback). (Right) The electrical shape setting approach produces more accurate results with less springback.

not specifically study setting curved shapes into Nitinol. An electrical heating method is attractive, in particular, when the part to be shape set has one relatively long dimension and the electrical current can be made to pass through all the material which should be heated.

Electrical heating has several advantages over other heating methods. Probably the most important of these is the ability to rapidly heat the part to shape setting temperatures, which avoids aging effects. Furthermore, the equipment required for electrical heating is minimal, consisting of only a battery and circuitry that controls the heating process. The applied voltage and current can also be easily monitored, making measurements of both the applied power and the part resistance readily available. We show in this section how to use the latter of these as a feedback signal to regulate the heating process and create a repeatable and accurate shape setting system.

### 2.8.1 Temperature Resistance Model

The temperature of the Nitinol sample can be inferred from measurement of the resistance, which is available during heating if the applied voltage and current are measured. Novák et al. reported an experimentally determined value of the linear austenitic temperature coefficient of

resistivity for Nitinol of $\partial\rho_A/\partial T = 5 \times 10^{-2}$ $\mu\Omega$-cm-°C$^{-1}$ [135], which means that over a 500 °C temperature swing we expect a change in resistivity of 25 $\mu\Omega$-cm. This represents a 25 % increase over the nominal resistivity provided by the manufacturer of $\rho_A(T_{room}) = 100$ $\mu\Omega$-cm, which is a measurable change in the part resistance that we use to infer the part temperature.

Assuming uniform heat transfer out of the part, we model the relative rise in the resistance of the part as a linear function of temperature $f(T) = \alpha T$, so that

$$\frac{R(T)}{R(T_{room})} - 1 = \alpha T \ . \tag{2.1}$$

After selecting a desired temperature $T_d$, the value $f(T_d)$ gives the relative rise in resistance, and $R(T)$ can then be controlled to achieve the desired value $R(T_d)$. Controlled application of the electrical power and accurate measurement of $R$ enables the loop to be closed on a proxy for a temperature measurement.

### 2.8.2 Shape Setting System

A block diagram of our shape setting system is shown in Figure 2.8, and a photograph of the physical circuit layout is provided in Figure 2.9. Power is provided from a 12 V lead acid deep cycle battery (BCI Group Size 27), which is able to supply several kilowatts of instantaneous power during shape setting. An Arduino microcontroller board ($\mu$C), based on the Atmel ATmega328P processor, is programmed to cycle between an on-state and an off-state to regulate the measured resistance of the heated part. A MOSFET (International Rectifier, IRFB7430) controls the flow of current in response to commands from the $\mu$C. The MOSFET drain tab is mounted directly to a block of polished aluminum, which acts as both the conductive path and a heat sink. The MOSFET source is mounted to a second block of polished aluminum which is separated from the first block by an air gap. Welding cables carry current from the battery to the MOSFET mounting blocks, and also carry this current from the mounting blocks to the load, where spring-loaded clamps soldered to the end of the welding cable can be used to connect to short lengths of smaller gauge wire.

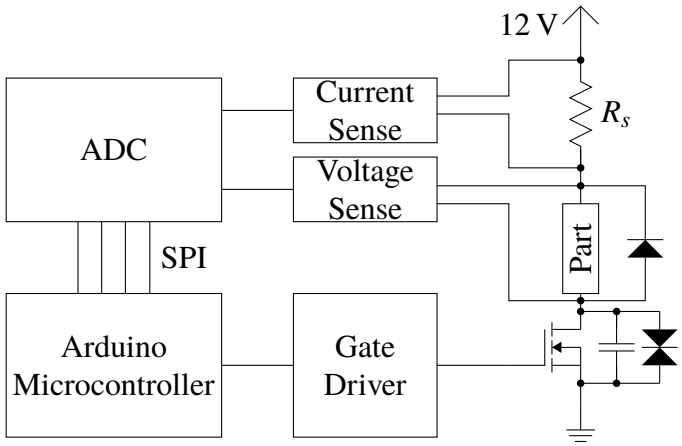


Figure 2.8: Block diagram of the system structure. The microcontroller controls the part resistance by measuring it while power is flowing through the part. The capacitor and TVS diode across the MOSFET, as well as the flyback diode across the part, protect the system from the inductive voltage spike caused at turn-off.

A gate driver (Texas Instruments, UCC37322P) provides high drive capability for the MOSFET gate, which allows the transistor to switch rapidly and prevents it from overheating. A 1 $\mu$F film capacitor and transient voltage suppression diode are placed across the MOSFET drain and source, in close proximity to the transistor, to snub inductive spikes, which result from the large $di/dt$ values during switching. A flyback diode is also present near the MOSFET mounting blocks to provide a current path for the small parasitic inductance in the cables carrying current from the switch to the load. The voltage drop across the heated part is measured by a separate set of sense leads, which connect to a resistor voltage divider and difference amplifier (Texas Instruments, INA132). The current is measured by a 0.5 m$\Omega$ high-side shunt resistor and current monitor (Texas Instruments, INA139). The analog signals from the current and voltage monitor circuits are sampled by a 24-bit analog to digital converter (Texas Instruments, ADS1255), and the data is communicated to the $\mu$C via a serial peripheral interface (SPI) connection at 2 MHz.

### 2.8.3 Shape Setting Program

The $\mu$C program flow is graphically depicted in Figure 2.10. The system is assumed to start with all parts at room temperature. The $\mu$C first closes the circuit and immediately thereafter

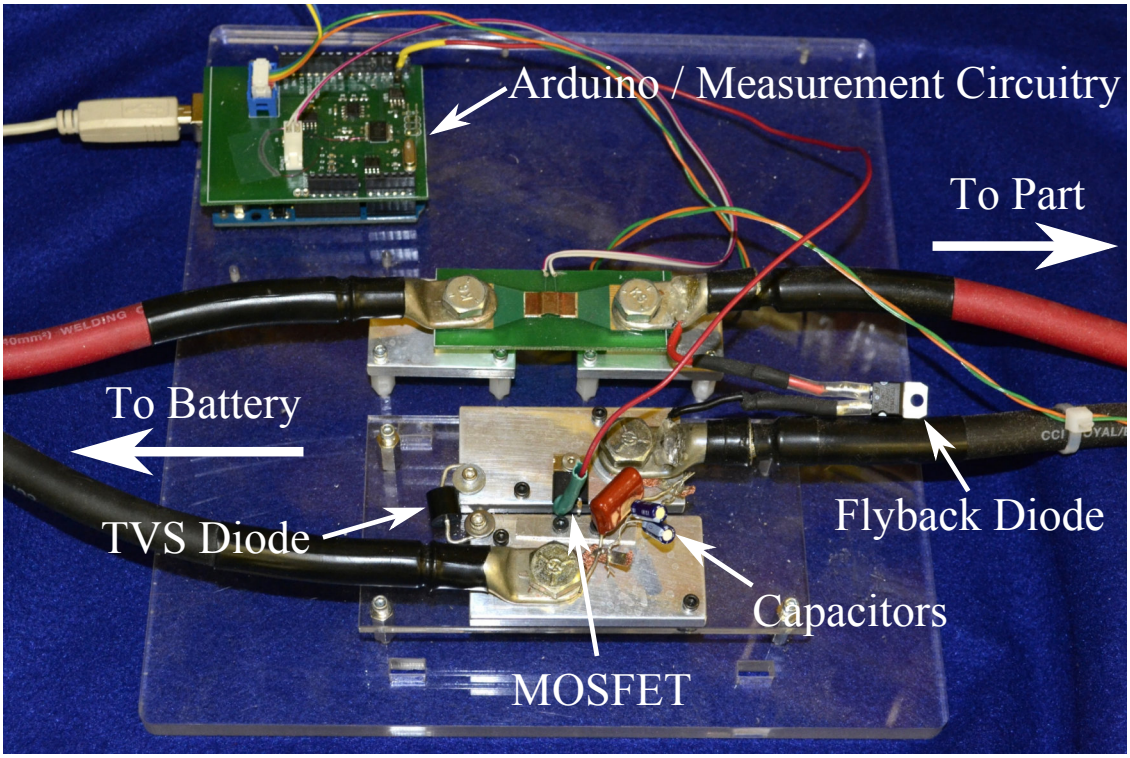


Figure 2.9: Photograph of the circuit layout. The lower aluminum blocks are mounting points for the MOSFET, and the upper aluminum blocks are mounting locations for the sense resistor.

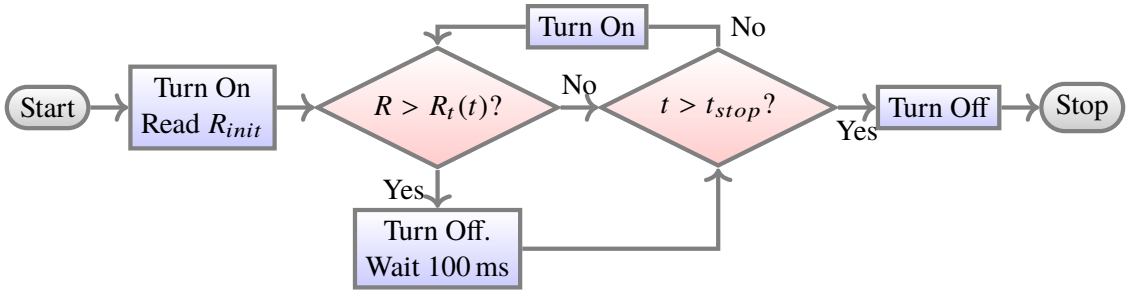


Figure 2.10: A flow chart of the $\mu$C program which controls the heating of the part. The inner loop runs at a rate such that the resistance check occurs every 1 ms when the power is turned on. At the start condition $t = 0$, and the value $t_{stop} = t_{ramp} + t_{hold}$.

measures the resistance of the part. Within each cycle of the $\mu$C code, the voltage and current measurements are interleaved in rapid succession and the resistance is then calculated with the pair of measurements. This initial resistance measurement $R_{init}$ is assumed to be at room temperature, and the target resistance $R_t$ is selected as a function of the time $t$ since the start command was given. The target resistance function $R_t(t)$ ramps linearly between the initial resistance and the final desired value $R_d = (1 + \alpha T_d)R_{init} = (\Delta R_d)R_{init}$, and is given by the equation

$$R_t(t) = \begin{cases} R_{init} + \frac{t}{t_{ramp}}(R_d - R_{init}) & t \leq t_{ramp} \\ R_d & t > t_{ramp} \end{cases} \tag{2.2}$$

The $\mu$C turns off the flow of current when $R(t) > R_t(t)$, and turns it back on 100 ms after it turns off, to repeat the cycle. While the heating circuit is turned on, resistance measurements are taken at a rate of 1 kHz. When the time $t$ exceeds a total heating time defined by $t_{ramp}$ and a second programmed interval $t_{hold}$, that is $t > t_{stop} = t_{ramp} + t_{hold}$, the system turns off and the part is left to cool without any additional quenching or forced cooling steps. Since the fixture is an insulator, the heating time is short, and the part has a low thermal mass, cooling occurs rapidly with natural convection. Additional information about fixturing is provided in the following section.

## 2.9 Fixture Design Guidelines

Due to the relatively low thermal mass of most of the parts that will be shape set, special care must be taken when designing the shape setting fixtures to promote uniform heating of the part. Both material selection and the jig shape are important in obtaining a successful shape setting. To minimize heat loss and promote uniform heating, the material for the fixture should have low thermal conductivity. Since the electrical path must not include the fixture, metallic jigs cannot be used. Ceramic materials are an option, but designing a custom fixture would involve substantial time spent machining the fixture. We have found that inexpensive medium density fiberboard (MDF) works well and can be fabricated into fixtures rapidly by laser cutting. It is electrically insulating

and has a low thermal conductivity of about 0.25 W/m-K (compare to air at about 0.05 W/m-K at 700 K) [136]. This material does have an autoignition temperature (flame point) of about 245 °C, but we have never experienced a case in which the MDF has caught fire, in part due to a thin layer of charred material that forms at the hot surface of the MDF. Nevertheless, a fire extinguishing solution should be accessible when this type of jig is used.

One must also carefully design the fixture so that the heat transfer from the heated part to the fixture is nearly uniform. Ideally, this means that the fixture should be cut by computerized tools, such as a laser cutter, computer numerical controlled milling machine, or other precise means of manufacturing so that the slot which is cut to hold the part fully constrains its shape along the entire length. Non-uniform contact may cause localized overheating alternated with regions which do not attain a sufficiently high temperature to become shape set. If the fixtures are made from MDF, they should be replaced after one or two parts have been shape set due to material removal which occurs at the charred surface of the jig.

Additionally, the electrical connections to the part should be either accommodated within the length of the fixture or placed immediately where the part exits the ends of the fixture, because any length of the part which is heated by current and is surrounded only by air may overheat. Conversely, the wires for power delivery and sensing are heat sinks, and lower temperatures are attained in close proximity to these connections. In practice this means that parts may be less precisely shaped near the ends of the fixture. In many cases this discrepancy can be accounted for in the design of the fixture. For example, to curve only the end of an otherwise straight part, straight lengths of about a centimeter may be added to either end of the curved portion of the fixture. The part can be trimmed to length after shape setting to produce a curve at the end of the tube or wire. Another option is to increase the jig curvature near the ends to compensate for any loss in curvature.

For planar parts, we recommend a jig which is split along the axial length of the part like the one in Figure 2.11 and can be clamped onto the part to hold it in place. Clamping pressure should be high enough to prevent movement of the part, but excessive pressure results in increased

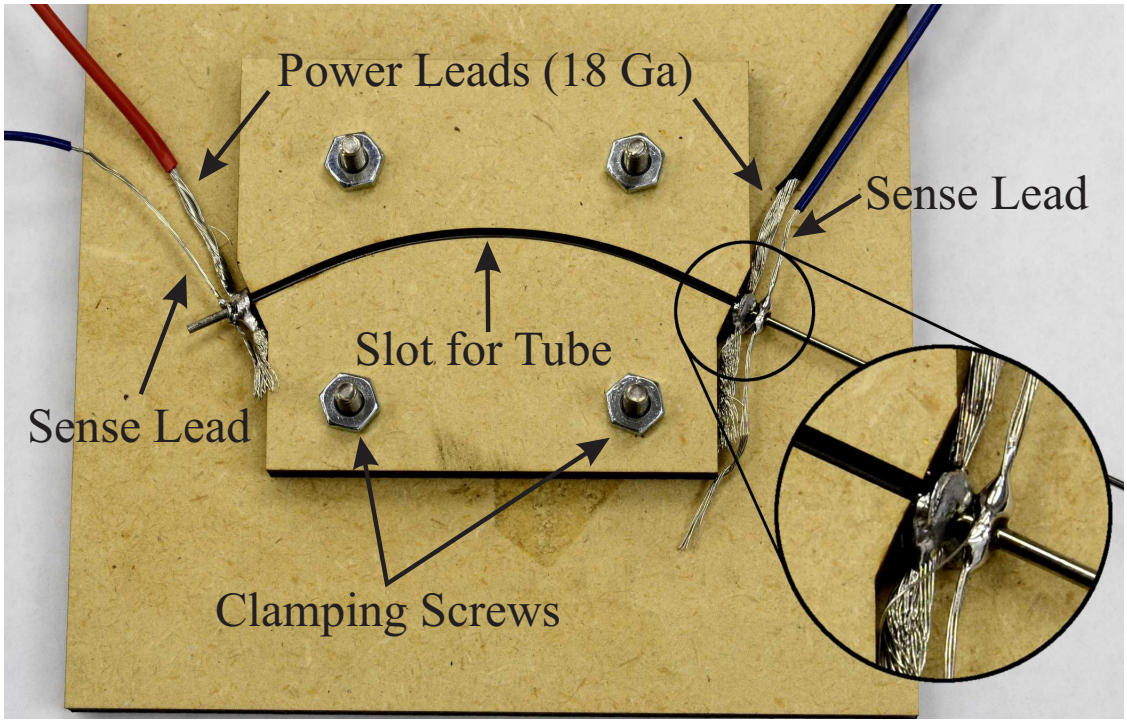


Figure 2.11: This fixture made of MDF was cut by a CNC laser cutter. The slot for the part is made to accommodate the diameter of the tube which it was designed for, accounting for the kerf width of the laser cutter. Wires are tied in an overhand knot and filled with solder to improve electrical contact.

charring of the jig and the possibility of crushing tubular parts. In our experience, these types of jigs result in sufficiently uniform heating, and they have the advantage that they can be fabricated and set up quickly.

## 2.10 Shape Setting System Performance

To evaluate the performance of the shape setting system, we have studied both the accuracy of the temperature regulation and the ability of the system to produce the desired final results. We will first present measurements of the part temperatures achieved by the system, and then show several case studies of parts that we have created with this method.

### 2.10.1 Thermal Regulation

To obtain temperature measurements, a type K thermocouple of 0.01 in diameter was used to measure the actual temperature of a Nitinol tube suspended in the air as it was heated by the system. A photograph of the experimental setup is shown in Figure 2.12. The thermocouple wire was wrapped around the tube with the junction located against the tube. The temperature measurement was taken with an Amprobe AM-270 multimeter, which was set to record the maximum value, and for each chosen test point $\Delta R_d$, the maximum temperature measured during the heating process was recorded.

Tests were performed on a single Nitinol tube with an outer diameter of 2.18 mm and an inner diameter of 2.02 mm. The length of tubing between the power leads was 7 cm. The manufacturer's material data sheet indicated the material is fully superelastic above 7.8 °C. The tube was supported at both ends and 18 Ga wires were tied in an overhand knot around the tube at each end. The knots were filled with 60/40 Sn/Pb solder to improve contact (note that this kind of solder does not wet to Nitinol, but the increased surface area improves electrical contact). The two voltage sensing clips were placed on the tube outside the supports, while the power wires were attached inside the supports to avoiding heating in the support regions where large contact areas are present.

The test points $\Delta R_d$ were chosen as 40 values ranging between 1.15 and 1.23, with the order

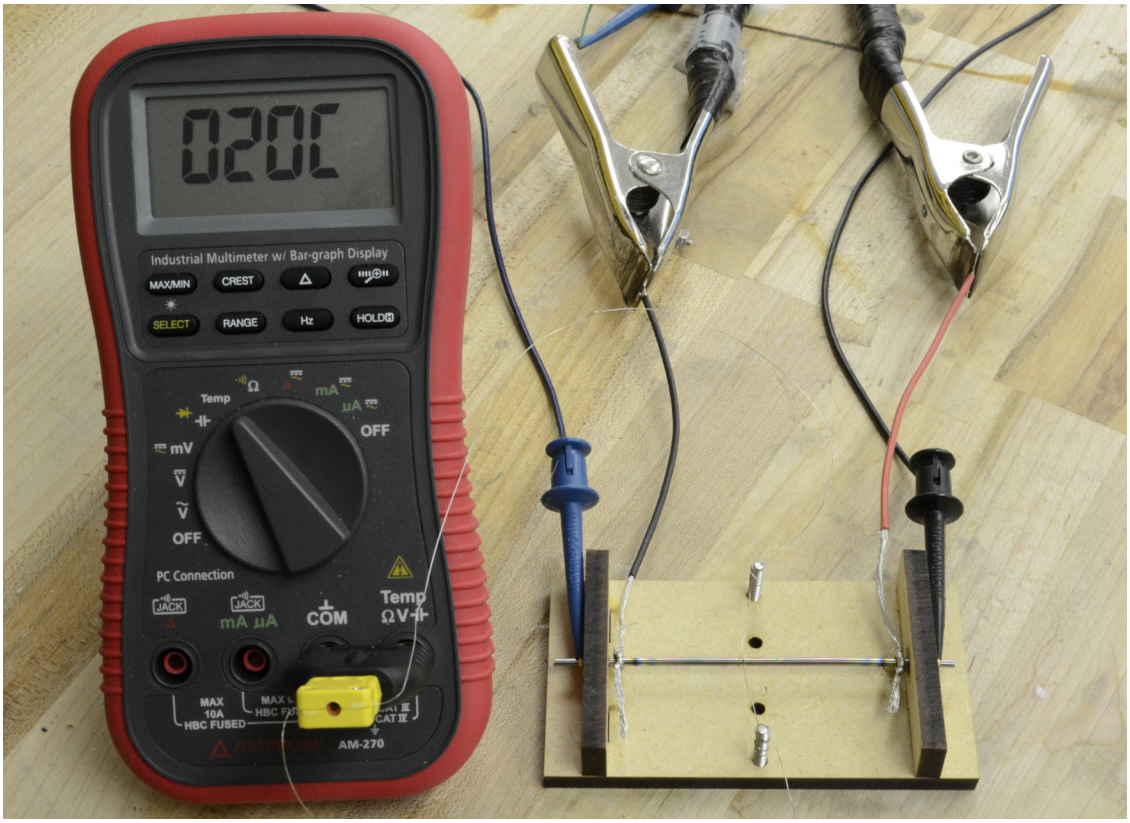


Figure 2.12: The experimental setup for collecting temperature data.

chosen randomly. The selected target resistance was programmed into the shape setting program of Section 2.8.3, with the parameters $t_{ramp} = 3\,\text{s}$ and $t_{hold} = 30\,\text{s}$. At least five minutes were provided for the system to cool to room temperature in between trials. Room temperature during the trials ranged between 20-22 °C, and was manually recorded immediately prior to the collection of each data point.

### 2.10.2 Thermal Regulation Results

Figure 2.13 shows that the increase in part temperature and the chosen value of $\Delta R_d$ correlate strongly ($R^2 = 0.97$). The best linear fit, when constrained to pass through the origin of the graph, has slope $1/\alpha = 2438\,°\text{C}$. Two outliers (not shown in the figure) were removed from the data before fitting. These outliers were the first two measurements, which were taken before the formation of a sufficient oxide layer on the surface of the tube to prevent electrical conduction from the tube to the bare thermocouple wire. The results of the experiment indicate that a relative increase in resistance may be used as a proxy for temperature measurement. The maximum absolute error between the temperature data and the best fit line is 29 °C, and the mean absolute error is 10 °C. 89% of the measurements fall within 20 °C of the best fit line.

Over the course of the trials, the initial resistance reading of the part varied between 116.2 mΩ at the first trial to 112.9 mΩ at the last trial. The average initial resistance reading across all 40 trials was 112.7 mΩ, with standard deviation 0.7 mΩ. This illustrates that the initial part resistance at room temperature is predictable despite the varying thermal treatment history across the trials.

Although the purpose of this experiment is not to accurately determine the material properties of Nitinol, it is possible to compare the linear fit to the temperature coefficient of resistivity of Nitinol provided by Novák et al. [135]. Using that coefficient, we estimate

$$\frac{1}{\alpha} = \frac{100\,\mu\Omega\text{-cm}}{5 \times 10^{-2}\,\mu\Omega\text{-cm-}°\text{C}^{-1}} = 2000\,°\text{C}\,, \tag{2.3}$$

assuming a nominal room temperature resistivity of austenitic Nitinol of 100 $\mu\Omega$-cm, as quoted by

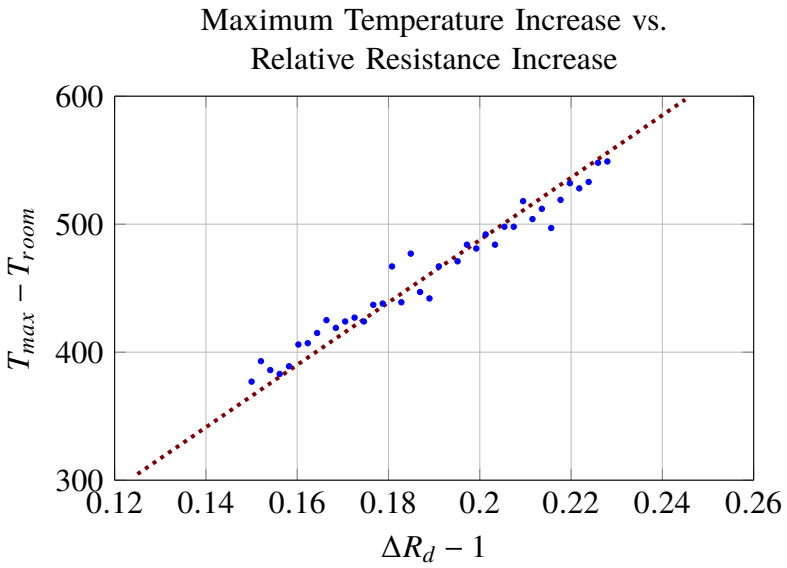


Figure 2.13: The correlation between temperature increase and target relative resistance increase. The coefficient of the best fit line, constrained to pass through origin, is $1/\alpha = 2438\,^{\circ}\mathrm{C}$.

manufacturers [132]. Considering the slight nonuniformity of heating caused by the heat sinking effect of the power leads, this comparison indicates that the shape setting system is operating correctly. We also note that if the linear fit is not constrained to pass through the origin, the slope of the best fit line becomes $1/\alpha = 2089\,^{\circ}\mathrm{C}$.

### 2.10.3 Planar Tubes

Figure 2.14 shows multiple Nitinol tubes that were successfully shape set using this method. For each tube, the heating method and parameters of Section 2.8.2 was used without modification. Each tube was placed into an MDF jig similar to the one of Figure 2.11 and heated twice. The jigs were designed to impart a constant radius of curvature to the centerline of the tube over an arc length ranging from 42-52 mm. The radii of curvature ranged from 130 mm to 60 mm. In a first heating cycle a desired resistance increase $\Delta R_d = 1.15$ was used, and in a second heating cycle, after the system was allowed to cool to room temperature, the desired resistance increase was set to $\Delta R_d = 1.21$. Performing multiple, separate heatings with increasing target temperatures can mitigate the effects of stress relaxation, as any stress relaxation that takes place will be accounted

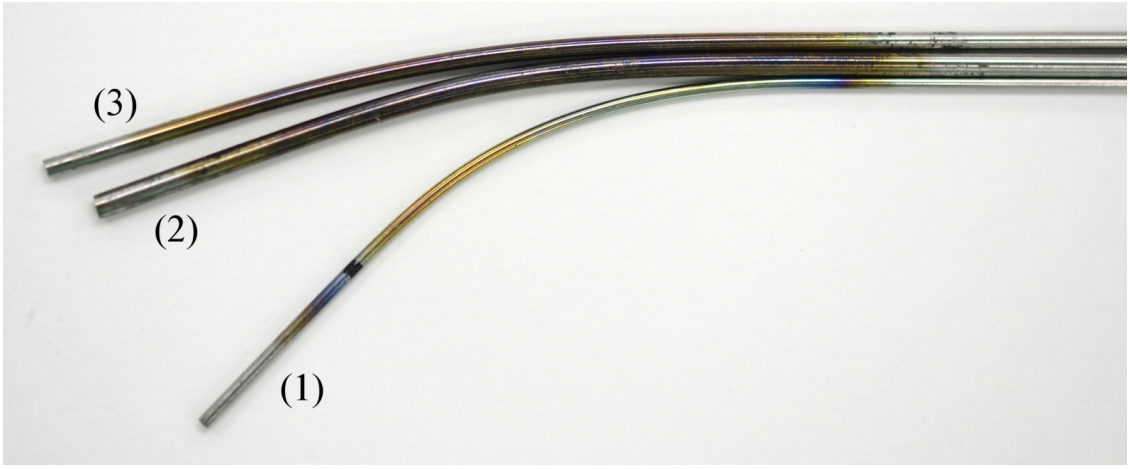


Figure 2.14: Multiple Nitinol tubes of varying diameters that have been shape set to different curvatures. This photograph was taken immediately after shape setting of each tube, before any additional cleaning or trimming operations. The coloration of the tubes in the heated region is a result of surface oxidation and fixture charring.

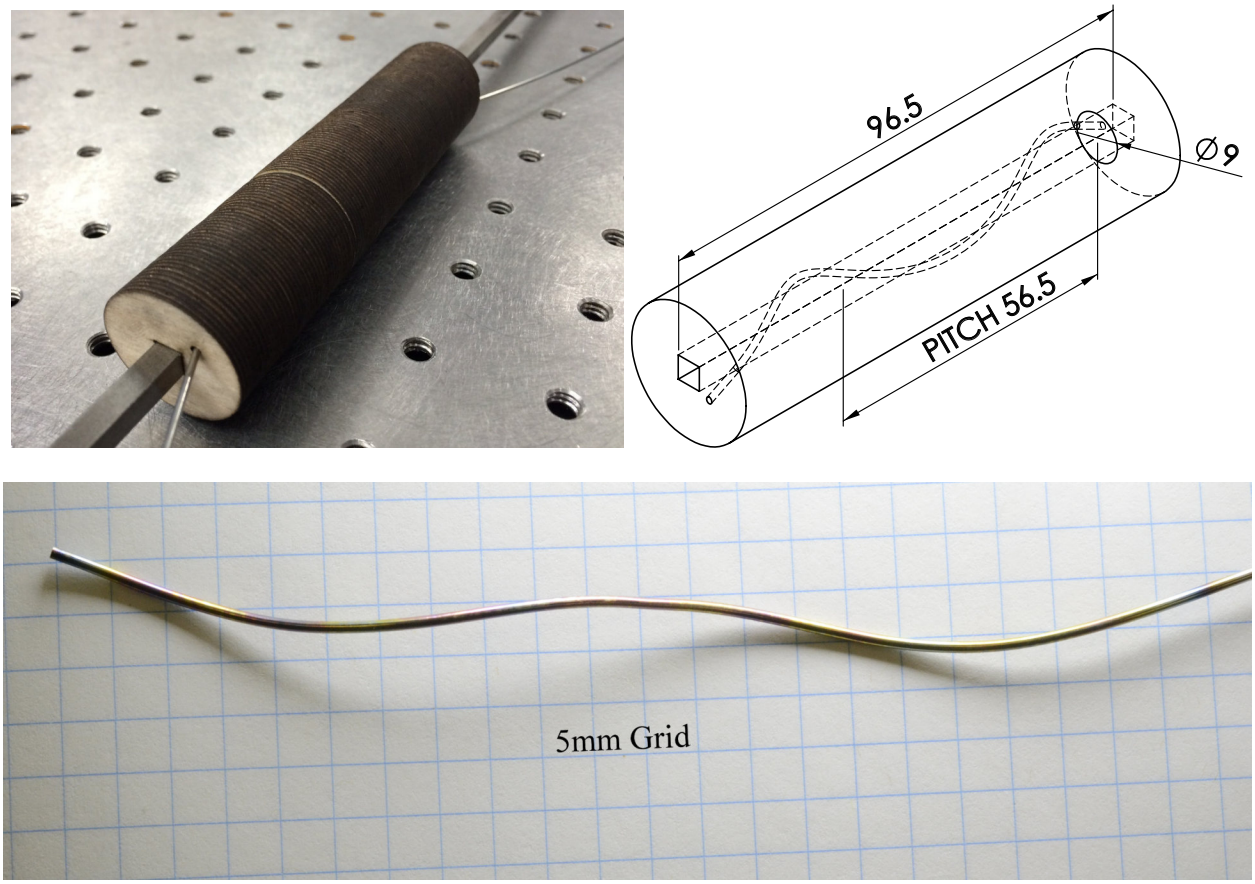


Figure 2.15: (Top Left) This jig for a helical tube was formed by slicing the fixture into discrete cross sections. Each cross section is made of a 0.85 mm thick sheet of birch plywood. (Top Right) Dimensions of the helix that the tube was constrained to. (Bottom) The tube is shown after shape setting.

| Tube | OD | ID | $r_{jig}$ | $r_{tube}$ |
|---|---|---|---|---|
| Fig. 2.14 (1) | 1.16 | 0.86 | 59.5 | 64.5 |
| Fig. 2.14 (2) | 1.92 | 1.57 | 129.9 | 144.8 |
| Fig. 2.14 (3) | 2.48 | 2.25 | 107.5 | 121.7 |
| Fig. 2.7 (Furnace) | 1.16 | 0.86 | 33.3 | 169.9 |
| Fig. 2.7 (Electrical) | 1.16 | 0.86 | 33.3 | 36.6 |

Table 2.1: Tube dimensions and radii of curvature of the jigs and resulting tube shapes. All values have units of mm.

for in the initial resistance measurement of subsequent heatings. In both heating cycles, the timing parameters were $t_{ramp} = 3$ s and $t_{hold} = 7$ s.

Table 2.1 shows the results for the three tubes in Figure 2.14 as well as the results for the two tubes which were compared in Figure 2.7. The value $r_{jig}$ describes the radius of curvature of the arc as designed into the fixture, and the value $r_{tube}$ describes the radius of curvature of the tube after shape setting.

### 2.10.4 Helical Tube

To explore whether we could shape set a non-planar curve we performed another experiment in which we sought to make a helical specimen. The tube we used has a 1.14 mm outer diameter and 0.97 mm inner diameter. The fixture was prepared by slicing (in a CAD program) the cylindrical solid model shown in Figure 2.15 into thin axial slices 0.85 mm thick, each of which was then laser cut from Birch plywood of the same thickness. The square shaft shown in the figure holds the slices in the correct orientation so that the shape is retained when the slices are assembled into the fixture and the wire inserted. This helix was created for an MRI compatible robot application involving thermal treatment for epilepsy in the brain (see [137] for further information).

## 2.11 Conclusions

This chapter has presented the design of a new system for endonasal surgery, which has been designed to improve upon existing designs in three major areas. The robot delivers four tools

through a single nostril, providing minimally invasive access to the skull base. The tools are designed to be modular, and easily snap on and off the actuation unit for replacement between surgeries or for tool changes during a surgery. Sterility is maintained through a bagging system, which protects the patient from non-sterile parts of the robot and prevents contaminants from entering the actuation unit.

In addition, an algorithm and system for rapid and accurate fabrication of the Nitinol tubes used in concentric tube robots was presented and experimentally characterized. This system regulates the power delivery of pulsed direct current to control the temperature of Nitinol parts with Joule heating. Experiments showed that the system regulates temperature within approximately 20 °C of the desired temperature when in air, and several examples were shown of successfully shape set tubes.

Concentric tube robots have the potential to facilitate easier access and more precise control during minimally invasive surgeries such as endoscopic endonasal surgery. It is our hope that the results presented in this chapter will pave the way for future development and the eventual deployment of concentric tube robots in the operating room.

# Chapter 3

# Endonasal System Software

In Chapter 1.7 the kinematic model for concentric tube robots was reviewed, and in the following chapters this model is analyzed for the purposes of predicting the onset of snapping instabilities and for the design of concentric tube robots as needles. This chapter presents the techniques that enable the kinematic equations to be solved in real-time and at rates an order of magnitude greater than previously reported. The material of this chapter is currently being prepared for submission to an archival journal for publication.

Real-time behavior is important for safety-critical systems like surgical robots, and the kinematic model is a crucial element of standard resolved-rate control techniques. The software described in this chapter for evaluation of the kinematic model is a key element of the endonasal surgical system. The ability to solve the model rapidly is also important for computational designers and motion planners which use statistical sampling methods to achieve optimal outcomes. Algorithmic approaches to design can generate designs faster with fast forward kinematic routines, and in-the-loop motion planners can perform better when they are able to compute more samples of the forward kinematic map. Although it was previously believed that the model for concentric tube robots is several orders of magnitude more expensive to compute than for other types of robots, this chapter shows that the number of operations is only about 60 times that required to compute the kinematics for a 6-dof serial robot, and that a careful implementation can achieve high solution rates.

## 3.1 Introduction

This quasistatic kinematic model has been applied to several interesting problems of optimal design and planning, and has also been used for kinematic model-based control of concentric tube robots. Computational design and analysis has allowed researchers to produce designs for concen-

tric tube robots which are optimally suited for surgeries at the skull base [14], in the ventricles of the brain and in the heart [118], and in the bronchi of the lungs [77]. These algorithms require many evaluations of the kinematic model. A volumetric, sampling-based workspace analysis, for example, requires millions of evaluations of the kinematic model to converge [138]. In the case of model-based control, the model must be evaluated rapidly in order to sustain a high enough control bandwidth, and moreover the control problem should be considered a hard real-time task given the safety requirements of surgical manipulators. Several solution techniques for evaluating the kinematics of concentric tube robots have appeared in the literature, many of which have been directed toward rapid evaluation.

Functional approximation is one way to speed up the computation of the kinematic model for use in manipulation tasks. Dupont et al. approximated the solutions to the differential equation with a more easily computed truncated Fourier series [48]. This functional approximation can be inverted efficiently to provide inverse kinematics at fast rates. The inversion is performed iteratively, so a careful implementation is required to guarantee hard real-time performance. The approximation must be computed in advance using either experimentally obtained data or model solutions from another solution method.

Xu et al. presented a different technique for speeding up the model evaluation, a piece-wise linearization scheme which separates the length of the robot into discrete sections and solves the model linearization in closed form over each length using the standard solution techniques for linear systems [61]. This method belongs to the class of geometric Lie-Euler methods, and is one possible implementation which satisfies the requirements for real-time operation. However, the convergency order of this method is low when compared to many other explicit integrator schemes.

Other methods which have appeared in the literature include collocation methods [36] and Galerkin method [139]. While these implicit methods typically have better stability properties [140], the differential equation we wish to solve is nonlinear, and these methods require iteration to converge to a solution.

When applied loads are known in the body-frame of the distal end of the robot, Hasanzadeh and Janabi-Sharifi showed that an explicit, algebraic method can solve the statics of rods, including the nonlinear geometry, without iteration [141]. This resulted in a fast, real-time statics method that they applied to real-time control of steerable catheters. This method was achieved by moving one set of boundary conditions to the distal end of the robot, effectively converting the boundary value problem to an equivalent initial value problem. Nakamura and Hanafusa also showed that by grouping as many boundary conditions as possible at one end of the problem domain, substantial computational cost savings could be achieved for an optimal control problem for robot manipulators [142]. The methods introduced in this chapter utilize the technique of solving an initial value problem rather than a boundary value problem to compute the kinematics quickly and without iteration.

This chapter describes a method for solving the concentric tube robot model in real-time at high rates, and analyzes the performance of the method in terms of numerical convergence and evaluation speed. The current implementation has achieved rates of 36 kHz for typical robot designs if only the shape of the robot is required. Also described is a variation on the efficient techniques first presented by Rucker et al. for computing the Jacobian matrices that describe differential changes in the robot state under differential configuration changes and external load changes [57]. Including computation of the Jacobian matrices is a significant computational burden, but even with the inclusion of external loads, rates in excess of 2 kHz are possible.

This chapter also provides the design of an algorithm which generates the integration "waypoints" defined by the overlapping tubes, a study of numerical convergence when using an $8^{\text{th}}$ order Runge-Kutta method to solve the equations, and timing results for several optimized C++ implementations in both a Windows environment and in the Simulink Real-Time operating system. Vectorized expressions are provided in appendix A.3 for all of the quantities needed when solving the kinematic model and computing the Jacobian matrices.

## 3.2 The Concentric-Tube Robot Model

### 3.2.1 Tube Description

In the undeformed state, each of the $N$ component tubes is described by an arc-length parametrized frame, denoted $\boldsymbol{g}_i^*(\sigma_i)$, where $\sigma_i \in [0, L_i]$ is the arc length parameter along the $i^{\text{th}}$ tube, which is zero at the proximal end of the tube and $L_i$ at the distal end. For numerical computation, the frame is most efficiently represented by a position vector and unit quaternion, as $\boldsymbol{g} = (\boldsymbol{p}, \boldsymbol{q})$, with the rigid transformation law given by $\boldsymbol{g}_1\boldsymbol{g}_2 = (\boldsymbol{p}_1 + \boldsymbol{q}_1\boldsymbol{p}_2\boldsymbol{q}_1^{-1}, \boldsymbol{q}_1\boldsymbol{q}_2)$. Each quaternion is represented by its scalar part $q_0$ and vector part $\boldsymbol{q}_v$, and juxtaposition indicates the usual quaternion multiplication law,

$$\boldsymbol{q}_1\boldsymbol{q}_2 = (q_{10}q_{20} - \boldsymbol{q}_{1v} \cdot \boldsymbol{q}_{2v} \ , \ q_{10}\boldsymbol{q}_{2v} + q_{20}\boldsymbol{q}_{1v} + \boldsymbol{q}_{1v} \times \boldsymbol{q}_{2v}) \tag{3.1}$$

and when a quaternion is multiplied against a pure vector such as a position vector, it is embedded into the quaternion $(0, \boldsymbol{p})$.

Each precurved frame has an associated curvature given by $\boldsymbol{u}_i^*(\sigma_i) = \omega(\boldsymbol{q}_i^*(\sigma_i), \boldsymbol{q}_i^{*\prime}(\sigma_i))$, where the prime denotes the partial derivative with respect to arc length and $\omega(\boldsymbol{q}, \boldsymbol{z}) = 2\boldsymbol{q}^{-1}\boldsymbol{z}$ is the function which maps the derivative of a quaternion into the body-frame angular velocity. The precurved frames are chosen so that the tangent vector satisfies $\boldsymbol{p}' = \boldsymbol{q}\boldsymbol{e}_3\boldsymbol{q}^{-1}$, where $\boldsymbol{e}_3$ is the third standard basis vector. We make the assumption that the third component of $\boldsymbol{u}_i^*$ is zero, which does not restrict the allowable precurved tube shapes [84].

Along with this precurvature, the scalar bending stiffness $k_{ib}(\sigma_i)$ and torsional compliance $c_{it}(\sigma_i)$ functions complete the necessary information for each component tube, as summarized in Table 3.2. All functions describing the tube are extended to the entire real line, where outside of $[0, L_i]$, each of $\boldsymbol{u}_i^*$, $k_{ib}$, and $c_{it}$ is assumed to be zero. The final shape is given by the arc-length parameterized frame $\boldsymbol{g}(s) = (\boldsymbol{p}(s), \boldsymbol{q}(s))$.

| Variable | Description | Size |
|---|---|---|
| $\boldsymbol{\sigma}$ | Material arc parameter of each tube in $[0, L_i]$ | $N \times 1$ |
| $\boldsymbol{\psi}$ | Angular displacement of each material frame | $N \times 1$ |
| $\boldsymbol{m}_z$ | Moment carried by each tube about the tangent | $N \times 1$ |
| $\boldsymbol{n}$ | Internal shear force in inertial frame | $3 \times 1$ |
| $\boldsymbol{m}$ | Internal moment in inertial frame | $3 \times 1$ |
| $\boldsymbol{p}$ | Centerline position | $3 \times 1$ |
| $\boldsymbol{q}$ | Quaternion describing Bishop frame orientation | $4 \times 1$ |

Table 3.1: Names and descriptions of the model states for simulation at a given arc length

| Variable | Description | Type |
|---|---|---|
| $\boldsymbol{u}_i^*(\sigma_i)$ | Curvature vector of undeformed Bishop frame | $\mathbb{R} \to \mathbb{R}^2$ |
| $k_{ib}(\sigma_i)$ | Bending stiffness (scalar) | $\mathbb{R} \to \mathbb{R}$ |
| $c_{it}(\sigma_i)$ | Torsional compliance | $\mathbb{R} \to \mathbb{R}$ |

Table 3.2: Functions describing the $i^{\text{th}}$ component tube

### 3.2.2 Differential State Equations

The state space $V = \mathbb{R}^{3N+6} \times SE(3)$ is composed of the variables shown in Table 3.1, and is a manifold of dimension $k = 3N+12$ which requires at least $3N+13$ numbers to specify without any representational singularities. The system state at a particular arc length is $\boldsymbol{y}(s)$. In Chapter 1.7 it was shown that under quasistatic conditions, the solutions to the mechanics problem for concentric tube robots are solutions of an ordinary differential equation,

$$\boldsymbol{y}' = \boldsymbol{f}(\boldsymbol{y}) \tag{3.2}$$

that evolves on the manifold $V$. The equations $\boldsymbol{f}(\boldsymbol{y})$ for the model without external loads are given by

$$\boldsymbol{\sigma}' = f_\sigma = \mathbf{1} \tag{3.3}$$

$$\boldsymbol{\psi}' = f_\psi = \mathbf{C}_t \boldsymbol{m}_z \tag{3.4}$$

$$\boldsymbol{m}_z{}' = f_{mz} = \boldsymbol{T}(\boldsymbol{y}) \tag{3.5}$$

$$\boldsymbol{p}' = f_p = \boldsymbol{q}\boldsymbol{e}_3\boldsymbol{q}^{-1} \tag{3.6}$$

$$\boldsymbol{q}' = f_q = \frac{1}{2}\boldsymbol{q}\boldsymbol{u}_B(\boldsymbol{y}) \ . \tag{3.7}$$

The matrix $\mathbf{C}_t$ is a diagonal matrix of the torsional compliances. The functions $\boldsymbol{T}$ and $\boldsymbol{u}_B$ are given in vectorized form in Appendix A.3.

There are two additional equations which describe the internal forces and moments that must be included if the effects of external loads are considered. These equations have been described in the literature in both a body frame version and an inertial frame version [55, 48]. Here the inertial frame version is selected due the simpler form:

$$\boldsymbol{n}' = f_n = \mathbf{0} \tag{3.8}$$

$$\boldsymbol{m}' = f_m = \boldsymbol{n} \times \boldsymbol{p}' \tag{3.9}$$

### 3.2.3 Boundary Conditions

At the arc length $s = L$, the individual tube arc length $\sigma_i$ is given by

$$\sigma_i(L) = L - \beta_i \tag{3.10}$$

At the proximal end of each tube, actuators impose rotational constraints given by

$$\psi_i(\beta) = 0 \tag{3.11}$$

providing $N$ boundary conditions. At the distal end of each tube the torsional moment $m_{zi}$ is assumed to vanish, which has also been shown to be the "natural" boundary condition which minimizes the stored elastic energy [36], given by

$$m_{zi}(L) = 0 \tag{3.12}$$

and providing another $N$ boundary conditions. If external loads are considered, the distal end is assumed to be moment free, so that

$$\boldsymbol{m}(L) = \boldsymbol{M}_{tip} \ . \tag{3.13}$$

If a force $\boldsymbol{F}_{tip}$ is specified at the tip of the robot, we have

$$\boldsymbol{n}(L) = \boldsymbol{F}_{tip} \tag{3.14}$$

Finally, the position and orientation of the robot $\boldsymbol{p}$ and $\boldsymbol{q}$ must be known for some arc length in some inertial frame. Surprisingly, it is often easiest to arbitrarily select $s = L$ for this arc length, that is to choose an inertial frame which happens to coincide with the tip location for the current configuration of the robot. These choices yield

$$\boldsymbol{p}(L) = \boldsymbol{0} \tag{3.15}$$

$$\boldsymbol{q}(L) = \begin{bmatrix} 1 & 0 & 0 & 0 \end{bmatrix}^T \tag{3.16}$$

Usually, the location and orientation of the robot will actually be known somewhere else (e.g. at $s = 0$) in another inertial frame defined by a piece of tracking equipment or an experimental setup. Fig. 3.1 shows the various frames, where $\boldsymbol{g}^*(0)$ as shown in the figure is taken to be known. Then the end effector location in the true inertial frame is

$$\boldsymbol{g}^*(L) = \boldsymbol{g}^*(0)\boldsymbol{g}^{-1}(0) \tag{3.17}$$

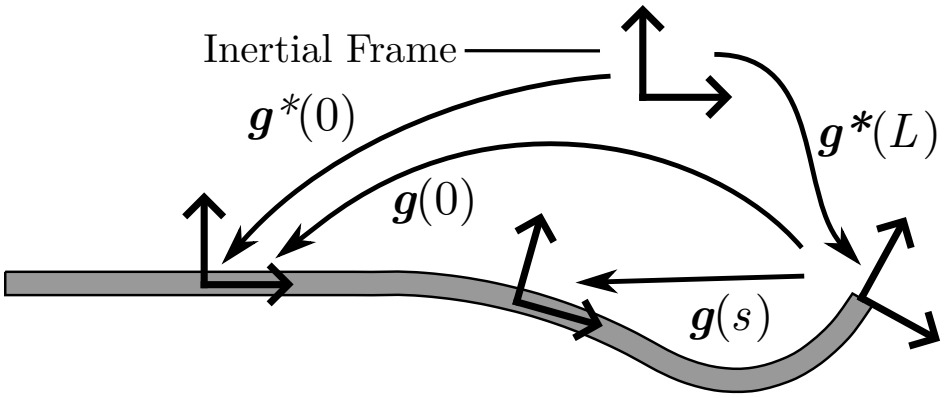


Figure 3.1: Frame assignments for the concentric tube robot mechanics.

where $g^{-1}(0)$ is provided by solution of the model equations.

When $F_{tip}$ is present, it is specified in coordinates of the end effector frame in order that (3.9) can be computed. Note that this is not always possible a-priori, and the appropriate solution must then be found by root finding.

### 3.2.4 Configuration Coordinates

A configuration coordinate space (C-space) consists of vectors $\boldsymbol{c} \in \mathbb{R}^m$, where the coordinate variables provide enough algebraic conditions on the states so that an initial value problem is well-defined and has a unique solution. All of the boundary conditions except (3.11) are already at $s = L$. For on-line operation, the boundary conditions for $\psi_i$ can simply be moved to the distal end, because these rotational variables are controlled by a feedback control system. The control system can just as well work at the distal end. The vector $\boldsymbol{c} = (\boldsymbol{\psi}(L), \boldsymbol{\beta}, \boldsymbol{n}(L), \boldsymbol{m}(L))$ provides a complete initial condition for general actuation and end-effector wrenches. The location of this initial condition is in general a function of the configuration coordinates, i.e. $L(\boldsymbol{c}) = \beta_1 + L_1$. In on-line use for model-based control, the solution of the differential equations provides $\boldsymbol{\psi}(\beta)$, which can then be used to drive the actuators.

### 3.2.5 Jacobian Matrices

When the coefficients $k_{ib}$, $c_{it}$ and precurvatures $\boldsymbol{u}_i^*$ are differentiable functions of arc length[1], the vector field $\boldsymbol{f}(\boldsymbol{y})$ is differentiable with respect to $\boldsymbol{y}$ at all arc lengths, and there is a matrix $\mathbf{J}$ at each arc length and configuration pair $(s, \boldsymbol{c})$, such that

$$\boldsymbol{\zeta} = \mathbf{J}(s, \boldsymbol{c})\dot{\boldsymbol{c}} \ , \tag{3.18}$$

where $\boldsymbol{\zeta} = (\dot{\boldsymbol{\sigma}}, \dot{\boldsymbol{\psi}}, \dot{\boldsymbol{m}}_z, \dot{\boldsymbol{n}}, \dot{\boldsymbol{m}}, \boldsymbol{v}, \boldsymbol{\omega})$ describes the time derivative of the state $\boldsymbol{y}(s, \boldsymbol{c})$ under the C-space time derivative $\dot{\boldsymbol{c}}$. The components $\boldsymbol{v}$ and $\boldsymbol{\omega}$ of $\boldsymbol{\zeta}$ are the body-frame linear and angular velocities of $\boldsymbol{g}$, and form 6-dimensional twist coordinates. The remaining components are the usual derivatives in a Euclidean space. The whole element $\boldsymbol{\zeta}$ is an element of the Lie algebra of the state space $\mathfrak{v}$.

In order to guarantee that a Jacobian matrix exists, additional assumptions are needed about the parameter functions in Table 3.2. In fact, it is not hard to see that the robot's end-effector position may not even be differentiable in some configurations, as shown by example in Fig. 3.2. The following additional assumptions suffice to guarantee differentiability of all states at all but a finite number of points along the length of the robot

- No two tubes begin or end at exactly the same arc length
- The precurvature functions $\boldsymbol{u}_i^*$ are $C^1$

With these additional assumptions, the matrix $\mathbf{J}$ exists everywhere except at arc lengths where $k_{ib}$ has a jump discontinuity (at the ends of tubes). The second of these assumptions also has the implication that $\boldsymbol{u}_i^*(0) = \boldsymbol{u}_i^*(L_i) = 0$, so a tube which is curved at its distal end is modeled by a function that has a steep but smooth transition between full curvature and zero curvature near $s = L$. We use a scaled and shifted version of a cubic polynomial function for this purpose.

[1]If the coefficients in the differential equations have jump discontinuities, such as modeling the tube stiffnesses as discontinuous steps at the tube endpoints, the Jacobian matrix does not exist at arc lengths where the coefficients have jumps, and an implicit "passage to the limit" usually allows the differential to be formulated for the remaining arc lengths [57].

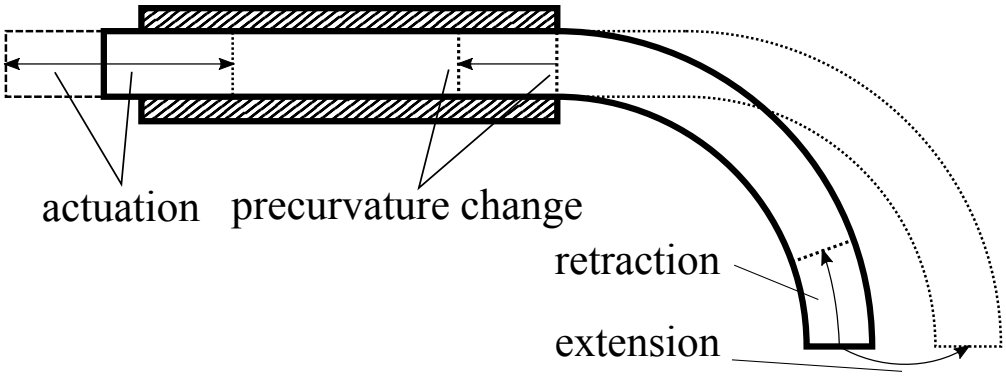


Figure 3.2: Non-differentiable configuration of a concentric tube robot. An inner tube which is straight and then precurved translates inside of a rigid outer tube. When the tubes are assumed to exhibit stiffness functions which are discontinuous at their endpoints, and the curvature also switches discontinuously along the length of a tube, translating the tube may result in different behaviors in each direction. The tip position is a continuous, but not differentiable, function of the tube translations.

Partition the state element $\boldsymbol{y} = (\boldsymbol{y}^o, \boldsymbol{y}^g)$ by the parts of the state on $\mathbb{R}^{3N+6}$ and $SE(3)$ respectively, and partition $\boldsymbol{\zeta}$ similarly. For each column vector $\boldsymbol{J}_i$, the rows are partitioned as $\boldsymbol{J}_i^o$ and $\boldsymbol{J}_i^g$. For $\boldsymbol{y}, \boldsymbol{x} \in V$, define

$$L_{\boldsymbol{y}}(\boldsymbol{x}) = (\boldsymbol{y}^o + \boldsymbol{x}^o, \boldsymbol{y}^g \boldsymbol{x}^g) \ . \tag{3.19}$$

Then, define the pushforward operator,

$$(L_{\boldsymbol{y}*})(\boldsymbol{\zeta}) = \left(\boldsymbol{\zeta}^o, \left(\boldsymbol{q}\boldsymbol{v}\boldsymbol{q}^{-1}, \frac{1}{2}\boldsymbol{q}\boldsymbol{\omega}\right)\right) \ . \tag{3.20}$$

Lastly, define the exponential map

$$\exp(\boldsymbol{\zeta}) = (\boldsymbol{\zeta}^o, \exp(\boldsymbol{\zeta}^g)) \tag{3.21}$$

where $\exp(\boldsymbol{\zeta}^g)$ is the standard exponential mapping from twists to rigid transformations [143].

Let $\boldsymbol{J}_i$ be the $i^{\text{th}}$ column of the Jacobian matrix. Define $\boldsymbol{\xi}(\boldsymbol{y})$ by re-writing equations (3.3) through (3.7) as $\boldsymbol{y}' = (L_{\boldsymbol{y}*})(\boldsymbol{\xi}(\boldsymbol{y}))$. Then the vector fields $(L_{\boldsymbol{y}*})(\boldsymbol{\xi})$ and $(L_{\boldsymbol{y}*})(\boldsymbol{J}_i)$ describe the flow of $\boldsymbol{y}(s, \boldsymbol{c})$ along the coordinate $s$ and along the coordinate $c^i$, respectively.

The two vector fields $(L_{\boldsymbol{y}*})(\boldsymbol{\xi}(\boldsymbol{y}))$ and $(L_{\boldsymbol{y}*})(\boldsymbol{J}_i)$ must have flows which commute since the following the flows of the fields in different orders cannot change the solution $y(s, \boldsymbol{c})$. This condition is equivalent to

$$(\boldsymbol{J}_i)' = \frac{\partial}{\partial c^i}\boldsymbol{\xi} - \mathrm{ad}_{\boldsymbol{\xi}}\boldsymbol{J}_i \ , \tag{3.22}$$

where

$$\mathrm{ad}_{\boldsymbol{\xi}}\boldsymbol{J}_i = \begin{bmatrix} \boldsymbol{J}_i^o \\ \boldsymbol{u}_B \times \boldsymbol{J}_i^v + \boldsymbol{e}_3 \times \boldsymbol{J}_i^\omega \\ \boldsymbol{u}_B \times \boldsymbol{J}_i^\omega \end{bmatrix} \tag{3.23}$$

The derivation of (3.22) is shown in more detail in Appendix A.4. The partial derivatives of $\boldsymbol{\xi}$ with respect to each C-space coordinate $c^i$ are computed via the chain rule using the directional derivatives

$$\frac{\partial}{\partial c^i}\boldsymbol{\xi} = \sum_k \tilde{E}_k^r(\boldsymbol{\xi}) J_i^k \ , \tag{3.24}$$

where

$$\tilde{E}_k^r(\boldsymbol{\xi}) = \frac{d}{dt}\left(\boldsymbol{\xi}(L_{\boldsymbol{y}}(\exp(t\boldsymbol{E}_k)))\right)\Big|_{t=0} \tag{3.25}$$

is the directional derivative of $\boldsymbol{\xi}$ along the $k^{\text{th}}$ standard basis direction $\boldsymbol{E}_k$ in the vector space containing $\boldsymbol{\zeta}$. The first standard basis vectors are simply the usual ones for a Euclidean space, $\boldsymbol{e}_1$, ..., $\boldsymbol{e}_{3N+6}$. The remaining standard basis vectors are the standard body-frame rigid-body velocities, consisting of unit linear velocities and unit angular velocities along or about each of the body-frame coordinate axes. This directional derivative operator $\tilde{E}_k^r$ is described in greater detail in [144]. Since the exponential map is defined as the identity map on all states except $\boldsymbol{p}$ and $\boldsymbol{q}$, this directional derivative agrees with the partial derivative for the states $\boldsymbol{y}^o$. For $\boldsymbol{p}$ and $\boldsymbol{q}$, the quantity $\tilde{E}_k^r(\boldsymbol{\xi}(\boldsymbol{y}))$ is the rate of change of $\boldsymbol{\xi}(\boldsymbol{y})$ along the standard body-frame twist coordinates. The matrix of directional derivatives $\tilde{E}_k^r(\xi^j)$ is denoted by

$$\left[\frac{\partial \boldsymbol{\xi}}{\partial \boldsymbol{y}}\right]_k^j = \tilde{E}_k^r(\xi^j) \ , \tag{3.26}$$

with $j$ the row index and $k$ the column index.

The matrix $\mathbf{J}$ is then partitioned into blocks $\mathbf{J}^{\alpha}_{\beta}$, where $\alpha \in \{\sigma, t, g, \ell\}$ and $\beta \in \{a, f\}$. These letters denote the rectangular partitionings by the state (rows) and configuration (columns), as described in Table 3.3. The blocks of the matrix $[\partial \boldsymbol{\xi}/\partial \boldsymbol{y}]$ are similarly denoted using $\boldsymbol{\xi}^{\alpha_1}_{\alpha_2}$. The differential equations defining each block are as follows:

$$(\mathbf{J}^t_a)' = \boldsymbol{\xi}^t_t \mathbf{J}^t_a + \boldsymbol{\xi}^t_\ell \mathbf{J}^\ell_a + \boldsymbol{\xi}^t_\sigma \mathbf{J}^\sigma_a + \boldsymbol{\xi}^t_g \mathbf{J}^g_a \tag{3.27}$$

$$(\mathbf{J}^g_a)' = \boldsymbol{\xi}^g_t \mathbf{J}^t_a + \boldsymbol{\xi}^g_\ell \mathbf{J}^\ell_a + \boldsymbol{\xi}^g_\sigma \mathbf{J}^\sigma_a + \boldsymbol{\xi}^g_g \mathbf{J}^g_a - \mathrm{ad}_{\boldsymbol{\xi}} \mathbf{J}^g_a \tag{3.28}$$

$$(\mathbf{J}^\ell_a)' = \boldsymbol{\xi}^\ell_g \mathbf{J}^g_a + \boldsymbol{\xi}^\ell_\ell \mathbf{J}^\ell_a \tag{3.29}$$

$$(\mathbf{J}^t_f)' = \boldsymbol{\xi}^t_t \mathbf{J}^t_f + \boldsymbol{\xi}^t_\ell \mathbf{J}^\ell_f + \boldsymbol{\xi}^t_g \mathbf{J}^g_f \tag{3.30}$$

$$(\mathbf{J}^g_f)' = \boldsymbol{\xi}^g_t \mathbf{J}^t_f + \boldsymbol{\xi}^g_\ell \mathbf{J}^\ell_f + \boldsymbol{\xi}^g_g \mathbf{J}^g_f - \mathrm{ad}_{\boldsymbol{\xi}} \mathbf{J}^g_f \tag{3.31}$$

$$(\mathbf{J}^\ell_f)' = \boldsymbol{\xi}^\ell_\ell \mathbf{J}^\ell_f + \boldsymbol{\xi}^\ell_g \mathbf{J}^g_f \,, \tag{3.32}$$

where $\boldsymbol{\xi}^g = [\boldsymbol{e}_3, \boldsymbol{u}_B]^T$ and where zero blocks of of the matrix of partial derivatives of $\boldsymbol{\xi}$ have been removed from the expressions. The notation $\mathrm{ad}_{\boldsymbol{\xi}}$ has been abused slightly here and corresponds to the operation in the second and third rows of (3.23). For a given configuration $\boldsymbol{c}$, the Jacobian matrix $\mathbf{J}(s, \mathbf{c})$ is known at $s = L(\boldsymbol{c})$, and the differential equations can be solved simultaneously with the state equations as an initial value problem to yield the Jacobian matrix at all arc lengths. If one of the Jacobian matrices is needed but not the others, the graph in Fig. 3.3 shows the other states need to be included in order to complete the computation.

The blocks $\mathbf{J}^\sigma_a$ and $\mathbf{J}^\sigma_f$ have constant solutions:

$$\mathbf{J}^\sigma_a(s, \boldsymbol{c}) = \begin{bmatrix} \mathbf{0} & -\mathbf{I} \end{bmatrix} \tag{3.33}$$

$$\mathbf{J}^\sigma_f(s, \boldsymbol{c}) = \mathbf{0} \,. \tag{3.34}$$

The remaining equations must be solved numerically with initial conditions given by

$$\mathbf{J}_a^t(L) = \begin{bmatrix} \mathbf{I} & \mathbf{0} \\ \mathbf{0} & \mathbf{0} \end{bmatrix} \tag{3.35}$$

$$\mathbf{J}_a^g(L) = -\begin{bmatrix} \boldsymbol{e}_3 \\ \mathbf{0} \end{bmatrix} \frac{\partial L(\boldsymbol{c})}{\partial \boldsymbol{c}} \tag{3.36}$$

$$\mathbf{J}_a^\ell(L) = \begin{bmatrix} \mathbf{0} \\ \boldsymbol{e}_3 \times \boldsymbol{n} \end{bmatrix} \frac{\partial L(\boldsymbol{c})}{\partial \boldsymbol{c}} \tag{3.37}$$

$$\mathbf{J}_f^t(L) = \mathbf{0} \tag{3.38}$$

$$\mathbf{J}_f^g(L) = \mathbf{0} \tag{3.39}$$

$$\mathbf{J}_f^\ell(L) = \begin{bmatrix} \mathbf{I} \\ \mathbf{0} \end{bmatrix} \tag{3.40}$$

Initial conditions (3.36) and (3.37) arise from the fact that the arc length $L(\boldsymbol{c})$ of the initial condition moves under some actuation.

Wherever a tube ends or begins, the stiffness coefficients are discontinuous and the Jacobian matrices $\mathbf{J}_a^t$ and $\mathbf{J}_a^g$ undergo a jump transition. If the stiffness of the $i^{\text{th}}$ tube is discontinuous at $s = \eta$, then the jump transitions

$$\boldsymbol{J}_{a,N+i}^t(\eta^+) - \boldsymbol{J}_{a,N+i}^t(\eta^-) = \boldsymbol{\xi}^t(\eta^-) - \boldsymbol{\xi}^t(\eta^+) \tag{3.41}$$

$$\boldsymbol{J}_{a,N+i}^g(\eta^+) - \boldsymbol{J}_{a,N+i}^g(\eta^-) = \boldsymbol{\xi}^g(\eta^-) - \boldsymbol{\xi}^g(\eta^+) \tag{3.42}$$

apply at this location for the $(N+i)^{\text{th}}$ columns of the matrices. Finally, to obtain the Jacobian matrix which relates changes in $\boldsymbol{c}$ with those in $\boldsymbol{g}^*(L)$, which is most often what is needed, the Adjoint transformation law is

$$\mathbf{J}_a^{g*}(L) = -\mathrm{Ad}_{g(0)}\mathbf{J}_a^g(0) \ . \tag{3.43}$$

Table 3.3: Partitions of $\mathbf{J}$ matrix

| Label | Meaning | Corresponding Variables |
|---|---|---|
| $\sigma$ | Arc lengths | $\boldsymbol{\sigma}$ |
| $t$ | Torsional | $\boldsymbol{\psi}$, $\boldsymbol{m}_z$ |
| $g$ | Geometry | $\boldsymbol{p}$, $\boldsymbol{q}$ |
| $\ell$ | Loads | $\boldsymbol{n}$, $\boldsymbol{m}$ |
| $a$ | Actuation | $\boldsymbol{\psi}_L$, $\boldsymbol{\beta}$ |
| $f$ | External Loads | $\boldsymbol{F}_{tip}$ |

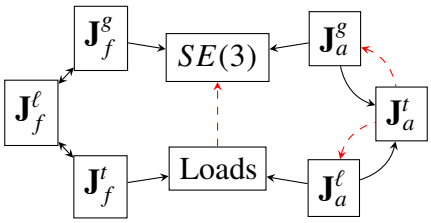


Figure 3.3: The dependency graph for the Jacobian blocks. In order to solve for one of these items, all items that are found by following the arrows must also be computed. The red dashed edges are active only when loads are included in the model.

## 3.3 Numerical Solution

In order to numerically evaluate the state equations and Jacobian equations, we use an initial value problem (IVP) solver. The selection of the initial value problem solver does affect the final performance of the model solver, and due to the fact that tubes may appear or disappear along the interval of integration, great care must be taken when solving the equations.

### 3.3.1 IVP Solver Choice

Since the states evolve on a manifold, it would at first seem that numerical integrators which preserve the manifold constraints would be preferred. However, the interval of integration is short, and loss of unit magnitude in the quaternion does not actually change the rotation that it represents. We use the 8th order method of Prince and Dormand to integrate the differential equations [145], and results presented in the next section show that a fixed, small number of integration steps leads to sufficient accuracy for designs that are similar to the prototypes shown in the literature. We have found experimentally that re-normalizing the quaternion prior to evaluating the differential

equation $\boldsymbol{f}$ can yield slightly better accuracy.

The choice of IVP solver also informed our earlier choices of representation in the model equations. Specifically, the inertial frame equations for the internal force and moment are more suitable for Runge-Kutta integration than the body-frame version of the equations. The body-frame equations involve a rotation of the coordinates for $\boldsymbol{n}$ and $\boldsymbol{m}$, counter to the rotating coordinate frame, since the physics holds in a stationary frame. While a rotation should preserve the magnitude of the vectors, explicit Runge-Kutta methods do not preserve these magnitudes, which can lead to noticeable growth of the solution if the step size is too large.

### 3.3.2 Integrating the Equations

Discontinuities in the bending and torsional stiffness coefficients prevent the use of a standard numerical IVP solver to solve the equation over the entire domain [57]. Instead, piecewise integration must be used, which stops and restarts the integrator at waypoints defined by the discontinuities.

The parameter functions for the $j^{\text{th}}$ tube contribute a list of intervals $I_{jk} = ([a_k, b_k], \chi_k)$, for $k = 1, ..., n_j$, each of which consists of a left and right endpoint $a_k$ and $b_k$ and a tag $\chi_k$ indicating whether the tube is precurved over the material arc lengths between the endpoints of the interval. There are four useful tag types, which indicate that over the interval the state equations can be solved "sparsely", "normally", "densely", or "discontinuously." The sparse tag applies to regions which are not precurved. The normal tag applies to regions which are precurved, and the dense tag applies to regions which mark smooth but rapid transitions between non-precurved and precurved sections. The discontinuous tag applies to locations where a tube begins or ends, which are the points where the stiffness functions have step discontinuities. When external loads a present, an extra interval with a normal tag type is added over the length $[0, L(\boldsymbol{c})]$ to account for a reaction load at $s = 0$, which forces the internal force and moment to zero for all $s < 0$.

In order for the software to integrate over each section only once, the set $\{I_k\}$ must be resolved into a set of adjacent non-overlapping intervals. The first step is to shift the intervals by the current

tube translations $\beta_j$ and collect all $I_{jk}$ into a single set

$$S = \bigcup_{j=1}^{N} \bigcup_{k=1}^{n_j} ([a_k + \beta_j, b_k + \beta_j], t_k) \ . \tag{3.44}$$

Every point in the final list of intervals should be assigned the highest tag for which it appears in any of the $S_k$. Additionally, we impose the requirement that the ends of dense intervals appear in the output as ends of intervals in the resolved set, ensuring that the integrator can accurately solve these regions even when they overlap.

The intervals are first converted to a set of endpoints $T_k = (s_k, t_k, \chi_k)$ in the following manner. Define the mapping $Ends(I_k) = (a_k, left, \chi_k) \cup (b_k, right, \chi_k)$. Then the endpoints are collected in the set

$$T = \bigcup_{I_k \in S} Ends(I_k) \ . \tag{3.45}$$

Additionally, we define the functions $\text{Loc}(T_k) \to s_k$, $\text{Tag}(T_k) \to \chi_k$, and $\text{Type}(T_k) \to t_k$.

The endpoint set $T$ is sorted by location as the primary key and type (left before right) as the secondary key. We use the sort implementation in our C++ compiler's standard template library. Then, a sweeping algorithm proceeds in order of increasing arc length to output the resolved intervals, using a heap $H$ to track which tags have been opened by left endpoints but not closed by right endpoints. Pseudocode is provided in Algorithm 1.

After this procedure, each interval in the output list is numerically integrated according to its tag. Sparse intervals may be integrated exactly with a first order Euler integrator. Normal intervals may be evaluated by a single step of the $8^{\text{th}}$ order Runge-Kutta integrator, and dense intervals may also be integrated by a single Runge-Kutta steps. Discontinuities do not affect the state $\boldsymbol{y}$, but the jump transitions in the Jacobian may apply at these locations.

**Algorithm 1** Resolve endpoint set to adjacent intervals

**procedure** AddTag($H, \chi$)
  **if** Size($H$) = 0 **then**
    $H \leftarrow$ Push($H, \chi$)
    **return** $(H, sparse, false)$
  **else**
    $\chi_{max} \leftarrow$ Peek($H$)
    $H \leftarrow$ Push($H, \chi$)
    **if** $(\chi > \chi_{max})$ or $(\chi = \chi_{max} = dense)$ **then**
      **return** $(H, \chi_{max}, true)$
    **else**
      **return** $(H, \chi_{max}, false)$
    **end if**
  **end if**
**end procedure**
**procedure** RemoveTag($H, \chi$)
  $\chi_{max} \leftarrow$ Peek($H$)
  $H \leftarrow$ Remove($H, \chi$)
  **if** Size($H$) > 0 **then**
    **if** Peek($H$) < $\chi_{max}$ or $\chi = dense$ **then**
      **return** $(H, \chi_{max}, true)$
    **else**
      **return** $(H, \chi_{max}, false)$
    **end if**
  **else**
    **return** $(H, \chi_{max}, true)$
  **end if**
**end procedure**
**procedure** Accept($H, T_k$)
  **if** Type($T_k$) = $left$ **then**
    **return** AddTag($H$, Tag($T_k$))
  **else**
    **return** RemoveTag($H$, Tag($T_k$))
  **end if**
**end procedure**
**procedure** Append($R, s_1, s_2, \chi, \chi_{max}$)
  **if** $s_2 > s_1$ or $\chi = \chi_{max} = discontinuity$ **then**
    **return** $(R \cup ([s_1, s_2], \chi), s_2)$
  **else**
    **return** $(R, s_1)$
  **end if**
**end procedure**

```
procedure RESOLVE(T)
    R ← ∅
    s ←LOC(T_1)
    H ←PUSH(H,TAG(T_1))
    for k ←2, size(T) do
        (H, χ_max, b) ← ACCEPT(H,T_k)
        if b = true then
            (R, s) ← APPEND(R, s, LOC(T_k), χ_max)
        end if
    end for
    return R
end procedure
```

## 3.4 Code Performance Evaluation

We have evaluated the performance of the proposed numerical routine in terms of both convergence and speed for three-tube robots, which are a common design seen in prior literature. For evaluation of convergence, we compare the solution using a single RK8 step over each integration interval with a solution on a much denser grid.

All model code is implemented in C++ with templated functions that evaluate only the parts of the model necessary to compute the desired information. This means, for example, that when none of the Jacobian matrices are needed, they are not defined as part of the state vector, and the graph of Fig. 3.3 is implemented in a template metaprogram that evaluates at compile-time. This functionality is implemented using the Boost Metaprogramming Libraries. The Eigen library is used for all matrix and vector arithmetic.

Since the code is designed for real-time use, no calls to dynamic memory allocation functions are used. All matrices are defined with templated sizes based on the number of tubes specified at compile time.

### 3.4.1 Convergence

To evaluate the convergence of the proposed method, we sampled designs and configurations from the feasible range of designs for three tubes which have a planar circular precurvature at

| Parameter | Distribution |
|---|---|
| $\gamma_i$ | $\mathcal{U}(0,90)$ [deg] |
| $L_{ci}$ | $\mathcal{U}(10,50)$ [mm] |
| $w_i$ | $\mathcal{U}(0.05,0.15)$ [mm] |
| $L_3$ | $\mathcal{U}(L_{c3},3L_{c3})$ [mm] |
| $L_2$ | $\mathcal{U}(\max(L_3,L_{c2}),\max(L_3,4L_{c2}))$ [mm] |
| $L_1$ | $\mathcal{U}(\max(L_2,L_{c1}),\max(L_2,5L_{c1}))$ [mm] |

Table 3.4: Distributions for design samples

their distal ends. Letting $\mathcal{U}(a,b)$ represent the uniform distribution between $a$ and $b$, designs were sampled from the distributions shown in Table 3.4. We simulated $10 \times 10^6$ designs from these distributions, and for each design a random configuration $\boldsymbol{c}$ was chosen according to the sampling distributions of Burgner et al. [138]. The error in $\boldsymbol{p}^*(L)$ is shown in Fig. 3.4.

Inner and outer tube diameters were generated by sampling wall thicknesses $w_i$, and starting from $ID_1 = 0.86\,\text{mm}$, generated by using $OD_i = ID_i + 2w_i$ and the clearance $OD_{i+1} = ID_i + 0.1\,\text{mm}$. Curvatures were generated by sampling the angles $\gamma_i = L_{ci}\kappa_i$, and the curved lengths $L_{ci}$, and computing $\kappa_i$ from these two values.

Interestingly, the distribution of the global 2-norm error in the position $\boldsymbol{p}^*(L)$ is approximately log normal. The logarithm of the error has a mean of -11.4 and standard deviation of 1.4 when the argument of the logarithm is expressed in meters, indicating that the solution has on average about 11 digits of accuracy. This level of numerical error is more than sufficient for purposes of planning, control, or analysis, since these errors are already many orders of magnitude smaller than the modeling error [55].

### 3.4.2 Evaluation Speed

For performance evaluation, we compiled the code in Windows 10 using the Microsoft Visual Studio 2015 compiler in 64-bit mode, and also implemented the code in a MATLAB Simulink diagram for Simulink Real-Time (32-bit) using the S-function API. In Windows the processor used was an Intel i7-4790 at 3.6 GHz, and for Simulink Real-Time the processor was an Intel

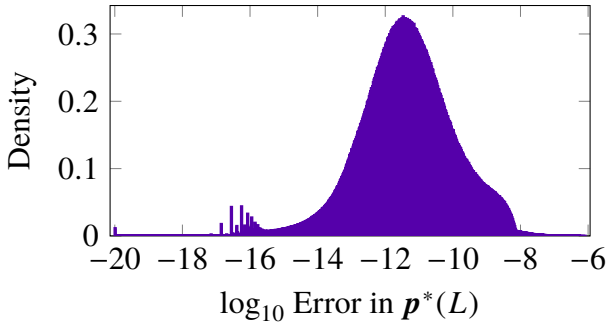


Figure 3.4: Distribution of errors in $\boldsymbol{p}^*(L)$ associated with the single-step RK8 method. The errors were computed by comparison to a second numerical solution $\widehat{\boldsymbol{p}}^*(L)$ computed with a much greater number of integration steps.

Celeron G530 at 2.4 GHz. In Windows we used the Microsoft Visual Studio 2015 compiler, and for Simulink Real-Time we used the Visual Studio 2013 compiler. For both cases all compiler optimizations were enabled, and the SSE2 instruction set was enabled for the 32-bit build. Table 3.5 shows the rates at which the methods in this paper compute solutions to the kinematics problem.

One feature of the code which facilitates high solution rates is the vectorization of the model equations in Appendix A.3. This leverages the substantial optimizations which are already implemented in the Eigen C++ linear algebra library. Other optimizations were the result of profiling. For example, we determined it was necessary to explicitly eliminate repeated calls to the function $\boldsymbol{u}_B$ and to the sin and cos functions inside of the differential equation function $\boldsymbol{f}$, because the compiler did not eliminate some redundant computations. We also rely heavily on the compiler's Return Value Optimization for avoiding temporary copies of variables.

Table 3.5: Rate of computation of model solutions (3 tubes)

| | Platform | |
|---|---|---|
| States | x86-64 (Windows 10) | x86 (Simulink RT) |
| $t, g$ | 36.92 kHz | 10.45 kHz |
| $t, g, \mathbf{J}_a^g$ | 9.70 kHz | 2.26 kHz |
| $t, g, \ell$ | 27.01 kHz | 8.05 kHz |
| $t, g, \ell, \mathbf{J}_a^g, \mathbf{J}_f^g$ | 2.69 kHz | 593 Hz |

### 3.4.3 Computational Complexity

The code was instrumented to count the number of floating point operations required in a single evaluation of the robot kinematics for a three-tube robot, including only the torsional states and the geometric states. Only the operations associated with solving equations (3.3) through (3.7) were counted, corresponding to the computation rates in the first row of table 3.5. Table 3.6 shows the operation counts. The row labeled "Vector Norm" counts three-element and four-element vector norm computations, which are computed with the Eigen library implementation.

For the sake of comparison, consider that the kinematics of a 6R rigid-link arm can be computed with 6 matrix multiplies of $4 \times 4$ matrices (672 multiply/add operations) and 12 trigonometric function evaluations, plus the few remaining operations needed to construct the transformations. Based alone on these operations, the kinematics for the three-tube concentric tube robot are about 60 times more computationally expensive using the techniques in this paper.

Table 3.6: Number of operations in a single kinematics computation

| Operation | Count |
|---|---|
| Multiply | 20,631 |
| Add | 19,674 |
| Divide | 655 |
| sin/cos | 786 |
| Vector Norm | 131 |

## 3.5 Conclusions

The techniques that are used to efficiently evaluate the kinematics of concentric tube robots have been described. By casting the kinematics problem as the solution of an initial value problem and using a high order Runge-Kutta method to solve these equations, solution rates an order of magnitude faster than those reported in the literature are possible in real-time and to an excellent level of accuracy. Without the Jacobian computation, the model equations for a six degree-of-freedom concentric tube robot are approximately 60 times more expensive to compute than a six degree-of-freedom serial manipulator. Computation of the Jacobian matrices comes at a substan-

tial expense in run-time, so the ability to exclude them from the computation when not needed is highly desirable.

# Chapter 4

## Model Analysis: Elastic Stability

Concentric tube robots may sometimes exhibit elastic instability, which is manifested by a rapid, uncontrollable release of stored elastic energy. Before these robots can be safely used in surgical procedures, this phenomenon needs to be adequately modeled and accurately predicted, which is the major contribution of this chapter. This work was published in Transactions on Robotics [146]. In what follows, the model introduced in chapter 1.7 is analyzed to determine when elastic instability is incipient through energy-based methods. In addition to predicting the onset of elastic instability, the insights gained from the analysis led to the design element of torque transmission tubes seen in chapter 2.

The predictions discussed near the end of the chapter indicate that beyond critical values of tube curvature or overlapped curved length of tubing, the usable robot workspace volume can rapidly disappear. This underlines the importance of performing a stability analysis on any new design before attempting to use it in practice.

### 4.1 Introduction

It was noted early in the development of concentric tube robots that unless gradual tube curvatures are used or minimal overlap of curved tube sections is ensured, tubes can exhibit elastic instabilities [47] (also previously referred to as "snaps" and "bifurcations"). Elastic instabilities occur due to torsional elastic energy storage in the tubes that make up a concentric tube robot. An instability occurs when this energy is rapidly released, and the robot "snaps" to a new configuration. Unforeseen snapping is clearly not desirable and could be dangerous in surgical applications.

The snapping problem has been approached from design, modeling, and planning perspectives. With the exception of the early work in [47], these studies have used the mechanics based model of concentric tube robots found in [55, 48]. For example, it has recently been shown that tubes can

be laser machined to reduce the ratio of bending to torsional stiffness, which improves stability [125, 147]. However, even using this approach, snaps will still occur if high curvatures are employed, so methods for design and snap prediction will still be needed. Another approach is to use non-constant precurvature tubes to enhance the elastic stability, as shown by Ha et al. [120]. In that work, analytical stability conditions for a planar two-tube robot are presented, and an optimal control problem is used to design tube precurvatures which result in a completely stable actuation space. Our work complements theirs by analyzing the stability of robots which possess unstable configurations in their actuation space. We also consider designs of an arbitrary number of tubes with more general precurvature.

It is also possible to plan stable paths for robots that do have the potential to snap, as shown by Bergeles et al. [118], by examining the relative axial angle between the base of a tube and its tip for all possible rotations for a given set of tubes. While this work provides a method to design and use high-curvature robots, the stability condition chosen by the authors was stated as a definition. One of our contributions is to derive a stability criterion from first principles. Another model-based approach is that of Xu et al. [148], who sought design parameter bounds for constant curvature robots to ensure a snap-free unloaded robot workspace. Xu et al. provided exact design bounds for a two-tube robot and non-exact, conservative bounds for robots with more than two tubes. In addition, the solutions in [148] for more than two tubes only apply to robot configurations where the precurved portions of tubes are precisely aligned in arc length.

In this chapter, we characterize the elastic stability of unloaded concentric tube robots with any number of tubes, each of which may be preshaped as a general space curve. We connect concentric tube robot stability analysis to the analysis of post-buckled Euler beams from the mechanics literature [149, 150, 151]. Based on this analysis, we also propose a metric for relative stability, which can be used to inform real-time controllers, planners, and automated designers to safely design and operate a robot that would otherwise snap.

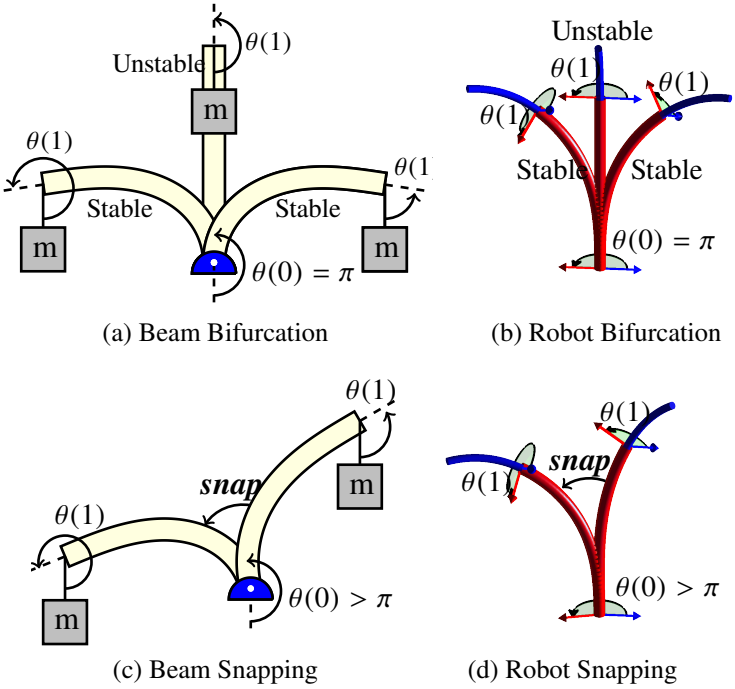


(a) Beam Bifurcation (b) Robot Bifurcation

(c) Beam Snapping (d) Robot Snapping

Figure 4.1: The analogy between an Euler beam and a two-tube concentric tube robot for $\lambda$ greater than its critical value. For the beam, $\theta(s)$ denotes the angle of the beam, while for the robot it denotes the angle between precurvature vectors. (a) There are three solutions when the base has been rotated to $\theta(0) = \pi$. The straight solution is unstable and the two buckled solutions are stable. (b) When the tube precurvatures are anti-aligned at the base there exists one torsionless unstable solution and two stable buckled solutions. (c) As the base angle approaches some value $\theta(0) > \pi$, the beam snaps into a new, stable configuration. (d) As the relative angle between the tubes approaches some value $\theta(0) > \pi$ the tubes snap into a new, stable configuration. Note that the value of $\theta(0)$ when the snap occurs depends on $\lambda$.

## 4.2 The Beam Buckling Analogy

A two-tube concentric tube robot and a loaded beam are analogous systems, and both systems exhibit buckling and snapping. To build intuition, we begin by describing these analogous behaviors. Concentric tube robots are controlled by prescribing relative translations and rotations at the proximal ends of the tubes. The tubes twist and bend one another along their arc length $s$. When there are two circularly precurved tubes the twist angle between them, $\theta(s)$, is governed by the same differential equation as a beam under a dead load as shown in Figure 4.1. The configuration

of both systems is determined by the nonlinear boundary value problem

$$\begin{aligned} f[\lambda, \theta(s)] = \theta'' - \lambda \sin(\theta) = 0 \\ \theta(0) = \theta_0 \\ \theta'(1) = 0 \, , \end{aligned} \tag{4.1}$$

where the equations have been normalized to unit length, so that $0 \leq s \leq 1$. For both the beam and the concentric tube robot, it is known that increasing values of the parameter $\lambda$ can lead to buckling and instability. For the beam, this parameter is controlled by the material properties, the geometry, and the magnitude of the dead load. Likewise, for the robot, $\lambda$ involves the material properties and geometry of the tubes, but the dead load is replaced by the influence of the tube precurvatures.

In the set of solutions to (4.1), two straight beam configurations exist: $\theta(s) = 0$ and $\theta(s) = \pi$, which represent the beam in pure tension and compression, respectively. Similarly, for concentric tubes, two torsionless solutions exist in which the tube precurvatures are aligned and anti-aligned, respectively. Just as a beam in tension cannot buckle, a robot configuration with aligned precurvatures is stable. In contrast, when the beam is compressed (Figure 4.1a) or when the concentric tube robot has anti-aligned precurvatures (Figure 4.1b), the configurations which are straight for the beam and torsionless for the robot can buckle if $\lambda$ exceeds a critical value. Buckling occurs because the solution to (4.1) becomes non-unique when $\lambda$ is large enough, and two new, energetically favorable solutions arise in a process known as bifurcation (see Figure 4.1a and 4.1b). The two new solutions are stable, and the original solution becomes unstable at the point of bifurcation.

For many applications of beam theory, like column buckling, the instability of the trivial, straight configuration is all that is important, but concentric tube robots typically operate far from these areas and may exhibit instability at other configurations and snap across their workspace as shown in Figure 4.1d. The equivalent phenomenon for a beam is shown in Figure 4.1c. Consider an active counter-clockwise rotation of $\theta(0)$ starting from $\theta(0) = 0$. If $\lambda$ is small enough, we expect that the beam will pass stably through a straight configuration when $\theta(0) = \pi$, and the concentric tube robot will pass stably through the configuration with anti-aligned precurvatures. On the other

hand, when $\lambda$ exceeds the critical value, even when $\theta(0) = \pi$, the beam will never straighten out and will instead settle into a buckled configuration, and the concentric tube robot will settle into a high-torsion configuration. Eventually, as $\theta(0)$ increases to some value beyond $\pi$, the buckled configuration becomes unstable and some of the stored energy is released as each system snaps to a new configuration.

In our stability analysis, since we control $\theta(0)$ for concentric tube robots, we seek the value of $\theta(0)$ at which a concentric tube robot will snap. In the beam buckling literature, this problem is referred to as the stability of postbuckled equilibrium states, and important results have emerged in this area in recent years [149, 150, 151]. There has also been recent interest in robotics in the stable quasistatic manipulation of rods [152]. In order to apply these results to concentric tube robots, we first present the mechanics model for concentric tube robots and review the necessary mathematical background for stability analysis.

## 4.3 Concentric Tube Robot Kinematics

Equations (1.18a) and (1.18b) are the equations which determine the angle of twist and torsional moment carried by each tube along its arc length. For the elastic stability analysis, we will focus on the second-order form of (1.18a) and (1.18b) taken together, along with the boundary conditions of (1.19b). The elastic stability is independent of (1.18c), (1.18d), and (1.19a).

The boundary conditions (1.19a) assume that the tubes are constrained at the location chosen as $s = 0$. If, additionally, some physical constraint is present which straightens the tubes when $s < 0$, then $\boldsymbol{u}_B = 0$ trivially over that region. We assume that there is an arc length $s^* > \beta_{max}$ such that

$$\boldsymbol{u}_B(s) = 0, \forall s < s^*, \tag{4.2}$$

which implies that tubes have no curvature between where the tubes are physically held. Where the $i^{\text{th}}$ tube does not physically exist, it is extended by a non-physical entity that has infinite torsional stiffness (i.e. $k_{it}^{-1} \to 0$), but zero bending stiffness (i.e. $k_{ib} = 0$). Intuitively, this must contribute no

energy, since neither an infinite nor zero-stiffness element stores energy, and therefore this modification will not change the solution to the energy minimization problem. This extension converts the multi-point boundary value problem uniquely into a two-point boundary value problem at $\beta$ and $L$ for the states $\psi_i$ and $(k_{it}\psi_i')$.

Although the most general results will apply to equations (1.18a) and (1.18b), we utilize the following simplification in the bifurcation analysis for the sake of finding closed form expressions. In the case that all tubes have planar precurvature, which is a common design, the precurvature functions can be expressed as $\boldsymbol{u}_i^* = \kappa_i(s)\boldsymbol{e}_1$, and the torsional evolution equation (1.18b) simplifies to

$$(k_{it}\psi_i')' = \begin{cases} \dfrac{k_{ib}}{k_b}\displaystyle\sum_{j=1}^{n} k_{jb}\kappa_i\kappa_j \sin(\psi_i - \psi_j) & 0 \le s_i(s) \le L_i \\ 0 & \text{otherwise}, \end{cases} \tag{4.3}$$

where $k_b = \sum_{i=1}^{N} k_{ib}$. Due to the difference of angles in the expression $\sin(\psi_i - \psi_j)$ on the right hand side, the evolution of torsion is invariant under a constant rotational offset of all angles. Equation (4.3) may thus be expressed in terms of relative angles $\theta_i = \psi_i - \psi_1$, which we will use for the analysis of two tubes and for plotting results for three tubes.

## 4.4 Local Stability Analysis for Two Tubes

The bifurcation analysis gives information on what parameters give rise to multiple kinematic solutions and insight into the local behavior of the system near equilibria, but it does not reveal information about stability away from the equilibria. To obtain this information, we look to the energy landscape of the system. Specifically, when are solutions to Euler's equations local minima of the energy functional? The answer to this question will also provide a measure of relative stability, which gives an indication of the proximity to loss of stability in the actuation space.

We begin by constructing the energy functional which corresponds to the simplified, non-

dimensional boundary value problem for two tubes. The functional

$$\begin{aligned} E[\theta] &= \int_{\beta_\sigma}^{0} \frac{1}{2}(\theta')^2 \, d\sigma + \int_{0}^{1} \left( \frac{1}{2}(\theta')^2 - \lambda \cos(\theta) \right) \, d\sigma \\ &= \int_{\beta_\sigma}^{1} F(\sigma, \theta, \theta') \, d\sigma \end{aligned} \tag{4.4}$$

will give the desired result after application of the Euler-Lagrange equation on each interval $[\beta_\sigma, 0]$ and $[0, 1]$,

$$\theta'' - \lambda u(\sigma) \sin\theta = 0 \, , \tag{4.5}$$

where $u(\sigma)$ is the standard unit step function. The problem has been non-dimensionalized by the length over which both tubes are present and pre-curved $L_c$. The dimensionless transmission length $\beta_\sigma$ is given by

$$\beta_{eq,\sigma} = \frac{\beta_{1,\sigma} k_{2t} + \beta_{2,\sigma} k_{1t}}{k_{1t} + k_{2t}} \, . \tag{4.6}$$

where $\beta_{i,\sigma} = \beta_i / L_c$. Note that equation 4.6 can be derived by combining the equation of torsional equilibrium with the equation $\theta = \psi_2 - \psi_1$. The energy functional (4.4) in terms of $\theta$ is related to the functional (1.12) by a scaling and constant offset, and therefore defines an equivalent minimization problem.

Much like the finite dimensional case where the eigenvalues of the Hessian matrix classify stationary points of functions into minima, maxima, and saddle points, we use the second order information about solutions to determine elastic stability. The second variation operator $\mathcal{S}$ takes the place of the Hessian matrix, and in the case where the mixed partial derivatives $F_{\theta\theta'} = 0$, it is given by

$$\mathcal{S}h = -\left(F_{\theta'\theta'} h'\right)' + F_{\theta\theta} h \, , \tag{4.7}$$

where $h$ is a variation of $\theta$ which satisfies the necessary boundary conditions, i.e. $(\theta + h)(\beta_\sigma) = \theta(\beta_\sigma)$ and $(\theta + h)'(1) = 0$. The elastic stability is determined by the eigenvalues of the operator $\mathcal{S}$, which is in this case a Sturm-Liouville operator. Some further details connecting the eigenvalues of $\mathcal{S}$ with the energy functional are provided in Appendix B.

From the energy functional 4.4, the second variation operator $\mathcal{S}$ is defined from (4.7) as

$$\mathcal{S}h = -h'' + \lambda u(\sigma)\cos(\theta)h \,, \tag{4.8}$$

together with its domain, where $u(\sigma)$ is the unit step function introduced for conciseness. The domain of $\mathcal{S}$ includes the boundary conditions $h(\beta_\sigma) = 0$ and $h'(1) = 0$, which are necessary for $\theta + h$ to satisfy the boundary values of the original problem. The second variation of the energy $\delta^2 E[h] > 0$ if and only if all eigenvalues of $\mathcal{S}$ are positive. A sufficient condition is given by solving the following initial value problem.

**Result 1** (Stability of Two-Tube Robots)**.** *A solution $\theta$ to the boundary value problem*

$$\theta'' - \lambda\sin(\theta) = 0,\ \theta(0) = \theta(\beta_\sigma) - \beta_\sigma\theta'(0),\ \theta'(1) = 0$$

*is stable if the solution to the initial value problem defined by*

$$\mathcal{S}h = 0,\ h(\beta_\sigma) = 0,\ h'(\beta_\sigma) = 1 \tag{4.9}$$

*satisfies $h'(\sigma) > 0$ for $\beta_\sigma \leq \sigma \leq 1$.*

See Appendix C.1 for a proof of this result.

This result indicates that a sufficient condition for determining the stability of a solution entails only an integration of an initial value problem, which can be performed numerically. Importantly, the exact same reasoning which produced Result 1 can be repeated in reverse in arc length, which produces the following corollary.

**Corollary 1.** *The stability of a solution $\theta$ can also be determined by solution of the initial value problem defined by*

$$\mathcal{S}h = 0,\ h'(1) = 0,\ h(1) = 1 \,. \tag{4.10}$$

*The solution is stable if $h(\sigma) > 0$ for $\beta_\sigma \leq \sigma < 1$.*

Due to the choice of the boundary conditions of the Corollary, and noting that $\mathcal{S}h = 0$ is equivalent to what we obtain if (4.5) is differentiated by $\theta(1)$, the solution $h$ of Corollary 1 can be interpreted as the slope $h(s) = \partial\theta(s)/\partial\theta(1)$. The equations and boundary conditions of Corollary 1 were previously derived in [120], but the result was not derived from system energy and the interpretation in terms of local stability was not explicitly stated. We also have the following corollary due to the continuity of $h'(1)$ and $h(\beta_\sigma)$ with respect to changes in $\lambda$ and $\alpha$ and the symmetry of the two stability problems.

**Corollary 2.** *The value $h'(1)$ in the result of Result 1, or the value of $h(\beta_\sigma)$ in the result of Corollary 1, may be used as a measure of relative stability when the conditions of Result 1 and Corollary 1 are met, where larger positive values indicate greater stability. Moreover, the the values $h'(1)$ and $h(\beta_\sigma)$ in the two tests are the same.*

The results of the stability test for a two-tube robot with different values of $\lambda$ and nonzero transmission length are shown in Figure 4.2 on an S-curve, which plots solutions to (4.5) at the proximal and distal endpoints. The S-curve was previously used to visualize the stability of two tubes by Dupont et al. [48]. The test clearly reproduces the known result that the negative slope region of the S-Curve is unstable and thus these configurations are not physically possible in concentric tube robots. Note especially that the relative stability metric varies continuously with respect to $\theta(1)$.

The stability analysis also reveals why the instability always appears first at equilibrium solutions. Compare a solution $h_\pi$ to the initial value problem of Result 1, where $\theta(\sigma) = \pi$, to a second solution $h_2$, with $\theta(\sigma) \neq \pi$. Note that $\theta = \pi$ maximizes the coefficient of $h$ in (4.8). If there is no zero in $h'_\pi$, then there cannot be a zero in $h'_2$, because everywhere in the domain $h''_\pi \leq h''_2$. This proves that if the equilibrium $\theta(s) = \pi$ has not bifurcated for a given $\lambda$, all tube rotations are elastically stable. This fact was formerly given by Ha et al. in [120].

## 4.5 Local Stability Analysis for $N$ Tubes

The local stability analysis of solutions for $n$ tubes is analogous to the procedure for two tubes. Just as for two tubes, the condition $\delta^2 E > 0$ is simplified to requiring all eigenvalues of the second

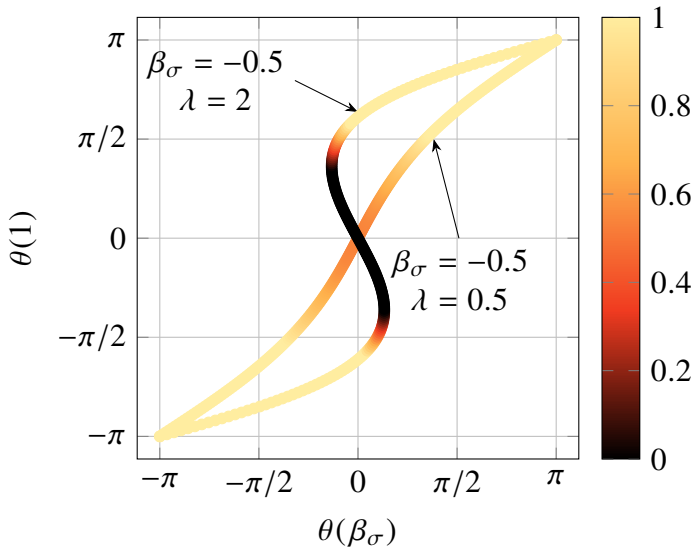


Figure 4.2: An S-Curve is shown for two different choices of parameters $\beta_\sigma$ and $\lambda$. The curve is colored based on the relative stability metric $h'(1)$, with the color axis truncated at 0 and 1.

variation operator $\boldsymbol{\mathcal{S}}$ to be positive. Fortunately, the eigenvectors of $\boldsymbol{\mathcal{S}}$ still form an orthonormal basis for the underlying space of allowable variations, but each eigenvector now consists of $n$ functions rather than a single function. The extension of the scalar Sturm-Liouville problem to a matrix Sturm-Liouville problem is considered in depth in [153].

It is a standard result in the calculus of variations that the generalization of the conjugate point test to $n$ unknown functions involves a condition on the determinant of the fundamental solution matrix of the Jacobi equations, which are the equations $\boldsymbol{\mathcal{S}}\boldsymbol{h} = 0$ [154]. As before, the result is usually only derived for Dirichlet boundary conditions. However, the modified test proposed by Manning [150] can be used for the $n$-unknowns case. A straightforward generalization of the argument in the proof of Result 1 for why the eigenvalues are positive on a small interval for the two-tube problem results in the conclusion that this also holds in the case of $n$ tubes. The following result provides the stability test for $n$ tubes at an arbitrary solution $\boldsymbol{\psi}(s)$ of Euler's equations.

**Result 2** (Stability of Solutions for $n$ Tubes)**.** *A solution $\boldsymbol{\psi}(s)$ to* (1.18)*, with boundary conditions*

(1.19), *is stable if the* $2N \times 2N$ *fundamental solution matrix* $\mathbf{H}$ *for the differential equations*

$$\mathbf{H}' = \Gamma\mathbf{H} \,,$$

$$\mathbf{H}(\beta) = \mathbf{I} \,,$$

*where the matrix*

$$\Gamma(s) = \begin{bmatrix} \mathbf{0} & \mathbf{F}^{-1}_{\psi'\psi'} \\ \mathbf{F}_{\psi\psi} & \mathbf{0} \end{bmatrix} \,,$$

*satisfies the condition* $\det \mathbf{H}_{22}(s) > 0$*, where* $\mathbf{H}_{22}$ *is the* $N \times N$ *lower-right sub-matrix of* $\mathbf{H}$*, for all* $s \in [\beta, L]$*. The matrices* $\mathbf{F}^{-1}_{\psi'\psi'}$*, and* $\mathbf{F}_{\psi\psi}$ *are defined element-wise, and as functions of arc length, as*

$$\mathbf{F}^{-1}_{\psi'\psi'}(i,j) = \begin{cases} k_{it}^{-1} & i = j \text{ and } s \in [\beta_i, \beta_i + L_i] \\ 0 & otherwise \end{cases}$$

$$\mathbf{F}_{\psi\psi}(i,j) = \begin{cases} 0 & s \notin [\beta_i, \beta_i + L_i] \cap [\beta_j, \beta_j + L_j] \\ F_{ii} & i = j \wedge s \in [\beta_i, \beta_i + L_i] \cap [\beta_j, \beta_j + L_j] \\ F_{ij} & i \neq j \wedge s \in [\beta_i, \beta_i + L_i] \cap [\beta_j, \beta_j + L_j] \end{cases}$$

*where*

$$F_{ii} = -\frac{\partial \boldsymbol{u}_B}{\partial \psi_i}^T \frac{\partial \mathbf{R}_{\psi_i}}{\partial \psi_i} \mathbf{K}_i \boldsymbol{u}_i^* - \boldsymbol{u}_B^T \frac{\partial^2 \mathbf{R}_{\psi_i}}{\partial \psi_i^2} \mathbf{K}_i \boldsymbol{u}_i^*$$

$$F_{ij} = -\frac{\partial \boldsymbol{u}_B}{\partial \psi_j}^T \frac{\partial \mathbf{R}_{\psi_i}}{\partial \psi_i} \mathbf{K}_i \boldsymbol{u}_i^*$$

See Appendix C.2 for a proof of this result.

**Corollary 3.** *The stability of a solution* $\boldsymbol{\psi}(s)$ *may also be determined by solution of the differential system of equations in Theorem 2 with initial condition* $\mathbf{H}(L) = \mathbf{I}$*, with the stability condition now replaced by* $\det \mathbf{H}_{11}(s) > 0$*.*

**Corollary 4.** *The value of* $\det \mathbf{H}_{22}(L)$ *in the result of Theorem 2, or the value of* $\det \mathbf{H}_{11}(\beta)$ *in the result of Corollary 3, may be used as a measure of relative stability when the solution is stable,*

Table 4.1: Data for Snapping and Bifurcation Experiments

| | Tube 1 | Tube 2 |
|---|---|---|
| Outer Dia. | 1.02 mm | 1.78 mm |
| Inner Dia. | 0.86 mm | 1.27 mm |
| Precurvature | 10.78 $m^{-1}$ | 9.96 $m^{-1}$ |
| Curved Length | 100 mm | 100 mm |

*where larger positive values indicate greater stability. Furthermore, the values* $\det \mathbf{H}_{22}(L)$ *and* $\det \mathbf{H}_{11}(\beta)$ *for the two tests are the same.*

A proof that the forwards and backwards methods provide the same indicator is included in Appendix C.3.

## 4.6 Experimental Validation

To validate the stability analysis, we performed experiments with two circularly precurved tubes. The tubes were designed so that they would snap or pass stably through the anti-aligned configuration depending on the choice of base location where the inner tube is grasped.

### 4.6.1 Materials & Methods

The physical data for the two tubes used are shown in Table 4.1. The experimental setup is shown in Figure 4.3. The outer tube is grasped and held fixed at the front plate of the actuation unit, while the inner tube is grasped at a varied distances proximal to this point. For each transmission length tested, one of four straight, rigid tubes may be added to the front of the robot which physically straightens the tubes over that length. It can be shown that the model predicts that this situation is equivalent to the tubes simply not having any precurvature over the length where the sheath is present, thus allowing us to test model predictions which vary over both dimensionless parameters $\lambda$ and $\beta_{eq,\sigma}$ with a single set of tubes.

The lengths of the sheaths, denoted by $L_{sheath}$, were 0, 10, 20, 30, and 40 mm, and the grasp locations for tube 1, denoted by $\beta_*$, were -23, -30, -40, -50, -60, -70, -80, -90, and -100 mm. Since

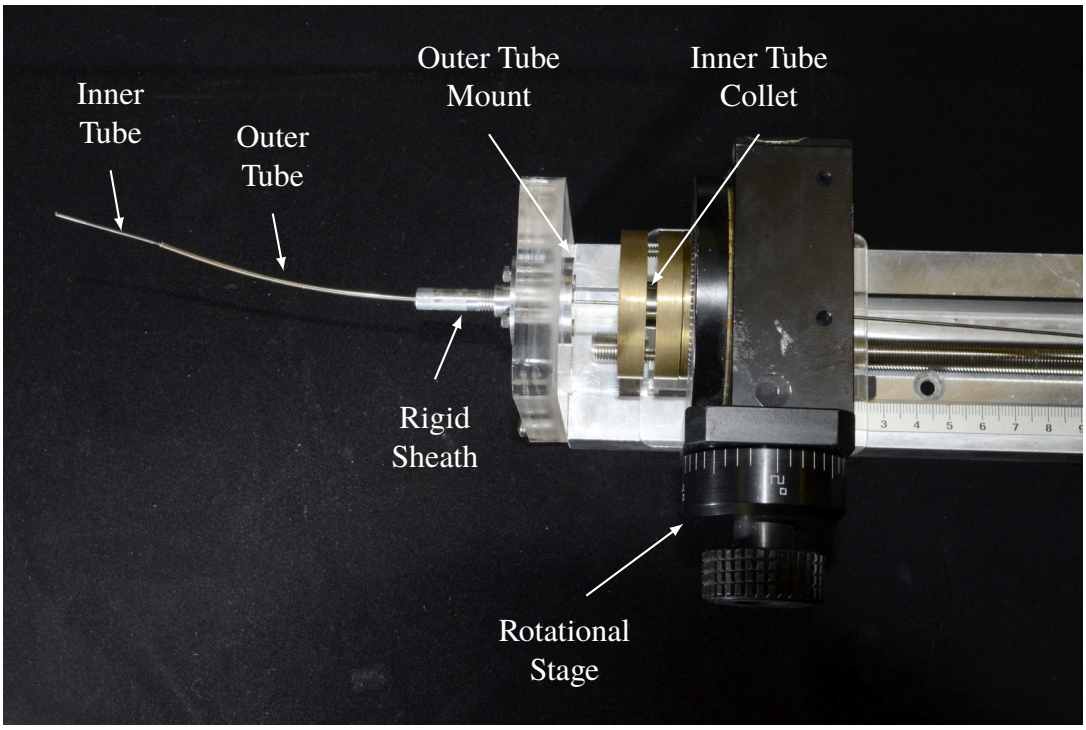


Figure 4.3: The experimental setup for the elastic stability experiments.

the point $s = 0$ is defined at the most distal point on the sheath, the values of $\beta_1$ and $\beta_2$ are given by

$$\beta_1 = \beta_* - L_{sheath} \qquad \beta_2 = -L_{sheath}. \tag{4.11}$$

Let $L_c$ be the overlapped length given by $L_c = 100\,\text{mm} - L_{sheath}$. Then, $\lambda$ is calculated as $\lambda = L_c^2 u_{1x}^* u_{2x}^* (1 + \nu)$. For Poisson's ratio $\nu$ we assume a value of 0.33 as quoted by Nitinol manufacturers.

For each pair $L_{sheath}$ and $\beta_*$ which were tested, the tubes were first checked for a bifurcation. Bifurcation was determined by attaching a flag to the end of the inner tube and observing whether all tip rotations were achievable and stable through rotations of the base. If some tip rotations were not achievable, then the snap angle was determined by rotating the tubes through four snaps. First, the snap was approached by rotating the inner tube base counter-clockwise as viewed from behind. When a snap was visibly or audibly observed, the angle was recorded. Second, the inner tube was rotated clockwise through a snap at the same speed, and the angle recorded. The third and fourth

observations were made by repeating the two previous steps. All rotations through the snaps were performed at a speed of approximately 1 degree/s.

Denote the four recorded angles $\theta_{ccw,1}$, $\theta_{cw,1}$, $\theta_{ccw,2}$, and $\theta_{cw,2}$. Because of the symmetry in the graph of Figure 4.2, the snap angle (in radians) is given by $\pi$ plus half of the average distance between the snaps,

$$\theta_{snap} = \pi + \left| \frac{\theta_{cw,1} - \theta_{ccw,1} + \theta_{cw,2} - \theta_{ccw,2}}{4} \right| . \tag{4.12}$$

For each experimental trial, the conditions of Result 3 were solved via a bisection routine to find the relative tip angle at which the condition $\det \mathbf{H}_{11}(\beta) = 0$ is met. The modeled relative base angle corresponding to the tip angle is then used as the modeled snap angle prediction for comparison against $\theta_{snap}$.

### 4.6.2 Results & Discussion

The results of the experiment are shown in Figure 4.4, which assesses the accuracy of the model predictions for stability. The figure shows the error in the modeled snap angle as a function of the observed snap angle. All errors were less than 20 °, and the general trend is for the error to increase as the snap angle does.

Sources of error in these predictions include both unmodeled effects such as friction and nonlinear material behavior, and measurement errors in the tube design parameters such as the curved length and precurvature. In addition, there is a small amount of uncertainty (±1 mm) in the value of $\beta_*$ since these lengths were measured by hand.

The predictions of snap angle can be made significantly more accurate by altering the assumed ratio of bending stiffness to torsional stiffness. It was previously noted by Lock and Dupont that a value of $\nu = 0.6$ yielded a good fit for the experimentally measured torsional relationship between tip and base angles [155]. Although this value of Poisson's ratio is not physically realistic, the material behavior of Nitinol under bending and torsion is known to differ from traditional strength of materials formulas due to tension/compression asymmetry, and thus the simplification $k_{ib}/k_{it} =$

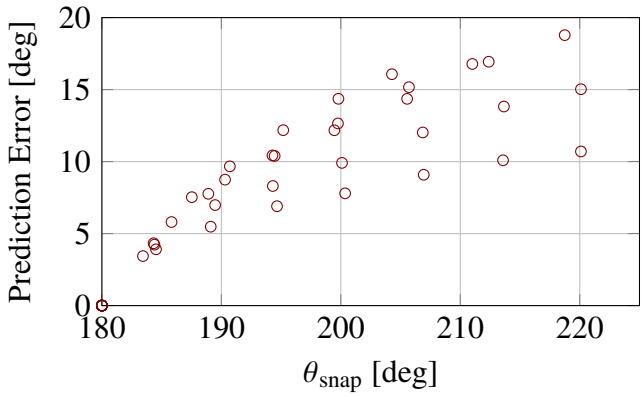


Figure 4.4: Graph of snap angle prediction error vs. the measured snap angle. Generally, as the snap angle increases the prediction becomes increasingly conservative. All model data predicts the snap at a lesser angle than was observed in practice.

$1 + \nu$ may not be valid even for small strains [156]. We used a nonlinear least-squares regression to fit the snap angle data and found a best fit of $k_{ib}/k_{it} = 1.605$, which resulted in a mean absolute prediction error of 2.06 °. This also corroborates the previous finding that $\nu \approx 0.6$. Although a more in-depth analysis of nonlinear material effects is outside the scope of this dissertation, it is possible that future work will be able to make better model predictions by taking into account the nonlinear elastic behavior of Nitinol.

## 4.7 Discussion

The preceding analysis reveals insights about the stability of concentric tube robots and enables new techniques for preventing snaps in high curvature robots. For example, the addition of a third tube may allow actuators to steer around instabilities. In addition, path planners and controllers can take advantage of the smooth relative stability metric to plan stable paths and to avoid instability during teleoperation.

The following example shows how the stability theory outlined above has ramifications for motion planners and controllers. Existing approaches for dealing with solution stability in motion planning methods have relied on the fact that the kinematic solutions are almost everywhere locally continuous with respect to the set of variables $\boldsymbol{q}_0 = \begin{bmatrix} \beta_1 & \dots & \beta_n & \alpha_1(\beta_1) & \dots & \alpha_n(\beta_n) \end{bmatrix}$. How-

ever, from the standpoint of the topology of the solutions, a much better choice for planning purposes is the distal angles $\alpha_1(L),...,\alpha_n(L)$, since this makes all components of the kinematic solution continuous with respect to the set of configuration variables $\boldsymbol{q}_L = \begin{bmatrix} \beta_1 & \dots & \beta_n & \alpha_1(L) & \dots & \alpha_n(L) \end{bmatrix}$. Then, the motion planning problem can be considered as finding continuous, admissible paths in both the physical space occupied by the robot and the configuration variable space.

Previously, without a test which could accurately determine the stability of an arbitrarily chosen configuration $\boldsymbol{q}_L$, sampling based planning methods could not guarantee that the resulting planned trajectory is everywhere elastically stable. Figure 4.5 shows for a three-tube robot how a continuous path in the distal angle space remains continuous in the proximal angles, but the shape of the trajectory becomes distorted when the relative stability metric approaches zero. If these distortions are allowed to become too large, then very small changes in the proximal relative angles of the tubes can result in large but stable angular displacements at the distal end. Near these points of ill-conditioning, modeling errors or unpredictable external loads may make it possible for the physical robot to snap.

One important consequence of the step from two tubes to three tubes is that the third tube can actually provide paths in actuation space for the tubes to make complete rotations with respect to one another without snapping, which would not be possible with only two tubes. This effect exists for designs that are beyond the bifurcation of the anti-aligned equilibria, but for which the regions of instability in the rotational actuation space have not yet connected. For circularly precurved tubes, we suspect the growth of instability from the bifurcating equilibria is a fundamental property regardless of the number of tubes, but we leave proof of this to future work. For complex, non-planar tube designs, there may not exist any equilibria, so it is less clear where instability will first arise; however, Result 2 still predicts the instability.

Note that the true rotational actuator space is of each angle modulo $2\pi$, so that the opposite edges of the graphs in Figure 4.6 are equivalent to one another. In the last plot of Figure 4.6, the connection between the unstable regions has prevented all paths which traverse complete relative rotations of any tube with respect to any other tube. In some cases such a full rotation is possible

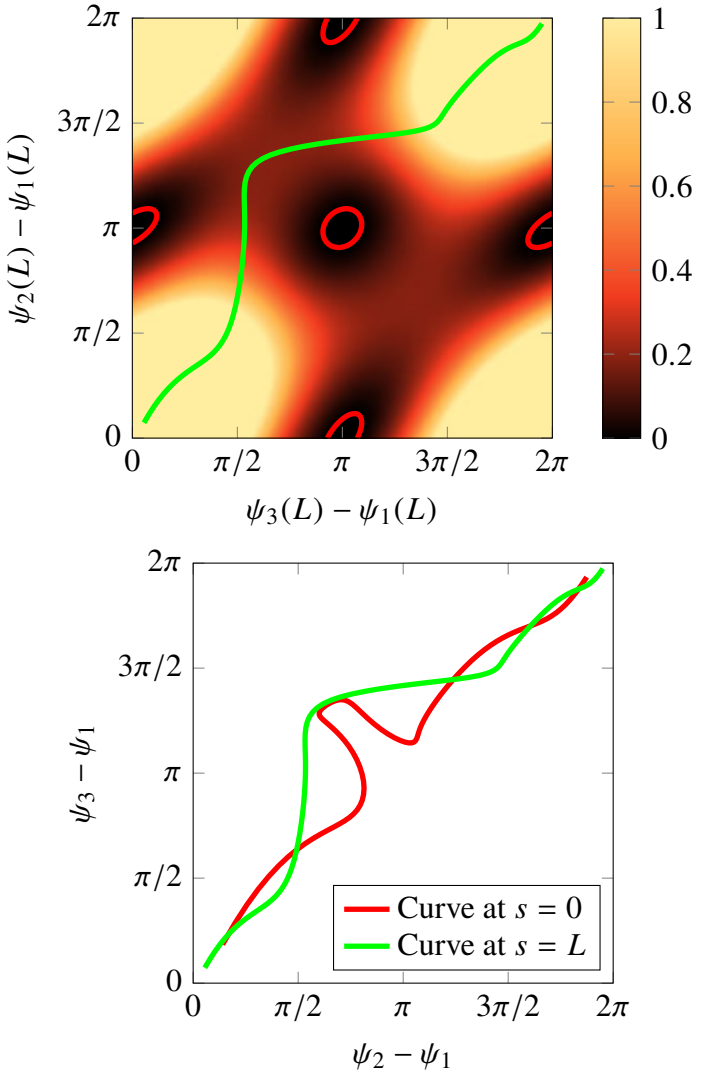


Figure 4.5: Here the stability metric $\det \mathbf{H}_{11}$ of Corollary 3 is shown on the left for a system of three tubes of equal stiffness and circular precurvature which subtend a total arc of 78.2 degrees in the undeformed state. Each tube is assumed to be actuated rotationally at $s = 0$, and is precurved over the entire length of the tube. If there were only two tubes, no continuous path would exist for the tubes to be rotated fully 360 degrees with respect to one another. With three tubes, however, a continuous path can be found which allows tubes 2 and 3 to be rotated 360 degrees with respect to tube 1. The green line drawn on the left chart shows a chosen stable path in the distal angle space, and the right chart shows how that path transforms to the proximal angles which are actuated. The amount of distortion in the curve is related to the stability measure, with lower stability measures indicating greater distortion.

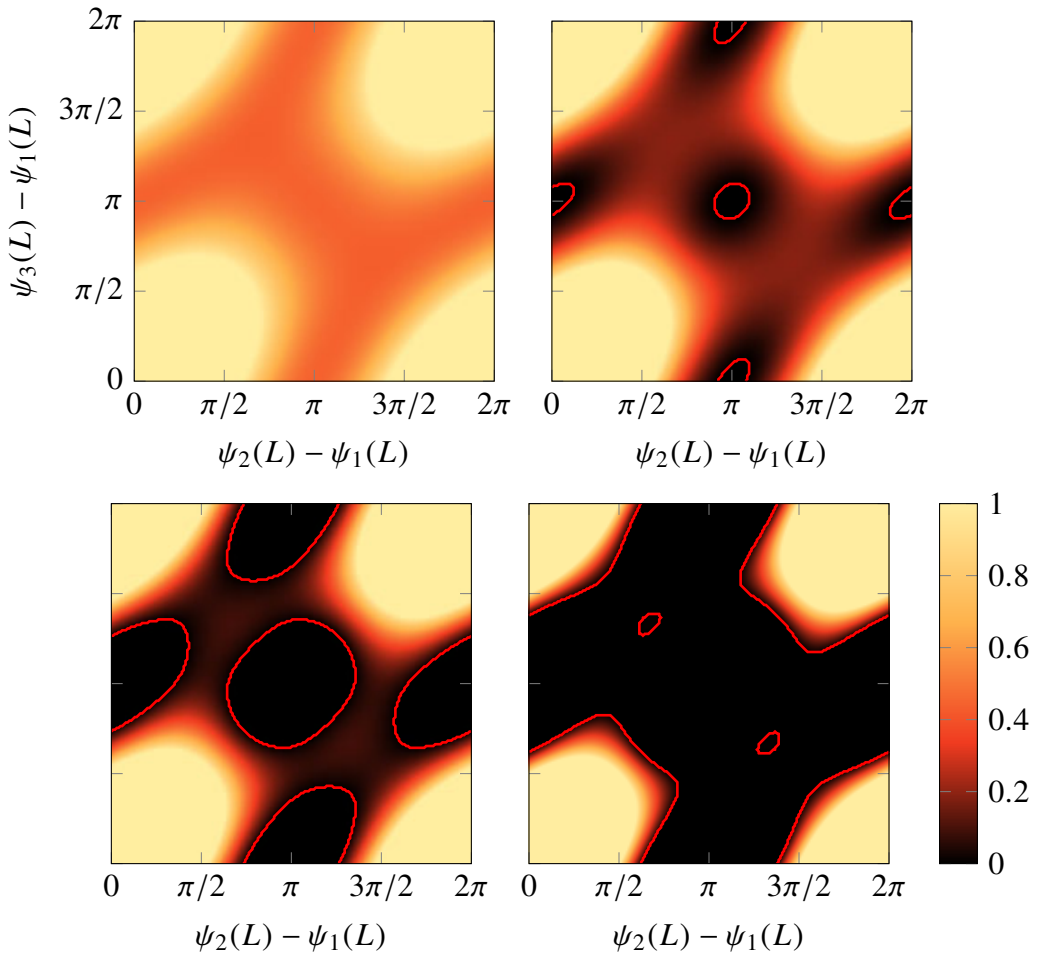


Figure 4.6: In these plots we show the effect of increasing component tube curvature on the relative stability metric. We simulated three fully overlapping tubes with zero transmission length and an overlapped length of 50 mm and equal curvature and stiffness. The curvatures, from left to right, are 21 $\mathrm{m}^{-1}$, 27.5 $\mathrm{m}^{-1}$, 31 $\mathrm{m}^{-1}$, and 36 $\mathrm{m}^{-1}$. As the curvature increases, the regions of instability grow from the bifurcated equilibria until they disconnect the stable equilibria. In the last figure it can be seen that very small contours surround the special case equilibria at $(2\pi/3, 4\pi/3)$ and $(4\pi/3, 2\pi/3)$, where the precurvatures are offset by 120°, which are remarkably still stable despite the entire area surrounding them being unstable.

between one pair of tubes but not another pair.

Resolved-rate style control methods can also take advantage of the stability metric for redundancy resolution or for a secondary weighted objective optimization. By computing or precomputing the gradient of the stability metric, $\nabla_{\boldsymbol{q}} \det(\mathbf{H}_{11}(\beta))$, resolved-rate methods can locally enforce a minimum stability measure to ensure that a sufficient distance is maintained from snapping configurations.

In terms of stability over the entire rotational actuation space, increasing transmission lengths and tube precurvatures tend to continuously destabilize the system. We show this effect by plotting the relative stability metric for every relative angle $\psi_i - \psi_1$ at the distal tip $L$. This space contains all possible configurations up to a rigid body rotation. Figure 4.6 shows how increases of the tube precurvature in a three tube robot cause instability to arise at the equilibria with curvatures anti-aligned, and the regions of instability eventually grow until the space of stable tip rotations becomes disconnected and traversing the full relative rotation of any tube can only occur through a snap.

## 4.8 Conclusions

In this chapter we have provided an analysis of bifurcation and elastic stability of unloaded concentric tube robots. The energy-based stability computation assigns a measure of stability to each configuration of the robot, which we believe will be useful for future work in control and motion planning. We have also connected existing frameworks from the mechanics literature on Euler beams to concentric tube robots.

One important future advancement to the stability theory will be the inclusion of externally applied loads, so that motion planning and control can incorporate stability information when the environmental interaction forces are large. Our result provide an approach to understanding concentric tube robot stability, and it is our hope that this work will facilitate the use of high curvature concentric tube robot designs that were previously avoided.

# Chapter 5

# Model Analysis: Follow-the-Leader Deployment

In this chapter, the mechanics-based kinematic model for concentric tube robots is used to predict the circumstances under which follow-the-leader insertion of a concentric tube robot is possible. With follow-the-leader deployment, where the body of the robot stays along the path traced by the tip as the robot elongates, concentric tube robots make an ideal needle with a pre-programmed shape. The contributions of this chapter are the model-based analysis and determination of the design and actuation conditions which allow perfect follow-the-leader deployment, as well as a new investigation of approximate follow-the-leader deployment in which the design and actuation requirements are relaxed. In particular, it is found that when the precurvatures are circular and the tubes are curved for as long as they are inserted, an appropriate choice of actuation will always allow the deployment to approximate follow-the-leader behavior. This material of this chapter was published as a regular paper in IEEE Transactions on Robotics [139].

## 5.1 Introduction

The desire to avoid critical structures and reach previously unreachable targets during needle biopsy and needle-delivered therapy has spurred the development of many kinds of steerable needles. Designs include bevel-tipped needles [30], needles with a pre-bent tip [31], needles that extend a curved stylet [33], and actively controlled needles [157], among others (for reviews, see [31, 32]). Early motivations for developing concentric tube continuum robots were (1) to generalize the steerability of steerable needles beyond soft tissues, to air or liquid filled cavities, and (2) to use this dexterity to create needle-diameter tentacle-like robot manipulators [55, 48]. A review of concentric tube robot history and applications can be found in [114]. While a great deal of the recent research in concentric tube robots has focused on the latter of these two motivations (see e.g. [14, 11]), efforts have also been made to address the former through motion planning (choos-

ing actuator sequences to keep the shaft of the robot within anatomical bounds during deployment [63]), and in using a special case with one curved tube and two straight tubes to hit targets in soft tissues (see e.g. [19] and many references in [114] including commercial products dating back to the 1980s).

This special case is useful because it can be deployed in a perfect follow-the-leader manner, wherein the shaft of the device exactly follows the path through space traced out by the tip at all times during insertion. The term "follow the leader" for deployment of a highly articulated robot was coined by Choset and Henning in 1999 [158], and Ikuta et al. proposed it for endoscope deployment in 1988 under the name "shift control" [127]. It has also been used advantageously in other highly articulated robots (see e.g. [159]). The term "follow the leader" was perhaps first applied to concentric tube robots in 2006 by Sears and Dupont [26], who provided design heuristics which enable approximate follow-the-leader behavior and showed that under the assumption of infinite torsional rigidity, general collections of tubes are able to deploy in a follow-the-leader manner.

It was later observed that torsion is typically significant in these robots in practice and that torsional deformation precludes follow-the-leader deployment, even for constant precurvature tubes. Models were subsequently developed that include the effects of torsion [47, 55, 36, 48]. These models were applied to the use of concentric tube robots as manipulators in many contexts. They have also been used to produce design heuristics [48] and motion planners [63] for approximate follow-the-leader deployment. But, the analysis of follow-the-leader behavior in concentric tube robots has not been revisited in light of them.

In soft tissues, a benefit of using concentric tube robots in comparison to other steerable needle technologies is that concentric tube robots rely on internal forces rather than tip-tissue forces to bend. This makes them able to steer through open or liquid-filled cavities, and through soft tissue with minimal deflection of the needle based on needle-tissue interaction forces. In contrast, the properties of bevel-steered needles (shaft stiffness, tip design, etc.) must be matched exactly to tissue properties to achieve appreciable curvature, and coping with the sensitivity of the needle's

behavior to small changes in tissue properties is one of the major current challenges in needle steering research (see [31] and references therein). Thus, both deployment through open cavities and reducing sensitivity to tissue properties during deployment through soft tissues motivate the question we seek to answer: Can concentric tube robots deploy in a follow-the-leader manner?

In what follows, exact solutions to the follow-the-leader deployment problem are described, and the model-predicted deviation from follow-the-leader behavior in approximate cases is analyzed. The primary contributions are the development of necessary and sufficient conditions for follow-the-leader behavior, the special case precurvatures we describe (including helical shapes not previously considered), a metric for measuring the similarity of a general deployment to a follow-the-leader deployment, and our neurosurgical illustration.

## 5.2 Follow-The-Leader Behavior

Before exploring special cases and approximations of follow-the-leader behavior, it is useful to have a mathematical description for follow-the-leader deployment of the robot. We proceed in this section by describing the follow-the-leader constraint on the space curve which describes the robot shape. The following sections will then connect this constraint to the mechanics model, which will reveal the resulting restrictions on both robot design and actuation sequences. We describe the shape of the robot using a time-varying, arc-length parameterized transformation $\mathbf{g}(s,t) \in SE(3)$, which assigns a position $\boldsymbol{p}(s,t) \in \mathbb{R}^3$ and orientation $\mathbf{R}(s,t) \in SO(3)$ to each arc length $s \in [0, L(t)]$ along the centerline of the tubes. The domain of $s$ depends on $t$, but the parameters $s$ and $t$ are independent of one another, and wherever mixed partial derivatives with respect to $s$ and $t$ occur, we assume their symmetry. We assign our frames such that the columns of the matrix $\mathbf{R}$ can be considered to be $\begin{bmatrix} \boldsymbol{x}(s,t) & \boldsymbol{y}(s,t) & \boldsymbol{z}(s,t) \end{bmatrix}$. The function $L(t)$ represents the exposed length of the robot, which increases during a deployment, and hence is a function of time. The differential kinematic equations describing the evolution of the transformation are given as $\mathbf{g}'(s,t) = \mathbf{g}(s,t)\widehat{\boldsymbol{\xi}}(s,t)$, where $\boldsymbol{\xi} \in \mathbb{R}^6$ contains the body frame twist coordinates $\boldsymbol{\xi}(s,t) = \begin{bmatrix} \boldsymbol{v}^T & \boldsymbol{u}(s,t)^T \end{bmatrix}^T$ and the prime denotes the partial derivative $\partial/\partial s$. The $\widehat{\cdot}$ operator converts a vector

in $\mathbb{R}^6$ to an element of the Lie algebra $\mathfrak{se}(3)$. The vector $\boldsymbol{u}$ may be thought of as the curvature or "angular velocity" (with respect to arc length) of the frame, and $\boldsymbol{v}$ as the "linear velocity" (with respect to arc length) of the frame $\mathbf{g}$. We assume that the $z$ axis of $\mathbf{R}$ is tangent to the curve, and the transformation propagates with unit velocity along the $z$-axis, meaning that $\boldsymbol{v} = \begin{bmatrix} 0 & 0 & 1 \end{bmatrix}^T$. Equivalently, the components of the transformation $\boldsymbol{g}$ can be expressed as

$$\mathbf{R}'(s,t) = \mathbf{R}(s,t)\widehat{\boldsymbol{u}}(s,t) \tag{5.1}$$

$$\boldsymbol{p}'(s,t) = \boldsymbol{z}(s,t) \tag{5.2}$$

where we also assume initial conditions $\mathbf{R}(0,t) = \mathbf{R}_z(\psi_0(t))$ (a rotation about the $z$-axis by angle $\psi_0$), and $\boldsymbol{p}(0,t) = \mathbf{0}$. These initial conditions model the physical robot, where a position and tangent vector are prescribed at one point of the robot centerline. The operation $\widehat{\cdot}$ is the isomorphism between a vector in $\mathbb{R}^3$ and its skew-symmetric cross product matrix.

For follow-the-leader deployment, we require that the position at any arc length does not change in time, or mathematically that

$$\dot{\boldsymbol{p}}(s,t) = \frac{\partial \boldsymbol{p}(s,t)}{\partial t} = 0 \, . \tag{5.3}$$

The overdot will continue to denote the partial derivative with respect to time. Intuitively the above assumptions result in a constraint on the curvature $\boldsymbol{u}(s,t)$. Since the space curve cannot change except to telescopically extend, the curvature function $\boldsymbol{u}(s,t)$ must not physically change except to allow growth in the domain of s. More precisely, we will prove that the follow-the-leader criterion of (5.3) is equivalent to the following: for the angular displacement function $\psi(s,t)$ which satisfies $\psi' = u_z$ and $\psi(0,t) = \psi_0(t)$, the projections of the curvature vector $u_x(s,t) = \boldsymbol{e}_1 \cdot \boldsymbol{u}(s,t)$ and $u_y(s,t) = \boldsymbol{e}_2 \cdot \boldsymbol{u}(s,t)$, with $\boldsymbol{e}_i$ the $i^{\text{th}}$ standard basis vector, satisfy

$$\frac{\partial}{\partial t}\begin{bmatrix} u_x(s,t) \\ u_y(s,t) \end{bmatrix} = \begin{bmatrix} 0 & \dot{\psi}(s,t) \\ -\dot{\psi}(s,t) & 0 \end{bmatrix}\begin{bmatrix} u_x(s,t) \\ u_y(s,t) \end{bmatrix} . \tag{5.4}$$

First, we show that (5.3) $\Longrightarrow$ (5.4). From (5.2) and (5.3), we can use the fundamental theorem of calculus and the commutativity of the partial derivatives to yield

$$\frac{\partial \boldsymbol{p}}{\partial t}(s,t) = \int_0^s \frac{\partial}{\partial s}\frac{\partial \boldsymbol{p}}{\partial t}(\sigma,t)\, d\sigma = \int_0^s \frac{\partial \boldsymbol{z}}{\partial t}(\sigma,t)\, d\sigma = 0, \tag{5.5}$$

which holds for all values of $s$ if and only if

$$\frac{\partial \boldsymbol{z}}{\partial t}(s,t) = 0\ . \tag{5.6}$$

This equation holds if and only if the time variation of $\mathbf{R}$ has the form

$$\frac{\partial \mathbf{R}}{\partial t}(s,t) = \mathbf{R}\,(\omega(s,t)\boldsymbol{e}_3)^\wedge\ , \tag{5.7}$$

where $\omega(s,t)$ is the scalar angular velocity function which is unknown except at $s = 0$, where $\omega(0,t) = \dot{\psi}(0,t)$.

Equating the mixed partial derivatives of $\mathbf{R}$ by taking the partial derivative of (5.7) with respect to $s$ and the partial derivative of (5.1) with respect to $t$ yields

$$\frac{\partial \mathbf{R}}{\partial t}\widehat{\boldsymbol{u}} + \mathbf{R}\left(\frac{\partial \boldsymbol{u}}{\partial t}\right)^\wedge = \frac{\partial \mathbf{R}}{\partial s}\,(\omega \boldsymbol{e}_3)^\wedge + \mathbf{R}\left(\frac{\partial \omega}{\partial s}\boldsymbol{e}_3\right)^\wedge\ . \tag{5.8}$$

Substituting again from (5.1) and (5.7), premultiplying by $\mathbf{R}^T$, applying the identity $(\boldsymbol{a}\times\boldsymbol{b})^\wedge = \widehat{\boldsymbol{a}}\widehat{\boldsymbol{b}} - \widehat{\boldsymbol{b}}\widehat{\boldsymbol{a}}$, and taking the inverse of the $\widehat{\cdot}$ operator on the entire equation yield that (5.8) is equivalent to the conditions

$$\frac{\partial \boldsymbol{u}}{\partial t} = -\omega \boldsymbol{e}_3 \times \boldsymbol{u} + \frac{\partial \omega}{\partial s}\boldsymbol{e}_3 \tag{5.9}$$

The third vector component of this equation is $\omega' = \dot{u}_z$, and from the definition of $\psi(s,t)$ we thus have $\omega' = \dot{\psi}'(s,t)$. The initial condition for $\mathbf{R}$ implies that $\omega(0,t) = \dot{\psi}(0,t)$, so that we can identify $\omega(s,t) = \dot{\psi}(s,t)$. Then, the first two vector components of (5.9) are given by (5.4), and the first part of the proof is complete.

We now show that (5.4) $\implies$ (5.3). We start with only (5.1), (5.2), (5.4), and the existence of the function $\psi' = u_z$. We now seek the time variation of $\mathbf{R}$, which is given by

$$\frac{\partial \mathbf{R}}{\partial t}(s,t) = \mathbf{R}(s,t)\widehat{\boldsymbol{\omega}}(s,t) \tag{5.10}$$

for an unknown vector function $\boldsymbol{\omega}(s,t)$. By again equating the mixed partial derivatives and making the necessary substitutions, we find a differential equation

$$\frac{\partial \boldsymbol{\omega}}{\partial s} = \boldsymbol{\omega} \times \boldsymbol{u} + \begin{bmatrix} \dot{\psi} u_y & -\dot{\psi} u_x & \dfrac{\partial^2 \psi}{\partial t \partial s} \end{bmatrix}^T . \tag{5.11}$$

By the initial condition $\mathbf{R}(0,t) = \mathbf{R}_z(\psi_0(t))$, we have the initial condition $\boldsymbol{\omega}(0,t) = \dot{\psi}(0,t)\boldsymbol{e}_3$. Therefore,

$$\boldsymbol{\omega}(s,t) = \frac{\partial \psi}{\partial t}(s,t)\boldsymbol{e}_3 \tag{5.12}$$

is the unique solution to this differential equation, which in turn implies that $\dot{\boldsymbol{z}}(s,t) = 0$, which is equivalent to the follow-the-leader condition of (5.3). Thus, (5.4) is a necessary and sufficient condition for follow-the-leader behavior. In the next section this equation is connected to a mechanics-based model for concentric tube robots. The curvature vector $\boldsymbol{u}$ from the previous section can be computed with a mechanics model for the robot. For this analysis a formulation of the model in terms of Frenet-Serret frames rather than Bishop frames is convenient, so the relevant equations from the literature are reviewed in this section [55, 48, 59]. Each component tube of the robot is grasped at its proximal end where translation and rotation are applied. We denote with $\beta_i(t)$ the positive length between the point where $s = 0$ and the point where $\sigma_i = 0$ for the $i^{th}$ tube, which is where an actuator will grasp the tube, and with $\alpha_i(t)$ the rotational actuation (see Figure 5.1). Let the variables $\psi_i(s,t)$ be the angular rotations of each tube, which may be thought of as the angular displacement about the local $z$-axis between the material frame and the zero-torsion or rotation-minimizing Bishop frame. The curvature $\boldsymbol{u}_i = \begin{bmatrix} u_{ix} & u_{iy} & u_{iz} \end{bmatrix}^T$ of each tube is written in the material frame of the respective tube. Here $i \in 1,...,N$ denotes the tube number with tube 1

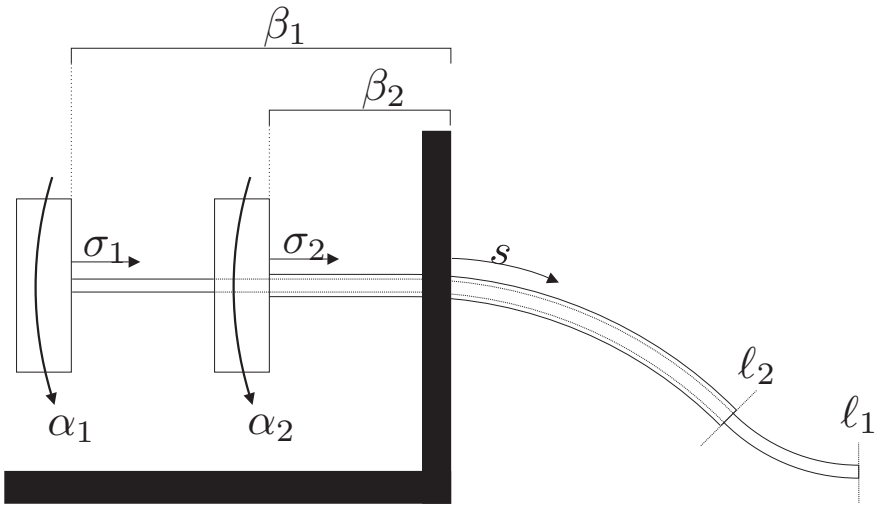


Figure 5.1: The tubes are grasped at their respective proximal ends, and the actuation variables $\alpha_i$ and $\beta_i$ denote the proximal base rotation and translation, respectively. The length $\ell_i$ is the length of each tube which is extended, as measured from the point $s = 0$ to the end of the tube.

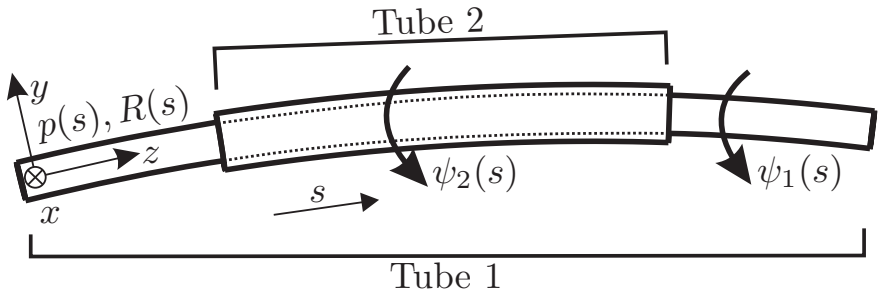


Figure 5.2: A diagram of a section of two concentric tubes showing relevant variables. The position and orientation are those of the innermost tube (tube 1), while each tube has its own angular displacement $\psi$. The tubes as illustrated here have a slight positive curvature about the $x$ axis.

being the tube with the smallest diameter. The precurved shape of each tube is expressed in the Frenet-Serret convention as $\boldsymbol{u}_i^*(\sigma_i) = \begin{bmatrix} u_{ix}^*(\sigma_i) & 0 & u_{iz}^*(\sigma_i) \end{bmatrix}^T$, where we will refer to $u_{ix}^*$ as the curvature and $u_{iz}^*$ as the torsion of the frame. We use $\sigma_i$ for arc length here to clarify that this length is measured with respect to a fixed point on the tube, not with respect to the fixed point in space where $s = 0$.

A diagram of the variables of interest is shown in Figure 5.2. From this point forward, as in the previous section, for notational brevity, the explicit dependence on both $s$ and $t$ will be suppressed except where not clear from context. The multi-point boundary value problem for a concentric

tube robot with no applied external loads is given in [59] as:

$$\begin{aligned}
\psi_i' &= u_{iz} \\
u_{iz}' &= u_{iz}'^{*}(s+\beta_i) + \\
&\quad \frac{1}{EI}\frac{E_i I_i}{G_i J_i}\sum_{k=1}^{N} E_k I_k u_{ix}^{*}(s+\beta_i) u_{kx}^{*}(s+\beta_k)\sin(\psi_i - \psi_k)
\end{aligned} \tag{5.13}$$

for $i = 1,...,N$, with boundary conditions

$$\begin{aligned}
\psi_i(0,t) &= \psi_{i0}(t) \qquad\qquad i = 1,...,N \\
u_{iz}(\ell_i,t) &= u_{iz}^{*}(\ell_i + \beta_i) \qquad i = 1,...,N.
\end{aligned} \tag{5.14}$$

The functions $u_{iz}$ are related to the torsional moments in equation (1.18b) through $m_{iz} = k_{it}(u_{iz}' - u_{iz}'^{*})$. The precurvature functions $u_{ix}^{*}$ and $u_{iz}'^{*}$ are evaluated at an arc length offset by the time-varying values $\beta_i(t)$, which accounts for possible translations of the tubes. Here $\psi_{i0}(t)$ specifies the initial z-axis rotation of tube $i$, which is produced by controlling an actuator $\alpha_i$ at some proximal location $\beta_i$, and the latter boundary conditions on $u_{iz}$ result from the fact that each tube must have zero torsional internal moment at its endpoint $s = \ell_i$ (i.e. the sum $\ell_i + \beta_i$ is constant). The values of $\psi_{i0}(t)$ are related to the rotational actuation variables $\alpha_i(t)$ through $\psi_{i0}(t) = \alpha_i(t) - \beta_i(t)u_{iz}(0,t)$. The term $EI$ is the sum over all the stiffnesses, $EI = \sum_{k=1}^{N} E_k I_k$. It is important to recognize that the sum is performed only over those tubes which exist at the arc length being evaluated, and that the equations are only valid for tube $i$ over the length that it exists.

The boundary value problem determines the tube torsion, but the local $\boldsymbol{xy}$-curvature is found in closed form as a weighted sum of the precurvatures rotated into the frame of tube 1,

$$\boldsymbol{u}_{xy}(s,t) = \frac{1}{EI}\sum_{j=1}^{N} E_j I_j \begin{bmatrix} \cos(\psi_j - \psi_1) \\ \sin(\psi_j - \psi_1) \end{bmatrix} u_{jx}^{*}(s+\beta_j), \tag{5.15}$$

where again the arguments to the functions $\psi_i(s,t)$ have been omitted for space. It is this frame which we define to be the central axis frame (i.e. the "backbone frame") of the robot. Thus, the

final robot curve is found by integrating (5.1) and (5.2) for the variables of tube 1.

The model equations also predict phenomena of elastic instability which are seen in concentric tube robots [48, 36, 148]. Note that the results in this chapter only apply to stable configurations. This means that, for example, two circularly precurved tubes which have a bifurcation cannot be rotated so that their curvatures exactly oppose one another. The results of chapter 4 can be used to determine whether a particular solution during an actuation sequence is stable. It should be emphasized that presence of multiple solutions does not imply elastic instability, and thus designs which have a bifurcation may be utilized in some approximate follow-the-leader cases if the user ensures the actuation does not give rise to elastic instability.

## 5.3 Special Cases of Follow-The-Leader Deployment

To determine conditions for concentric tube follow-the-leader deployment, first note that the definition of $\psi_1'(s,t)$ in (5.13) allows $\boldsymbol{u}_{xy}$ and $\dot{\psi}_1$ to be substituted into the follow-the-leader condition of (5.4). Performing this substitution and making simplifications, two constraint equations emerge:

$$\begin{aligned}\sum_{j=1}^{N} E_j I_j \left[\cos(\psi_j - \psi_1) u_{jx}^* \dot{\psi}_j + \sin(\psi_j - \psi_1) u_{jx}'^* \dot{\beta}_j\right] &= 0 \\ \sum_{j=1}^{N} E_j I_j \left[\sin(\psi_j - \psi_1) u_{jx}^* \dot{\psi}_j - \cos(\psi_j - \psi_1) u_{jx}'^* \dot{\beta}_j\right] &= 0.\end{aligned} \tag{5.16}$$

These two differential equations, if satisfied, guarantee that an $N$-tube robot follows the leader. Note that all of the rotational configuration functions $\psi_i$ appear in these conditions, as well as their time derivatives. The precurvature functions also appear, and due to actuation their derivatives with respect to $s$ also appear. Note that they are evaluated at $s + \beta_j$. For a follow-the-leader insertion, the differential equations (5.16) must be consistent with the mechanics of the robot (5.13).

### 5.3.1 Two-Tube Case with Planar Constant Precurvatures

One prototype design which is appealingly simple is that of two tubes which have precurvatures that are constant in arc length and planar (i.e. precurvatures that are circular arcs). Since the tubes have constant precurvature, $u_{jx}'^{*} = 0$. The constraints (5.16) simplify to

$$\begin{aligned} E_1 I_1 u_{1x}^{*} \dot{\psi}_1 + E_2 I_2 \cos(\psi_2 - \psi_1) u_{2x}^{*} \dot{\psi}_2 = 0 \\ E_2 I_2 \sin(\psi_2 - \psi_1) u_{2x}^{*} \dot{\psi}_2 = 0. \end{aligned} \tag{5.17}$$

All of the variables which appear in these equations are determined by actuation and the mechanics, so we seek the ways in which these equations can be satisfied through choice of precurvature and/or actuation. We first show that if both precurvatures are nonzero, then (5.17) implies that $\psi_2 - \psi_1 = n\pi$. To see this fact, first assume that $\psi_2 - \psi_1 \neq n\pi$. Then the two equations of (5.17) imply that follow-the-leader deployment requires $\dot{\psi}_1 = \dot{\psi}_2 = 0$. However, we will show that this cannot happen due to the torsional mechanics. The robot is deploying and increasing in total arc length, so the arc length $\ell_i$ at which the distal boundary condition in (5.14) is evaluated is an increasing function of time $\ell_i(t)$. The total derivative of the distal boundary condition for each tube in (5.14) must be equal to zero by definition, and this is expressed mathematically by

$$\frac{\partial u_{iz}}{\partial s}(\ell_i(t),t)\frac{d\ell_i}{dt}(t) + \frac{\partial u_{iz}}{\partial t}(\ell_i(t),t) = 0. \tag{5.18}$$

During a deployment, $d\ell_i/dt$ is positive, and from (5.13) we have that $\partial u_{iz}/\partial s$ is nonzero as long as both precurvatures are nonzero and $\psi_2 - \psi_1 \neq n\pi$. Then, the second term in (5.18) must also be nonzero. This implies by (5.13) that $\partial u_{iz}/\partial t = \dot{\psi}_i' \neq 0$ and therefore $\dot{\psi}_i$ cannot be zero everywhere. Thus, (5.17) is satisfied only if $\psi_2 - \psi_1 = n\pi$. In this case, (5.13) indicates that the tubes experience no torsional twisting and thus with no applied rotational actuation we have $\dot{\psi}_1(s,t) = \dot{\psi}_2(s,t) = 0$, which trivially satisfies (5.17) and ensures follow-the-leader deployment.

There are also two special cases in which (5.17) can hold. If one of the tubes has zero precur-

vature, then follow-the-leader behavior is guaranteed by simply ensuring no rotational actuation of the other, precurved tube. Additionally, if $E_1 I_1 u_{1x}^* = E_2 I_2 u_{2x}^*$ and the tube rotations are chosen so that $\psi_2 - \psi_1 = n\pi$ with $n$ odd, then the two fully overlapped tubes can be rotated with equal angular velocity $\dot{\psi}_1 = \dot{\psi}_2$.

### 5.3.2 Helical Precurvatures

If either of the precurved shapes is a helix, then by the arguments in the previous subsection, $\psi_2 - \psi_1$ will not equal $n\pi$ at all arc lengths unless additionally both tubes have the same helical torsion $u_z^*$. If they did not, $\psi_1'(L) = u_{1z}^*(L) \neq u_{2z}^*(L) = \psi_2'(L)$, which implies that $\psi_2(s,t) - \psi_1(s,t)$ is not constant with respect to arc length. Equal torsion in the Frenet-Serret sense is therefore a necessary condition for follow-the-leader deployment of two helical tubes.

### 5.3.3 Stability of Solutions

The odd and even solutions for $n$ in the previous two subsections represent different solutions. The odd solutions are only stable in a robot that does not have bifurcations (see Chapter 4, [47, 36], or [48] for further information on bifurcations) in the boundary value problem of (5.13). As the system approaches a critical overlapped length during an actuation, the odd solutions become progressively "less stable" and so any designer wanting to leverage the odd solutions in a device designed to follow the leader would likely want to maintain some margin of safety below this critical value, and the inclusion of straight transmission segments in the tubes will require a design with lower curvature than one without transmission segments.

### 5.3.4 Required Deployment Sequences

In cases of follow the leader insertion, the deployment procedure for two tubes of constant curvature proceeds in two stages. The first stage is the insertion of both tubes together (fully overlapping). The second, optional, stage is the continued insertion of one tube only while holding

the other fixed. These tubes will be called the "moving" and "fixed" tubes respectively for this stage of insertion. Since the moving tube has a constant curvature design, the interaction of the two tubes will remain unchanged as long as the actuation satisfies the requirement that $\psi_i(0,t)$ is constant in time. If the moving tube has any precurved torsion, an actuator will have to rotate the tube base, which is at negative arc length, to maintain a constant angle at $s = 0$. If the fixed tube is moved at all after the moving tube has been extended, then the condition $u_{ix}^{\prime *} = 0$ has been violated at the discontinuity where the fixed tube ends, and the simplifications from (5.16) to (5.17) are no longer valid. Thus, the follow-the-leader behavior will cease in this case, and the shaft of the robot will deviate from the path traced previously by its tip. For the same reason, a step change in the curvature of a tube (e.g. a tube with an initial straight transmission followed by a circularly precurved tip section) will not be able to deploy in a follow the leader manner if the change in curvature occurs in the length from $s = 0$ to $s = L$.

### 5.3.5 Summary of Follow-The-Leader Cases

Based on the discussions in preceding sections, we can now describe some potentially useful cases where follow-the-leader behavior is possible for two tubes:

1. $\mathbf{u}_{\mathbf{2x}}^* = \mathbf{0}$ or $\mathbf{u}_{\mathbf{1x}}^* = \mathbf{0}$. In this case one but not both of the tubes has zero precurvature, meaning that the final shape consists of two tangent circular or helical arcs with different curvatures. This case was identified and elaborated upon previously for circular tubes in [80].

2. $\mathbf{u}_{\mathbf{1z}}^* = \mathbf{u}_{\mathbf{2z}}^* = \mathbf{0}$. Both tubes are circular in precurvature and we ensure that $\psi_2 - \psi_1 = n\pi$. The final shape consists of two circular arcs (which may have different radii based on tube stiffnesses and precurvatures) that lie in the same plane, and are tangent to one another. For even $n$, these two arcs will curve in the same direction, while for odd $n$, they may curve in opposite directions in the plane, depending on the choice of tube stiffnesses and precurvatures.

3. $\mathbf{u}^*_{\mathbf{1z}} = \mathbf{u}^*_{\mathbf{2z}} \neq \mathbf{0}$. Both tubes are helical in shape with the same helical torsion, but not necessarily the same curvature. The interaction results in a piecewise helical final shape as long as $\psi_2 - \psi_1 = n\pi$, where again the even and odd solutions are different. The even solutions will always contain two helical segments which curve in the same direction and have equal torsion. The segments of the odd solutions may curve in the same or opposite directions.

In agreement with previous results mentioned in the introduction, the follow-the-leader solutions are the ones which have no internal material torsion. This fact is evident from (5.13) since $\sin(\psi_i - \psi_k) = 0$ and therefore $u_{iz} = u^*_{iz}$ along the whole length of each tube. Note that the precurvature must be constant for all $s > 0$, which means that before insertion this precurved segment of the tube must lie at an arc length less than zero. This requirement imposes some restrictions on the actuation mechanism, since it must either be able to accommodate the load of straightening the tube in between $s = 0$ and $s = -\beta_i$, or there must be some straight length of tube at the proximal end so that the precurved portion can be retracted into a rigid sleeve.

### 5.3.6 The Space of Curves Enabled by Helical Precurvatures

The case of two helically precurved tubes provides a large family of overall device curves to the robot designer, even though there are only two tubes. For a visual aid, two final shapes for a single tube set are shown in Figure 5.3b. Parameters that can be selected include the handedness of the helices (whether $u^*_z$ is positive or negative), the curvature of each tube, the overlapped insertion arc length, the non-overlapped insertion length of one tube extending beyond the overlapped section, and a rigid rotation of the entire final shape. In a practical application involving insertion through a winding lumen or through soft tissue (as discussed in the Introduction), one could envision having many helical tubes pre-made, and allowing a planning algorithm to select the best pair of tubes, based on the target location and any relevant obstacles and tissue boundaries. A useful fact is that the solutions are easy to compute because the torsional mechanics do not need to be solved and the kinematics can be solved in closed form [47].

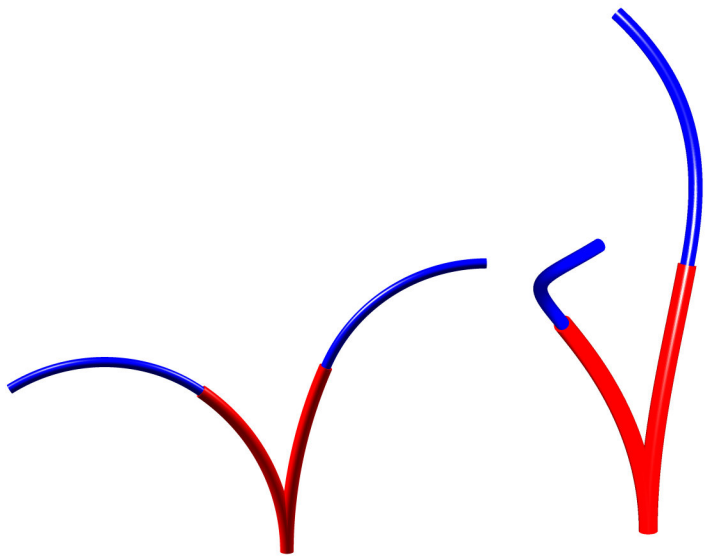

(a) Circular Tubes (b) Helical Tubes

Figure 5.3: (a) Two circular tubes are shown. These tubes have an overall insertion length of 12 cm, with an overlapped tube length of 6 cm. The left solution has the tubes aligned, while the right solution has the inner tube rotated the opposite direction. (b) The same tube curvatures are used, but both tubes are given the same pre-curved torsion, resulting in two helical tubes. All of these configurations can be reached in a perfect follow-the-leader manner.

## 5.4 Follow The Leader With General Tube Sets

In the general case where we cannot simplify the constraints further than (5.16), it is less clear for which special cases of precurvature follow-the-leader deployment will be possible. Certainly, any set of circularly precurved tubes could follow the leader if the angle between every combination of two tubes is $n\pi$ for any integer $n$. This assumes that the insertion length is sufficiently short and the tubes have low enough curvatures that the boundary value problem associated with (5.13) and (5.14) has not undergone a bifurcation, since this would cause the solutions with odd $n$ to be unstable and not achievable in the physical system. The solution would be planar and could have changes in the direction of the curvature. By a similar argument, three helices with equal torsion could also follow the leader.

It is possible that other special case functions exist for which the constraints in (5.16) can be consistent with the torsional mechanics in (5.13) for more general solutions of $\psi$ and more general, non-constant choices of precurvature. Identifying them (if they exist), and determining whether they are potentially useful in various applications remain open research questions. As with the special case solutions we have described, any new solutions will involve both specific precurvatures and specific deployment sequences, because the torsional mechanics are completely defined (i.e. the time derivatives of all $\psi_i$ are determined completely by the mechanics model of the robot). Thus, the two additional constraints from Section 5.3 are unlikely to be satisfied except in very special cases. Maintaining the constraints, which are infinite-dimensional, with only a finite number of actuator inputs is a challenging endeavor that will require assistance from special properties of the precurvature functions selected.

One potential way to solve this problem through design is to 'key' the tubes together, which constrains their rotational motion with respect to one another. Effectively, this causes $\dot{\psi}_i = 0$ for constant-precurvature tube shapes at any initial angular displacement. One way that has been suggested to achieve this [160], and which has been recently prototyped in [117], is to use non-annular tube shapes. In this case, any number of constant-precurvature tubes can be made to follow the leader by using an insertion sequence similar to that described earlier for two tubes, namely one in

which all tubes advance together initially, with one or more stopping sequentially at specified arc length points and then remaining stationary after stopping.

## 5.5 Approximate Follow-The-Leader Deployment

In some cases, approximate follow the leader deployment may be sufficient to accomplish a given task. In order to measure closeness to exact follow the leader deployment, we define an error metric that quantifies the maximum displacement of any point along the backbone:

$$E = \max_{t_1} \max_{t_2} \max_{\sigma} \|\boldsymbol{p}(\sigma, t_1) - \boldsymbol{p}(\sigma, t_2)\|, \tag{5.19}$$

where $\sigma$ denotes arc lengths along the robot which exist for both times $t_1$ and $t_2$. That is, $\sigma \in [0, L_e]$ with $L_e = \min(L(t_1), L(t_2))$. This error metric captures the largest movement of the backbone at any arc length point during the entire deployment period, and has units which are the same as $\boldsymbol{p}$. This error metric does not perfectly capture the amount of "stretching" that would occur in a tissue surrounding the needle path, because some component of the difference $\boldsymbol{p}(\sigma, t_1) - \boldsymbol{p}(\sigma, t_2)$ may be tangential to the path. The tangential component will often be small, however, due to the comparison occurring at equal arc lengths. Note that the error is non-decreasing with time, which for an insertion corresponds also to non-decreasing error with insertion length. Minimizing this error over the set of possible actuator trajectories would give a best-case follow-the-leader behavior for a given robot design. This error metric could also provide a bound for planning and design algorithms which seek to design both the properties of the tube set and the actuation sequence to be used for a specific task.

We now apply this error metric to explore two cases. The first is that of two circularly precurved tubes in the case that $\psi_2 - \psi_1 \neq n\pi$, meaning that the curvatures lie out of plane and the torsional mechanics become nontrivial. The second case is of two helical tubes with opposite handedness. We show that under certain conditions these tubes approximately follow the leader. For all simulations the deployment proceeds with both tubes fully overlapping and extending in

length.

### 5.5.1 Dimensionless Model for Two Constant-Precurvature Tubes

The equations for two circularly precurved tubes may be conveniently nondimensionalized, which reduces the number of design parameters to a minimal set and allows conclusions to be drawn without regard to the overall size of a particular design. We first replace $\psi_1(s,t)$ and $\psi_2(s,t)$ with $\theta(s,t) = \psi_2(s,t) - \psi_1(s,t)$. The arc length is then transformed into normalized arc length $\tilde{s} = s/L \in [0,1]$. Let the symbol '$\sim$' over the top of a variable represent the quantity as nondimensionalized and as a function of the normalized arc length. Then the precurvatures of the tubes may be nondimensionalized as $\tilde{\boldsymbol{u}}_i^* = L\boldsymbol{u}_i^*$. The torsional boundary value problem for two tubes (see [36]) is then given in nondimensional form by

$$\tilde{\theta}'' - \lambda \sin(\tilde{\theta}) = 0 \tag{5.20}$$

subject to the boundary conditions

$$\begin{aligned} \tilde{\theta}(0,t) &= \tilde{\theta}_0(t) \\ \tilde{\theta}'(1,t) &= \tilde{u}_{2z}^* - \tilde{u}_{1z}^*. \end{aligned} \tag{5.21}$$

Note that under the assumption of circularly precurved tubes and that Poisson's ratio $\nu$ is the same for both tubes, the bifurcation parameter $\lambda = \tilde{u}_1^*\tilde{u}_2^*(1+\nu)$. The dependence on squared length is not omitted in this expression, rather it is present through the definition of $\tilde{u}_1$ and $\tilde{u}_2$. We assume for the remainder of this section that $\nu = 0.33$, the value quoted for Nitinol by the manufacturer, for both tubes. The differential kinematic equations may also be nondimensionalized as

$$\tilde{\boldsymbol{p}}' = \tilde{z} \tag{5.22}$$

$$\tilde{\mathbf{R}}' = \tilde{\mathbf{R}}\widehat{\tilde{\boldsymbol{u}}} \tag{5.23}$$

where the relations hold that $L\tilde{\boldsymbol{p}}(\tilde{s}) = \boldsymbol{p}(L\tilde{s})$ and $\tilde{\mathbf{R}}(\tilde{s}) = \mathbf{R}(L\tilde{s})$. The normalized curvature $\tilde{\boldsymbol{u}}$ is computed as $\tilde{\boldsymbol{u}} = L\boldsymbol{u}$, which is more explicitly found as

$$\begin{aligned}\tilde{\boldsymbol{u}}_{xy} &= \frac{1}{1+\gamma_b}\tilde{u}^*_{1x}\begin{bmatrix}1\\0\end{bmatrix} + \frac{\gamma_b}{1+\gamma_b}\tilde{u}^*_{2x}\begin{bmatrix}\cos\tilde{\theta}\\ \sin\tilde{\theta}\end{bmatrix} \\ \tilde{u}_z &= -\frac{\gamma_t}{1+\gamma_t}\tilde{\theta}'\end{aligned} \tag{5.24}$$

where $\gamma_b$ is the dimensionless bending stiffness ratio $E_2I_2/E_1I_1$ and $\gamma_t$ is the dimensionless torsional stiffness ratio $G_2J_2/G_1J_1$. For tubes which have the same value of Poisson's ratio, $\gamma = \gamma_t = \gamma_b$, which will be assumed with some loss of generality for the remainder of this section. Additionally, let $\eta = \tilde{u}^*_2/\tilde{u}^*_1$ represent the precurvature ratio. We then choose the following set of parameters that uniquely define the entire solution space up to a rigid transformation of the backbone: $\gamma$, $\eta$, $\nu$, $\lambda$, and $\tilde{\theta}_0$. Fixing $\nu$ leaves only four parameters determining the forward kinematic problem.

The objective of the metric is to find the maximum movement of the backbone at any arclength point. Since the domain of $\tilde{s}$ is $[0,1]$ for any solution $\tilde{\boldsymbol{p}}$, we must take care to compare points which correspond to the same physical arc length. Note that during any particular deployment, the only term not constant in $\lambda$ is $L$, meaning that we may find that for arbitrary times $t_1$ and $t_2$ at which the tubes have nonzero length, $\sqrt{\lambda_2/\lambda_1} = L_2/L_1$. Furthermore, we may parameterize the deployment by $\lambda$ rather than by time. Considering these facts, the error metric may be nondimensionalized as

$$\begin{aligned}&\tilde{E}(\lambda) = \\ &\max_{\substack{\lambda_1 \\ \lambda_1<\lambda}} \max_{\substack{\lambda_2 \\ \lambda_2<\lambda_1}} \max_{\tilde{\sigma}\in[0,1]} \left\| \sqrt{\frac{\lambda_1}{\lambda}}\tilde{\boldsymbol{p}}(\tilde{\sigma}\sqrt{\lambda_2/\lambda_1}, \lambda_1) - \sqrt{\frac{\lambda_2}{\lambda}}\tilde{\boldsymbol{p}}(\tilde{\sigma}, \lambda_2)\right\|\end{aligned} \tag{5.25}$$

where we assume, without loss of generality, that $\lambda_1 > \lambda_2$. Note that to compute $\tilde{E}(\lambda)$ for an insertion sequence, we must additionally know the actuator history $\tilde{\theta}_0(\lambda)$, stiffness ratios, Poisson's ratio, and the curvature ratio, and these additional parameters have been suppressed from the notation. Once equipped with this nondimensionalized error, the error may be computed by $E(L,\lambda) = L\tilde{E}(\lambda)$ for a deployment which has final overlapped tube length $L$. This nondimen-

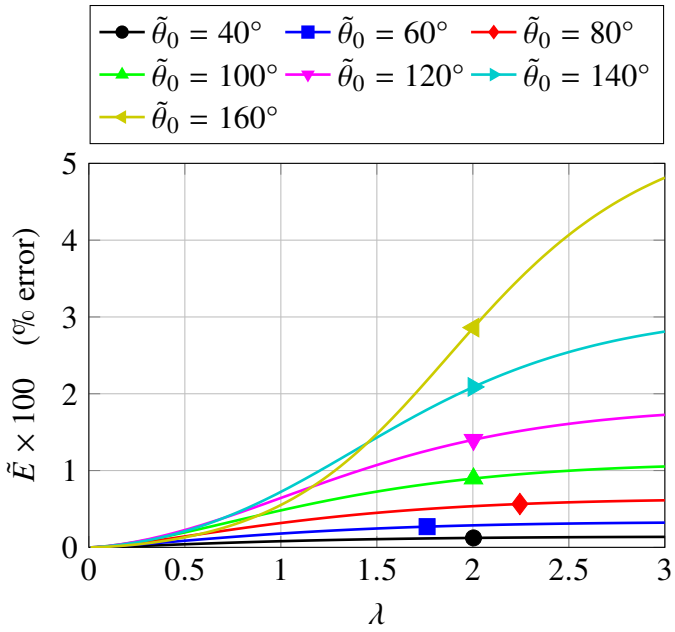


Figure 5.4: The dimensionless follow-the-leader error at a stiffness ratio of $\gamma = 1$ and curvature ratio $\eta = 1$. The value $\tilde{\theta}_0$ represents the relative angle between the tubes at $s = 0$, which is held constant during the insertion.

sionalized error metric, unlike the original metric, is *not* non-decreasing. This fact may be seen from the division by $\sqrt{\lambda}$ on the right hand side of (5.25) and is consistent with the fact that longer insertions may incur less error on a percentage basis of the final length.

In the subsections that follow we investigate the behavior of this error metric for varying choices of tube designs and actuation. In all cases the model equations are solved via a nonlinear Galerkin method, using MATLAB's `fsolve` to perform the minimization of the weighted residual equations. Once this solution is obtained, the kinematic equations are integrated via `ode45` and interpolated to 2000 evenly spaced points.

### 5.5.2 The Effect of Initial Angular Difference

In order to investigate the follow-the-leader error for varying angular differences between the tubes, we choose tubes that have circular precurvature and vary the nondimensional parameters of the model. The actuator history is given by $\tilde{\theta}_0(0,t) = \text{constant}$.

The dimensionless error is shown in Figure 5.4 for the case of equal stiffnesses and equal

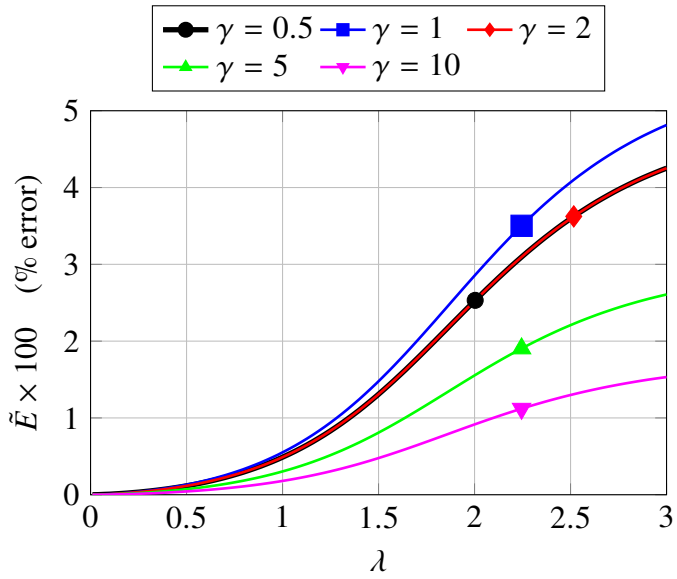


Figure 5.5: The dimensionless follow-the-leader error at an initial angle $\tilde{\theta}_0 = 160°$ and curvature ratio $\eta = 1$ for varying stiffnesses.

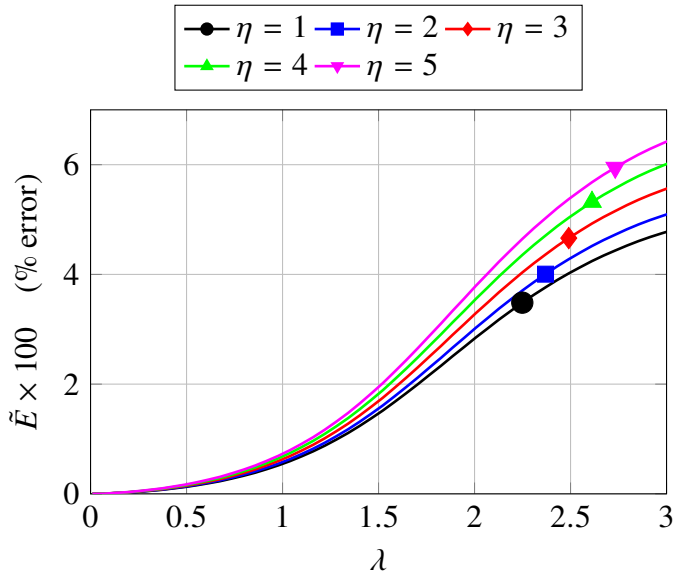


Figure 5.6: The dimensionless follow-the-leader error at an initial angle $\tilde{\theta}_0 = 160°$ and stiffness ratio $\gamma = 1$ for varying curvature ratios.

curvatures for various initial angular differences at $s = 0$. It is seen that a maximum in the error occurs near an initial angle of 160 °.

### 5.5.3 The Effect of Tube Stiffness Ratio

Figure 5.5 displays the dimensionless error for varying stiffness ratios, using the worst-case angular difference from the previous subsection of 160 ° and tubes of equal curvature. The maximum amount of error occurs when the stiffnesses are equal, and is reduced as one tube becomes stiffer relative to the other.

### 5.5.4 The Effect of Tube Curvature Ratio

Figure 5.6 shows the dimensionless error for varying curvature ratios with equal stiffness tubes at a 160 ° relative angle. It is seen that the minimum occurs at unity. However, the effect of varying the curvature ratio is clearly less significant than the effect of varying stiffness ratio. Unlike varying stiffness, the error is slightly increased as the tubes deviate from unity curvature ratio.

### 5.5.5 The Effect of Actuation Sequence

It is important to note that the proximal boundary conditions $\tilde{\theta}(0,t) = \text{constant}$ and $\mathbf{R}(0,t) = \text{constant}$ which were chosen for the previous subsections imply a particular actuation sequence during the deployment, because the tubes must be grasped at a location $s < 0$ in order for the insertion to extend from $s = 0$ forward. Torsional windup in the section $s < 0$ must be compensated so that the two boundary conditions $\tilde{\theta}(0,t)$ and $\mathbf{R}(0,t)$ are held fixed. Note further that there is no guarantee that this choice of actuation provides the minimum follow-the-leader error. Rather, this choice makes the equations amenable to the preceding analysis. One subtle benefit of this choice is that the graphs in Figures (5.4)-(5.6) may be labeled simply '$\lambda$' along the abscissa because it does not matter whether the value is taken at the end of an insertion or during the middle of an insertion.

In order to give one comparison to a different choice of actuation, however, we examine the

case where one applies no rotational actuation during the insertion. In all physical prototypes built to date of which we are aware, there is a section of tube which is not precurved present before the curved section, termed a transmission length. To account for this length, if it is present, we introduce the parameter $\lambda_s = L_s^2 u_{1x}^* u_{2x}^* (1+\nu)$, where $L_s$ is the straight length of tube located at $\tilde{s} < 0$. We term this actuation with no rotational motion "uncompensated," and $\tilde{\theta}(-d(t),t) = \alpha$, where $d$ is the non-dimensional length (nondimensionalized by the currently overlapped length $L(t)$ of the tubes) of the portion of the tubes physically located at $\tilde{s} < 0$ and $\alpha$ is the rotational actuator relative angle. The value $d$ may then be computed as

$$d = \sqrt{\frac{\lambda_s}{\lambda(t)}} + \sqrt{\frac{\lambda_f}{\lambda(t)}} - 1, \tag{5.26}$$

with $\lambda_f$ being the value of $\lambda$ at the end of the insertion sequence, and where $\lambda(t) > 0$. Then, the proximal boundary condition changes to $\tilde{\theta}(0,t) = \alpha + d\tilde{\theta}'(0,t)$, and we must also account for the change in the initial axial rotation of tube 1 at $\tilde{s} = 0$. This rotation is $\mathbf{R}(0,t) = \mathbf{R}_z(-d(t)\tilde{\theta}'(0,t)\gamma_t/(1+\gamma_t))$.

Figure 5.7 shows the error metric as a function of $\lambda_f$ for various choices of the ratio $\lambda_s/\lambda_f$, with $\gamma = 2$, $\eta = 1$, and $\tilde{\theta}(-d(t),t) = 160\,^\circ$. Note that with this choice of actuation, $\lambda$ is no longer the only changing parameter in the torsional boundary value problem and forward kinematic problem, because $\lambda$, $\lambda_f$, and $d$ must all be known in order to find the correct solution to the kinematic equations part-way through an insertion. It is for this reason that Figure 5.7 shows $\lambda_f$ on the abscissa. For high values of $\lambda_f$, the follow-the-leader error is lower in magnitude than those for the previous, compensated actuation method. However, a direct comparison is not valid since the relative angle $\tilde{\theta}(s,t)$ is significantly lower for most of the uncompensated solutions when compared to the $160\,^\circ$ compensated solution. As the straight length increases, the torsional windup in the region $\tilde{s} < 0$ increases, lowering the effective relative angle for the region $\tilde{s} > 0$ and thus decreasing the follow-the-leader error. However, for lower values of $\lambda_f$, where most prototypes have been built to date, the error increases substantially with increasing transmission length. Thus, where

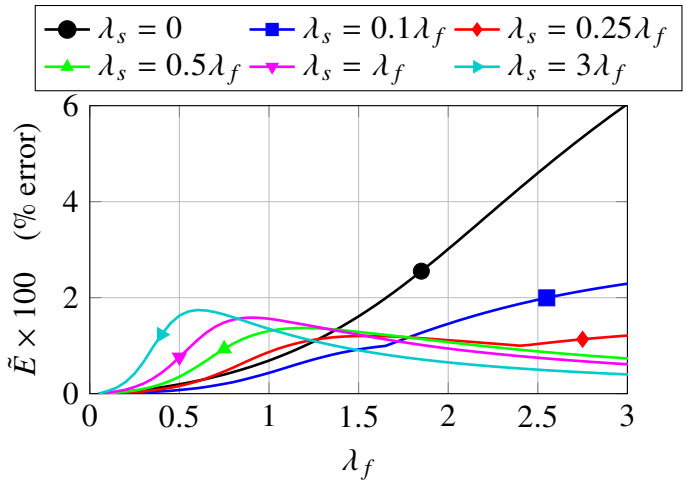


Figure 5.7: The follow-the-leader error has a more complex pattern with respect to the straight transmission length. Here $\tilde{\theta}(-d)$ is set to 160 °, $\gamma = 2$, and $\eta = 1$. As $\lambda_s$ is increased relative to $\lambda_f$, the error at low values of $\lambda_f$ increases, but the error at high values of $\lambda_f$ decreases.

it is feasible, the compensated actuation method should be preferred to this uncompensated one when follow-the-leader deployment is desired. We note that in some cases excessive transmission length will prevent all values of $\tilde{\theta}_0$ from being achievable due to bifurcation.

### 5.5.6 Helically Precurved Tubes

Another case that provides interesting study is that of two opposite-handed helices. For this simulation we will choose a set of tubes and an insertion length that results in a bifurcation parameter $\lambda > \pi^2/4$. It is harder to span many values of curvature in this case because there is a two-parameter family of both torsion and curvature for each tube. For illustrative purposes, we will choose the parameters $EI_1 = EI_2 = 1$, and $u^*_{1z} = -25\,\mathrm{m}^{-1}$ and $u^*_{2z} = +25\,\mathrm{m}^{-1}$. When $\psi_2(0,t) - \psi_1(0,t) = 0$ is maintained and the curvature is high enough, the tubes will conform to a planar shape and "unwind" so that $\psi_2(s,t) - \psi_1(s,t)$ stays less than $\pi$ over the entire length of the insertion. Figure 5.8 depicts how the two helical shapes conform to a common centerline. Since no error will occur during the second stage of insertion when the inner tube continues to deploy beyond the outer one, an overall robot curve featuring a first almost-circular segment followed by a second helical segment can be achieved in a quasi follow-the-leader manner. For three choices of

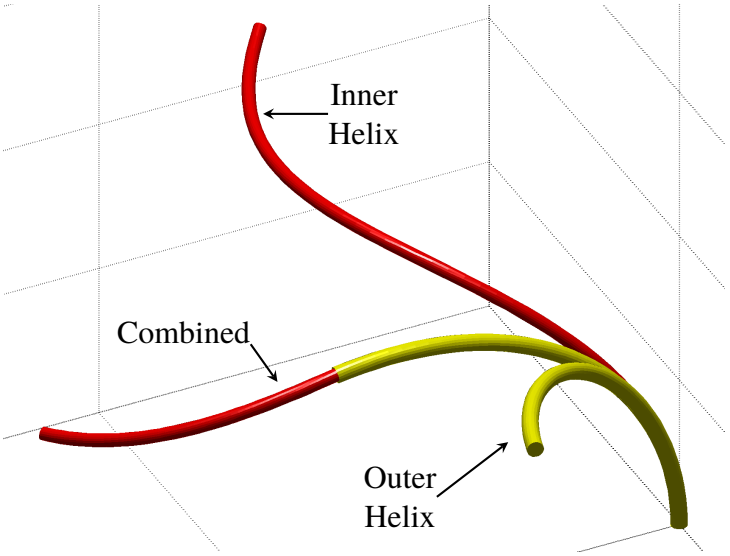


Figure 5.8: Two helically precurved tubes of opposite handedness and equal stiffness combine to form an almost-circular section followed by a helical section. Where the two helices interact they twist each other into a common plane. This configuration can be reached in a quasi follow-the-leader manner.

curvature which are sufficiently high, the follow-the-leader error versus insertion length is shown for the first stage of fully overlapped insertion in Figure 5.9. For this simulation the density of the discretization is again 2000 points along the length of each solution, with 1000 discrete insertion steps in order to obtain a smooth result.

Unlike the two circularly precurved tubes, the helices conforming to a plane have better tip-following behavior when the curvature is increased. This is easily explained by the fact that the higher curvature allows $\psi_2 - \psi_1$ to stay closer to zero, which would be a perfect follow-the-leader case for circularly precurved tubes. Essentially, the preset torsion of the tubes is "removed" by the material twisting when the curvature is sufficiently high. From a design perspective this is a trade-off where increasing the torsion allows the second segment of the insertion to more rapidly leave the plane of the first segment, but also requires higher curvature to achieve the desired behavior.

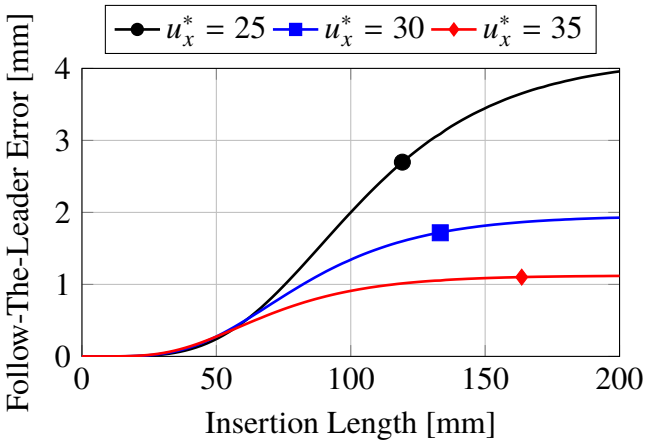


Figure 5.9: For the helical "unwinding" case, again error increases with insertion length, but decreases with increasing curvature.

### 5.5.7 How to Use Nondimensional Approximate Follow the Leader Results in Practice

Given a physical robot design and motion plan, Figures 5.4, 5.5, and 5.6 can be used to predict the follow-the-leader error. For example, consider two tubes with curvatures of $u_{1x}^* = 20\,\mathrm{m}^{-1}$ and $u_{2x}^* = 15\,\mathrm{m}^{-1}$, where each tube is precurved for its entire final length of insertion. Consider a motion plan in which the two tubes will be deployed together for 50 mm, and then the inner tube deploys by itself another 50 mm. Assume that the plan uses the compensated actuation method discussed in Section 5.5.5, and prescribes an initial angle $\theta(0,t) = 90\,^\circ$.

We wish to know how much follow-the-leader error can be expected from these tubes and this deployment plan. First, note that since the overlapped length $L = 50\,\mathrm{mm}$, the dimensionless parameter $\lambda = L^2 u_{1x}^* u_{2x}^* (1 + 0.33) = 1.0$. From Figure 5.4, we see that at $\lambda = 1$, equal stiffness tubes at $\theta(0,t) = 90\,^\circ$ would be predicted to have a follow-the-leader error less than 1 % of $L$. Figure 5.5 tells us that the effect of the stiffness ratio is to slightly reduce the error, and Figure 5.6 shows us that the curvature ratio $u_{2x}^*/u_{1x}^* = 1.33$ will slightly increase the error, roughly canceling the effect of the stiffness ratio. Therefore, we predict an error of less than 1 % of $L = 50\,\mathrm{mm}$, or 0.5 mm, during the first stage of deployment, and no error during the second stage.

## 5.6 Experimental Helical Case Demonstration

In this section we examine the follow-the-leader behavior of a physical prototype. The experiment shows the case of two same-handed helices inserted in free space, providing a proof-of-concept demonstration of an odd solution case. We emphasize that this section is not intended to be a conclusive, statistical statement about practically achievable distributions of errors. In this section we present the results of measurement of the follow-the-leader error of a single insertion as a proof of concept for follow-the-leader deployment of helically precurved concentric tubes, which has never before been demonstrated.

### 5.6.1 Experimental Protocol

An outer tube and an inner wire were first independently shape-set via heat treatment into helical shapes. To create a helix with the correct precurvature we converted $u_x^*$ and $u_z^*$ into the more physically intuitive helical pitch $2\pi p$ and radius $r$, using the following relationships:

$$r = \frac{u_x^*}{u_x^{*2} + u_z^{*2}} \qquad p = \frac{u_z^*}{u_x^{*2} + u_z^{*2}}. \tag{5.27}$$

Note that here a negative value for $p$ would indicate a left-handed helix, and a positive value a right-handed helix.

To set the helical precurved shape, the tube and wire were each wrapped in a helical profile with a pitch of $2\pi p = 160\,\text{mm}$ around a steel cylinder 19 mm in diameter, with the proximal part of the tube/wire left free to leave the surface of the fixture in order to remain in a straight configuration. Figure 5.11 shows the process. The tube and wire were placed in an air furnace at 500 °C for 30 minutes. This heating was followed by an immediate quench in room-temperature water, followed by a second heating period at 600 °C for 5 minutes. A second water quench was performed immediately after the second heating period. Note that the full theory of heat treating Nitinol is a complex metallurgy problem and the interested reader is directed to [161, 162] for further information. Broadly speaking, the first heat treatment period sets the shape, while the

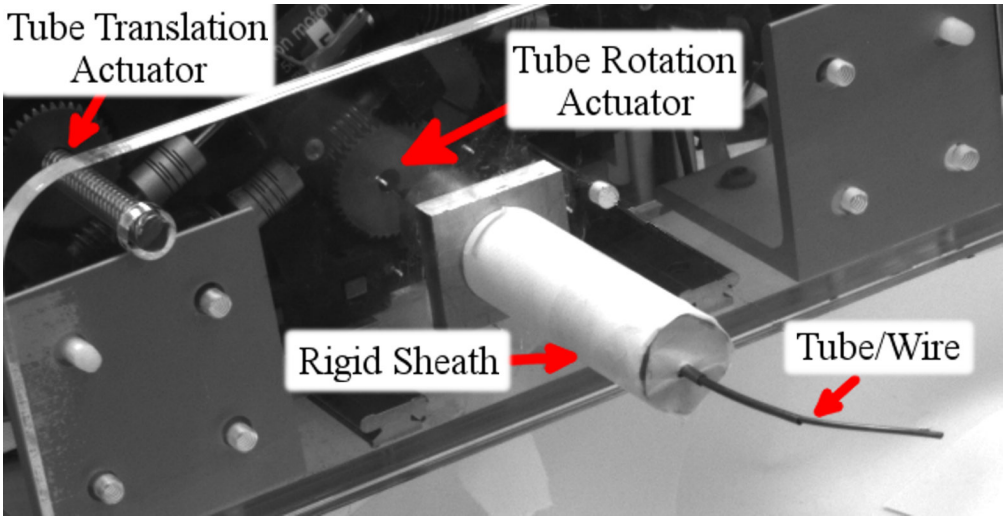


Figure 5.10: The robot grasps the tube and wire at their respective bases where rotation and translation are applied. The rigid sheath straightens the precurved portions of the tube and wire when they are retracted.

second moves the transition point between Austenite and Martensite back below room temperature so that the sample is superelastic at room temperature. Accounting for the diameters of the tube and wire, by (5.27), they were constrained around the steel cylinder with $u_{1x}^* = 13.64$, $u_{1z}^* = -33.75$, $u_{2x}^* = 13.92$, and $u_{2z}^* = -33.48$ before heat treating began, where all values are in units of rad/m.

The robot described in [29] was used to independently control the insertion and rotation of the concentric tube and wire, which passed through a rigid sheath that served to constrain the tubes to be straight at arc lengths $s < 0$. Since both tubes are helical, the bases of the tubes must be turned during insertion in order to maintain the angles $\psi_i(0)$ at a constant value. The rate of twist must be equal to the precurved helical torsion, which can be seen from the fact that the tubes undergo no material torsion at negative arc lengths. A photograph of the experimental setup is shown in Figure 5.10.

All measurements were taken with a stereo camera system of two Sony XCD-X710 firewire cameras, calibrated using a rectangular 10 mm square grid and the Camera Calibration Toolbox for MATLAB. To triangulate points, a point in one image was clicked, and then the intersection of the epipolar line and the feature of interest was selected in the second image.

The insertions were performed according to the steps outlined in Section 5.3.4. Before begin-

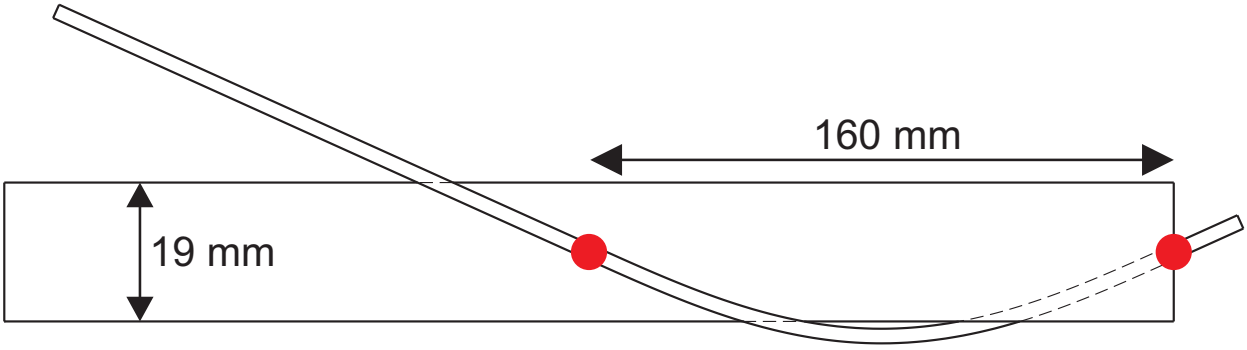


(a) Fixture (Top View)

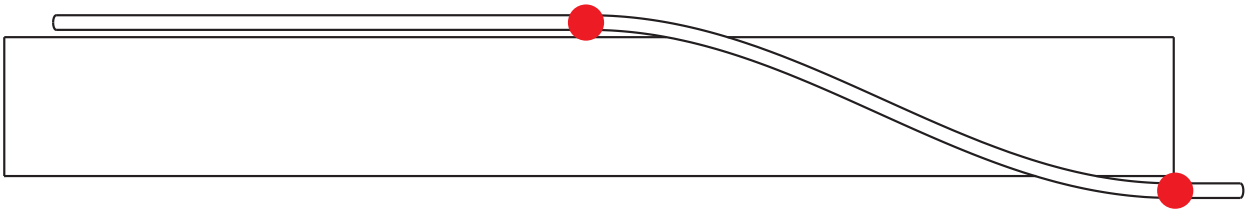

(b) Fixture (Front View)

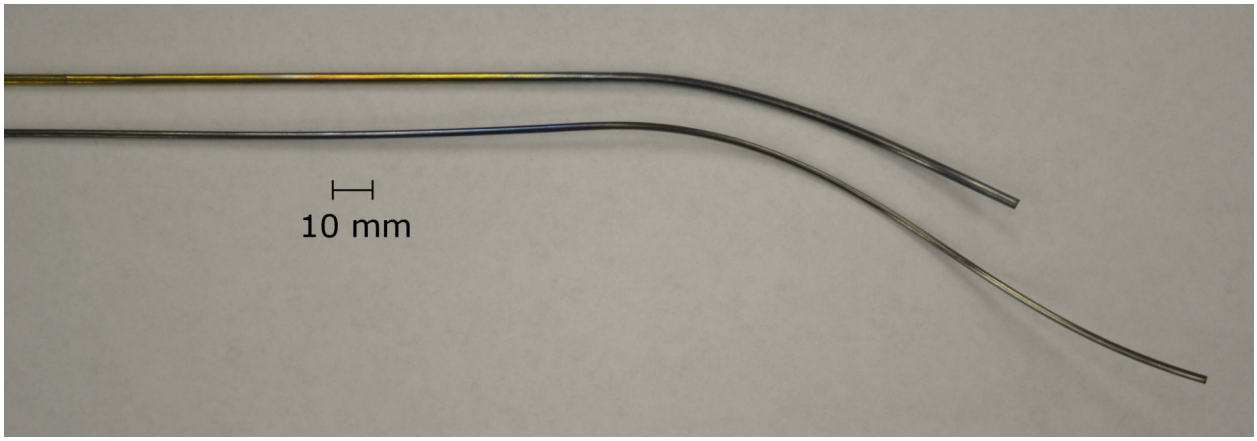


(c) Shape Set Tube/Wire

Figure 5.11: The tube and wire were constrained to the surface of a cylinder in a helix at two points, with the proximal end of the tube left free. The dots indicate the locations of the constraints. The tube and wire after the shape setting process are shown after trimming to length.

| Parameter | Outer Tube | Inner Wire | |
|---|---|---|---|
| Outer Diameter | 2.18 | 1.58 | mm |
| Inner Diameter | 2.02 | 0.00 | mm |
| Curvature ($u_x^*$) | 8.4 | 9.9 | $m^{-1}$ |
| Torsion ($u_z^*$) | -31.6 | -34.3 | $m^{-1}$ |

Table 5.1: Tube parameters after the shape-setting process. The tube diameters and Poisson's ratio are taken from manufacturer's data.

ning the insertion the two helices were aligned, with their tips at $s = 0$. Next, the inner wire was inserted forward while holding $\psi_1(0) = 0$. It was then rotated to $\psi_1(0) = \pi$ and finally retracted while holding $\psi_1(0) = \pi$. This initial setup procedure minimizes frictional effects by reducing the arc length of overlapping tube and wire during initial rotation and also causing the tubes to slide relative to one another after rotation. Since it is known that friction between the tubes induces a hysteresis between the relative base angle $\psi_2(0) - \psi_1(0)$ and the relative tip angle $\psi_2(\ell) - \psi_1(\ell)$ (see [155]) frictional effects additionally need to be considered when designing a real device, as the base actuators must be able to maintain sufficient control over the axial rotation of the tubes. The steps of Section IV-E were implemented 0.5 cm at a time, with an insertion velocity of approximately 0.5 cm/s. After each 0.5 cm step insertion was paused and a pair of stereo images was captured for analysis. The backbone shape was discretized in each image pair manually using the triangulation technique discussed above with a density of approximately 1 point every 2 to 5 mm.

### 5.6.2 Experimental Results

Table 5.1 lists the tube parameters as measured after heat treatment. The radius and pitch were estimated from points collected with the stereo cameras using a nonlinear regression. The results indicate that the curvature ($u_{1x}^*$ and $u_{2x}^*$) relaxed approximately 40 percent after removal from the steel cylinder. In contrast, the torsion (in the helical parameter sense, not a material sense) did not change appreciably. This makes sense intuitively, because there is no internal torsional strain associated with wrapping the tube around the cylinder as we did before heat treating. The tube and wire after shape setting and trimming to length are shown in Figure 5.11.

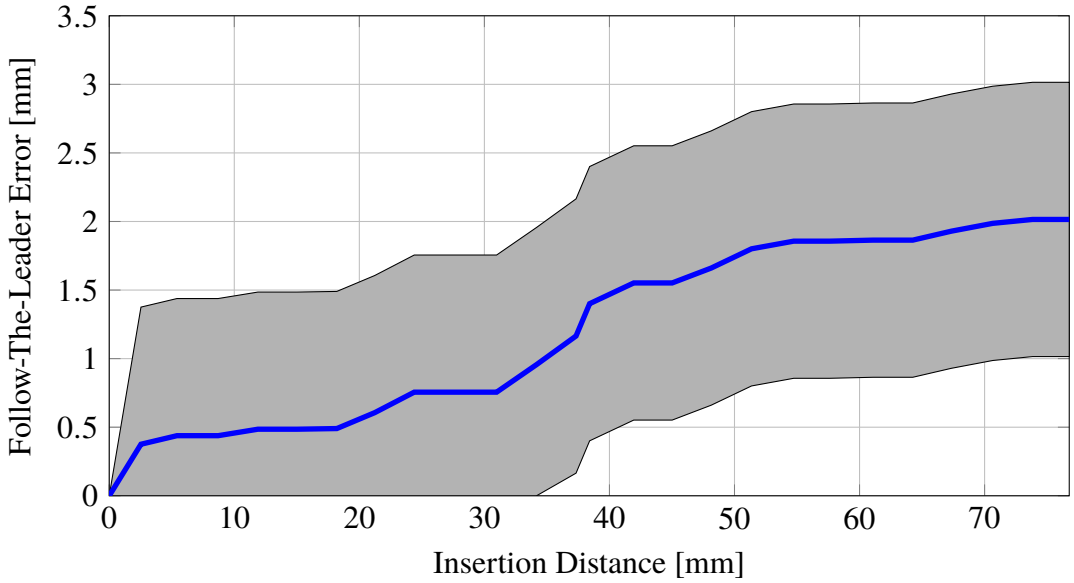


Figure 5.12: The experimental follow-the-leader error for two helical tubes in free space. The gray shaded area denotes the margin of error using our estimate of 0.5 mm measurement error at any point along the insertion.

Experimental results for a single free space insertion are shown in Figure 5.12. The graph of error versus insertion distance reveals that for an 80 mm insertion, overall error is only 2 mm. The most likely sources of error are the unmodeled effects of diametral clearances between tubes, friction between the tubes, and manufacturing error in the shapes of the tubes. Note that this demonstration is not designed to corroborate the simulation cases presented before, since the model would predict zero error for this experiment. What the experiment does demonstrate is that the modeling errors are small enough that such an insertion could be practical.

## 5.7 A Neurosurgical Example

Consider epilepsy treatment as a motivating clinical example for follow-the-leader deployment. This application was suggested in [24] which addressed the design of a magnetic resonance imaging (MRI) compatible concentric tube robot actuation system, but did not address tube design or deployment strategy. Epilepsy is estimated to affect 1% of the global population at some point in their lives. Anti-seizure medications are the first line of defense, but about 20-30% of people

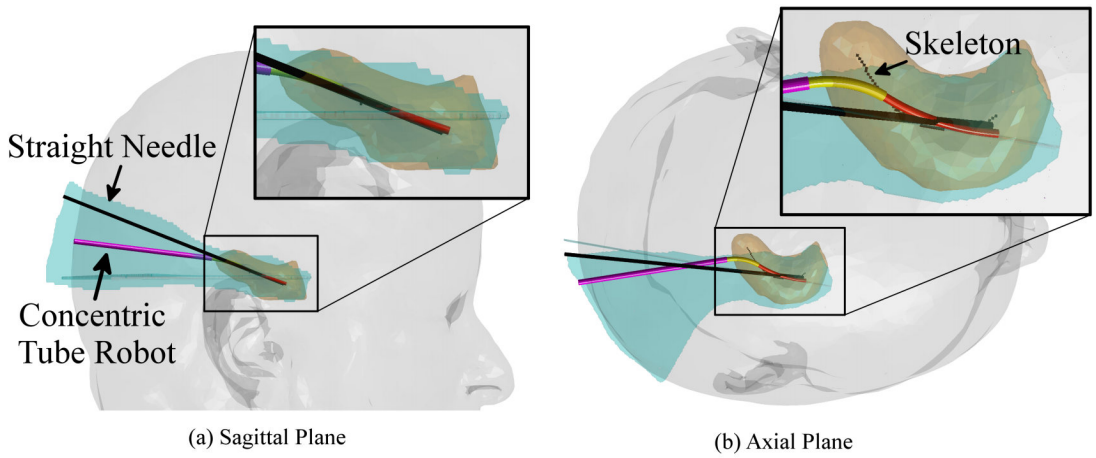


(a) Sagittal Plane (b) Axial Plane

Figure 5.13: Two views showing the trajectory of a two-tube concentric tube robot with helical precurvatures. At all times the path stays within the safe area (shown in blue) designated by an experienced neurosurgeon. The helical shape allows the path to stay nearer to the middle of the allowable area in the axial plane, while traveling approximately along the Euclidean skeleton of the hippocampus. The straight needle shown in black must pass much closer to the boundaries of the blue insertion zone in order to remain close to the skeleton. Mean distance to the skeleton is 1.5 mm for the concentric tube robot and 2.4 mm for the straight needle. The concentric tube robot enters through a straight, rigid tube.

do not respond to them [163]. For many of these patients, surgical removal of the hippocampus is highly effective in controlling seizures, but carries with it all the risks (bleeding, inadvertent damage to nearby critical brain structures, blood vessels, etc.) typically associated with a major surgery on the brain. As discussed in [24], it would be highly desirable to perform a less-invasive needle-based treatment in which thermal energy is deployed from the tip of a needle that is inserted along the axis of the hippocampus, while monitoring brain temperatures using magnetic resonance imaging (MRI) temperature maps. Recent clinical results of minimally invasive MRI-Guided laser ablation of the hippocampus indicate that straight needles are able to surgically treat on average 60 % of the desired volume [164].

To explore whether helical follow-the-leader trajectories might be useful in this application, an experienced neurosurgeon first defined the bounds of a safe insertion region, using an occipital approach, for the cannula by drawing contours on an MRI image set of a patient's head. The safe insertion zone geometry the surgeon indicated is shown in blue on Figure 5.13. The surgeon also

segmented the target portion of the hippocampus to be ablated (shown in brown on the Figure). Next, we considered delivery of an ablator that radiates energy radially around the needle tip, such as the acoustic ablation probe in [18]. With such a probe, it would be desirable to deliver the ablator along the central axis of the hippocampus. This central axis, known as the Euclidean skeleton, was computed for a voxelized image of the hippocampus using the method of Lee et al. [165]. We used the mean distance between the skeleton points and the concentric tube robot trajectory as a measure of how well an ablator could thermally treat the hippocampus by radiating energy evenly in all radial directions.

To demonstrate that our helical case can provide a more desirable result than a straight needle, we generated an optimal straight needle trajectory using principal component analysis (PCA). Using all skeleton points results in a trajectory that lies outside the insertion zone, so points were gradually excluded from the tail of the hippocampus, toward the posterior side of the head, until a trajectory was found that passed entirely inside the safe insertion zone marked by the surgeon. This straight needle trajectory results in a mean distance to the skeleton of 2.4 mm.

We then considered designs with two helical tubes of identical helical torsion, with the objective of staying within the safe region of the brain and minimizing the mean distance to the skeleton. A design consisting of tube curvatures and lengths was manually selected and the resulting shape was positioned and rotated using `fminsearch` in MATLAB to minimize the mean distance to the hippocampus skeleton. This design is shown in Figure 5.13. The resulting tubes have a stiffness ratio of 2.3, and curvatures of 20 $m^{-1}$ and 80 $m^{-1}$ for the inner and outer tubes, respectively. Both tubes have a helical torsion of -10 $m^{-1}$. The curved tubes enter through a third, straight, rigid tube, which is assumed to be stiff enough to completely straighten the curved tubes when they are retracted inside of it.

The helical tubes have a smaller mean distance to the skeleton of 1.5 mm, and they would allow ablation of tissues in the tail of the hippocampus that cannot be reached with the straight needle, which is important given that correlations exist between higher resection volume and better clinical outcomes [166]. The ability to treat the tail of the hippocampus may increase the potential

for seizure freedom. Furthermore, as can be seen in Figure 5.13 the helical tubes do not require a needle trajectory that is very close to the boundary of the safe zone for the entire deployment (meaning that a small registration error could potentially significantly damage the patient's brain). Using helical tubes also provides the ability to alter the insertion point without substantially reducing the covered volume by slightly altering the tube design, thus avoiding patient-specific obstacles such as sulci near the surface of the brain.

We note that in future work, automated planners could design the tubes for this application, and could consider all design objectives including obstacle avoidance and desired insertion points. However, such optimization routines are an active area of research themselves (see e.g. [78]) and are beyond the scope of this dissertation. It is also worth noting that the example described in this section shows that even a hand-selected (i.e. not optimized) helical design was capable of performing the desired surgical task better than the optimal straight needle trajectory.

## 5.8 Conclusions

In this chapter we have explored follow-the-leader behavior as it relates to concentric tube robots, showing that it is possible, but only with appropriate precurvature selections and deployment sequences. We derived the conditions that must hold for follow-the-leader deployment in general, and explored various two-tube cases in depth. Fortunately, even these "simple" circular and helical precurvature special cases provide a large design space of possible curves. Thus, we expect them to enable a number of new clinical applications where concentric tube robots act as steerable needles in both soft tissues and open or liquid-filled spaces in the human body — cases where the robot operates in a manner conceptually similar to our epilepsy treatment illustration. We anticipate that approximate follow-the-leader behavior will also be useful in applications like traversing a lumen where a tolerance exists between the robot and wall, or in tissues where some stretching is permitted. In such cases, our metric for comparing a general deployment to a follow-the-leader deployment will be useful in assessing the ability of an existing robot to achieve the surgical task at hand. The metric may also be useful in future design and motion planning studies

for concentric tube robots. In summary, follow-the-leader deployment appears to be a useful attribute for concentric tube robots. It enables them to act like steerable needles that do not depend on tissue interaction to steer. This ability to travel along desired curved trajectories through both soft tissue and open space may enable a variety of minimally invasive interventions to be developed in the future.

# Chapter 6

# Sensing: Intrinsic Force Sensing

Concentric tube robots, like other robots with a continuously flexible backbone, possess the promising capability of intrinsic force sensing. In theory, if the robot backbone is predicted to be at one location but is observed at another, one can infer that a load has been applied. If enough information is present, the entire three-dimensional force can be estimated in this way. Existing studies have either made simplifying assumptions that drastically alter the mechanics of the model or have used expensive embedded sensing technologies that can directly measure strains to infer the applied loads. Position measurement is a feasible option with the widespread deployment of magnetic trackers in surgical suites, but to date there has not been a complete demonstration of force sensing for a generally designed concentric tube robot undergoing large torsional deformations under externally applied loads. The contribution of this chapter is the validation of a fixed-interval smoothing framework for the estimation of the entire state of the robot along its full length. A simulation demonstrates accurate force estimation, and an experimental trial indicates performance that is acceptable but with substantial noise present.

## 6.1 Introduction

Concentric tube robots enable access to difficult-to-reach surgical sites, and have been investigated for applications including endonasal surgery [29], cardiac surgery [9], lung surgery [7], and fetal surgery [15], among others. In addition to enhancing access and dexterity, concentric tube robots may become even more powerful surgical devices if they are endowed with force sensing capabilities. Sensed forces could be used to help doctors "feel" tissues to discern differences in tissue stiffness that indicate subsurface objects like tumors, blood vessels, nerves, or anatomical planes, the locations of which are often critical to the outcome of the surgical procedure. This information can be presented to the surgeon using graphical displays [167], or machine learning

techniques can be used to autonomously differentiate tissue types [168]. The forces of interaction can also simultaneously provide information about the robot itself, to provide data for localization at the surgical site and registration to the body [169].

However, sensing the forces of interaction with the environment is challenging for concentric tube robots due to their small size (typically 1-2 mm, and sometimes even smaller) making direct integration of traditional force sensors along the shaft of the robot impractical. Due to their inherent flexibility, concentric tube robots have the potential to achieve intrinsic force sensing. Known equivalently known as "manipulator as sensor," and "deflection-based force sensing," this concept has been demonstrated in multi-backbone continuum robots [83], continuum robots modeled as a single elastic backbone [67], and suggested for tendon-driven continuum robots [170], but has never before been applied to concentric tube robots of general designs which incur substantial twisting deformations under external loads (see Fig. 6.1).

By leveraging the mechanics model of Chapter 1.7, the sensed forces can be inferred from the observed discrepancy between the predicted and actual shapes of the robot backbone. Given enough sensors and an accurate enough model, the shape provides sufficient information to estimate multiple contact loads. In this chapter, a single external load at the tip of the robot is estimated by incorporating two five-degree-of-freedom magnetic tracking sensors into the shaft of a concentric tube robot. To generate the force estimate, the problem is viewed as a state reconstruction problem for the differential equations that govern the state of the robot along its length. A Kalman filter and backwards smoother are used to create a fixed-interval smoother that estimates the internal force and moment as one part of the complete system state. In this method the filter acts in space rather than in time.

The sensor feedback is provided by magnetic tracking in the experiments, although in principle any position measurement method could be used. Magnetic tracking is advantageous due to its nearly ubiquitous deployment in neurosurgical suites and non-contact, non-line-of-sight measurements.

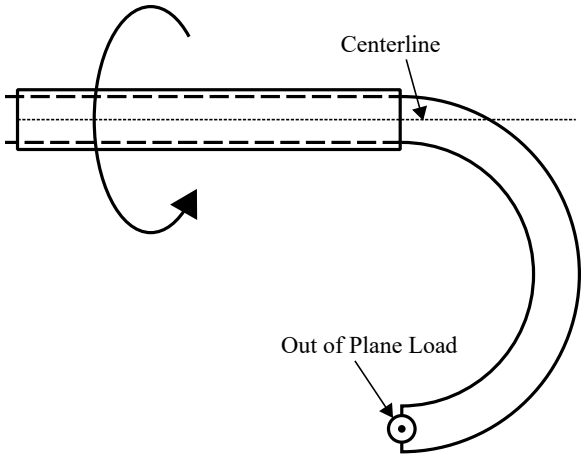


Figure 6.1: A load placed at the tip of a robot, out of the plane of the robot and in the plane of the page. This load will cause a twisting deformation in the shaft of the inner tube, and in the case where the outer sheath is very stiff this will be initially the predominant mode of deformation. Existing approximations made for force inference do not handle this situation correctly.

## 6.2 Related Work

A concentric tube robot consists of concentric, precurved, superelastic tubes. Changing the translation and rotation of each tube causes the resultant equilibrium conformation to change and provides a means of actuating the robot. Mechanics models have been previously developed [48, 55, 57] that can provide the forward kinematic solution, the differential kinematics of the robot, and the compliance matrix which maps differential external wrenches to differential twists at any location along the length of the robot.

Concentric tube robots fall within a broader robot classification called continuum robots, all of which are capable of some kind of intrinsic force sensing. Other devices are also capable of this – an early illustration of the end-effector-as-sensor concept was a study on tensegrity structures that are amenable to force sensing [171]. It has also been demonstrated with parallel robots operating near singular configurations [172]. The first application in continuum robots was the work of Xu and Simaan [83, 173], who demonstrated that one could deduce wrenches applied to a multi-backbone continuum robot using load cells measuring the tension/compression in each backbone. Bajo and Simaan described how to infer the location of a point of contact of the robot and environment using the relative position of points on the robot shape [174]. The work in this

chapter also uses measurements of multiple points along the length of the robot to provide robustness to modeling errors. Shape reconstruction, the dual problem to force reconstruction, has also been considered using PVDF deflection sensors for hyper-flexible beams [175]. Strain measurements with fiber Bragg grating sensors have also been used to provide force sensing capability in concentric tube robots and shape reconstruction in other continuum devices. [73, 71, 176].

Towards achieving intrinsic force sensing via position feedback, Rucker and Webster developed an Extended Kalman Filter (EKF) approach for the general class of continuum robots, and provided the specific example of applying it in simulation to a tendon-driven robot [170]. For continuum robots whose deformation (deviation from the unloaded shape) can be modeled as a single elastica, Mahvash and Dupont developed real-time force sensing and compliance control methods [67], and applied them to a concentric tube robot composed of two fully overlapping tubes that did not slide axially with respect to one another, which are together well-approximated by a single elastica. An elliptic integral interpolation map was employed by Wei et al. to provide a real-time estimation of applied forces on a concentric tube robot used for microstent delivery [23]. This method leverages the fact that the exact solutions for the planar deflections of a beam can be accurately interpolated with polynomials based on the total bending angle and the direction of the applied load as interpolation parameters. The values of these interpolation parameters are then found in real-time to match the observed robot tip location. Hasanzadeh and Janabi-Sharifi demonstrated the solution of the inverse problem for applied loads on intracardiac catheters. They used a nonlinear, discretized quasi-static model of the catheter and used the Levenberg-Marquardt method to solve for the applied load as an unknown parameter in the model given observations of the tip location of the catheter [177].

The methods developed in this chapter share similarities with several of these previous works but also generalize them. In particular, the approach presented here allows for the natural incorporation of as many sensors as desired, allows for general three-dimensional deflections of the robot, and accounts for uncertainty in the position measurements, the actuation, and the quasi-static model.

## 6.3 Technical Approach

### 6.3.1 Overview

The approach taken here combines information from the model, the measured actuator values, a measured registration to the base of the robot, and magnetic tracker measurements along the centerline of the robot. Except for the model equations, all other information is treated as measurements with associated statistical uncertainty. A continuous-domain Kalman filter is used to first estimate the states in a forward integration of the model equations (from the base to the tip of the robot), and a Rauch-Tung-Striebel smoother is then used in a backwards integration of the model equations to provide an optimal estimate of the entire state of the robot, including the internal force and moment. Since we assume a single point load at the tip of the robot, the internal force is simply equal to the applied force by Newton's law, and is therefore used as the final estimate.

The estimation is performed in a quasi-static sense, meaning that time-dynamics are explicitly ignored. The underlying assumption is that both the actuation and the external loads are slowly changing in time. Specifically, both of these changing quantities must be on a slower time scale than the vibrational dynamics of the robot, which are unmodeled.

### 6.3.2 The Extended Kalman Filter Prediction

A continuous-discrete Kalman filter provides a natural framework within which to incorporate the sensor measurements and estimate the state of the robot. A convenient formulation of the Kalman filter allows the system state, which naturally lies on a manifold due to the presence of a rotation element, be represented in terms of a matrix group structure.

The system state $\boldsymbol{y}$ is embedded in a matrix group. The state is split into a part $\boldsymbol{y}^o = (\boldsymbol{\sigma}, \boldsymbol{\psi}, \boldsymbol{m}_z, \boldsymbol{n}, \boldsymbol{m})$ and a part $\boldsymbol{y}^g = (\boldsymbol{p}, \boldsymbol{q})$, where $\sigma_i$ is the material arc length along the $i^{\text{th}}$ tube, $\psi_i$ is the rotational displacement of the tube relative to the Bishop frame, $m_{iz}$ is the torsional moment carried by the $i^{\text{th}}$ tube, $\boldsymbol{p}$ is the position of the robot centerline, $\boldsymbol{q}$ is the orientation of the Bishop frame, $\boldsymbol{n}$ is the

internal force, and $\boldsymbol{m}$ is the internal moment. These parts then placed in a matrix as

$$\boldsymbol{y} = \begin{bmatrix} \mathbf{X} & \mathbf{0} \\ \mathbf{0} & \boldsymbol{y}^g \end{bmatrix} \tag{6.1}$$

where

$$\mathbf{X} = \begin{bmatrix} \mathbf{I}_{n\times n} & \boldsymbol{y}^o \\ \mathbf{0}_{1\times n} & 1 \end{bmatrix} \tag{6.2}$$

The dimension of the state is $p = 3N + 12$ where $N$ is the number of tubes, but $3N + 13$ numerical values are used so that the rotation element $\boldsymbol{q}$ can be represented without a singularity as a quaternion. It is straightforward to verify that matrix multiplication results in addition for the part $\boldsymbol{y}^o$, and multiplication (the homogeneous transformation law) on the geometry part $\boldsymbol{y}^g$.

The mechanics model propagates the state along the arc length:

$$\boldsymbol{y}' = \boldsymbol{y}\widehat{\boldsymbol{\chi}}(\boldsymbol{y}) \tag{6.3}$$

The quantity $\widehat{\boldsymbol{\chi}}(\boldsymbol{y})$ is an element of the Lie algebra, which encodes derivatives of $\boldsymbol{x}$ and $\boldsymbol{g}$. This matrix has the form

$$\widehat{\boldsymbol{\chi}} = \begin{bmatrix} \mathbf{T} & \mathbf{0} \\ \mathbf{0} & \widehat{\boldsymbol{\xi}} \end{bmatrix}, \qquad \mathbf{T} = \begin{bmatrix} \mathbf{0}_{n\times n} & \boldsymbol{f}(\boldsymbol{y}) \\ \mathbf{0}_{1\times n} & 0 \end{bmatrix} \tag{6.4}$$

so that on each respective part of the state one has

$$\begin{aligned} \frac{\partial}{\partial s}\boldsymbol{y}^g &= \boldsymbol{y}^g\widehat{\boldsymbol{\xi}}(\boldsymbol{y}) \\ \frac{\partial}{\partial s}\boldsymbol{y}^o &= \boldsymbol{f}(\boldsymbol{y}) \end{aligned} \tag{6.5}$$

Define the natural mapping between $\mathbb{R}^{(3N+12)}$ and the elements $\widehat{\boldsymbol{\chi}}$ as

$$\boldsymbol{\chi} = \begin{bmatrix} \boldsymbol{f}(\boldsymbol{y}) \\ \boldsymbol{\xi} \end{bmatrix} = [\widehat{\boldsymbol{\chi}}]^\vee \tag{6.6}$$

and the inverse mapping is provided by

$$\begin{bmatrix} f(y) \\ \xi \end{bmatrix}^{\wedge} = \widehat{\chi} \tag{6.7}$$

The "vee" and "hat" notation is overloaded to work for both the full state vector and for only the geometric part. On the geometric part of the equations $\xi = \begin{bmatrix} v^T & \omega^T \end{bmatrix}^T$ is the usual 6-dimensional twist vector describing a rigid body velocity.

The extended Kalman filter propagates the mean and covariance according to a process model with noise and discrete measurement updates. The process noise model is additive with $\widehat{\chi}$, so that the process is given by

$$y' = y(\widehat{\chi} + \widehat{n}_{\chi}) \tag{6.8}$$

The noise term is normally distributed so that $\mathrm{cov}(n_{\chi}, n_{\chi}) = \mathbf{Q}$. $\mathbf{Q}$ is a symmetric matrix whose entries depend on the nature and magnitude of the noise in each of the state equations.

The mean state $\mu(s)$ is a group element and the covariance matrix $\mathbf{P}(s)$ describes the uncertainty in the body frame, such that a sample $\tilde{y}$ is drawn from the distribution through $\tilde{y} = \mu \exp(\widehat{z})$, where $z$ is independently normally distributed with covariance $\mathrm{cov}(z, z) = \mathbf{P}$. The exponential on this product group is given by

$$\exp(\widehat{z}) = (z^o, \exp(\widehat{z^g})) \tag{6.9}$$

The filter propagates these in arc length according to the differential equations

$$\mu' = \mu\widehat{\chi}(\mu) \tag{6.10}$$

$$\mathbf{P}' = \mathbf{F}\mathbf{P} + \mathbf{P}\mathbf{F}^T + \mathbf{Q} \tag{6.11}$$

where

$$\mathbf{F} = \mathbf{J}_{\chi} - \mathrm{ad}(\chi) \tag{6.12}$$

and

$$\mathrm{ad}(\boldsymbol{\chi}) = \begin{bmatrix} \mathbf{0} & \mathbf{0} \\ \mathbf{0} & \mathrm{ad}_{se3}(\boldsymbol{\xi}) \end{bmatrix} \tag{6.13}$$

In this last equation the term $\mathrm{ad}(\boldsymbol{\xi})$ is defined by

$$\mathrm{ad}_{se3}(\boldsymbol{\xi}) = \begin{bmatrix} \widehat{\omega} & \widehat{v} \\ 0 & \widehat{\omega} \end{bmatrix} \tag{6.14}$$

The Jacobian matrix $\mathbf{J}_\chi$ is the matrix of all directional derivatives of $\boldsymbol{\chi}(\boldsymbol{y})$ with respect to perturbations of $\boldsymbol{y}$ along the standard basis directions $\boldsymbol{e}_1, ..., \boldsymbol{e}_n$ and $\boldsymbol{E}_1, ...\boldsymbol{E}_6$ in the body frame convention. In block matrix form,

$$\mathbf{J}_\chi = \begin{bmatrix} \mathbf{A} & \mathbf{B} \\ \mathbf{C} & \mathbf{D} \end{bmatrix} \tag{6.15}$$

the blocks are defined element-wise by

$$\begin{aligned} A_{ij} &= \frac{\partial f_i}{\partial x_j}, \quad B_{ij} &&= \tilde{E}_j^r(f_i) \\ C_{ij} &= \frac{\partial \xi_i}{\partial x_j}, \quad D_{ij} &&= \tilde{E}_j^r(\xi_i) \end{aligned} \tag{6.16}$$

Blocks **B** and **D** use the directional derivative operator

$$\tilde{E}_i^r(f) = \frac{d}{d\gamma} f(\boldsymbol{x}, \boldsymbol{g}\exp(\gamma \boldsymbol{E}_i))\Big|_{\gamma=0} \tag{6.17}$$

The basis vectors $\boldsymbol{E}_i = \widehat{\boldsymbol{e}_i}$ for $i = 1$ through 6, which are the standard basis elements for the Lie algebra $\mathfrak{se}(3)$.

### 6.3.3 The EKF Measurement Updates

The update step is carried out at discrete measurement locations where information is added by sensing partial information about the state. In the case of the magnetic tracking data used in the

experiments, the sensors measure the position $\boldsymbol{p}(s)$ and the tangent axis $\boldsymbol{z}(s)$ of the centerline of the curve at discrete points $s_k$ on the robot. The Kalman filter update equations

$$\begin{aligned}
\mathbf{K}_k &= \mathbf{P}^- \mathbf{H}_k^T (\mathbf{H}_k \mathbf{P}^- \mathbf{H}_k^T + \mathbf{C}_k)^{-1} \\
\delta\boldsymbol{\mu} &= \mathbf{K}_k \boldsymbol{z}_k \\
\boldsymbol{\mu}^+ &= \boldsymbol{\mu}^- (\mathbf{I} + \delta\boldsymbol{\mu}^\wedge) \\
\mathbf{P}^+ &= (\mathbf{I} - \mathbf{K}_k \mathbf{H}_k) \mathbf{P}^- (\mathbf{I} - \mathbf{K}_k \mathbf{H}_k)^T + \mathbf{K}_k \mathbf{C}_k \mathbf{K}_k^T
\end{aligned} \tag{6.18}$$

apply at this location, with the state $(\boldsymbol{\mu}^-, \mathbf{P}^-)$ becoming $(\boldsymbol{\mu}^+, \mathbf{P}^+)$ across the discontinuity in the solution where the sensor adds new information to the estimate. Equation (6.18) conveniently encodes the update step for both the mechanics part of the state and the geometry part of the state. The innovation $\boldsymbol{z}_k$ is defined as the difference between the measured value and the predicted measurement. The matrix $\mathbf{H}_k$ maps the body-frame state "error" $\delta\boldsymbol{\mu}$ onto the difference in actual and predicted measurements:

$$\mathbf{H}_k \delta\boldsymbol{\mu} = \boldsymbol{z}_k \tag{6.19}$$

For $\boldsymbol{z}_k$ to be a difference in position in the spatial frame, for example, the matrix $\mathbf{H}_k$ must rotate the relevant part of $\delta\boldsymbol{\mu}$ from the body-frame representation to the spatial frame representation, yielding for a robot with $N$ tubes that

$$\mathbf{H}_k = \begin{bmatrix} \mathbf{0}_{3\times(3N+6)} & \mathbf{0}_{3\times3} & \mathbf{R}(\boldsymbol{q}^-) & \mathbf{0}_{3\times3} \end{bmatrix} \tag{6.20}$$

for the position sensors. For the tangent axis measurement the matrix $\mathbf{H}_k$ is given by

$$\mathbf{H}_k = \begin{bmatrix} \mathbf{0}_{3\times(3N+6)} & \mathbf{0}_{3\times3} & -\mathbf{R}(\boldsymbol{q}^-)\widehat{\boldsymbol{e}}_3 \end{bmatrix} \tag{6.21}$$

The matrix $\mathbf{R}(\boldsymbol{q})$ is the rotation matrix associated with the unit quaternion $\boldsymbol{q}$.

### 6.3.4 Smoothing and Iterating

The smoothed estimate $\boldsymbol{\mu}_s$ and associated covariance $\mathbf{P}_s$ are solved for in a backwards integration step (from the tip to the base of the robot) once the posterior mean $\boldsymbol{\mu}$ and covariance $\mathbf{P}$ are known from solving the forward filter equations. The equations governing the smoothed estimate and smoothed covariance are

$$\begin{aligned} \boldsymbol{\mu}_s' &= \boldsymbol{\mu}_s \left[ \boldsymbol{\chi}(\boldsymbol{\mu}_s) + \mathbf{Q}\mathbf{P}^{-1}(s)(\boldsymbol{\mu}^{-1}\boldsymbol{\mu}_s - \mathbf{I})^{\vee} \right] \\ \mathbf{P}_s' &= (\mathbf{F} + \mathbf{Q}\mathbf{P}^{-1})\mathbf{P}_s + \mathbf{P}_s(\mathbf{F} + \mathbf{Q}\mathbf{P}^{-1})^T - \mathbf{Q} \end{aligned} \tag{6.22}$$

The continuity of the solution is guaranteed by these differential equations [178].

The smoothed estimate is then used as the force estimate and partially as a new estimate for the unknown boundary conditions at the base of the robot. The distal boundary conditions, $\boldsymbol{b}(\boldsymbol{y}(L)) = 0$ as a function of the state vector, act as an additional measurement on the state. This false measurement is added to the list of measurements during the forward sweep of the Kalman filter, and at the end of the backwards sweep the unknown initial states $\boldsymbol{y}_u(L)$ have been partially updated to the necessary values in order that the distal boundary function is approximately maintained. Upon solving the smoothing equations backwards, the initially unknown parts of the state at the proximal end of the robot, namely the torsional moments $\boldsymbol{m}_z$ and the internal force and torque $\boldsymbol{n}$ and $\boldsymbol{m}$ are updated and then used as the initial condition for the subsequent forward solve.

The new configuration variables $\boldsymbol{c}^{i+1}$, which describe the actuator locations at the next time, are incorporated into the state as new initial conditions at the base of the robot, and combine with the estimated unknowns from the prior solve to form a complete initial condition for the forward solution. Although in principle the covariance could be propagated forward in time after each solve and the new actuation could be treated as a measurement like any other, the simpler approach of simply resetting the covariance matrix to a fixed value for each new time step prevents some numerical instability issues and also ensures that the filter does not "lock-on" to a fixed value for the external loads and become too slow in its future estimations.

### 6.3.5 Observability

This procedure requires a set of measurements for which the complete state is observable. However, the observability requirement is not particularly restrictive, which is easily shown through a heuristic argument. In the absence of external forces the boundary value problem is solvable using only known information, that is without any additional measurements. If the compliance map relating differential changes in the applied loads and the additional external sensor measurements provides information which is linearly independent or "full-rank", the system remains observable in the presence of external loads. In particular, a single three dimensional force can be predicted from a single, additional three-dimensional position measurement at a point along the robot which experiences a three-dimensional deflection under that force.

On the other hand, if the observability matrix relating changes in the sensor measurements to changes in the system state is singular or nearly so, as would be the case for an infinitely rigid, straight rod with an axially applied force, then the force cannot be observed from the deflection. This implies the requirement that the robot be substantially curved, but since precurvature is the principle which enables actuation at all in concentric tube robots, a single applied force at the robot end-effector is observable.

## 6.4 Experimental Validation

### 6.4.1 Materials & Methods

The above framework was tested using an NDI Aurora magnetic tracking system for position-based feedback in a three-tube concentric tube robot. The experimental setup is shown in Figure 6.3. The constrained exit point of the tubes was first registered using a point-based registration to fiducial marks embedded in the front of the robot, providing the rigid transformation between the tracker frame and the robot base frame. In order to ensure that this registration provides a consistent initial tangent orientation for the duration of the experiment, the tube was placed through a rigidly mounted PTFE sleeve with a slight interference fit that supports approximately 2 cm of the

tube length.

The concentric tubes were designed as a straight segment followed by a curved segment. The initial, unconstrained shapes of the tubes were determined by pulling a tracking coil down the center of each tube at a rate of a few millimeters per second while it was fixed to a flat table with a temporary adhesive. Approximately 2,500 data points were collected along the length of each tube. These measurements were then fit with a piecewise polynomial having 20 segments to produce a function $\boldsymbol{p}(s)$ describing the tube, parameterized by the arc length variable with $ds = \sqrt{dx^2 + dy^2 + dz^2}$, and the derivatives of the fit curve were used to compute the curvature function for each tube according to the Bishop frame equations,

$$\begin{aligned} u_{ix}^* &= -(\boldsymbol{p}_i^*)''(s) \cdot \boldsymbol{y}_i^*(s) \\ u_{iy}^* &= (\boldsymbol{p}_i^*)''(s) \cdot \boldsymbol{x}_i^*(s) \end{aligned} \tag{6.23}$$

where $\boldsymbol{x}_i^*$ and $\boldsymbol{y}_i^*$ are the vectors of the Bishop frame which satisfies the equations

$$\begin{aligned} \frac{\partial}{\partial s}\boldsymbol{p}_i^* &= \mathbf{R}_i^* \boldsymbol{e}_3 \\ \frac{\partial}{\partial s}\mathbf{R}_i^* &= \mathbf{R}_i^* \widehat{\boldsymbol{u}}_i^* \end{aligned} \tag{6.24}$$

with $\boldsymbol{u}_i^* = \begin{bmatrix} u_{ix}^* & u_{iy}^* & 0 \end{bmatrix}^T$. The fit $\boldsymbol{p}_i^*(s)$ was chosen by a nonlinear optimization of the piecewise polynomial control points to minimize the mean distance from the collection of points to the spline curve. The resulting curvature functions are shown in Figure 6.2. The largest (primary) component of the curvature function is shown for each tube The shapes are approximately planar, making the other non-zero curvature component close to zero. The secondary component of the curvature, not shown in the figure, was retained for use in the model.

The remaining tube parameters such as the length and diameter are shown in Table 6.1. The overall length of each tube was measured with a standard ruler by straightening the tube against the ruler edge. The outer and inner diameters were provided from manufacturer's data, and are provided for scale. They are not needed for the model, and the directly measured stiffnesses were

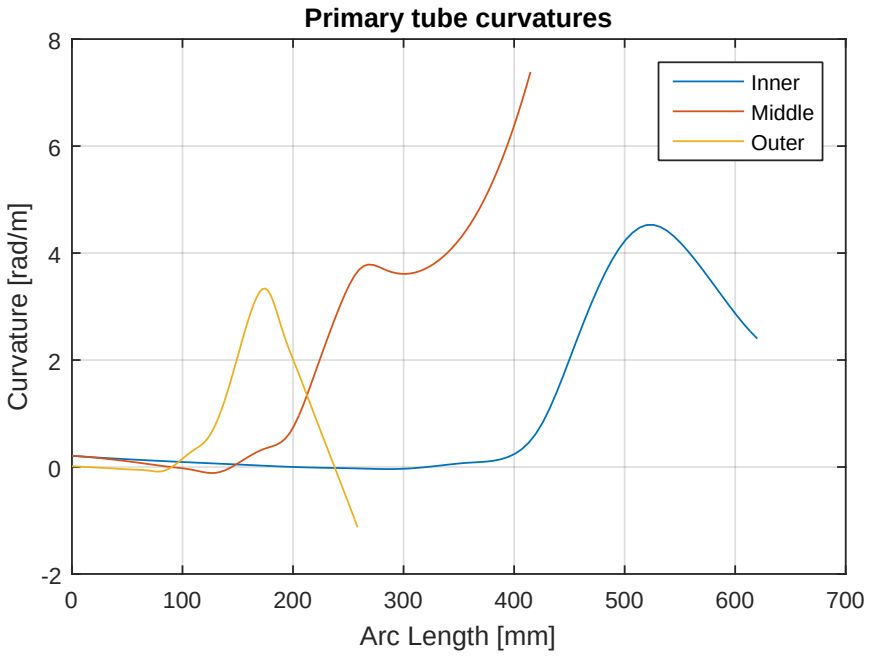


Figure 6.2: Primary tube curvatures along the local $\boldsymbol{x}_i^*$ axis.

used in the experimental data analysis instead of a calculated stiffness. The bending stiffness of each tube was characterized by a three-point bending test. Using the standard formula for the cross-sectional second area moment, a computed value of Young's modulus for each tube fell within the range of 59 - 67 GPa, which is within manufacturer's estimates for Nitinol. The only other relevant material parameter for the mechanics model is Poisson's ratio, or equivalently the ratio between bending and torsional stiffness. The value 0.33 was used for Poisson's ratio based on manufacturer's data.

The magnetic tracking coils were placed at two locations along the length of the robot. The first coil was placed 7.8 mm from the distal tip, and the second coil was placed 114 mm from the distal tip. Each coil measures the position in coordinates of the tracker's base frame and the tangent vector which points along the axis tangential to the robot centerline.

| Parameter | Inner | Middle | Outer |
|---|---|---|---|
| Length [mm] | 620 | 415 | 258 |
| O.D. [mm] | 1.27 | 1.92 | 2.54 |
| I.D. [mm] | 1.07 | 1.58 | 2.25 |
| Stiffness [mN-m$^2$/rad] | 3.749 | 23.90 | 46.88 |

Table 6.1: The tube parameters for the force-sensing experiment.

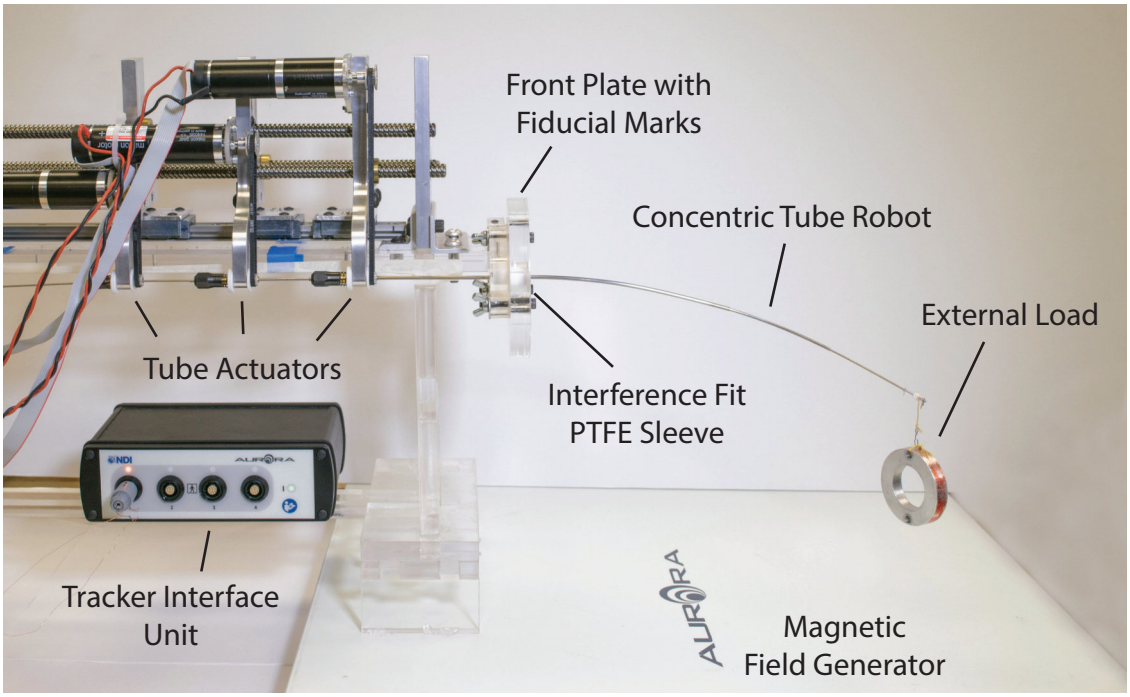


Figure 6.3: Experimental setup for testing intrinsic force estimation

### 6.4.2 Calibration

The robot was driven to 20 randomly generated positions with the actuators following piece-wise linear trajectories between the points. No load was placed on the robot. As the robot moved through the programmed trajectory, the actuator positions were recorded at 50 Hz and the positions of two magnetic tracking coils were recorded at 40 Hz. These two streams were post-processed to time-align them and were then resampled to 5 Hz for analysis. This set of data was then trimmed to remove artifacts that resulted from the resampling step.

The remaining set of 11,906 data points was then used to calibrate nuisance parameters to achieve an optimal fit between the forward kinematic model and the recorded data in terms of

| Parameter | Value |
|---|---|
| $r_x$ [rad] | 0.0178881 |
| $r_y$ [rad] | 0.000376569 |
| $\beta_{1h}$ [mm] | -292.6 |
| $\beta_{2h}$ [mm] | -219.9 |
| $\beta_{3h}$ [mm] | -126.7 |
| $\psi_{1h}$ [rad] | -0.271 |
| $\psi_{2h}$ [rad] | 0.132 |
| $\psi_{3h}$ [rad] | 0.040 |
| $d_s$ [mm] | 106.7 |

Table 6.2: Calibrated parameters for the force sensing experiment

the mean absolute error between corresponding pairs of points. Parameters calibrated included two rotational parameters in the registration corresponding to the axes in the plane of the front of the robot, the six actuator home locations, and the distance between the tracking coils. The rotational parameters are denoted $r_x$ and $r_y$, the actuator home rotations by $\psi_{ih}$ and translations by $\beta_{ih}$, and the inter-sensor distance by $d_s$. The resulting parameters are shown in Table 6.2. The final mean error between the open-loop forward kinematic model and the measured sensor data was approximately 4 mm.

### 6.4.3 Experimental Protocol

A hanging mass of 27.1 g was suspended from the end effector of the robot while it was moved through a preprogrammed trajectory. The robot was driven to 20 randomly generated positions with the actuators following piecewise linear trajectories between the points. Figure 6.4 shows the actuator paths over the course of the experiment, which lasted for a duration of 2,505 seconds. The rotational actuation was constrained so as not to induce snapping or instability under the applied load. During this time, the magnetic tracker was set to record the locations and orientations of two tracking coils placed in the central lumen of the robot. After the actuator locations and tracker data data was collected, it was processed to time-align, resample and decimate to 5 Hz.

The forward Kalman filter and backward RTS equation were programmed to use all of the available data with varying levels of uncertainty. The initial covariance matrix (initial in arc length)

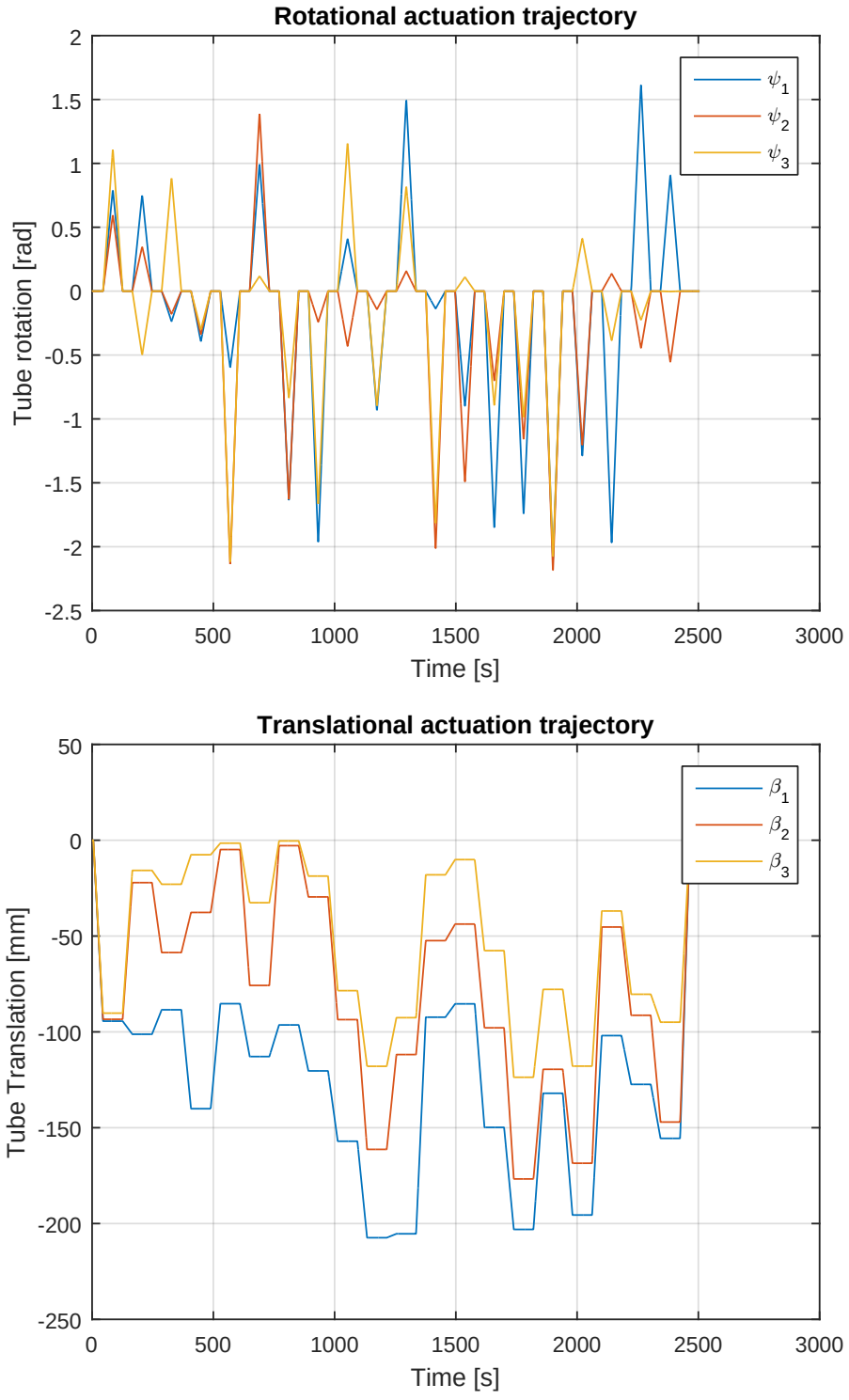


Figure 6.4: The actuator trajectories during the force sensing experiment. The random rotational and translational actuation was performed over 2,505 s to generate a set of continuous test configurations.

is set to a constant value for each time point at the most proximal actuator location, then integrated forward and backwards to achieve the complete estimate. The filter was set up to estimate all of the model states, but the Kalman update equation excludes the update for $\boldsymbol{\sigma}$, which is known to a high degree of certainty from the inextensibility of the tubes. Updating $\boldsymbol{\sigma}$ could also cause the unpleasant possibility of a tube ending at one arc length and then reappearing at a later arc length due to a measurement changing the value of $\sigma_i$. At the end of the backwards smoother solution, the residual value of $\sigma_1$ was used to offset the actuator location for the innermost tube. This closes the loop on tangential error and prevents mismatches between the true arc length at the first sensor and the modeled arc length, which would produce large force estimates. The modeled distance between the two sensors was fixed, however, for the entire estimation period.

The initial covariance matrix was set to a diagonal matrix, with blocks specified according to each component of the state. The initial conditions, with units, were as follows:

$$\begin{aligned}
\mathbf{P}_{\sigma\sigma}(\beta) &= 1.0 \times 10^{-6}\ \mathbf{I}_{3\times3} \quad (\mathrm{m}^2) \\
\mathbf{P}_{\psi\psi}(\beta) &= 2.7 \times 10^{-4}\ \mathbf{I}_{3\times3} \quad (\mathrm{rad}^2) \\
\mathbf{P}_{m_z m_z}(\beta) &= 1.0 \times 10^{-4}\ \mathbf{I}_{3\times3} \quad (\mathrm{N}^2\mathrm{m}^2) \\
\mathbf{P}_{pp}(0) &= 1.0 \times 10^{-4}\ \mathbf{I}_{3\times3} \quad (\mathrm{m}^2) \\
\mathbf{P}_{qq}(0) &= 8.1 \times 10^{-3}\ \mathbf{I}_{3\times3} \quad (\mathrm{rad}^2) \\
\mathbf{P}_{NN}(\beta) &= 1.0 \times 10^{-4}\ \mathbf{I}_{3\times3} \quad (\mathrm{N}^2) \\
\mathbf{P}_{MM}(\beta) &= 1.0 \times 10^{-4}\ \mathbf{I}_{3\times3} \quad (\mathrm{N}^2\mathrm{m}^2)
\end{aligned} \tag{6.25}$$

The arc length $\beta$ is defined as the minimum arc length of any of the tubes' grasped locations. Note that the covariance for the states $\boldsymbol{p}$ and $\boldsymbol{q}$ is known at the front of the robot, where the registration is measured, rather than at the actuators. To transform these to the arc length $\beta$, the

adjoint transformation law is used [179],

$$\begin{bmatrix} \mathbf{P}_{pp}(\beta) & \mathbf{P}_{pq}(\beta) \\ \mathbf{P}_{qp}(\beta) & \mathbf{P}_{qq}(\beta) \end{bmatrix} = \begin{bmatrix} \mathbf{R} & \widehat{\boldsymbol{p}}\mathbf{R} \\ 0 & \mathbf{R} \end{bmatrix} \begin{bmatrix} \mathbf{P}_{pp}(0) & \mathbf{P}_{pq}(0) \\ \mathbf{P}_{qp}(0) & \mathbf{P}_{qq}(0) \end{bmatrix} \begin{bmatrix} \mathbf{R} & \widehat{\boldsymbol{p}}\mathbf{R} \\ 0 & \mathbf{R} \end{bmatrix}^T \tag{6.26}$$

where $\mathbf{R}$ and $\boldsymbol{p}$ in this expression are the rotation and translation from the front of the robot to the most proximal actuator location, typically given by $\mathbf{R} = \mathbf{I}$ and $\boldsymbol{p} = \beta \boldsymbol{e}_3$. The derivatives required for the integration of the covariance matrix are provided in Appendix A.3. The process covariance matrix is set to zero except for the block corresponding to the body-frame angular velocity of $\boldsymbol{q}$ and the equation for $\boldsymbol{m}_z'$. The former covariance block was set to $\mathbf{Q}_{qq} = 2.5 \times 10^{-5}\ \mathbf{I}_{3\times3}$, and the latter to $\mathbf{Q}_{m_z m_z} = 1.0\ \times 10^{-4}\ \mathbf{I}_{3\times3}$.

For each measurement in time, the filter equations were applied once with a single forward and backward integration. The initial conditions for the states $\boldsymbol{\sigma}$, $\boldsymbol{\psi}$, $\boldsymbol{p}$, and $\boldsymbol{q}$ are specified by measurements at $s = \beta$. The remaining states $\boldsymbol{n}$, $\boldsymbol{m}$, and $\boldsymbol{m}_z$ are carried forward based on the solution provided by the solution of the RTS equations at the previous time step, modeling quasistatic (slowly moving) conditions.

The Kalman filter incorporated eight separate measurements during the forward integration. At each of the sensors a measurement was made on the position $\boldsymbol{p}(s_k)$, $k = 1,2$ and the tangent vector $\mathbf{R}(s_k)\boldsymbol{e}_3$. The measurement covariance matrices for these sensors measurements were chosen to be $1 \times 10^{-6}\ \mathbf{I}_{3\times3}$ and $2.5 \times 10^{-3}\ \mathbf{I}_{3\times3}$, respectively. Their units are $\mathrm{m}^2$ and $\mathrm{rad}^2$, respectively. At the endpoint of each tube, a false measurement was made that the torsional moment $m_{iz}$ is zero. For the innermost tube, this measurement had covariance $1 \times 10^{-12}\ \mathrm{N}^2\mathrm{m}^2$, and for the outer two tubes, the measurement had covariance $1 \times 10^{-6}\ \mathrm{N}^2\mathrm{m}^2$. Additionally, at the distal end of the robot, a measurement was made at each time step that no internal moment is present (it must vanish at the end of the robot), and this measurement was simulated to have covariance $1 \times 10^{-12}\ \mathrm{N}^2\mathrm{m}^2$.

In addition to processing the physical data, the code was validated to function correctly by simulating the same trajectory as was followed by the hardware. The 266 mN load was simulated in a downward direction, and the magnetic tracking sensors were simulated without noise or bias.

## 6.5 Results

The results of the software validation are shown in Figure 6.5. The state estimation system rapidly converges to a small steady-state error, and a small amount of noise is present due to the time-varying inputs, which are not accounted for in the quasistatic filtering system. The results of the physical experiment are shown in Figures 6.6 through 6.8. The filter does not converge on an estimate for the force because of the choice of a constant initial covariance matrix. The force magnitude, shown in Figure 6.7 is estimated with error between minimum and maximum bounds of -20% and +20% error after the initial ramp up period and before the final ramp down period. During this central period the magnitude error has mean -2.6% and standard deviation 7.5%. The initial and final ramp up and down are due to the fact that in the starting and ending configurations the dead mass was resting on the surface of the tracker and therefore applied a smaller load to the robot. The angular error, shown in Figure 6.8, in the force prediction is similarly small, with the mean angular error of 8.6 degrees and standard deviation of 3.2 degrees.

## 6.6 Discussion

The technique of using state-reconstruction techniques for the estimation of the internal loads is useful from the standpoint that only a-priori knowledge and a basic calibration are required for the estimation procedure. This is in contrast to a data-fitting approach which uses regression models, which would require an extremely rich data set to accomodate all of the possible loading scenarios. The mechanics model provides rich information which would be expensive and time-consuming to learn from a large, high-dimensional data set.

The errors present in the force prediction arise from the discrepancy between the physical robot and the model. Although the filter maintains the estimate within reasonable bounds through the incorporation of model uncertainty, there is an inherent tradeoff between the speed and accuracy of the prediction and the risk of instability and filter divergence due to rapidly changing estimates on the underlying nonlinear problem. This tradeoff is managed through the selection of the covariance

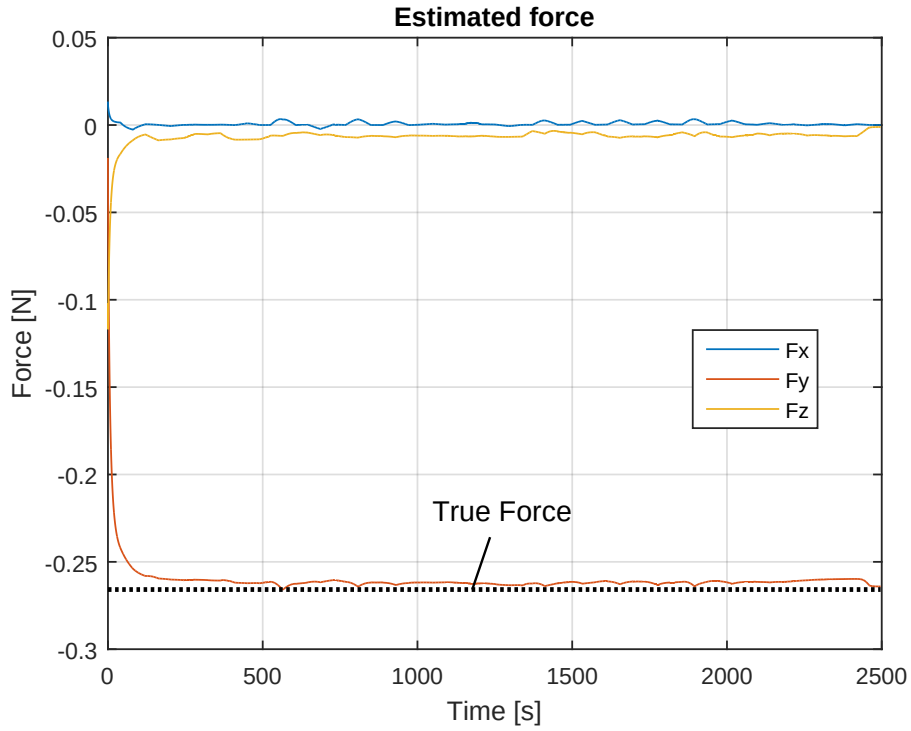


Figure 6.5: The simulated force sensing system validates correct operation of the software.

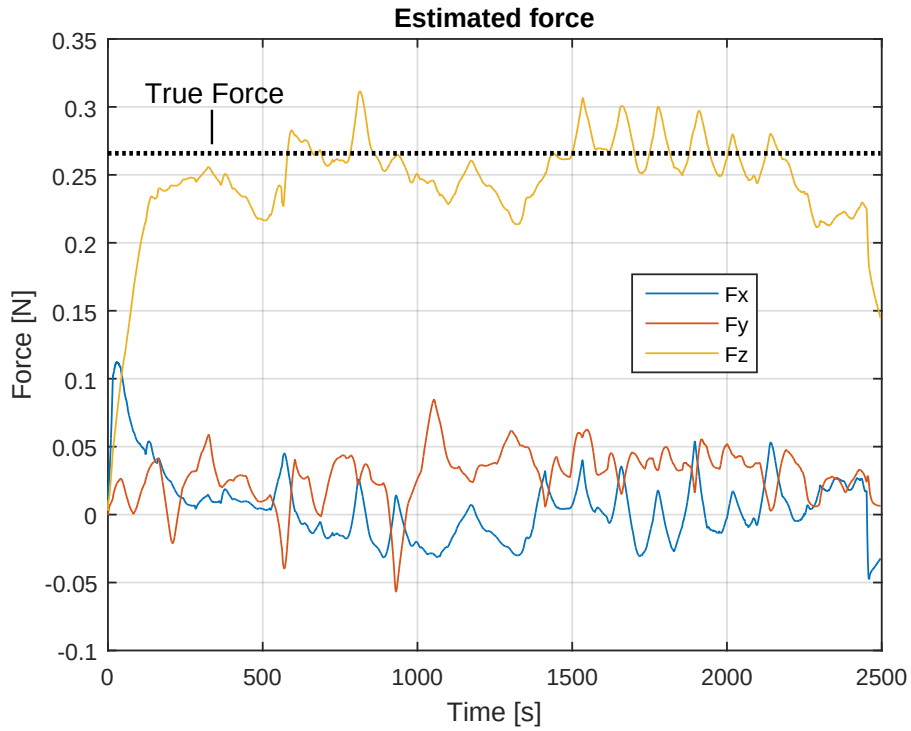


Figure 6.6: The estimated forces over the complete experimental trial.

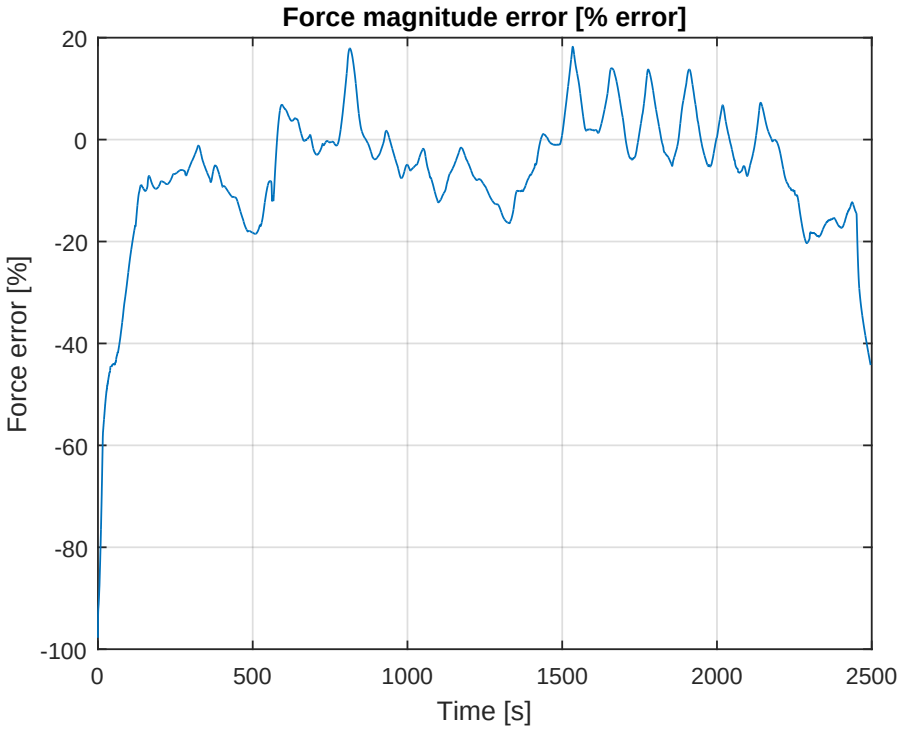


Figure 6.7: The magnitude error in the force estimation.

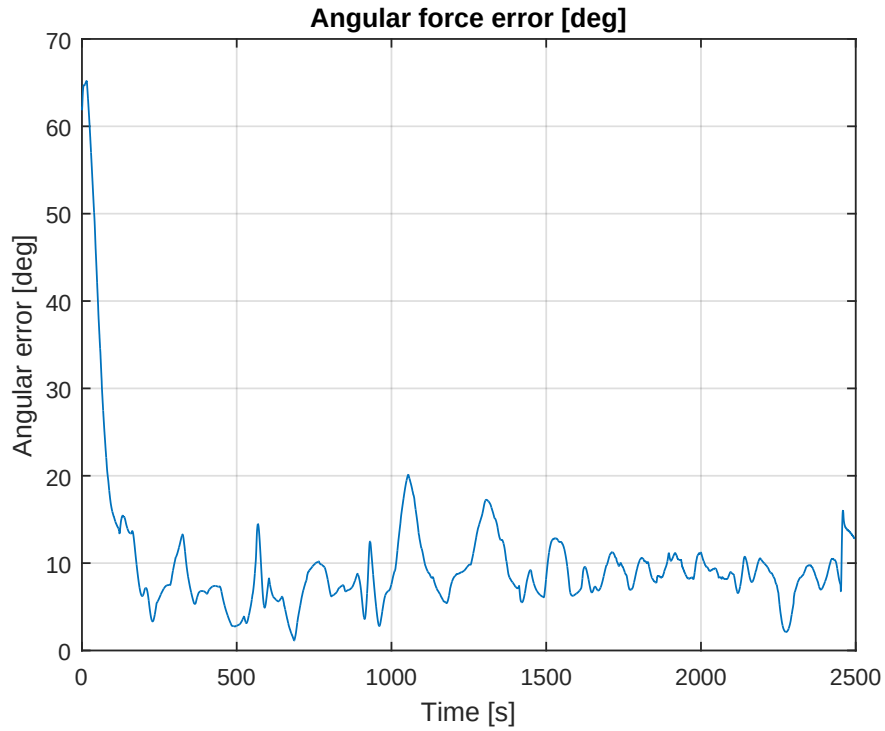


Figure 6.8: The angular error in the force estimation.

matrices, where lower model and process covariance result in greater trust in the model.

It was observed that the performance of the method is highly sensitive to the selected covariance matrices. For example, despite the fact that the true measurement covariance on the magnetic tracking coils is much lower than the values used for the tangent axis measurement in the Kalman filter, it was observed that lowering this value to even half as much as the values reported caused the estimation to diverge. This is likely due to the fact the measured values are "unlikely" according to the model. Physically constraining a rod to pass through two points at prescribed arc lengths and with specified tangent angles may create large forces and torques. In selecting the covariance matrices, one must be careful to consider ways in which the model may be overly constrained by the measurements.

There is an underlying assumption that the time-history of the robot is known when the filter is initialized, and that the initial state of the filter is in sufficient agreement with the first set of sensor measurements to avoid divergence of the filter in the initial steps. Because of the possibility of bifurcation in some concentric tube robots, it may not always be sufficient to compute the kinematics using only the known actuator values, since this could result in a solution which is not close to the current physical state of the robot. One way to resolve this is to start the robot in a configuration with the property that the actuator locations specify a unique configuration, such as with all curvatures aligned in a robot with planar tube precurvatures.

The quasistatic conditions imply that the state of the system is slowly changing, thus guaranteeing for most time steps that the solution at the previous time step is close enough to the current state of the robot that the linearization in the filter is a valid approximation. Due to the possibility of snapping, even slowly changing actuation or loads can induce rapid changes in the state, which would likely cause instability in the filter as a result of the linearization being a poor approximation of the model. Two possibilities for resolving this are (1) to run the filter at a very high rate in time, or (2) to alter the Kalman update equation to constrain the state update to remain within a trust region of the linearization, and then iterating the forward and backwards integration steps multiple times at each time step. This second option would convert the Kalman filter (EKF) into an iterated

extended Kalman filter (IEKF) [180]. If the filter state is allowed to drift too far from the actual physical robot state, it may not be possible to guarantee that the filter will converge to an accurate estimate of the physical state.

Associated with the issue of axial stiffness is the possibility of a tracking sensor being at a different true arc length than the modeled sensor. Achieving the low angular error in the force predictions requires the estimation of a length offset for the sensor. The offset parameter is estimated and then applied to the (modeled) value of $\beta_1$ after each iteration in time to correct the modeled sensor arc length to match. Keeping the covariance associated with this parameter small prevents the modeled sensor location from moving too rapidly and causing instability. This approach works well as long as the tube is not nearly straight and under an axial load, in which case a true deflection under load could be estimated as an error in the sensor location.

As can be seen from the results, possible disadvantages of this method are the lack of convergence to a constant load and relatively high noise floor. While the predictive power is adequate for some applications like contact detection with bone during surgery, the filtering approach may not be sufficient for applications requiring high fidelity force estimates on the order of millinewtons of resolution. The noise floor is at about 50 millinewtons in this experiment, which is due to the fact that the filter cannot adequately distinguish, for small external loads, the difference between open-loop modelling error and applied loads. The only ways to resolve this would be to either make the model more accurate or incorporate different sensors which measure information more sensitive to the applied loads (e.g. internal material strains). The former approach could use regression-based models to estimate and correct for the open-loop model error, and the latter approach could incorporate sensors such as fiber-bragg grating strain sensors. Both of these approaches are possible areas of future work.

Another disadvantage of the spatial filter approach is that this method is computationally expensive in comparison to interpolation-based approaches, and a real-time implementation is currently challenging with general purpose processors. The covariance matrices add significant computational burden, and in particular the smoothing equation is difficult to compute due to the required

linear system solves. One possible area of future work for accelerating the computations is parallelization of the methods, which would allow computation with highly parallel graphics processing units or field programmable gate arrays.

Finally, it should be noted that even though the Kalman filter equations are derived to be optimal, many of the assumptions in this derivation are violated in this particular usage. Hence, it is not technically accurate to say that this approach is statistically optimal. The most significant abuse is that equation (6.8) assumes the error in the model consists of only Gaussian, zero-mean noise. In the case of this system, that assumption is not satisfied. Most of the error in the model is due to unmodeled effects such as tube clearance, friction, and imperfect knowledge of the tube precurvatures. These effects tend to create a bias in the model rather than noise. Because of this, the process covariance is difficult to estimate, and in this work was simply manually selected to achieve reasonable performance. As a result, it would probably be more correct to call this method a state observer than a true Kalman filter. It may be possible to improve the performance through the optimal selection of the covariance matrices, which is a possible area for future work.

## 6.7 Conclusions

Intrinsic force sensing and the manipulator-as-sensor paradigm provide new opportunities for gathering force information with the addition of only position and orientation sensing. Through the use of optimal state estimation techniques, the internal loads in concentric tube robots can be estimated based on observed sensor measurements. A Kalman filter and optimal smoother were demonstrated on a prototype concentric tube robot predict a constant dead load at the end effector with mean magnitude error of only 2.7% and mean angular error of only 8.6 degrees. A noise floor was additionally observed at 50 mN for a prototype robot. These force estimates will be useful for future work incorporating environmental contact detection and awareness into surgical robot platforms. Future work will focus on improvement of dynamic algorithm performance, the incorporation of novel sensors, and improvements to the calibration procedure for mitigating the effects of open-loop modeling error.

# Chapter 7

# Future Work and Conclusions

## 7.1 Future Work in Hardware Design

The actuation unit design presented in this thesis builds upon the previously designed actuation units and provides a solution which solves many of the problems encountered in the previous prototypes. It uses modularity to facilitate tool exchange and at the same time to allow for a sterile barrier between the patient and the robot. It also solves the problem of placing multiple tools through the narrow opening of the nostrils. However, several design problems remain open. One such opportunity for design advancement is the incorporation of additional sensing technologies, such as magnetic tracking or fiber Bragg grating strain sensors, while maintaining sterility barriers. The fixed endoscope in the design, which makes sense for pituitary tumor removals, would be better replaced with a flexible robotic endoscope to match the curvilinear capabilities of the concentric tube robots. The incorporation of a robotic stereo endoscope into a small enough package for endoscopic skull base surgery will be challenging, but would vastly improve the system usability.

The shape setting system is currently useful for laboratory prototyping, but could be improved upon by considering other fixture materials which do not suffer the charring and resulting slight error in the final tube shape. One exciting area of research is the possibility for patient-customized robot designs. In order for such a system to be practical for concentric tube robots, there is a need for rapid and accurate shape setting. One possibility is the development of robotic shape setting techniques using fully automated, combined heating and bending robots. Future advancements to the algorithm which drives the shape setting system, and verification of the material properties of the tubes after shape setting may enable rapid fabrication of customized surgical robots which can be ordered to specifications made by automated or semi-automated designers.

## 7.2 Future Work in Modeling and Analysis

The follow-the-leader analysis of Chapter 5 and the elastic stability analysis of Chapter 4 can be extended in many different ways. The basis tenets of the analysis could be applied to other continuum robot architectures. Any continuum structure which is cantilevered will buckle, but robots which have additional complexity stemming from flexible actuation and the associated additional energy storage should provide opportunities for unique analyses. A complete understanding of elastic stability becomes necessary if one wants to take continuum robots to their absolute performance limits. Although the inherent flexibility of continuum robots has been generally presented as an advantage, stability is one price that is paid to gain these advantages. Controllers and motion planners which are "stability-aware" will in the future enable continuum robots to perform tasks with significantly greater dynamic performance and with much greater loads.

When used as needles, concentric tube robots are surrounded by tissue that stabilizes the path which was originally cut, as though there were an additional outer concentric tube. Depending on the tissue properties, this restoring force may allow significant expansion in the set of allowable paths that can be stably traversed by concentric tube robots, whereby an initial straight section of the path, stabilized by the tissue, is then followed by a highly curved section. Although the same type of trajectory could be achieved by including a stiff outer tube, having two curved tubes, opposed in curvature and stabilized by the tissue, would enable more interesting opportunities for steering the needle after it has been partially inserted. This is similar to the design approach of Loser [25], but the stabilizing influence of the tissue has never been modeled or considered.

Similarly, follow-the-leader behavior is a useful strategy for traversing tortuous paths through human anatomy or cluttered environments, and further extensions to the follow-the-leader theory could provide, for example, on-line controllers that correct for follow-the-leader error during an actuation sequence based on feedback from physical measurements. In addition, the follow-the-leader model presented in this thesis assumes that a trajectory which is spatially invariant is optimal. This may not be the case once inhomogeneous tissues or the cutting forces of penetrating tissue are considered. The inclusion of tissue models may reveal greater insight into optimal

follow-the-leader strategies.

Future advancements to the model for concentric tube robots may also warrant revisiting these analyses. The incorporation of additional model effects such as friction, non-concentricity and non-tangency of the tubes will all have some effect on follow-the-leader behavior. The current model, moreover, does not include the effects of the superelastic stress-strain response of Nitinol, which may be responsible for a portion of the observed error in the kinematic model predictions. Despite the fact that the strains encountered are often below the nominal threshold for the onset of superelasticity, multiple calibrations have now found fitted parameter values which lie outside of the physically realistic bounds for the ratio of bending and torsional stiffness of each component tube.

## 7.3 Future Work in Intrinsic Force Sensing

The intrinsic force sensing technique and the experimental results in Chapter 6 are an initial implementation and investigation of what might be possible with intrinsic geometry-based force sensing. There remains much work to do in this area, and future studies will focus on improving the quality of the predictions and on how to use the force estimates for useful purposes during surgery.

Toward the first of these goals, the most likely means of substantial improvement in the force estimates is probably to improve the open-loop kinematic modeling accuracy. As demonstrated in simulation, when the filter receives input data that matches the model perfectly, the resulting performance is quite good. Regression-based error modeling to "close-the-gap" between the mechanics model and the observed experimental data could provide a correction term which is learned through observation. An alternative means to improving the estimates could be to use more sophisticated filtering methods such as filters based on the unscented transform or other non-Gaussian error models. Additional experiments are also necessary to characterize the dynamic performance of the geometry-based force sensing for concentric tube robots. The filtering algorithm should be improved by explicitly incorporating the known information about how the state changes through

time, including the time-varying actuation in particular.

The second goal of using the estimates for surgeons' benefit remains relatively uncharted territory with many opportunities for new ideas and experiments. Even if the fidelity of the estimated forces is not high enough to provide direct feedback to a surgeon through haptics, the robot may still be able to use this information to enforce virtual fixtures around observed critical anatomy, detect the puncture of a suture and provide assistance, or to localize itself within the environment.

## 7.4 Conclusion

Chapter 2 presented the design of a new system for endonasal surgery. The major improvements of this system beyond the already existing prototypes are the implementation of a sterility barrier, the introduction of modular tools, and the ability to deliver four tools through a single nostril. This chapter also presented a method for fabricating the Nitinol tubes used for concentric tube robots by using an electrical heating method under feedback control. Several successful examples of shape setting were demonstrated.

Chapter 3 introduced techniques for efficiently evaluating the kinematics and statics of concentric tube robots. Using the already existing model, this work explored solutions to the problems of real-time computation and computational efficiency, and showed that solution rates an order of magnitude faster than previously reported are possible with careful implementation. The real-time constraint is important for surgical systems, and the ability to solve the model rapidly will facilitate research in motion planning and computational design. A high-order runge kutta method was shown to be accurate and efficient in solving the model equations due to its ability to take large integration steps. Real-time implementation was achieved by conversion of the two-point boundary value problem typically associated with the model differential equations into an initial value problem that can be explicitly solved without iteration.

Chapter 4 provided an analysis of the elastic energy stored by concentric tube robots, and showed that snapping behavior is predicted by the second variation of the stored energy functional. Making the analogy to buckled beams resulted in a connection to the existing literature on the elas-

tic stability of post-buckled beams, from which the tools of analysis were adapted to the concentric tube robot model. A stability computation was introduced, based on a conjugate point condition, that assigns a relative measure of stability to each configuration of the robot, which we believe will be useful for future work in control and motion planning, and it was shown that the addition of a third tube might have benefits in terms of stability over two-tube robots. A physical experiment demonstrated the correctness of the predictions. It was also shown that the behavior can sometimes be avoided in the configuration space when there are more than two tubes, and that three tubes can sometimes be stably rotated through full relative rotations even when two tubes of the same design cannot.

Chapter 5 analyzed follow-the-leader behavior in concentric tube robots, in which the shaft of the robot stays exactly along the path traced by the tip of the robot as it elongates. This type of behavior is useful for traversing solid tissue or constrained lumens. It was shown that perfect behavior is only possible in a subset of designs using a strict subset of actuation, but that all circularly precurved designs of two tubes can closely mimic follow-the-leader behavior with only slight error, and some helical designs may also provide approximately correct behavior. In order to analyze "closeness" to follow-the-leader behavior, a scalar error metric was presented to measure the deviation from the ideal behavior during a given actuation trajectory. A specific actuation sequence in both translation and rotation was chosen for two tubes which resulted in a low follow-the-leader error. An example application in the treatment of epilepsy was examined using these results.

Lastly, Chapter 6 examined the ability of concentric tube robots to act as force sensors. By observing the deflection of the robot under an external load, both the magnitude and direction of that load can in general be inferred. A spatial statistical filter was developed to estimate the configuration of the robot from measurements of the boundary conditions and measurements of the position at two locations along the robot. The combination of a forwards filtering integration and a backwards smoothing integration results in a complete estimate of the state of the robot at every point along its length. This configuration estimate in turn provides a direct estimate of the applied load. It was experimentally demonstrated that the force on a three-tube robot undergoing

large deflections could be inferred with a mean magnitude error of only 2.7%, and with worst case bounds of ± 20% over widely varying tube translations and rotations.

In summary, the hardware design and shape setting method presented in Chapter 2 and the real-time software presented in Chapter 3 together provide a complete endonasal surgical robot. The model analysis of Chapters 4 and 5 provide the means to design concentric tube robots for tasks requiring follow-the-leader deployment and the ability to avoid elastic instabilities. The former is important for tasks requiring traversal of winding lumens or insertion through solid tissues, and the latter is critical to safe operation as both a needle and a manipulator. Concentric tube robots possess many advantageous properties as minimally invasive surgical devices, and it is my hope that this work will be used by future researchers to continue the advancement of continuum robotics in surgery.

# BIBLIOGRAPHY


[1] G. Robinson and J. B. C. Davies. Continuum robots – a state of the art. In *IEEE International Conference on Robotics and Automation*, pages 2849–2854, 1999.

[2] D. Trivedi, C. D. Rahn, W. M. Kier, and I. D. Walker. Soft robotics: Biological inspiration, state of the art, and future research. *Applied Bionics and Biomechanics*, 5(3):99–117, 2008.

[3] R. J. Webster III and B. A. Jones. Design and Kinematic Modeling of Constant Curvature Continuum Robots: A Review. *The International Journal of Robotics Research*, 29(13):1661–1683, June 2010.

[4] E. J. Butler, R. Hammond-Oakley, S. Chawarski, A. H. Gosline, P. Codd, T. Anor, J. R. Madsen, P. E. Dupont, and J. Lock. Robotic Neuro-Endoscope with Concentric Tube Augmentation. In *IEEE/RSJ International Conference on Intelligent Robots and Systems*, pages 2941–2946, 2012.

[5] R. J. Webster III. *Design and Mechanics of Continuum Robots for Surgery*. PhD thesis, The Johns Hopkins University, 2007.

[6] R. J. Webster III, J. M. Romano, and N. J. Cowan. Kinematics and Calibration of Active Cannulas. In *IEEE International Conference on Robotics and Automation*, pages 3888–3895, 2008.

[7] L. A. Lyons, R. J. Webster III, and R. Alterovitz. Planning active cannula configurations through tubular anatomy. In *IEEE International Conference on Robotics and Automation*, pages 2082–2087, 2010.

[8] R. J. Webster III, A. Okamura, and N. J. Cowan. Toward Active Cannulas: Miniature Snake-Like Surgical Robots. In *IEEE/RSJ International Conference on Intelligent Robots and Systems*, pages 2857–2863. IEEE, October 2006.

[9] C. Bedell, J. Lock, A. Gosline, and P. E. Dupont. Design Optimization of Concentric Tube Robots Based on Task and Anatomical Constraints. *IEEE International Conference on Robotics and Automation*, pages 398–403, 2011.

[10] N. V. Vasilyev, P. E. Dupont, and P. J. del Nido. Robotics and Imaging in Congenital Heart Surgery. *Future Cardiolgy*, 8(2):285–296, 2012.

[11] A. H. Gosline, N. V. Vasilyev, E. J. Butler, C. Folk, A. Cohen, R. Chen, N. Lang, P. J. Del Nido, and P. E. Dupont. Percutaneous intracardiac beating-heart surgery using metal MEMS tissue approximation tools. *The International Journal of Robotics Research*, 31(9):1081–1093, August 2012.

[12] A. H. Gosline, N. V. Vasilyev, A. Veeramani, M. Wu, G. Schmitz, R. Chen, V. Arabagi, P. J. del Nido, and P. E. Dupont. Metal MEMS Tools for Beating-heart Tissue Removal. In *IEEE International Conference on Robotics and Automation*, pages 1921–1926. Ieee, May 2012.

[13] R. J. Hendrick, C. R. Mitchell, S. D. Herrell, and R. J. Webster III. Hand-held transendoscopic robotic manipulators: A transurethral laser prostate surgery case study. *The International Journal of Robotics Research*, pages 1559–1572, 2015.

[14] J. Burgner, D. C. Rucker, H. B. Gilbert, P. J. Swaney, P. T. Russell III, K. D. Weaver, and R. J. Webster III. A Telerobotic System for Transnasal Surgery. *IEEE/ASME Transactions on Mechatronics*, 19(3):1–11, 2014.

[15] J. Furusho, T. Katsuragi, T. Kikuchi, T. Suzuki, H. Tanaka, Y. Chiba, and H. Horio. Curved Multi-Tube Systems for Fetal Blood Sampling and Treatments of Organs like Brain and Breast. *International Journal of Computer Assisted Radiology and Surgery*, 1(S1):223–226, May 2006.

[16] M. Terayama, J. Furusho, and M. Monden. Curved multi-tube device for path-error correction in a needle-insertion system. *The International Journal of Medical Robotics and Computer Assisted Surgery*, 3(2):125–134, 2007.

[17] M. S. Berns, E. Y. Tsai, J. Austin-breneman, J. C. Schulmeister, E. Sung, C. K. Ozaki, and C. J. Walsh. Single Entry Tunneler [SET] for Hemodialysis Graft Procedures. In *Design of Medical Devices Conference*, pages 1–8, 2011.

[18] E. C. Burdette, D. C. Rucker, P. Prakash, C. J. Diederich, J. M. Croom, C. Clarke, P. Stolka, T. Juang, E. M. Boctor, and R. J. Webster III. The ACUSITT Ultrasonic Ablator: The First Steerable Needle with an Integrated Interventional Tool. In *Medical Imaging 2010: Ultrasonic Imaging, Tomography, and Therapy*, volume 7629, pages 76290V–1–76290V–10, March 2010.

[19] J. Burgner, P. J. Swaney, T. L. Bruns, M. S. Clark, D. C. Rucker, and R. J. Webster III. An Autoclavable Steerable Cannula Manual Deployment Device: Design and Accuracy Analysis. *Journal of Medical Devices*, 6(4):041007–1–041007–7, 2012.

[20] C. J. Walsh, J. Franklin, A. H. Slocum, and R. Gupta. Design of a Robotic Tool for Percutaneous Instrument Distal Tip Repositioning. In *International Conferennce of the IEEE EMBS*, pages 2097–2100, 2011.

[21] W. Wei, R. E. Goldman, H. F. Fine, S. Chang, and N. Simaan. Performance Evaluation for Multi-arm Manipulation of Hollow Suspended Organs. *IEEE Transactions on Robotics*, 25(1):147–157, 2009.

[22] H. Yu, J.-H. H. Shen, K. M. Joos, and N. Simaan. Design, Calibration and Preliminary Testing of A Robotic Telemanipulator for OCT guided Retinal Surgery. In *IEEE International Conference on Robotics and Automation*, pages 225–231, 2013.

[23] W. Wei and N. Simaan. Modeling, Force Sensing, and Control of Flexible Cannulas for Microstent Delivery. *ASME Journal Dyn. Sys. Meas. Control*, 134(4):41004–41012, 2012.

[24] D. B. Comber, E. J. Barth, and R. J. Webster III. MR-Compatible Precision Pneumatic Active Cannula Robot. *ASME Journal of Medical Devices (In Press)*, 2013.

[25] M. Loser. A New Robotic System for Visually Controlled Percutaneous Interventions under {X-r}ay or {CT}-Fluoroscopy. Master's thesis, The Albert-Ludwig-University, Germany, September 2005.

[26] P. Sears and P. Dupont. A Steerable Needle Technology Using Curved Concentric Tubes. In *IEEE/RSJ International Conference on Intelligent Robots and Systems*, pages 2850–2856. IEEE, October 2006.

[27] C. M. Graves, A. Slocum, R. Gupta, and C. J. Walsh. Towards a Compact Robotically Steerable Thermal Ablation Probe. In *IEEE International Conference on Robotics and Automation*, pages 709–714, 2012.

[28] P. E. Dupont, A. Gosline, N. Vasilyev, J. Lock, E. Butler, C. Folk, A. Cohen, R. Chen, G. Schmitz, H. Ren, and P. del Nido. Concentric Tube Robots for Minimally Invasive Surgery. In *Hamlyn Symposium on Medical Robotics*, pages 3–5, 2012.

[29] J. Burgner, P. J. Swaney, D. C. Rucker, H. B. Gilbert, S. T. Nill, P. T. Russell III, K. D. Weaver, and R. J. Webster III. A Bimanual Teleoperated System for Endonasal Skull Base Surgery. In *IEEE/RSJ International Conference on Intelligent Robots and Systems*, pages 2517–2523. IEEE, September 2011.

[30] R. J. Webster III, N. J. Cowan, G. S. Chirikjian, and A. M. Okamura. Nonholonomic Modelling of Needle Steering. *International Journal of Robotics Research*, 25(5/6):509–526, 2006.

[31] K. Reed, A. Majewicz, V. Kallem, R. Alterovitz, K. Goldberg, N. Cowan, and A. Okamura. Robot-Assisted Needle Steering. *IEEE Robotics & Automation Magazine*, 18(4):35–46, 2011.

[32] N. Abolhassani, R. Patel, and M. Moallem. Needle insertion into soft tissue: a survey. *Medical Engineering & Physics*, 29(4):413–31, 2007.

[33] S. Okazawa, R. Ebrahimi, J. Chuang, S. E. Salcudean, and R. Rohling. Hand-Held Steerable Needle Device. *IEEE/ASME Transactions on Mechatronics*, 10(3):285–296, 2005.

[34] H. B. Gilbert and R. J. Webster III. Can Concentric Tube Robots Follow The Leader? In *IEEE International Conference on Robotics and Automation*, pages 4866–4872, 2013.

[35] J. Furusho, T. Ono, R. Murai, T. Fujimoto, Y. Chiba, and H. Horio. Development of a Curved Multi-Tube(CMT) Catheter for Percutaneous Umbilical Blood Sampling and Control Methods of CMT Catheters for Solid Organs. In *IEEE International Conference on Mechatronics and Automation*, pages 410–415, 2005.

[36] D. C. Rucker, R. J. Webster III, G. S. Chirikjian, and N. J. Cowan. Equilibrium Conformations of Concentric-tube Continuum Robots. *The International Journal of Robotics Research*, 29(10):1263–1280, April 2010.

[37] M. Schwartz. *New Materials, Processes, and Methods Technology*. CRC Press, 2005.

[38] A. Melzer, A. Schmidt, K. Kipfmüller, D. Grönmeyer, and R. Seibel. Technology and principles of tomographic image-guided interventions and surgery. *Surg. Endosc.*, 11(1):946–956, 1997.

[39] W. R. Daum. Deflectable Needle Assembly. US Patent 6,572,593, 2003.

[40] J. Burgner, P. J. Swaney, R. A. Lathrop, K. D. Weaver, and R. J. Webster III. Debulking From Within: A Robotic Steerable Cannula for Intracerebral Hemorrhage Evacuation. *IEEE Transactions on Biomedical Engineering*, 60(9):2567–2575, September 2013.

[41] L. B. Kratchman, M. M. Rahman, J. R. Saunders, P. J. Swaney, and R. J. Webster III. Toward robotic needle steering in lung biopsy: a tendon-actuated approach. In *SPIE*, pages 79641I–79641I–8, 2011.

[42] A. Melzer, M. O. Schurr, M. M. Lirici, B. Klemm, D. Stöckel, and G. Buess. Future Trends in Endoscopic Suturing. *Endoscopic Surgery and Allied Technologies*, 2(1):78–82, 1994.

[43] D. Stoeckel and A. Melzer. New Developments in Superelastic Instruments for Minimally Invasive Surgery. In *Presentation for "Changing Surgical Markets – Increasing Efficiency and Reducing Cost Through New Technology and Procedure Innovation*, 1993.

[44] A. Melzer. Instruments for Endoscopic Surgery. In A. Cuschieri, G. Buess, and J. Périssat, editors, *Operative Manual of Endoscopic Surgery*, page 35. Springer-Verlag, 1992.

[45] A. Cuschieri and G. Buess. Future Advances in Endoscopic Surgery. In A. Cuschieri, G. Buess, and J. Périssat, editors, *Operative manual of endoscopic surgery*, pages 339–347. Springer-Verlag, Berlin, 1992.

[46] T. Duerig and A. Pelton. Nitinol: The Book. http://www.nitinol.com/nitinon-the-book/a-historical-perspective.

[47] R. J. Webster III, J. M. Romano, and N. J. Cowan. Mechanics of Precurved-Tube Continuum Robots. *IEEE Transactions on Robotics*, 25(1):67–78, 2009.

[48] P. E. Dupont, J. Lock, B. Itkowitz, and E. Butler. Design and Control of Concentric-Tube Robots. *IEEE Transactions on Robotics*, 26(2):209–225, April 2010.

[49] D. C. Rucker and R. J. Webster III. Mechanics-Based Modeling of Bending and Torsion in Active Cannulas. In *IEEE/RAS-EMBS International Conference on Biomedical Robotics and Biomechatronics*, pages 704–709, 2008.

[50] D. C. Rucker and R. J. Webster III. Mechanics of Bending, Torsion, and Variable Precurvature in Multi-Tube Active Cannulas. In *IEEE International Conference on Robotics and Automation*, pages 2533–2537, 2009.

[51] P. E. Dupont, J. Lock, and E. Butler. Torsional Kinematic Model for Concentric Tube Robots. In *IEEE International Conference on Robotics and Automation*, volume 2009, pages 2964–2971, May 2009.

[52] M. Mahvash and P. E. Dupont. Bilateral Teleoperation of Flexible Surgical Robots. In *Proc. New Vistas and Challenges in Telerobotics Workshop, IEEE International Conference on Robotics and Automation*, pages 58–64, 2008.

[53] J. Lock, G. Laing, M. Mahvash, and P. E. Dupont. Quasistatic Modeling of Concentric Tube Robots with External Loads. In *IEEE/RSJ International Conference on Intelligent Robots and Systems*, pages 2325–2332, 2010.

[54] D. C. Rucker, B. A. Jones, and R. J. Webster III. A Model for Concentric Tube Continuum Robots Under Applied Wrenches. In *IEEE International Conference on Robotics and Automation*, pages 1047–1052, 2010.

[55] D. C. Rucker, B. A. Jones, and R. J. Webster III. A Geometrically Exact Model for Externally Loaded Concentric Tube Continuum Robots. *IEEE Transactions on Robotics*, 26(5):769–780, 2010.

[56] M. Mahvash and P. E. Dupont. Stiffness Control of a Continuum Manipulator in Contact with a Soft Environment. In *IEEE/RSJ International Conference on Intelligent Robots and Systems*, volume 2010, pages 863–870, December 2010.

[57] D. C. Rucker and R. J. Webster III. Computing Jacobians and compliance matrices for externally loaded continuum robots. In *IEEE International Conference on Robotics and Automation*, pages 945–950. IEEE, May 2011.

[58] R. Xu, A. Asadian, A. S. Naidu, and R. V. Patel. Position Control of Concentric-Tube Continuum Robots using a Modified Jacobian-Based Approach. In *IEEE International Conference on Robotics and Automation*, pages 5793–5798, 2013.

[59] D. C. Rucker and R. J. Webster III. Parsimonious Evaluation of Concentric-Tube Continuum Robot Equilibrium Conformation. *IEEE Transactions on Biomedical Engineering*, 56(9):2308–2311, 2009.

[60] L. Dieci, R. D. Russell, and E. S. Van Vleck. Unitary Integrators and Applications to Continuous Orthonormalization Techniques. *SIAM Journal of Numerical Analysis*, 31(1):261–281, 1994.

[61] R. Xu and R. V. Patel. A Fast Torsionally Compliant Kinematic Model of Concentric-Tube Robots. In *34th Annual International Conference of the IEEE EMBS*, volume 2012, pages 904–907, January 2012.

[62] L. A. Lyons, R. J. Webster III, and R. Alterovitz. Motion Planning for Active Cannulas. In *IEEE/RSJ International Conference on Intelligent Robots and Systems*, pages 801–806, 2009.

[63] L. G. Torres and R. Alterovitz. Motion Planning for Concentric Tube Robots Using Mechanics-based Models. In *IEEE/RSJ International Conference on Intelligent Robots and Systems*, pages 5153–5159. Ieee, September 2011.

[64] R. Alterovitz, S. Patil, and A. Derbakova. Rapidly-Exploring Roadmaps: Weighing Exploration vs. Refinement in Optimal Motion Planning. *IEEE International Conference on Robotics and Automation*, pages 3706–3712, January 2011.

[65] J. J. Abbott, P. Marayong, and A. M. Okamura. Haptic Virtual Fixtures for Robot-Assisted Manipulation. *Springer Tracts Adv. Robot.*, 28:49–64, 2007.

[66] R. J. Webster III, J. P. Swensen, J. M. Romano, and N. J. Cowan. Closed-Form Differential Kinematics for Concentric-Tube Continuum Robots with Application to Visual Servoing. In *International Symposium on Experimental Robotics*, pages 485–494, 2008.

[67] M. Mahvash and P. E. Dupont. Stiffness Control of Surgical Continuum Manipulators. *IEEE Transactions on Robotics*, 27(2):334–345, April 2011.

[68] Y.-L. Park, S. Elayaperumal, B. Daniel, S. C. Ryu, M. Shin, J. Savall, R. J. Black, B. Moslehi, and M. R. Cutkosky. Real-Time Estimation of 3-D Needle Shape and Deflec-

tion for {MRI}-Guided Interventions. *IEEE/ASME Transactions on Mechatronics*, 15(6), 2010.

[69] R. J. Roesthuis, M. Kemp, J. J. van den Dobbelsteen, and S. Misra. Three-Dimensional Needle Shape Reconstruction Using an Array of Fiber Bragg Grating Sensors. *IEEE/ASME Transactions on Mechatronics*, 19(4):1115–1126, 2014.

[70] I. Iordachita, Z. Sun, M. Balicki, J. U. Kang, S. J. Phee, J. Handa, P. Gehlbach, and R. Taylor. A sub-millimetric, 0.25 mN resolution fully integrated fiber-optic force-sensing tool for retinal microsurgery. *International Journal of Computer Assisted Radiology and Surgery*, 4(4):383–390, 2009.

[71] S. C. Ryu and P. E. Dupont. Fbg-based shape sensing tubes for continuum robots. In *Robotics and Automation (ICRA), 2014 IEEE International Conference on*, pages 3531–3537. IEEE, 2014.

[72] P. Puangmali, K. Althoefer, L. D. Seneviratne, D. Murphy, and P. Dasgupta. State-of-the-Art in Force and Tactile Sensing for Minimally Invasive Surgery. *IEEE Sensors J*, 8(4):371–381, 2008.

[73] R. Xu, A. Yurkewich, and R. V. Patel. Curvature, torsion, and force sensing in continuum robots using helically wrapped fbg sensors. *IEEE Robotics and Automation Letters*, 1(2):1052–1059, July 2016.

[74] V. Arabagi, A. Gosline, R. J. Wood, and P. E. Dupont. Simultaneous Soft Sensing of Tissue Contact Angle and Force for Millimeter-scale Medical Robots. In *IEEE International Conference on Robotics and Automation*, pages 4381–4387, 2013.

[75] A. H. Gosline, V. Arabagi, A. Kassam, and P. E. Dupont. Achieving Biocompatibility in Soft Sensors for Surgical Robots. In *Hamlyn Symposium on Medical Robotics*, pages 5–6, 2013.

[76] T. Anor, J. R. Madsen, and P. Dupont. Algorithms for Design of Continuum Robots Using the Concentric Tubes Approach: A Neurosurgical Example. In *IEEE International Conference on Robotics and Automation*, pages 667–673, May 2011.

[77] L. G. Torres, R. J. Webster III, and R. Alterovitz. Task-Oriented Design of Concentric Tube Robots Using Mechanics-Based Models. In *IEEE/RSJ International Conference on Intelligent Robots and Systems*, 2012.

[78] J. Burgner, H. B. Gilbert, and R. J. Webster III. On the Computational Design of Concentric Tube Robots : Incorporating Volume-Based Objectives. In *IEEE International Conference on Robotics and Automation*, pages 1185–1190, 2013.

[79] P. J. Swaney, J. M. Croom, J. Burgner, H. B. Gilbert, D. C. Rucker, K. D. Weaver, P. T. Russell III, and R. J. Webster III. Design of a Quadramanual Robot for Single-Nostril Skull Base Surgery. In *ASME Dynamic Systems and Control Conference*, 2012.

[80] H. Su, D. C. Cardona, W. Shang, A. Camilo, G. A. Cole, D. C. Rucker, R. J. Webster III, and G. S. Fischer. A MRI-Guided Concentric Tube Continuum Robot with Piezoelectric Actuation: A feasibility study. In *IEEE International Conference on Robotics and Automation*, pages 1939–1945. IEEE, May 2012.

[81] D. B. Comber, D. Cardona, R. J. Webster III, and E. J. Barth. Precision Pneumatic Robot for MRI-Guided Neurosurgery. In *Design of Medical Devices Conference*, volume 35, 2012.

[82] E. J. Butler, C. Folk, A. Cohen, N. V. Vasilyev, R. Chen, P. J. del Nido, and P. E. Dupont. Metal MEMS Tools for Beating-heart Tissue Approximation. In *IEEE International Conference on Robotics and Automation*, pages 411–416, May 2011.

[83] K. Xu and N. Simaan. An Investigation of the Intrinsic Force Sensing Capabilities of Continuum Robots. *IEEE Transactions on Robotics*, 24(3):576–587, June 2008.

[84] R. L. Bishop. There is more than one way to frame a curve. *The American Mathematical Monthly*, 82(3):246–251, 1975.

[85] H. Gilbert and R. Webster III. Rapid, reliable shape setting of superelastic nitinol for prototyping robots. *IEEE Robotics and Automation Letters*, 1:98–105, 2015.

[86] S. Ezzat, S. L. Asa, W. T. Couldwell, C. E. Barr, W. E. Dodge, M. L. Vance, and I. E. McCutcheon. The prevalence of pituitary adenomas: a systematic review. *Cancer*, 101(3):613–619, 2004.

[87] P. Cappabianca. *Cranial, craniofacial and skull base surgery*. Springer, 2009.

[88] A. M. Bhatki, R. L. Carrau, C. H. Snyderman, D. M. Prevedello, P. A. Gardner, and A. B. Kassam. Endonasal surgery of the ventral skull base–endoscopic transcranial surgery. *Oral and Maxillofacial Surgery Clinics of North America*, 22(1):157–68, 2010.

[89] C. H. Snyderman, H. Pant, R. L. Carrau, D. Prevedello, P. Gardner, and A. B. Kassam. What are the limits of endoscopic sinus surgery?: The expanded endonasal approach to the skull base. *The Keio Journal of Medicine*, 58(3):152–60, 2009.

[90] J. a. F. Nogueira, A. Stamm, and E. Vellutini. Evolution of endoscopic skull base surgery, current concepts, and future perspectives. *Otolaryngologic Clinics of North America*, 43(3):639–52, 2010.

[91] Central Brain Tumor Registry of the United States (CBTRUS), 2011.

[92] F. G. Barker. Transsphenoidal Surgery for Pituitary Tumors in the United States, 1996-2000: Mortality, Morbidity, and the Effects of Hospital and Surgeon Volume. *Journal of Clinical Endocrinology & Metabolism*, 88(10):4709–4719, October 2003.

[93] B. A. Kohler, E. Ward, B. J. McCarthy, M. J. Schymura, L. A. G. Ries, C. Eheman, A. Jemal, R. N. Anderson, U. A. Ajani, and B. K. Edwards. Annual report to the nation on the status

of cancer, 1975-2007, featuring tumors of the brain and other nervous system. *Journal of the National Cancer Institute*, 103(9):714–36, 2011.

[94] P. Castelnuovo, I. Dallan, P. Battaglia, and M. Bignami. Endoscopic endonasal skull base surgery: past, present and future. *European Archives of Oto-Rhino-Laryngology*, 267(5):649–63, 2010.

[95] A. R. Dehdashti, A. Ganna, I. Witterick, and F. Gentili. Expanded endoscopic endonasal approach for anterior cranial base and suprasellar lesions: indications and limitations. *Neurosurgery*, 64(4):677–89, 2009.

[96] A. B. Kassam, D. M. Prevedello, R. L. Carrau, C. H. Snyderman, A. Thomas, P. Gardner, A. Zanation, B. Duz, S. T. Stefko, K. Byers, and M. B. Horowitz. Endoscopic endonasal skull base surgery: analysis of complications in the authors' initial 800 patients. *Journal of Neurosurgery*, 114(6):1544–68, 2011.

[97] L. M. Cavallo, F. Esposito, and P. Cappabianca. Surgical limits in transnasal approach to opticocarotid region and planum sphenoidale: an anatomic cadaveric study. *World Neurosurgery*, 73(4):301–3, 2010.

[98] D. B. Camarillo, C. F. Milne, C. R. Carlson, M. R. Zinn, and J. K. Salisbury. Mechanics Modeling of Tendon-Driven Continuum Manipulators. *IEEE Transactions on Robotics*, 24(6):1262–1273, 2008.

[99] V. Karimyan, M. Sodergren, J. Clark, G.-Z. Yang, and A. Darzi. Navigation systems and platforms in natural orifice translumenal endoscopic surgery (NOTES). *International Journal of Surgery*, 7(4):297–304, 2009.

[100] N. Simaan, K. Xu, A. Kapoor, W. Wei, P. Kazanzides, R. Taylor, and P. Flint. Design and Integration of a Telerobotic System for Minimally Invasive Surgery of the Throat. *International Journal of Robotics Research*, 28(9):1134–1153, September 2009.

[101] F. Borumandi, M. Heliotis, C. Kerawala, B. Bisase, and L. Cascarini. Role of robotic surgery in oral and maxillofacial, and head and neck surgery. *The British Journal of Oral & Maxillofacial Surgery*, pages 6–10, 2011.

[102] M. Piccigallo, U. Scarfogliero, C. Quaglia, G. Petroni, P. Valdastri, A. Menciassi, and P. Dario. Design of a Novel Bimanual Robotic System for Single-Port Laparoscopy. *IEEE/ASME Transactions on Mechatronics*, 15(6):871–878, 2010.

[103] P. F. Escobar, M. Kebria, and T. Falcone. Evaluation of a novel single-port robotic platform in the cadaver model for the performance of various procedures in gynecologic oncology. *Gynecologic Oncology*, 120(3):380–4, 2011.

[104] A. Bajo, R. E. Goldman, L. Wang, D. Fowler, and N. Simaan. Integration and Preliminary Evaluation of an Insertable Robotic Effectors Platform for Single Port Access Surgery. In *IEEE International Conference on Robotics and Automation*, pages 3381–3387, 2012.

[105] J. Wurm, T. Dannenmann, C. Bohr, H. Iro, and K. Bumm. Increased safety in robotic paranasal sinus and skull base surgery with redundant navigation and automated registration. *International Journal of Medical Robotics and Computer Assisted Surgery*, 01(03):42, 2005.

[106] T. Xia, C. Baird, G. Jallo, K. Hayes, N. Nakajima, N. Hata, and P. Kazanzides. An integrated system for planning, navigation and robotic assistance for skull base surgery. *International Journal of Medical Robotics and Computer Assisted Surgery*, 4(4):321–30, 2008.

[107] C. H. Nimsky, J. Rachinger, H. Iro, and R. Fahlbusch. Adaptation of a hexapod-based robotic system for extended endoscope-assisted transsphenoidal skull base surgery. *Minimally Invasive Neurosurgery*, 47(1):41–6, 2004.

[108] K. W. G. Eichhorn and F. Bootz. Clinical Requirements and Possible Applications of Robot Assisted Endoscopy in Skull Base and Sinus Surgery. *Acta Neurochirurgica*, 109:237–240, 2011.

[109] H.-S. Yoon, S. M. Oh, J. H. Jeong, S. H. Lee, K. Tae, K.-C. Koh, and B.-J. Yi. Active bending endoscope robot system for navigation through sinus area. In *IEEE/RSJ International Conference on Intelligent Robots and Systems*, pages 967–972, 2011.

[110] V. A. Schriever, T. Hummel, J. N. Lundström, and J. Freiherr. Size of nostril opening as a measure of intranasal volume. *Physiology & Behavior*, 110-111:3–5, February 2013.

[111] J. M. Jani, M. Leary, A. Subic, and M. A. Gibson. A review of shape memory alloy research, applications and opportunities. *Materials and Design*, 56:1078–1113, 2014.

[112] J. Ding, R. E. Goldman, K. Xu, P. K. Allen, D. L. Fowler, and N. Simaan. Design and Coordination Kinematics of an Insertable Robotic Effectors Platform for Single-Port Access Surgery. *IEEE/ASME Transactions on Mechatronics*, 18(5):1612–1624, 2013.

[113] R. J. Murphy, M. D. M. Kutzer, S. M. Segreti, B. C. Lucas, and M. Armand. Design and kinematic characterization of a surgical manipulator with a focus on treating osteolysis. *Robotica*, 32(6):835–850, 2014.

[114] H. B. Gilbert, D. C. Rucker, and R. J. Webster III. Concentric tube robots: The state of the art and future directions. In M. Inaba and P. Corke, editors, *Robotics Research: The 16th International Symposium ISRR*, pages 253–269. Springer International Publishing, 2016.

[115] M. Torabi, R. Gupta, and C. J. Walsh. Compact Robotically Steerable Image-Guided Instrument for Multi-Adjacent-Point ({MAP}) Targeting. *IEEE Transactions on Robotics*, 30(4):802–815, 2014.

[116] P. P. Poncet. Nitinol Medical Device Design Considerations. In *International Conference on Shape Memory and Superelastic Technologies*, pages 441–455, 2000.

[117] P. J. Swaney, A. Mahoney, H. B. Gilbert, A. Remirez, E. Lamers, B. Hartley, R. Feins, R. Alterovitz, and R. J. Webster III. Tendons, concentric tubes, and a bevel tip: Three

steerable robots in one transoral lung access system. In *IEEE International Conference on Robotics and Automation*, pages 5378–5383, 2015.

[118] C. Bergeles, A. H. Gosline, N. V. Vasilyev, P. J. Codd, P. J. del Nido, and P. E. Dupont. Concentric Tube Robot Design and Optimization Based on Task and Anatomical Constraints. *IEEE Transactions on Robotics*, 31(1):67–84, 2015.

[119] R. J. Hendrick, S. D. Herrell, and R. J. Webster III. A Multi-Arm Hand-Held Robotic System for Transurethral Laser Prostate Surgery. In *IEEE International Conference on Robotics and Automation*, pages 2850–2855, 2014.

[120] J. Ha, F. C. Park, and P. E. Dupont. Achieving Elastic Stability of Concentric Tube Robots Through Optimization of Tube Precurvature. In *IEEE/RSJ International Conference on Intelligent Robots and Systems*, pages 864–870, 2014.

[121] R. J. Hendrick, H. B. Gilbert, and R. J. Webster III. Designing snap-free concentric tube robots: A local bifurcation approach. In *IEEE International Conference on Robotics and Automation*, pages 2256–2263, 2015.

[122] A. R. Pelton, J. Dicello, and S. Miyazaki. Optimisation of processing and properties of medical grade Nitinol wire. *Minimally Invasive Therapy & Allied Technologies*, 9(2):107–118, January 2000.

[123] N. B. Morgan and M. Broadley. Taking the art out of smart! - Forming processes and durability issues for the application of NiTi shape memory alloys in medical devices. In *Medical Device Materials: Proceedings of the Materials & Processes for Medical Devices Conference*, pages 247–252, 2003.

[124] S. A. Smith and D. E. Hodgson. Shape Setting Nitinol. In *Medical Device Materials: Proceedings of the Materials & Processes for Medical Devices Conference*, pages 266–270, 2003.

[125] J.-S. Kim, D.-Y. Lee, K. Kim, S. Kang, and K.-J. Cho. Toward a solution to the snapping problem in a concentric-tube continuum robot: Grooved tubes with anisotropy. In *IEEE International Conference on Robotics and Automation*, pages 5871–5876. IEEE, 2014.

[126] B. Malard, J. Pilch, P. Sittner, V. Gartnerova, and H. Grenoble. Microstructure and Functional Property Changes in Thin Ni-Ti Wires Heat Treated by Electric Current - High Energy X-Ray And TEM Investigations. *Functional Materials Letters*, 2(2):45–54, 2009.

[127] K. Ikuta, M. Tsukamoto, and S. Hirose. Shape memory alloy servo actuator system with electric resistance feedback and application for active endoscope. In *IEEE International Conference on Robotics and Automation*, pages 427–430, 1988.

[128] G. Song, V. Chaudhry, and C. Batur. Precision tracking control of shape memory alloy actuators using neural networks and a sliding-mode based robust controller. *Smart Materials and Structures*, 12(2):223–231, 2003.

[129] N. Ma, G. Song, and H. J. Lee. Position control of shape memory alloy actuators with internal electrical resistance feedback using neural networks. *Smart materials and structures*, 13(4):777–783, 2004.

[130] S. M. Dutta and F. H. Ghorbel. Differential Hysteresis Modeling of a Shape Memory Alloy Wire Actuator. *IEEE/ASME Transactions on Mechatronics*, 10(2):189–197, 2005.

[131] M. Ho, A. B. McMillan, J. M. Simar, R. Gullapalli, and J. P. Desai. Toward a Meso-Scale {SMA}-Actuated {MRI}-Compatible Neurosurgical Robot. *IEEE Transactions on Robotics*, 28(1):213–222, 2012.

[132] Johnson Matthey Medical Components. Nitinol Shape Setting.

[133] Nitinol Devices & Components, Inc. Nitinol Facts.

[134] Y. B. Wang, Y. F. Zheng, and Y. Liu. Effect of short-time direct current heating on phase

transformation and superelasticity of {Ti-50.8at.%Ni} alloy. *Journal of Alloys and Compounds*, 477(1):764–767, 2009.

[135] V. Novák, P. Šittner, G. N. Dayananda, F. M. Braz-Fernandes, and K. K. Mahesh. Electric resistance variation of NiTi shape memory alloy wires in thermomechanical tests: Experiments and simulation. *Materials Science and Engineering: A*, 481-482:127–133, May 2008.

[136] J. Zhou, H. Zhou, C. Hu, and S. Hu. Measurements of Thermal and Dielectric Properties of Medium Density Fiberboard with Different Moisture Contents. *BioResources*, 8(3):4185–4192, 2013.

[137] D. B. Comber, E. J. Barth, and R. J. Webster III. Design and Control of an Magnetic Resonance Compatible Precision Pneumatic Active Cannula Robot. *ASME Journal of Medical Devices*, 8(1):11003, 2014.

[138] J. Burgner-Kahrs, H. B. Gilbert, J. Granna, P. J. Swaney, and R. J. Webster III. Workspace Characterization for Concentric Tube Continuum Robots. In *IEEE/RSJ International Conference on Intelligent Robots and Systems*, pages 1269–1275, 2014.

[139] H. B. Gilbert and R. J. Webster III. Concentric tube robots as steerable needles: Achieving follow-the-leader deployment. *IEEE Transactions on Robotics*, 31(2):246–258, 2015.

[140] E. Süli and D. F. Mayers. *An introduction to numerical analysis*. Cambridge university press, 2003.

[141] S. Hasanzadeh and F. Janabi-Sharifi. An efficient static analysis of continuum robots. *Journal of Mechanisms and Robotics*, 6(3), 2004.

[142] Y. Nakamura and H. Hanafusa. Optimal redundancy control of robot manipulators. *International Journal of Robotics Research*, 6(1):32–42, 1987.

[143] R. M. Murray, Z. Li, and S. S. Sastry. *A Mathematical Introduction to Robotic Manipulation*. CRC Press, 1994.

[144] G. S. Chirikjian. Conformational modeling of continuum structures in robotics and structural biology: A review. *Advanced Robotics*, 29(13):817–829, 2015.

[145] P. J. Prince and J. R. Dormand. High order embedded runge-kutta formulae. *Journal of Computational and Applied Mathematics*, 7(1):67–75, 1981.

[146] H. B. Gilbert, R. J. Hendrick, and R. J. Webster III. Elastic stability of concentric tube robots: A stability measure and design test. *IEEE Transactions on Robotics*, 32(1):20–35, Feb 2016.

[147] H. Azimian, P. Francis, T. Looi, and J. Drake. Structurally-Redesigned Concentric-Tube Manipulators with Improved Stability. *IEEE/RSJ International Conference on Intelligent Robots and Systems*, pages 2030–2035, 2014.

[148] R. Xu, S. F. Atashzar, and R. V. Patel. Kinematic Instability in Concentric-tube Robots: Modeling and Analysis. In *IEEE International Conference on Biomedical Robotics and Biomechatronics*, 2014.

[149] K. Hoffman and R. Manning. An Extended Conjugate Point Theory with Application to the Stability of Planar Buckling of an Elastic Rod Subject to a Repulsive Self-potential. *SIAM Journal on Mathematical Analysis*, 41:465–494, 2009.

[150] R. S. Manning. Conjugate points revisited and Neumann-Neumann problems. *SIAM review*, 51(1):193–212, 2009.

[151] S. V. Levyakov and V. V. Kuznetsov. Stability analysis of planar equilibrium configurations of elastic rods subjected to end loads. *Acta Mechanica*, 211(10):73–87, 2009.

[152] T. Bretl and Z. McCarthy. Quasi-static manipulation of a Kirchoff elastic rod based on a geometric analysis of equilibrium configurations. *International Journal of Robotics Research*, 33(1):48–68, 2014.

[153] H. I. Dwyer and A. Zettl. Eigenvalue Computations for Regular Matrix Sturm-Liouville Problems. *Electronic Journal of Differential Equations*, 1995(5):1–13, 1995.

[154] I. M. Gelfand and S. V. Fomin. *Calculus of Variations*. Dover Publications, Mineola, NY, 2000.

[155] J. Lock and P. E. Dupont. Friction Modeling in Concentric Tube Robots. In *IEEE International Conference on Robotics and Automation*, pages 1139–1146, January 2011.

[156] A. R. Pelton, N. Rebel, T. W. Duerig, and A. Wick. Experimental and {FEM} Analysis of the Bending Behavior of Superelastic Tubing. In *Proceedings of the First International Conference on Shape Memory and Superelastic Technologies*, pages 353–358, 1994.

[157] S. C. Ryu, Z. F. Quek, P. Renaud, R. J. Black, B. L. Daniel, and M. R. Cutkosky. An optical actuation system and curvature sensor for a MR-compatible active needle. In *IEEE International Conference on Robotics and Automation*, pages 1589–1594, 2012.

[158] H. Choset and W. Henning. A Follow-the-Leader Approach to Serpentine Robot Motion Planning. *Journal of Aerospace Engineering*, 12(2):65–73, April 1999.

[159] A. Degani, H. Choset, B. Zubiate, T. Ota, and M. Zenati. Highly articulated robotic probe for minimally invasive surgery. In *International Conference of the IEEE Engineering in Medicine and Biology Society*, pages 4157–4172, January 2006.

[160] E. E. Greenblatt, K. I. Trovato, A. Popovic, and D. Stanton. Interlocking Nested Cannula. U.S. Patent Application No. 13/123,591, 2011.

[161] M. J. Drexel, G. S. Selvaduray, and A. R. Pelton. The Effects of Cold Work and Heat

Treatment on the Properties of Nitinol Wire. In *Proceedings of the International Conference on Shape Memory and Superelastic Technologies*, pages 447–454. ASM International, 2006.

[162] A. R. Pelton, S. M. Russell, and J. DiCello. The Physical Metallurgy of Nitinol for Medical Applications. *JOM*, 55(5):33–37, 2003.

[163] W. H. Smithson and M. C. Walker. What is Epilepsy? Incidence, Prevalence and Aetiology. In *ABC of Epilepsy*, chapter 1, pages 1–3. Wiley, 1 edition, 2012.

[164] J. T. Willie, N. G. Laxpati, D. L. Drane, A. Gowda, C. Appin, C. Hao, D. J. Brat, S. L. Helmers, A. Saindane, S. G. Nour, and R. E. Gross. Real-Time Magnetic Resonance-Guided Stereotactic Laser Amygdalohippocampotomy for Mesial Temporal Lobe Epilepsy. *Neurosurgery*, 74(6):569–585, 2014.

[165] T. C. Lee, R. L. Kashyap, and C. N. Chu. Building Skeleton Models via {3-D} Medial Surface/Axis Thinning Algorithms. *{CVGIP}: Graphical Models and Image Processing*, 56(6):462–478, 1994.

[166] A. R. Wyler, B. P. Hermann, and G. Somes. Extent of Medial Temporal Resection on Outcome from Anterior Temporal Lobectomy: A Randomized Prospective Study. *Neurosurgery*, 37(5):982–991, 1995.

[167] T. Yamamoto, B. Vagvolgyi, K. Balaji, L. L. Whitcomb, and A. M. Okamura. Tissue property estimation and graphical display for teleoperated robot-assisted surgery. In *IEEE International Conference on Robotics and Automation*, pages 4239–4245, 2009.

[168] K. A. Nichols and A. M. Okamura. Autonomous robotic palpation: Machine learning techniques to identify hard inclusions in soft tissues. In *IEEE International Conference on Robotics and Automation*, pages 4384–4389, 2013.

[169] S. Tully, A. Bajo, G. Kantor, H. Choset, and N. Simaan. Constrained filtering with contact detection data for the localization and registration of continuum robots in flexible environ-

ments. In *IEEE International Conference on Robotics and Automation*, pages 3388–3394, 2012.

[170] D. C. Rucker and R. J. Webster III. Deflection-Based Force Sensing for Continuum Robots: A Probabilistic Approach. In *IEEE/RSJ International Conference on Intelligent Robots and Systems*, pages 3764–3769, 2011.

[171] C. Sultan and R. Skelton. A force and torque tensegrity sensor. *Sensors and Actuators A: Physical*, 112(2):220–231, 2004.

[172] R. Ranganath, P. Nair, T. Mruthyunjaya, and A. Ghosal. A force–torque sensor based on a Stewart Platform in a near-singular configuration. *Mechanism and machine theory*, 39(9):971–998, 2004.

[173] K. Xu and N. Simaan. Intrinsic wrench estimation and its performance index for multisegment continuum robots. *IEEE Transactions on Robotics*, 26(3):555–561, 2010.

[174] A. Bajo and N. Simaan. Finding lost wrenches: Using continuum robots for contact detection and estimation of contact location. In *IEEE International Conference on Robotics and Automation*, pages 3666–3673, 2010.

[175] Y. Shapiro, G. Kosa, and A. Wolf. Shape tracking of planar hyper-flexible beams via embedded pvdf deflection sensors. *Mechatronics, IEEE/ASME Transactions On*, 19(4):1260–1267, 2014.

[176] H. Liu, A. Farvardin, S. A. Pedram, I. Iordachita, R. H. Taylor, and M. Armand. Large deflection shape sensing of a continuum manipulator for minimally-invasive surgery. In *IEEE International Conference on Robotics and Automation*, pages 201–206, 2015.

[177] S. Hasanzadeh and F. Janabi-Sharifi. Model-based force estimation for intracardiac catheters. *IEEE/ASME Transactions on Mechatronics*, 21(1):154–162, 2016.

[178] A. Gelb. *Applied optimal estimation*. MIT press, 1974.

[179] Y. Wang and G. S. Chirikjian. Error propagation on the euclidean group with applications to manipulator kinematics. *IEEE Transactions on Robotics*, 22(4):591–602, 2006.

[180] Y. Bar-Shalom, X. R. Li, and T. Kirubarajan. *Estimation with applications to tracking and navigation*. John Wiley & Sons, 2004.

[181] A. Zettl. *Sturm-Liouville Theory*. American Mathematical Society, 2005.

[182] J. H. Maddocks. Restricted Quadratic Forms and Their Application to Bifurcation and Stability in Constrianed Variational Principles. *SIAM Journal on Mathematical Analysis*, 16(1), 1985.

[183] P. B. Bailey, W. N. Everitt, J. Weidmann, and A. Zettl. Regular approximations of singular Sturm-Liouville problems. In *Results in Mathematics*, pages 3–22, 1993.

# Appendix A

## Model Derivation and Equations

### A.1 Derivation of the Model Equations

The energy functional is given explicitly by

$$E[\boldsymbol{u}_B, \psi_1, ..., \psi_n] = \frac{1}{2}\int_0^L \sum_{i=1}^{N} \Delta \boldsymbol{u}_i^T \mathbf{K}_i \Delta \boldsymbol{u}_i \, ds \tag{A.1}$$

Using the relationship that $\boldsymbol{u}_i = \mathbf{R}_{\psi_i}^T \boldsymbol{u}_B + \psi_i' \boldsymbol{e}_3$, and the fact that $\mathbf{R}_z^T \mathbf{K}_i \mathbf{R}_z = \mathbf{K}_i$ for any $z$-axis rotation $\mathbf{R}_z$,

$$E[\boldsymbol{u}_B, \psi_1, ..., \psi_N] = \frac{1}{2}\int_0^L \sum_{i=1}^{N} \Delta \bar{\boldsymbol{u}}_i^T \mathbf{K}_i \Delta \bar{\boldsymbol{u}}_i \, ds \tag{A.2}$$

where $\Delta \bar{\boldsymbol{u}}_i = \mathbf{R}_{\psi_i} \Delta \boldsymbol{u}_i$. Expanding, $\Delta \bar{\boldsymbol{u}}_i = \boldsymbol{u}_B - \mathbf{R}_{\psi_i} \boldsymbol{u}_i^* + \psi_i' \boldsymbol{e}_3$. Then the Euler-Lagrange equations describing the first-order necessary conditions for a stationary energy functional are

$$\begin{aligned} -\frac{\partial L}{\partial \boldsymbol{u}_B} &= 0 \\ \frac{\partial}{\partial s}\frac{\partial L}{\partial \psi_i'} - \frac{\partial L}{\partial \psi_i} &= 0 \end{aligned} \tag{A.3}$$

The first equation expands to become

$$\left(\sum_{i=1}^{N} k_{ib}\right) \boldsymbol{u}_B - \sum_{i=1}^{N} k_{ib} \mathbf{R}_{\psi_i} \boldsymbol{u}_i^* = 0 \tag{A.4}$$

Note that the torsional term $\psi_i' \boldsymbol{e}_3$ drops out because of the chain rule, which invokes the relationship

$$\frac{\partial \Delta \bar{\boldsymbol{u}}_i}{\partial \boldsymbol{u}_B} = \begin{bmatrix} 1 & 0 & 0 \\ 0 & 1 & 0 \\ 0 & 0 & 0 \end{bmatrix} \tag{A.5}$$

due to the two-dimensional nature of $\boldsymbol{u}_B$. Equation (A.4) is easily solved for $\boldsymbol{u}_B$.

For the second of the Euler-Lagrange equations, for the functions $\psi_i$, the second equation in (A.3) may be expanded and the following simplifications applied:

$$\begin{aligned} \boldsymbol{e}_3^T \mathbf{K}_i \frac{\partial \mathbf{R}_{\psi_i}}{\partial \psi_i} \boldsymbol{u}_i^* = 0 \qquad & \qquad \boldsymbol{u}_i^{*T} \mathbf{R}_{\psi_i}^T \mathbf{K}_i \frac{\partial \mathbf{R}_{\psi_i}}{\partial \psi_i} \boldsymbol{u}_i^* = 0 \\ \boldsymbol{u}_B^T \mathbf{K}_i \boldsymbol{e}_3 = 0 \qquad & \qquad \boldsymbol{u}_i^{*T} \mathbf{R}_{\psi_i}^T \mathbf{K}_i \boldsymbol{e}_3 = 0 \end{aligned} \tag{A.6}$$

These identities may be verified via the basic matrix arithmetic rules. After applying the simplifications, the resulting equation of motion is

$$(k_{it} \psi_i')' - \boldsymbol{u}_B^T \mathbf{K}_i \frac{\partial \mathbf{R}_{\psi_i}}{\partial \psi_i} \boldsymbol{u}_i^* = 0 \tag{A.7}$$

## A.2 Derivation of Generalized Forces

In order to incorporate external loads, the generalized forces associated with these loads must be found and placed on the right hand side of the appropriate Euler-Lagrange equations. In this section a derivation is performed for the case of an applied force at the tip of the robot, $F_{tip}$. This derivation is carried out using vector calculus methods, and in this section most vector quantities represent physical vectors rather than coordinates, so that, for example $\boldsymbol{u}_B = u_{Bx}\boldsymbol{x}_B + u_{By}\boldsymbol{y}_B$ instead of $\boldsymbol{u}_B = \begin{bmatrix} u_{Bx} & u_{By} & 0 \end{bmatrix}^T$. Equations in which symbols denote coordinate vectors are noted.

The virtual work associated with the tip force is

$$\delta W = F_{tip} \cdot \delta \boldsymbol{p}(L) \tag{A.8}$$

where $\delta \boldsymbol{p}(L)$ is the virtual (vector) displacement at the tip of the robot. In order to express the Euler-Lagrange equations the generalized force $Q_u$ must be found for which

$$\delta W = \int_0^L Q_u \cdot \delta_r \boldsymbol{u}_B^b \, ds \tag{A.9}$$

The variation $\delta_r \boldsymbol{u}_B$ is a "coordinate variation" of $\boldsymbol{u}_B$, defined as

$$\delta_r \boldsymbol{u}_B = \delta u_{Bx} \boldsymbol{x}_B + \delta u_{By} \boldsymbol{y}_B \tag{A.10}$$

This is distinguished from the vector variation $\delta \boldsymbol{u}_B$, which must also include the variation of the frame vectors $\boldsymbol{x}_B$ and $\boldsymbol{y}_B$.

By the commutativity of the $\delta$ process with integration and differentiation,

$$\delta \boldsymbol{p}(L) = \int_0^L \delta \boldsymbol{p}'(s)\, ds = \int_0^L \delta \boldsymbol{z}_B(s)\, ds \tag{A.11}$$

Since $\boldsymbol{z}_B$ is constrained to be a unit vector, the variation $\delta \boldsymbol{z}_B$ must be orthogonal to $\boldsymbol{z}_B$, and the variation is parameterized by the angular variation $\delta \boldsymbol{\omega}$ of the frame, such that

$$\begin{aligned} \delta \boldsymbol{x}_B &= \delta \boldsymbol{\omega} \times \boldsymbol{x}_B \\ \delta \boldsymbol{y}_B &= \delta \boldsymbol{\omega} \times \boldsymbol{y}_B \\ \delta \boldsymbol{z}_B &= \delta \boldsymbol{\omega} \times \boldsymbol{z}_B \end{aligned} \tag{A.12}$$

The variation $\delta \boldsymbol{\omega}$ is not independent of $\delta \boldsymbol{u}_B$; there can only be one variation $\delta \boldsymbol{z}_B$, yet both of the former variations influence the latter. The relationship between $\delta \boldsymbol{\omega}$ and $\delta \boldsymbol{u}_B$ is derived from the requirement that $(\delta \boldsymbol{z}_B)' = \delta(\boldsymbol{z}_B')$.

$$(\delta \boldsymbol{\omega} \times \boldsymbol{z}_B)' = \delta(\boldsymbol{u}_B \times \boldsymbol{z}_B) \tag{A.13}$$

After expanding, substituting, and applying the Jacobi rule,

$$\delta \boldsymbol{\omega} \times (\boldsymbol{u}_B \times \boldsymbol{z}_B) = -\boldsymbol{u}_B \times (\boldsymbol{z}_B \times \delta \boldsymbol{\omega}) - \boldsymbol{z}_B \times (\delta \boldsymbol{\omega} \times \boldsymbol{u}_B)$$

one finds that

$$(\delta \boldsymbol{\omega}' + (\delta \boldsymbol{\omega} \times \boldsymbol{u}_B) - \delta \boldsymbol{u}_B) \times \boldsymbol{z}_B = 0 \tag{A.14}$$

After noting that analogous equations must hold for the other frame vectors $\boldsymbol{x}_B$ and $\boldsymbol{y}_B$, the conclusion is that the term in parentheses is identically zero, i.e.

$$\delta\boldsymbol{\omega}' = \delta\boldsymbol{u}_B - (\delta\boldsymbol{\omega} \times \boldsymbol{u}_B) \tag{A.15}$$

Re-writing the principle of virtual work,

$$\delta W = F_{tip} \cdot \int_0^L \delta\boldsymbol{\omega} \times \boldsymbol{z}_B \, ds = \int_0^L (\boldsymbol{z}_B \times \boldsymbol{F}_{tip}) \cdot \delta\boldsymbol{\omega} \, ds \tag{A.16}$$

Define the function $\boldsymbol{m}$, up to a constant, such that

$$\boldsymbol{m}' = -\boldsymbol{z}_B \times \boldsymbol{F}_{tip} \tag{A.17}$$

Then,

$$\delta W = \int_0^L -\boldsymbol{m}' \cdot \delta\boldsymbol{\omega} \, ds \tag{A.18}$$

Integrating by parts,

$$\delta W = -\left[\boldsymbol{m} \cdot \delta\boldsymbol{\omega}\right]_0^L + \int_0^L \boldsymbol{m} \cdot \delta\boldsymbol{\omega}' \, ds \tag{A.19}$$

Expanding $\delta\boldsymbol{\omega}'$ using the constraint of equation (A.15),

$$\delta W = -\left[\boldsymbol{m} \cdot \delta\boldsymbol{\omega}\right]_0^L + \int_0^L \boldsymbol{m} \cdot (\delta\boldsymbol{u}_B - \delta\boldsymbol{\omega} \times \boldsymbol{u}_B) \, ds \tag{A.20}$$

The vector variation $\delta\boldsymbol{u}_B$ is re-written in terms of the coordinate variation and the variation of the frame vectors. This relationship is provided by the transport theorem

$$\delta\boldsymbol{u}_B = \delta_r \boldsymbol{u}_B + \delta\boldsymbol{\omega} \times \boldsymbol{u}_B \tag{A.21}$$

Plugging in, the terms $\delta\boldsymbol{\omega} \times \boldsymbol{u}_B$ cancel, and

$$\delta W = -\left[\boldsymbol{m} \cdot \delta\boldsymbol{\omega}\right]_0^L + \int_0^L \boldsymbol{m} \cdot \delta_r \boldsymbol{u}_B \, ds \tag{A.22}$$

The generalized force along $\delta_r \boldsymbol{u}_B$ is found as $Q_u = \boldsymbol{m}$. The natural boundary condition on $\boldsymbol{m}$ is $\boldsymbol{m}(L) = 0$ since $\delta\boldsymbol{\omega}$ is unconstrained at this point. At $s = 0$, $\delta\boldsymbol{\omega} = 0$ as a result of the boundary condition on $\mathbf{R}_B(0)$.

The equation for the curvature $\boldsymbol{u}_B$, expressed in the notation of coordinate vectors, is

$$-\left(\sum_{i=1}^{N} k_{ib}\right)\boldsymbol{u}_B + \sum_{i=1}^{N} k_{ib}\mathbf{R}_{\psi_i}\boldsymbol{u}_i^* = (\mathbf{R}^T\boldsymbol{m})_{1:2} \tag{A.23}$$

where it is assumed that $\boldsymbol{m}$ is represented by coordinates in the inertial frame, so that $\mathbf{R}^T\boldsymbol{m}$ rotates these coordinates into the body frame. The subscript $(1:2)$ denotes that only the components of $\boldsymbol{m}$ along $\boldsymbol{x}$ and $\boldsymbol{y}$ are applied to this equation. This is a result of the fact that $\delta u_{Bz} = 0$.

## A.3 Expressions for State Equations and Derivatives

In this appendix, all of the quantities needed to compute the state equations and the nonzero blocks of $[\partial\boldsymbol{\xi}/\partial\boldsymbol{y}]$ are listed. They have been placed in matrix-vector form where possible for ease of converting to a computer program and for efficiency of implementation. Note that $[\cdot]_{xy}$ means either the top 2 rows, the left two columns or the upper-left $2 \times 2$ block, depending on context. The curvature vector $\boldsymbol{u}_B$ has been compressed from 3D to 2D. The nonzero terms of the matrix $\partial\xi^i/\partial y^j$ are given in the following equations.

$$\frac{\partial\xi_\psi}{\partial\boldsymbol{\sigma}} = \operatorname{diag}\left(\frac{\partial c_{it}(\sigma_i)}{\partial\sigma_i}\right)\operatorname{diag}\left(\boldsymbol{m}_z\right) \qquad \frac{\partial\xi_\psi}{\partial\boldsymbol{m}_z} = \mathbf{C}_t \tag{A.24}$$

$$\frac{\partial\xi_{mz}}{\partial\boldsymbol{\sigma}} = \frac{\partial\boldsymbol{T}}{\partial\boldsymbol{\sigma}} \qquad \frac{\partial\xi_{mz}}{\partial\boldsymbol{\psi}} = \frac{\partial\boldsymbol{T}}{\partial\boldsymbol{\psi}} \qquad \frac{\partial\xi_{mz}}{\partial\boldsymbol{m}} = \frac{\partial\boldsymbol{T}}{\partial\boldsymbol{m}} \tag{A.25}$$

$$\frac{\partial \xi_{mz}}{\partial \boldsymbol{q}} = \frac{\partial \boldsymbol{T}}{\partial \boldsymbol{q}} \tag{A.26}$$

$$\frac{\partial \xi_q}{\partial \boldsymbol{\sigma}} = \frac{\partial \boldsymbol{u}_B}{\partial \boldsymbol{\sigma}} \qquad \frac{\partial \xi_q}{\partial \boldsymbol{\psi}} = \frac{\partial \boldsymbol{u}_B}{\partial \boldsymbol{\psi}} \qquad \frac{\partial \xi_q}{\partial \boldsymbol{m}} = \frac{\partial \boldsymbol{u}_B}{\partial \boldsymbol{m}} \tag{A.27}$$

$$\frac{\partial \xi_m}{\partial \boldsymbol{n}} = -\left(\boldsymbol{p}'\right)^{\wedge} = -(\boldsymbol{q}\boldsymbol{e}_3\boldsymbol{q}^{-1})^{\wedge} \tag{A.28}$$

$$\frac{\partial \xi_m}{\partial \boldsymbol{q}} = \begin{bmatrix} -\widehat{\boldsymbol{n}}\boldsymbol{q}\boldsymbol{e}_2\boldsymbol{q}^{-1} & \widehat{\boldsymbol{n}}\boldsymbol{q}\boldsymbol{e}_1\boldsymbol{q}^{-1} & \mathbf{0}_{3\times 1} \end{bmatrix} \tag{A.29}$$

$$\boldsymbol{k}_b = \begin{bmatrix} k_{1b}(\sigma_1) & \dots & k_{Nb}(\sigma_N) \end{bmatrix}^T \tag{A.30}$$

$$\mathbf{K}_b = \operatorname{diag}(\boldsymbol{k}_b) \tag{A.31}$$

$$\mathbf{F} = \begin{bmatrix} F_1 & \dots & F_N \end{bmatrix} \qquad F_i = \mathbf{R}_z(\psi_i)\boldsymbol{u}_i^*(\sigma_i) \tag{A.32}$$

$$\mathbf{G} = \begin{bmatrix} G_1 & \dots & G_N \end{bmatrix} \qquad G_i = \mathbf{R}_z(\psi_i)\frac{\partial \boldsymbol{u}_i^*(\sigma_i)}{\partial \sigma_i} \tag{A.33}$$

$$\boldsymbol{T}(\boldsymbol{y}) = \mathbf{K}_b\mathbf{F}^T\mathbf{S}\boldsymbol{u}_B(\boldsymbol{\sigma}, \boldsymbol{\psi}, \boldsymbol{m}_{xy}^b) \tag{A.34}$$

$$\mathbf{K}_{b,\sigma} = \operatorname{diag}\left(\frac{\partial k_{ib}(\sigma_i)}{\partial \sigma_i}\right) \tag{A.35}$$

$$\frac{\partial \boldsymbol{T}}{\partial \boldsymbol{\sigma}} = \mathbf{K}_{b,\sigma}\text{diag}(\mathbf{F}^T\mathbf{S}\boldsymbol{u}_B) + \mathbf{K}_b\text{diag}\left(\mathbf{G}^T\mathbf{S}\boldsymbol{u}_B\right) + \mathbf{K}_b\mathbf{F}^T\mathbf{S}\frac{\partial \boldsymbol{u}_B}{\partial \boldsymbol{\sigma}} \tag{A.36}$$

$$\frac{\partial \boldsymbol{T}}{\partial \boldsymbol{\psi}} = \mathbf{K}_b\text{diag}\left(\mathbf{F}^T\boldsymbol{u}_B\right) + \mathbf{K}_b\mathbf{F}^T\mathbf{S}\frac{\partial \boldsymbol{u}_B}{\partial \boldsymbol{\psi}} \tag{A.37}$$

$$\frac{\partial \boldsymbol{T}}{\partial \boldsymbol{m}} = -\mathbf{K}_b\mathbf{M}^T\frac{\partial \boldsymbol{u}_B}{\partial \boldsymbol{m}} \tag{A.38}$$

$$\frac{\partial \boldsymbol{T}}{\partial \boldsymbol{q}} = \mathbf{K}_b\mathbf{F}^T\mathbf{S}\frac{\partial \boldsymbol{u}_B}{\partial \boldsymbol{q}} \tag{A.39}$$

$$k_{tot} = \sum_{i=1}^{N} k_{ib}(\sigma_i) \qquad \frac{\partial k_{tot}}{\partial \boldsymbol{\sigma}} = \begin{bmatrix} \frac{\partial k_{1b}}{\partial \sigma_1} & \cdots & \frac{\partial k_{Nb}}{\partial \sigma_N} \end{bmatrix} \tag{A.40}$$

$$\boldsymbol{u}_B(\boldsymbol{y}) = \frac{1}{k_{tot}}\left(\mathbf{F}\boldsymbol{k}_B + \left[\boldsymbol{q}^{-1}\boldsymbol{m}\boldsymbol{q}\right]_{xy}\right) \tag{A.41}$$

$$\frac{\partial \boldsymbol{u}_B}{\partial \boldsymbol{\sigma}} = -\frac{1}{k_{tot}}\boldsymbol{u}_B\frac{\partial k_{tot}}{\partial \boldsymbol{\sigma}} + \frac{1}{k_{tot}}\mathbf{F}\mathbf{K}_{b,\sigma} + \frac{1}{k_{tot}}\mathbf{G}\mathbf{K}_b \tag{A.42}$$

$$\frac{\partial \boldsymbol{u}_B}{\partial \boldsymbol{\psi}} = \frac{1}{k_{tot}}\mathbf{M}\mathbf{K}_b \tag{A.43}$$

$$\frac{\partial \boldsymbol{u}_B}{\partial \boldsymbol{m}} = \frac{1}{k_{tot}}\left[\mathbf{R}^T(\boldsymbol{q})\right]_{xy} \tag{A.44}$$

$$\frac{\partial \boldsymbol{u}_B}{\partial \boldsymbol{q}} = \frac{1}{k_{tot}}\left[(\mathbf{R}^T(\boldsymbol{q})\boldsymbol{m})^\wedge\right]_{xy} \tag{A.45}$$

$$\mathbf{R}_z(\psi) = \begin{bmatrix} \cos(\psi) & -\sin(\psi) \\ \sin(\psi) & \cos(\psi) \end{bmatrix} \tag{A.46}$$

$$\mathbf{S} = \begin{bmatrix} 0 & -1 \\ 1 & 0 \end{bmatrix} \tag{A.47}$$

$$\mathbf{R}(\boldsymbol{q}) = \begin{bmatrix} \boldsymbol{q}\boldsymbol{e}_1\boldsymbol{q}^{-1} & \boldsymbol{q}\boldsymbol{e}_2\boldsymbol{q}^{-1} & \boldsymbol{q}\boldsymbol{e}_3\boldsymbol{q}^{-1} \end{bmatrix} \tag{A.48}$$

## A.4 Derivation of the Jacobian Equations

Define $\boldsymbol{J}_i$ as the $i^{\text{th}}$ column of the Jacobian matrix. In order to derive the equation governing the Jacobian matrix, we make use of the facts that the state can be embedded in a matrix group and that flows along the fields $\boldsymbol{f} = \boldsymbol{y}\boldsymbol{\xi}$ and $\boldsymbol{h}_i = \boldsymbol{y}\boldsymbol{J}_i$ must commute. Therefore,

$$\frac{\partial}{\partial s}\left(\boldsymbol{y}\boldsymbol{J}_i\right) - \frac{\partial}{\partial c^i}\left(\boldsymbol{y}\boldsymbol{\xi}\right) = 0 \tag{A.49}$$

Using the product rule to expand the partial derivative with respect to $c^i$ and multiplying by $\boldsymbol{y}^{-1}$ on the left,

$$\frac{\partial}{\partial s}\boldsymbol{J}_i = \boldsymbol{J}_i\boldsymbol{\xi} - \boldsymbol{\xi}\boldsymbol{J}_i + \frac{\partial}{\partial c^i}\boldsymbol{\xi} \tag{A.50}$$

Noting the commutator,

$$\frac{\partial}{\partial s}\boldsymbol{J}_i = -\mathrm{ad}_{\boldsymbol{\xi}}\boldsymbol{J}_i + \frac{\partial}{\partial c^i}\boldsymbol{\xi} \tag{A.51}$$

Now, using the directional derivative operator $\tilde{E}^r_k$, we compute the partial of $\boldsymbol{\xi}$ with respect to $c^i$, yielding

$$\frac{\partial}{\partial s}\boldsymbol{J}_i = -\mathrm{ad}_{\boldsymbol{\xi}}\boldsymbol{J}_i + \sum_{k=1}^{N} \tilde{E}^r_k(\boldsymbol{\xi}) J^i_k \tag{A.52}$$

# Appendix B

## The Second Variation

In the calculus of variations, it is well known that Euler's equation is a necessary but not sufficient condition for a minimum, and it is equivalent to the first variation functional being equal to zero,

$$\delta E[\boldsymbol{h}] = \int_{\mathcal{D}} [F_{\boldsymbol{x}}\boldsymbol{h} + F_{\boldsymbol{x}'}\boldsymbol{h}']\, d\sigma = 0$$

for all admissible variations $\boldsymbol{h}$ for which $\boldsymbol{x}_0 + \boldsymbol{h}$ satisfies the boundary conditions of the problem. The quantities $F_{\boldsymbol{x}}$ and $F_{\boldsymbol{x}'}$ are evaluated along the extremal curve $\boldsymbol{x}_0$ for which Euler's equation is satisfied. The expression $F_{\boldsymbol{x}}\boldsymbol{h}$ is interpreted as a row vector multiplied by a column vector.

It is also well known that for $\boldsymbol{x}_0$ to be a weak minimum of the energy functional, the second variation $\delta^2 E[\boldsymbol{h}]$ must be strictly positive for all nonzero admissible variations $\boldsymbol{h}$. The second variation is given by

$$\delta^2 E[\boldsymbol{h}] = \frac{1}{2}\int_{\mathcal{D}} (F_{\boldsymbol{x}\boldsymbol{x}}\boldsymbol{h}, \boldsymbol{h}) + 2(F_{\boldsymbol{x}\boldsymbol{x}'}\boldsymbol{h}', \boldsymbol{h}) + (F_{\boldsymbol{x}'\boldsymbol{x}'}\boldsymbol{h}', \boldsymbol{h}')\, d\sigma \tag{B.1}$$

where $F_{\boldsymbol{x}\boldsymbol{x}}$, $F_{\boldsymbol{x}\boldsymbol{x}'}$, and $F_{\boldsymbol{x}'\boldsymbol{x}'}$ are the matrices of second partial derivatives, evaluated as before along the extremal curve $\boldsymbol{x}_0$, and the parentheses denote the scalar product $(a, b) = \sum a_i b_i$.

For the problems generated by the concentric tube robot problem, we have that the mixed partial derivatives $F_{\boldsymbol{x}\boldsymbol{x}'} = 0$. An integration by parts reveals that (B.1) is equivalent to

$$\delta^2 E[\boldsymbol{h}] = \langle \boldsymbol{\mathcal{S}}\boldsymbol{h}, \boldsymbol{h}\rangle = \int_D (\boldsymbol{\mathcal{S}}\boldsymbol{h}, \boldsymbol{h})\ d\sigma \tag{B.2}$$

which is an inner product on the underlying Hilbert space of admissible variations. Then, the spectral theorem for self-adjoint operators on Hilbert spaces shows that the second variation is

strictly positive only when all eigenvalues of the second variation operator $\mathcal{S}$, defined by

$$\mathcal{S}\boldsymbol{h} = -\left(F_{x'x'}\boldsymbol{h}'\right)' + F_{xx}\boldsymbol{h} \ ,$$

are positive.[1] It is a prerequisite for the condition $\delta^2 E[\boldsymbol{h}] > 0$ to be transformed into the condition on the eigenvalues of $\mathcal{S}$ that the eigenvectors of $\mathcal{S}$ form a complete orthonormal set for the underlying Hilbert space. For the operators generated by the concentric tube robot model, the eigenvectors of $\mathcal{S}$ do form such a basis, as guaranteed by Theorem 1 of Dwyer and Zettl, which says that $\mathcal{S}$ is a self-adjoint operator [153]. The eigenvalue equation $\mathcal{S}\boldsymbol{\psi} = \rho\boldsymbol{\psi}$ is a Sturm-Liouville eigenvalue problem, which has a countably infinite number of orthonormal eigenvectors with eigenvalues that are all real and bounded below. Because there are an infinite number of eigenvalues, a direct computation will not suffice for a feasible numerical test of stability.

Fortunately, continuous changes in $F_{xx}$, $F_{x'x'}$ and the endpoints of the interval $\mathcal{D}$ cause continuous changes in the spectrum of $\mathcal{S}$ [181]. The basic idea for a numerical test is the following: if one can show that $\mathcal{S}$ has positive eigenvalues on some shortened domain which is a subset $J \subset \mathcal{D}$, then the endpoints of $J$ can be continuously varied to the endpoints of $\mathcal{D}$ while watching for zero-crossings in the eigenvalues of $\mathcal{S}$ [150]. If $\mathcal{S}$ has a zero eigenvalue for some choice of $J$, then we have an equation $\mathcal{S}\boldsymbol{h} = 0$ on that domain with boundary conditions on $\boldsymbol{h}$ also satisfied at the endpoints of $J$.

If the problem has Dirichlet boundary conditions, it is well known that stability is determined by looking for conjugate points [154], and the conjugate point formulation and the eigenvalue characterization have been shown to be equivalent [150, 182]. For concentric tube robots, the boundary conditions are not Dirichlet, and therefore the conjugate point condition must be modified. We must first verify that all eigenvalues of $\mathcal{S}$ are positive when the operator is taken to act on a shorter domain. For concentric tube robots, this means a shorter robot. Second, we look for conjugate points, which occur when $\mathcal{S}\boldsymbol{h} = \boldsymbol{0}$ is solved for an admissible variation $\boldsymbol{h}$, which is

[1] A technical note is that admissible variations are only those such that each component of $(F_{x'x'}\boldsymbol{h}')'$ is absolutely continuous. For the concentric tube robot kinematics, $\boldsymbol{h}$ represents a variation in the rotational angles of the tubes, the variation in moment is differentiable and has a continuous derivative.

precisely when $\boldsymbol{\mathcal{S}}$ has an eigenvalue at zero. This two-part modification is explained in detail by Hoffman et al. [149].

We are no longer guaranteed that a conjugate point results in an increase in the number of negative eigenvalues [150], because the Neumann boundary condition, in general, prevents the eigenvalues from being strictly decreasing functions the domain length. Nevertheless, we can still conclude that the absence of a conjugate point implies positive eigenvalues, making it a sufficient condition.

# Appendix C

# Proofs

## C.1 Proof Of Result 1

We define the family of related eigenvalue problems

$$\boldsymbol{\mathcal{S}}\phi = \rho\phi,\ \phi(\beta) = 0,\ \phi'(a) = 0 \tag{C.1.1}$$

for the variable endpoint $a$, with $\beta < a \leq 1$. It is known that the eigenvalues $\rho_i$, $i = 1, 2, \ldots$, move continuously with respect to continuous changes in $a$ [150, 181]. The basic idea of the test is that if there is a small enough $a$ where all eigenvalues are positive, then for an eigenvalue of the problem (C.1.1), with $a = 1$, to be negative, it must cross zero as $a$ varies between $\beta$ and 1. This condition can be checked with a simple test.

To look for an eigenvalue at zero in any of the related problems (C.1.1), we assume that zero is an eigenvalue, with eigenvector $h$, by setting $\boldsymbol{\mathcal{S}}h = 0$, i.e. we set $-h'' + \lambda\cos(\theta)h = 0$. It follows that there exists a length $\sigma$ for which $\boldsymbol{\mathcal{S}}h = 0$, $h(\beta) = 0$, and $h'(\sigma) = 0$. Since we do not know $\sigma$, we begin at the proximal boundary, where we know that $h(\beta) = 0$. Because $\boldsymbol{\mathcal{S}}$ is linear, the eigenvectors have arbitrary scale, so that if $h$ is an eigenvector, $h'(\beta)$ may be arbitrarily chosen by scaling ($h$ must be non-trivial). We choose $h'(\beta) = 1$, and integrate the differential equation forward. In doing this, we have enforced both the differential form and the proximal boundary of the entire family of operators (C.1.1). If the distal boundary condition $h'(\sigma) = 0$ is not satisfied for any $\sigma$, then zero is not an eigenvalue for any of the operators of the family (C.1.1), contradicting the assumption of an eigenvalue at zero.

Since zero is not an eigenvalue for any of the problems, and if the problem has no negative eigenvalues for a sufficiently small value of $a$, it is not possible that the boundary value problem on the whole interval has a negative eigenvalue by continuity of the spectrum with changes in the

interval endpoint $a$.

To see that no eigenvalues are negative for small $a$, note that $\boldsymbol{\mathcal{S}}$ can be decomposed into $\boldsymbol{\mathcal{S}} = \mathcal{T} + \mathcal{Q}$, with $\mathcal{T}h = -h''$ and $\mathcal{Q}h = \lambda\cos(\theta)h$. As $a$ becomes smaller, it is known that the eigenvalues of $\mathcal{T}$ become larger. The operator $\mathcal{Q}$ can be seen as a perturbation of $\mathcal{T}$, and when the eigenvalues of $\mathcal{T}$ are made sufficiently large by choosing $a$ sufficiently small, the perturbation $\mathcal{Q}$, being bounded in magnitude, is incapable of moving an eigenvalue negative. The argument of this paragraph is made rigorously by Hoffman and Manning in [149].

## C.2 Proof Of Result 2

We begin by showing that the eigenvalues of the problem are positive when the boundary conditions at $L$ are moved to be close to the boundary conditions at $\beta$. Here the allowable variation $h_i$ belongs to the space $\mathcal{D}_i([\beta_i, a_i]) = \{f, (k_{it}f') \in AC([\beta_i, a_i]) : f(\beta_i) = 0, (k_{it}f')(a_i) = 0\}$, and the collection $\boldsymbol{h}$ belongs to the Cartesian product $\mathcal{D}(\boldsymbol{\mathcal{S}}) = \mathcal{D}_1 \times ... \times \mathcal{D}_n$. Consider the eigenvalue problem in which $a_i = \beta_i + \epsilon$ for some small $\epsilon$. Then, we still have the decomposition of $\boldsymbol{\mathcal{S}}$ as in the proof of Theorem 1 as $\boldsymbol{\mathcal{S}} = \mathcal{T} + \mathcal{Q}$. The operator $\mathcal{T}$ acts diagonally on the $h_i$, and so the eigenvalues $\gamma$ of $\mathcal{T}\boldsymbol{h} = \gamma\boldsymbol{h}$ may be found as the eigenvalues of $n$ independent problems. The eigenvalues are positive and the smallest eigenvalue can be made arbitrarily large by the choice of $\epsilon$. Consider the extension of $h_i$ to the whole interval $[\beta, L]$, where it must be that $h(\beta) = h(\beta_i)$ and $h'(L) = h'(\beta_i + L_i)$ since the two-point extension of (1.18) simulates the tubes as having infinite torsional stiffness and zero bending stiffness in the regions $[\beta, \beta_i]$ and $[\beta_i + L_i, L]$. The operator $\mathcal{Q}$ is identically the zero operator over the interval $[\beta, \beta_{max}]$ due to the restriction of equation (4.2) and the form of $\mathbf{F}_{\psi\psi}$. The extended domain of the operator will be called $\mathcal{D}_{[\beta,L]}(\boldsymbol{\mathcal{S}})$. We will refer to $\boldsymbol{h}$ as the extension, since any solution on the domain $\mathcal{D}(\boldsymbol{\mathcal{S}})$ can be extended to a solution on the domain $\mathcal{D}_{[\beta,L]}(\boldsymbol{\mathcal{S}})$. The eigenvalues of $\boldsymbol{\mathcal{S}}$ do not change during the extension to the left when all $\beta_i$ are moved to the left to $\beta$. The eigenvalues may change as all $a_i$ which are less than $\beta_{max}$ are increased to $\beta_{max}$, but all remain strictly greater than zero since the equations are decoupled and still of the form $\mathcal{T}\boldsymbol{h} = \gamma\boldsymbol{h}$. Finally, the eigenvalues may change by a bounded amount as the

$a_i$ are increased to $\beta_{\max} + \epsilon$, but by choice of $\epsilon$ we can guarantee that this change will not cause the eigenvalues to become negative. Thus, there is some domain for which the eigenvalues are all positive. As $a_i$ are then increased together, $a_i = a \to L$, if an eigenvalue crosses zero we have a sub-problem on the interval $[\beta, a]$ for which $\boldsymbol{\mathcal{S}}\boldsymbol{h} = 0$ has a non-trivial solution $\boldsymbol{h}$, which is to say that there is a choice of constants $\boldsymbol{c}$ with $\boldsymbol{c} \neq \mathbf{0}$ so that $\mathbf{H}_{22}(a)\boldsymbol{c} = 0$, and therefore $\boldsymbol{h}(s) = \mathbf{H}_{12}\boldsymbol{c}$ is an eigenvector with eigenvalue zero. If, on the other hand, we do not have $\det \mathbf{H}_{22}(a) = 0$ for any $a$, then it must be that if zero is not an eigenvalue of $\boldsymbol{\mathcal{S}}\boldsymbol{h} = 0$ on any interval $[\beta, a]$, and since the spectrum changes continuously with $a$, $\det \mathbf{H}_{22} > 0$ on the whole interval thus guarantees that $\boldsymbol{\mathcal{S}}$ has only positive eigenvalues on the whole domain $[\beta, L]$.

The proof tacitly assumes that the eigenvalues move continuously with changes in the endpoint of the interval on which $\boldsymbol{\mathcal{S}}$ is defined, which is known to be true for the scalar Sturm-Liouville problem [181]. It is reasonable to assume this remains true for the matrix problem due to the fact that the resolvent operators of $\boldsymbol{\mathcal{S}}$ on different domains with "close" endpoints are close in precise sense. For a discussion of resolvent convergence in the context of Sturm-Liouville problems, see for example [183].

## C.3 Proof of Corollary 4

The stability metrics are determined by behavior of solutions to an ODE of the following form

$$\mathbf{H}' = \begin{bmatrix} \mathbf{0} & \mathbf{D} \\ \mathbf{F} & \mathbf{0} \end{bmatrix} \mathbf{H}, \tag{C.3.1}$$

where $\mathbf{H} \in \mathbb{R}^{2n \times 2n}$, $\mathbf{D} \in \mathbb{R}^{n \times n}$, with $\mathbf{D} = \mathbf{D}^T$, and $\mathbf{F} \in \mathbb{R}^{n \times n}$, with $\mathbf{F} = \mathbf{F}^T$. To analyze this system, we partition the matrix $\mathbf{H}$ into four equal size blocks

$$\mathbf{H} = \begin{bmatrix} \mathbf{H}_{11} & \mathbf{H}_{12} \\ \mathbf{H}_{21} & \mathbf{H}_{22} \end{bmatrix} \tag{C.3.2}$$

We have two solutions to this equation, $\mathbf{A}$ and $\mathbf{B}$, with the initial conditions $\mathbf{A}(0) = \mathbf{I}$ and $\mathbf{B}(1) = \mathbf{I}$. We aim to prove that $\det \mathbf{A}_{11}(1) = \det \mathbf{B}_{22}(0)$. Because of the full-rank initial condition $\mathbf{A}(0) = \mathbf{I}$, we may form the state transition matrix $\Phi(t,s) = \mathbf{A}(t)\mathbf{A}^{-1}(s)$. Then, we have the following solutions:

$$\begin{aligned} \mathbf{A}(1) &= \Phi(1,0)\mathbf{A}(0) \\ \mathbf{B}(0) &= \Phi(0,1)\mathbf{B}(1) \end{aligned} \tag{C.3.3}$$

Examining $\mathbf{B}(0)$ more closely, we find that due to the initial conditions,

$$\mathbf{B}(0) = \mathbf{A}^{-1}(1). \tag{C.3.4}$$

Consider the block form of $\mathbf{A}^{-1}$, as

$$\mathbf{A}^{-1} = \begin{bmatrix} \tilde{\mathbf{A}}_{11} & \tilde{\mathbf{A}}_{12} \\ \tilde{\mathbf{A}}_{21} & \tilde{\mathbf{A}}_{22} \end{bmatrix}. \tag{C.3.5}$$

Then, we have that $\mathbf{B}_{22}(0) = \tilde{\mathbf{A}}_{22}$. We form the differential equation on $\mathbf{A}^{-1}$, as

$$(\mathbf{A}^{-1})' = -\mathbf{A}^{-1} \begin{bmatrix} \mathbf{0} & \mathbf{D} \\ \mathbf{F} & \mathbf{0} \end{bmatrix} \mathbf{A}\mathbf{A}^{-1} = -\mathbf{A}^{-1} \begin{bmatrix} \mathbf{0} & \mathbf{D} \\ \mathbf{F} & \mathbf{0} \end{bmatrix} \tag{C.3.6}$$

Now, due to the symmetry of $\mathbf{D}$ and $\mathbf{F}$ we consider the transpose of this equation,

$$\begin{bmatrix} \tilde{\mathbf{A}}_{11}^T & \tilde{\mathbf{A}}_{21}^T \\ \tilde{\mathbf{A}}_{12}^T & \tilde{\mathbf{A}}_{22}^T \end{bmatrix}' = - \begin{bmatrix} \mathbf{0} & \mathbf{F} \\ \mathbf{D} & \mathbf{0} \end{bmatrix} \begin{bmatrix} \tilde{\mathbf{A}}_{11}^T & \tilde{\mathbf{A}}_{21}^T \\ \tilde{\mathbf{A}}_{12}^T & \tilde{\mathbf{A}}_{22}^T \end{bmatrix} \tag{C.3.7}$$

Thus we see that

$$\begin{aligned} (\tilde{\mathbf{A}}_{22}^T)' &= -\mathbf{D}\tilde{\mathbf{A}}_{21}^T \\ (\tilde{\mathbf{A}}_{21}^T)' &= -\mathbf{F}\tilde{\mathbf{A}}_{22}^T \end{aligned} \tag{C.3.8}$$

with initial conditions $\tilde{\mathbf{A}}_{22}^T(0) = \mathbf{I}$ and $\tilde{\mathbf{A}}_{21}^T(0) = \mathbf{0}$ due to the initial condition $\mathbf{A}(0) = \mathbf{I}$. Now, note that the differential equations which govern $\mathbf{A}_{11}$ are

$$\begin{aligned} \mathbf{A}_{11}' &= \mathbf{D}\mathbf{A}_{21} \\ \mathbf{A}_{21}' &= \mathbf{F}\mathbf{A}_{11} \end{aligned} \tag{C.3.9}$$

with initial conditions $\mathbf{A}_{11}(0) = \mathbf{I}$ and $\mathbf{A}_{21}(0) = \mathbf{0}$. A change of variables on equation (C.3.8) which lets $\mathbf{V} = -\tilde{\mathbf{A}}_{21}^T$ so that the negative signs become flipped in (C.3.8), yields exactly the same system on $\tilde{\mathbf{A}}_{22}^T$ as on $\mathbf{A}_{11}$, and so we have by the existence and uniqueness theorems on IVPs that $\mathbf{A}_{11}(1) = \tilde{\mathbf{A}}_{22}^T(1)$. Finally, we have that

$$\mathbf{B}_{22}(0) = \mathbf{A}_{11}^T(1) \tag{C.3.10}$$

and thus we are guaranteed that $\det \mathbf{B}_{22}(0) = \det \mathbf{A}_{11}(1)$, as was to be proven.